Conformational Changes Of Vinculin Tail Upon F-Actin And Phospholipid Binding Studied By EPR Spectroscopy

Dissertation

submitted for the degree of
Dr. rer. nat. (Doctor of Natural Sciences)
in the Department of Physics
University of Osnabrueck, Germany

by

Dipl.-Phys. Christoph Abé

UNIVERSITÄT OSNABRÜCK

2010

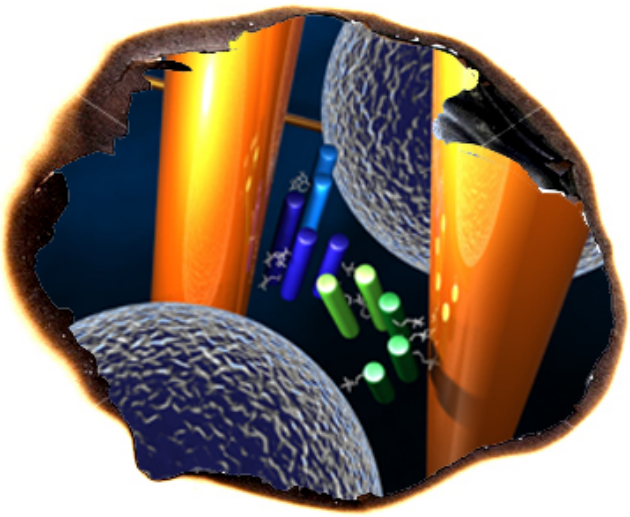

"Exercise your human mind as fully as possible, knowing it is only an exercise. Build beautiful artifacts, solve problems, explore the secrets of the physical universe, savor the input from all the senses, feel the joy and sorrow, the laughter, the empathy, compassion and tote the emotional memory in your travel bag."

(*Ryan Power in Waking Life*)

Contents

1 Introduction and Motivation **1**

2 Background Information **3**

2.1 Cell migration and adhesion 3
2.2 Vinculin: state of the art 5
2.2.1 Vinculin structure 5
2.2.2 Vinculin function and regulation 7
2.2.2.1 Vinculin tail and acidic phospholipids 7
2.2.2.2 Vinculin tail and F-actin 7
2.2.2.3 Competition between F-actin and acidic lipids . 9
2.3 The methodology of SDSL and EPR spectroscopy 10
2.4 Aim of this work 13

3 EPR Spectroscopy **15**

3.1 The electron spin 15
3.2 The MTSSL and the total spin Hamiltonian 17
3.2.1 The MTS spin label 17
3.2.2 The total spin Hamiltonian 18
3.2.3 Electron Zeeman interaction and g-anisotropy 18
3.2.4 Nuclear Zeeman interaction 21
3.2.5 Hyperfine interaction and A-anisotropy 21
3.2.6 Electron-Electron dipolar interaction 24
3.2.7 Heisenberg spin exchange 25
3.3 Continuous wave (*cw*) EPR 27
3.3.1 Single crystal and powder spectra 27
3.3.2 Side chain dynamics and mobility measurements 29
3.3.2.1 Mobility regimes 29
3.3.2.2 Mobility parameters 32
3.3.3 Polarity and distance measurements 34
3.3.3.1 Polarity measurements 34
3.3.3.2 Distance determination 36
3.3.3.3 Low temperature *cw*-spectra fitting 36
3.3.4 Accessibility measurements 37
3.3.4.1 Collision reagents and relaxation times 37

3.3.4.2 Theoretical background and accessibility parameters . . . 39
3.3.4.3 The immersion depth parameter Φ . . . 41
3.4 Pulse EPR . . . 43
3.4.1 Distance measurements with DEER spectroscopy . . . 43
3.4.2 Orientation selective DEER (OS-DEER) spectroscopy . . . 51
3.4.2.1 Orientation selectivity of the applied pulses . . . 51
3.4.2.2 Orientationally uncorrelated spin pairs . . . 53
3.4.2.3 Fully correlated spin pairs and OS-DEER . . . 53

4 Material and Methods **57**
4.1 EPR measurements and procedures . . . 57
4.1.1 Sample preparations . . . 57
4.1.1.1 Vt preparation . . . 57
4.1.1.2 Vt in lipid vesicle solutions . . . 58
4.1.1.3 F-actin binding assay . . . 59
4.1.1.4 Lipid and F-actin competition measurements . . . 60
4.1.2 *Cw*-EPR measurements . . . 60
4.1.2.1 Mobility measurements . . . 60
4.1.2.2 Accessibility measurements . . . 61
4.1.2.3 Polarity and distance measurements . . . 62
4.1.3 Pulse EPR measurements . . . 62
4.1.3.1 DEER spectroscopy . . . 62
4.1.3.2 OS-DEER spectroscopy . . . 63
4.1.3.3 OS-DEER data analysis . . . 63
4.2 Other computational methods . . . 67
4.2.1 MD simulation . . . 67
4.2.2 The rotamer library analysis . . . 69
4.2.3 Determination of the molecular alignment within the Vt-dimer . . . 70
4.3 Fluorescence laser scanning microscopy . . . 73

5 Results and Discussion **75**
5.1 Vinculin Tail structure in aqueous buffer solution . . . 75
5.1.1 Mobility measurements . . . 75
5.1.2 Polarity and accessibility measurements . . . 77
5.1.2.1 Accessibility measurements . . . 77
5.1.2.2 Polarity determination . . . 79
5.1.3 Rotamer analysis . . . 80
5.1.4 Distance determination on Vt double mutants . . . 82
5.1.4.1 EPR distance measurements . . . 82

5.1.4.2 RLA and MD distance distributions 87
5.1.5 Distance measurements on Vt single mutants reveal dimerization 91
5.1.5.1 DEER measurements on Vt single mutants . . . 91
5.1.5.2 Determination of the molecular alignment within the Vt dimer 94
5.2 Structure of Vinculin Tail bound to acidic lipids 103
5.2.1 Mobility measurements 103
5.2.2 Polarity and accessibility measurements 106
5.2.2.1 System calibration 106
5.2.2.2 Accessibility measurements 108
5.2.2.3 Polarity measurements 110
5.2.3 Distance determination 112
5.2.3.1 Singly labeled Vt 112
5.2.3.2 Doubly labeled Vt 115
5.2.4 Molecular model of Vt bound to PS-lipids 119
5.3 Structure of Vinculin Tail bound to F-actin 123
5.3.1 Mobility measurements 123
5.3.2 Polarity measurements 126
5.3.3 Distance measurements 128
5.3.3.1 *Cw*-EPR distance measurements 128
5.3.3.2 DEER distance measurements 130
5.3.4 Molecular model of Vt bound to F-actin 137
5.4 Competition between F-actin and acidic lipids 145
5.4.1 EPR spectroscopy 145
5.4.2 Fluorescence laser scanning microscopy 149
5.5 Orientation selective DEER measurements 151
5.5.1 Experimental results 151
5.5.2 Pake pattern simulation and spectra analysis 153
5.5.3 Comparison between OS-DEER results and RLA 157

6 Summary and Outlook **163**

7 Appendix **169**
literature . . . . . A

1 Introduction and Motivation

Embryogenesis, tissue regeneration, wound healing and immune response are very important processes for the development of eukaryotic multicellular organisms and their maintenance. These processes are based on cell adhesion and cell migration events. The ability of cells to link the actin cytoskeleton to the cell adhesion protein receptors is necessary for this function. Malfunctions occurring in these processes promote e.g. the formation of tumor cells and metastases [20]. The cytoskeletal protein vinculin plays a key role in the control of cell-cell or cell-matrix adhesions [82]. It is involved in the assembly and disassembly of focal adhesions and affects their mechanical stability. It was shown that vinculin deficiency leads to embryonical lethality. Vinculin-null mice died after day 8 of embryogenesis caused by defects in neuronal and heart development [81]. Furthermore, it is known that vinculin can influence apoptosis (programmed cell death) and plays a pivotal role in the control of cell rigidity, motility and tension [76, 50, 51], suggesting an impact of vinculin expression on tumour development and metastasis formation. While many facts highlight the importance and significance of vinculin for vital processes, its precise role in the regulation of cell adhesions is still only partially understood and requires further elucidation at the molecular level.

Clarifying protein structures contributes extensively to the understanding of their functionality. At the present day, the stage of medical design would not have been so highly developed without this knowledge. Most of the available protein structures ($\approx$ 90 percent) have been determined by X-ray crystallography. This method allows the determination of the 3D density distribution of electrons in crystallized proteins, whereby the 3D coordinates of protein atoms can be determined up to sub-atomic resolutions. Nuclear Magnetic Resonance (NMR) techniques are also used for protein structure determination. The percentage of the known protein structures clarified by NMR methods accounts to roughly nine percent. A further approach, which has recently become a valuable mean of determining protein structures, is cryo-electron microscopy (cryo-EM). This method is well applicable on very large protein complexes and enables 3D reconstructions of these complexes. One of the disadvantages of Cryo-electron microscopy is the minor resolution of ca. 0.8 nm. This fact prohibits for example the determination of small structural changes and protein

side chain orientations.
The here applied approaches of *cw*- and pulse electron paramagnetic resonance (EPR) spectroscopy in combination with site directed spin labeling (SDSL) has evolved as a valuable tool to study protein structures and conformational changes [3]. This method provides detailed information on protein structure and dynamics and has become one of the most powerful tools to investigate proteins under more physiological conditions [13], compared to e.g. X-ray crystallography.
Various EPR methods are used in this work in order to study the vinculin tail domain in an aqueous buffer solution and its structural changes induced by the interaction with binding partners such as F-actin and acidic lipids.

2 Background Information

2.1 Cell migration and adhesion

The central process of the movement of single cells or cell groups during the development and maintenance of living organisms is called cell migration. Cell migration is coordinated by adhesion protein complexes linking the cell cytoskeleton with the adhered substrate ("extracellular matrix", ECM). These complexes occur in different cell regions. The stable elongated focal contacts in outer cell regions are called focal adhesions, which are mediated by transmembrane proteins belonging to the family of integrins. These proteins have mechanical connections with the actin-cytoskeleton. Figure 2.1 shows a schematic view of this interaction.

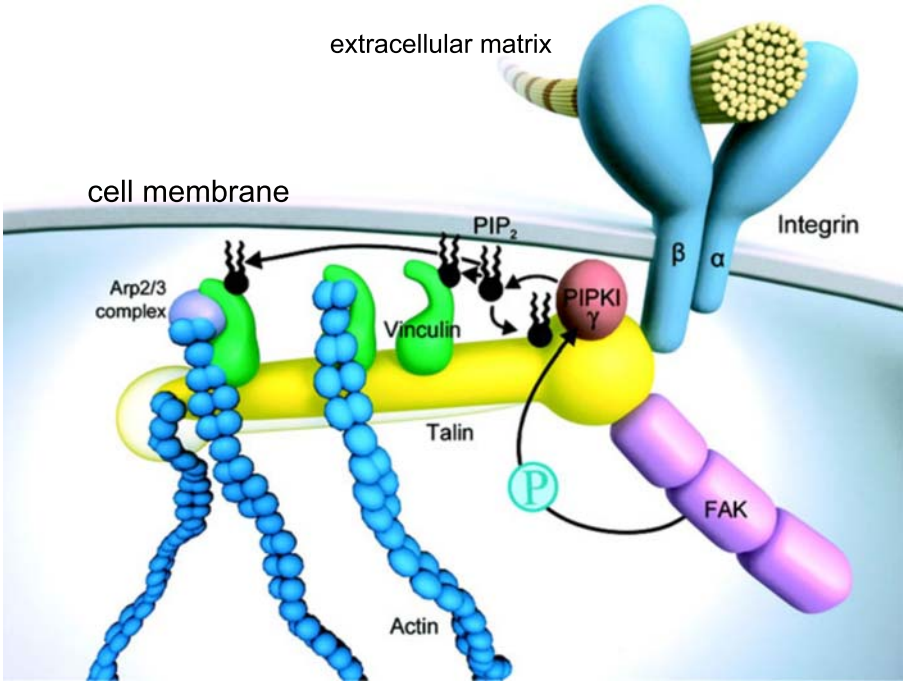

Figure 2.1: Sketch of a cell adhesion site. The cell anchors on an extracellular matrix via integrin, which connects the ECM (here e.g. a collagen fibre) with the actin-cytoskeleton with the help of talin and vinculin. Modified from [14].

Integrin, consisting of α - and β -subunits, binds to proteins of the ECM and in the cell interior to talin, which besides other proteins acts as a linker to the

actin filaments (F-actin). Vinculin acts as adaptor protein, which binds via its head domain to talin, and the tail domain to F-actin. Thus, this protein creates a linkage between the adhesion protein complexes and actin filaments and, in addition, stabilizes the focal contacts [82]. Figure 2.2 shows a fluorescence microscopy image of a cell adhered to a substrate. The picture shows the distribution of vinculin and actin in cell adhesion regions. Vinculin and actin rich regions are identified by green and red colors, respectively, distinguishable by the use of different fluorescence markers. It is obvious that filamentous actin extends throughout the whole cell, whereas vinculin is highly present perinuclear and at focal adhesion sites.

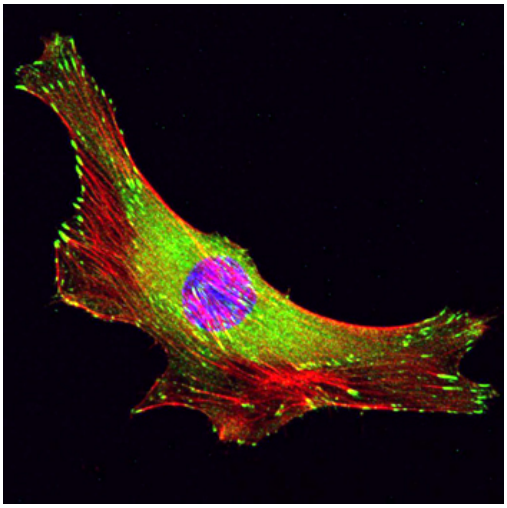

Figure 2.2: Focal adhesions: vinculin (green), actin (red), cell nucleus (blue) in a myoblast cell. Image by Zeinab Al-Rekabi [www.pellinglab.net]

Beside others, the binding of vinculin to F-actin allows the mechanical coupling of cell matrix adhesions with the actin cytoskeleton, which plays a major role in the highly orchestrated multistep process of cell migration. To put it simply, at the cell front (leading edge) actin assembly drives the extension of membrane protrusions (lamellipodia and filopodia). At the leading edge of the cell adhesions are formed, which connect the extracellular matrix to the actin cytoskeleton to anchor the protrusion and tract the cell body. Finally, to move forward, the cell retracts its trailing edge by combining actomyosin (actin-myosin-complexes) contractility and disassembly of adhesions at the rear [17]. These processes are associated with the strongly regulated and frequently occurring assembly and disassembly events of cell-matrix contacts.

2.2 Vinculin: state of the art

2.2.1 Vinculin structure

Vinculin, consisting of 1066 amino acids, is a 116 kDa, ubiquitously expressed actin-binding protein, which is localized on the cytoplasmic face of integrin-mediated cell-extracellular matrix junctions (focal adhesions) and cadherin-mediated cell-cell junctions. It is made up of a globular head (domains D1-D4), linked to a tail domain (Vt, also called domain D5) by a proline-rich region (figure 2.3 a)) [82, 6].

a)

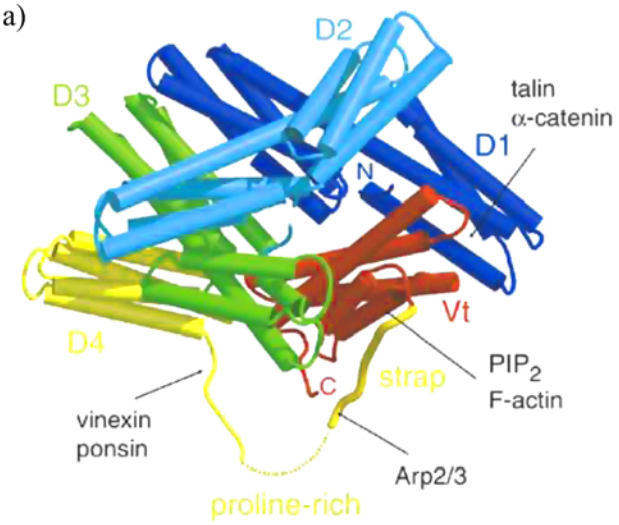

b)

Ligand	Vinculin domain
Talin	D1
α-Actinin	D1
IpaA	D1
α-Catenin	D1–D3
β-Catenin	D1–D3
(intra.)	D1 and D4
Vinexin	PRR
Ponsin	PRR
VASP	PRR, FPPPP
Arp 2/3	PRR, P876/P878
Paxillin	Vt (D5)
F-actin	Vt (D5)
PKCα	Vt (D5), C-terminal arm
Acidic phospholipids	Vt (D5)

Figure 2.3: a):Crystal structure of full-length vinculin in its auto-inhibited state. The particular Domains are shown in different colors: D1, residues 6-252; D2, 253-485; D3, 493-717; D4, 719-835; D5 (Vt), 896-1066. The proline-rich region (838-878) precedes a strap (residues 878-890) located across the surface of Vt and the C terminus (C). Binding sites are indicated. Picture taken from [6]. b): Binding partners of vinculin, extracted from [82]. Abbreviations: PRR: proline-rich region, FPPPP: PheProProPro-Pro motif.

The crystal structure of full length vinculin was recently determined revealing several binding sites to be obscured by parts of other molecular domains [6]. Especially, the actin binding vinculin tail (Vt) domain is grabbed in a pincer-like manner by domains D1-D3 and remains in an auto-inhibitory and inactive conformation due to the intramolecular interaction between the head and tail domain. This situation inhibits the release of Vt from the vinculin head, sterically blocking its interaction with F-actin [6, 37]. In addition, the contacts between Vt and D1 inhibit the conformational changes in D1, that would allow the binding of talin. This fact points out that an activation mechanism accompanied with structural changes within vinculin is required to allow ligand interaction, thus to facilitate its function. Furthermore, vinculin head

binds Vt with very high affinity ($K_d < 10^{-9}M$ [82]). This binding is thought to be too strong for a single ligand to activate vinculin leading to the proposal of a combinatorial activation mechanism requiring at least two binding partners [18, 6]. However, the activation mechanism, as well as details about accompanied structural changes within vinculin, are still unresolved.
Vinculin exhibits numerous ligand binding sites. These interaction sites have been assigned to different domains, extractable from figure 2.3 b). Domain D1 exhibits binding sites for talin, α-catenin and α-actinin. the proline-rich region located between D4 and Vt binds to VASP, vinexin, ponsin and the Arp2/3 complex. Vt was found to bind besides others actin and acidic lipids, such as phosphatidylserine (PS) and Phosphatidylinositol-4,5-bisphosphate (PIP_2) [82]. The main focus of this work is the Vt domain, therefore, its structure and function is discussed in more detail.

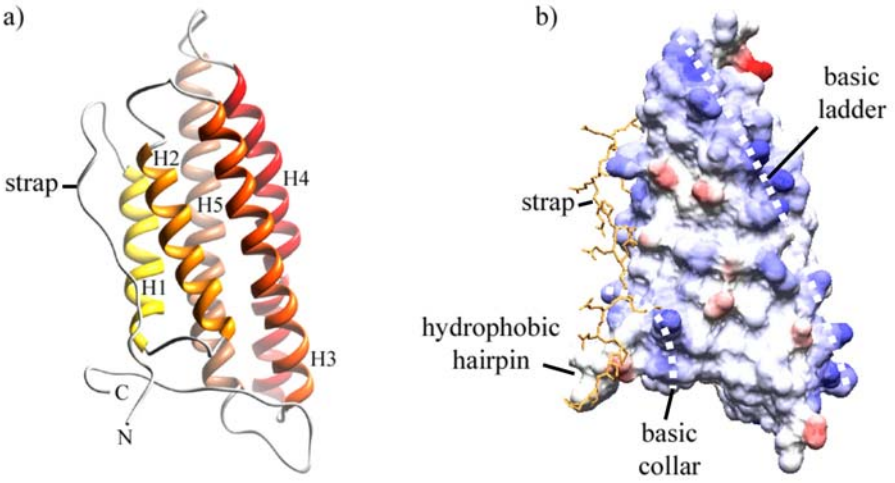

Figure 2.4: a): Crystal structure of Vt in ribbon representation (pdb: 1ST6). The five amphipathic and antiparallel helices are connected via short loops regions. The particular helices are highlighted by different colors: helix one (H1): yellow, helix two (H2): light orange, helix three (H3): orange, helix four (H4): red, helix five (H5): dark red. b): Solvent-accessible surface of Vt. The coloring is according to electrostatic potential: blue for positive, red for negative charges. Salient features are indicated.

The crystal structure reveals Vt to form a bundle of five antiparallel α-helices exhibiting N- and C-terminal extensions [7]. The five amphipathic helices are connected via short (3-8 amino acids) loop regions and their hydrophobic faces are pointing into the protein interior. Due to the amino acid composition helices 1-4 are characterized as alkaline. In contrast, helix 5 is categorized as acidic. Two main regions on the outer surface of Vt are positively charged. This is on one side the *basic ladder* (residues 945-973) located in helix 3, whereas the C-terminal *basic collar* (including amino acids 910, 911, 1049, 1060, and

1061) together with the hydrophobic hairpin (C-terminal residues 1062-1066) constitute the second positively charged main region (figure 2.4) [7].

2.2.2 Vinculin function and regulation

2.2.2.1 Vinculin tail and acidic phospholipids

Being part of cell membranes, acidic phospholipids, such as PS and PIP_2, play an essential role in cell migration. They are of great importance in the regulation of the assembly and disassembly of focal contacts, and assist the linking of the actin-cytoskeleton with the cell membrane, e.g. by exposing the integrin-binding site on talin [45]. The association of PIP_2 to Vt is thought to dissociate the head to tail interaction, exposing binding sites for talin and actin, and thereby promoting assembly of focal adhesions [7, 24]. The *basic ladder*, the *hydrophobic hairpin* and the *basic collar* regions are supposed to mediate the first contact to acidic lipids or the lipid membrane, respectively. In turn, the hydrophobic hairpin is thought to insert into the lipid bilayer, resulting in an unfurl of its five-helix bundle [7, 6]. Experiments with vinculin-LD, deficient in acidic phospholipid binding yet with functional actin binding sites, show that PIP_2 binding is not essential for vinculin activation as previously suggested. Instead, it is proposed that PIP_2 regulates the uncoupling of adhesion sites from the actin cytoskeleton with vinculin functioning as a sensor [16]. Moreover, recently it was shown that talin and α-actinin are involved in vinculin activation [53, 12], and that vinculin phosphorylation plays an important role in vinculin activation, stabilization and ligand binding. Enhancing vinculin exchange by phosphorylation at amino acid Y1065 leads to a mechanical destabilization of the whole adhesion complex [49].
However, the importance of the interaction of acidic lipids and vinculin for its function in cell migration processes is indisputable. As it could be shown by biochemical cross-link experiments, PS or PIP_2 even induce Vt dimer- and/or higher oligomerization [28], but detailed structural models of vinculin tails conformation bound to acidic lipids are still not available and remain to be revealed.

2.2.2.2 Vinculin tail and F-actin

Vinculin binds to F-actin, enabling the connection of the cytoskeleton to the cell membrane at focal adhesion sites. Therefore, as already mentioned, vinculin has to undergo a conformational change to expose the actin binding sites in Vt. The work of Bakolitsa et al. [7] supports a conformational change in Vt upon actin binding. Johnson et al. demonstrated the existence of a dimerization site in Vt, which is activated upon binding to F-actin [38]. Hence, binding of F-actin to the vinculin tail promotes Vt dimerization and thereby actin cross-linking

[82].

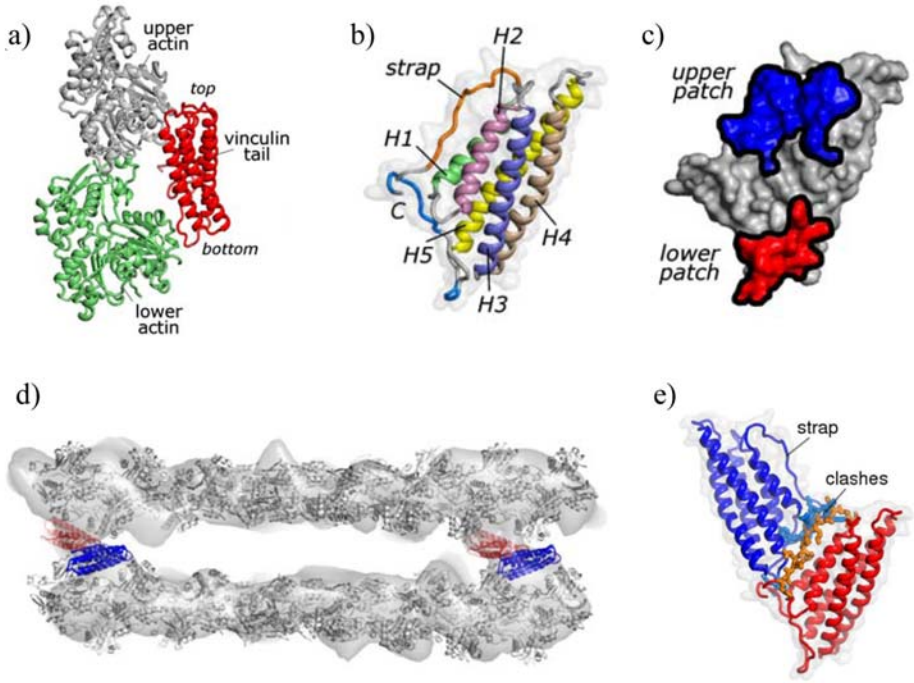

Figure 2.5: a): Model of a Vt molecule (red) in contact with two actin monomers along the filament (gray and green). The top and the bottom of the Vt helix bundle are indicated. b): Vt structure in ribbon representation, c): Solvent-exposed surface representation of Vt mapped with the actin-contacting residues (upper patch: blue, lower patch: red). Orientation is the same as in b). d): Two actin filaments (gray) with attached vinculin-tail molecules docked into the tomographic cryo-EM reconstruction. e): Enlarged view of the vinculin-tail dimer extracted from d). Molecular clashes between the two Vt molecules are marked in orange and indicate small structural changes in the clash-involved domain of Vt. Pictures taken from [33]

Janssen et al. recently introduced a three-dimensional model of the Vt-dimer bound to actin filaments [33]. They showed that the actin-binding site on Vt comprises two distinct sub-sites. One binding site is exposed in the auto-inhibited conformation, whereby the second is sterically shielded by the N-terminal domain of vinculin (figure 2.5 a), b), c)). However, they found that the overall five-helix bundle structure of Vt is preserved and that there are no large-scale conformational changes ($\approx$ 1 nm) upon F-actin binding. This model was obtained by cryo-electron microscopy and 3D reconstruction (figure 2.5 d)). The crystal structure of Vt was fitted into the thus obtained 3D electron density map using molecular docking programs leading to the mutual arrangement of the two Vt-molecules within the actin bound Vt-dimer. Their model reveals clashes between the C-terminal loop of one Vt molecule and the N-terminal strap region of the other Vt molecule of the dimer (figure 2.5

e)). Thus, their results implicate a two-step process for F-actin crosslinking in which actin binding of Vt triggers conformational changes in the strap and the C-terminal loop of Vt, which in turn potentiates Vt dimerization. Figure 2.6, taken from Janssen et al., provide an overview about their and several previous works by mapping different contact and mutation sites onto the Vt sequence.

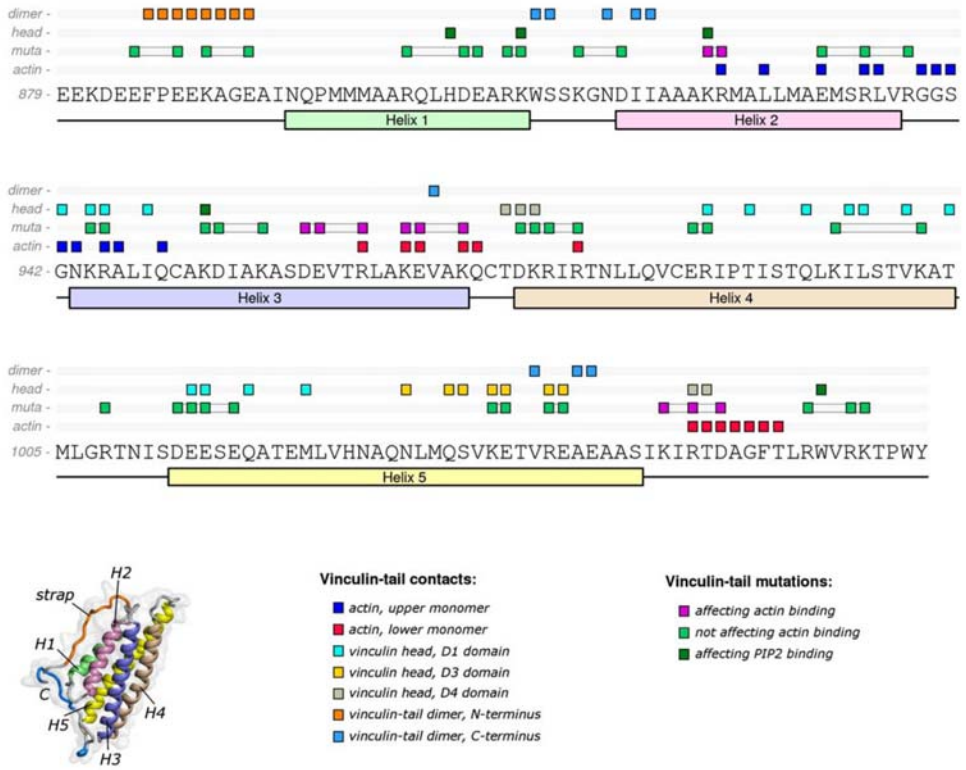

Figure 2.6: Correlations between interaction probabilities, mutations, head-tail and dimer contacts of Vt are shown by mapping these sites (indicated as colored squares) onto the Vt (amino acid) sequence. Picture slightly changed from [33].

However, this method (3D cryo-EM) is restricted in resolution. Especially flexible protein domains can not be resolved with the same accuracy as rigid parts. Thus a determination of detailed structural rearrangements of Vt within the obtained electron density map is very difficult. The detailed structural rearrangement of secondary structure elements and the C- and N-terminal end of Vt upon actin binding is still unknown.

2.2.2.3 Competition between F-actin and acidic lipids

As already mentioned, cell migration processes are strongly associated with the regulation of the frequently assembly and disassembly of cell-matrix-contacts. It is suggested that vinculin, which leaves the focal adhesion, would revert to

the auto-inhibited conformation and re-enter the soluble cytoplasmic pool of inactive vinculin [82]. As already mentioned vinculin phosphorylation plays an important role in these turn over processes. Beside this, the interaction with PIP_2 is proposed to regulate the uncoupling of adhesion sites from the actin cytoskeleton, that is, besides others, the Vt-actin contacts. Furthermore, it is known that phospholipids inhibit the interactions between vinculin and F-actin *in vitro* [73]. Therefore, a competition between actin and acidic phospholipid binding exists, which even induces a disassembly of vinculin in focal contacts and consequently a release of these contacts at high lipid concentrations [25, 16]. This fact shows that F-actin, Vt and acidic phospholipids act in a cooperative manner, which is essential for the assembly and disassembly of focal contacts, enabling cell migration. Consequently, vinculin has continuously to undergo a cycle between actin bound, lipid bound and solubilized states. Nevertheless, how the frequently occurring assembly and disassembly is accomplished or regulated is not well understood at present.

2.3 The methodology of SDSL and EPR spectroscopy

As its name implies, the applicability of electron paramagnetic resonance (EPR) spectroscopy requires paramagnetic species, meaning that only spins of unpaired electrons contribute to the EPR signal. The EPR investigation of proteins, which are usually not of paramagnetic nature, is enabled by the method of site directed spin labeling (SDSL) developed by W. L. Hubbell and coworkers in the 1990s [3, 29]. Figure 2.7 shows a scheme of this methodology. Thereby a synthetic side chain containing a paramagnetic center is site specifically bound to the sulfhydryl group of a cysteine, in case of the commonly used methanethiosulfonate spin label (MTSSL) by means of a disulfide bridge. The cysteine either occurs in the amino acid sequence of the natural wild type protein or can be introduced into the sequence at an arbitrary position by site-directed mutagenesis [77]. In the latter case a mutation in the genetic code of the cells used for protein expression is carried out. After expression, the protein exhibits a cysteine on a wanted position in its amino acid sequence instead of the native amino acid. If unwanted cysteines are present in the protein sequence under investigation, they are usually replaced by alanine or serine residues, if this can be done without impairing protein structure and/or function. Depending on the purpose even more than one spin label can be incorporated.

The size of the commonly used MTSSL is in the range of typical amino acid side chains such as phenylalanine or tryptophane, meaning that the protein structure is in general not disturbed by the attachment of MTSSL on the cysteine. However, the natural wild type structure is modified by this method and

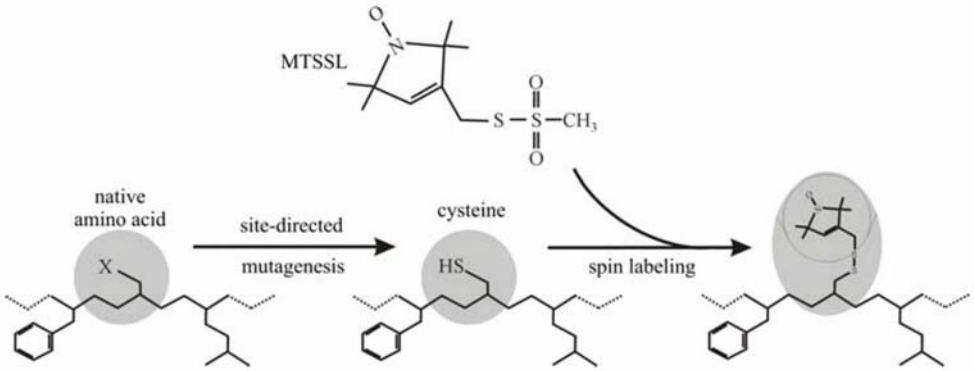

Figure 2.7: The method of site-directed spin labeling. A native amino acid (left) is substituted by a cysteine (center) using site-directed mutagenesis. The cystein is spin labeled with methanethiosulfonate (MTSSL). The figure was adapted from [79].

consequently biological tests are required to assure that the modified proteins are still functional.

SDSL in combination with continuous wave (*cw*) or pulse EPR approaches has evolved as a valuable tool to study protein structures and conformational changes (see [74, 13] for an overview). The methodology of EPR takes advantage of the splitting of normally degenerated spin energy states in a static homogeneous magnetic field. The information can be derived from the resonant absorption of incident microwave radiation. The resonance condition says that the microwave frequency is proportional to the magnetic field strength. At the present day EPR spectroscopy is carried out in the range of 1.5 GHz up to 670 GHz depending on the desired information about the sample under investigation. The most common and in this work used microwave frequency is 9.5 GHz (X-band), which corresponds to a magnetic field strength of approximately 3300 G (330 mT).

The shape of *cw*-EPR spectra recorded at room temperature is sensitive to the reorientational motion of the protein-bound spin label side chain (in the following abbreviated by R1), providing information on the motional restriction of the nitroxide due to sterical interaction with secondary and tertiary structure elements [57, 13]. Power saturation measurements enable the investigation of the spin label accessibility to certain paramagnetic quencher molecules contained in the solvent, or in case of membrane proteins, in the lipid phase. This information can be used to assign different spin labeled positions to be solvent exposed, protein buried, or located in lipid membrane phases. In addition, *cw*-EPR measurements at temperatures below 200 K provide information about the polarity of the spin label environment and furthermore allow the determination of inter spin distances up to 2 nm, whereas pulse EPR methods such as DEER spectroscopy (at 50 K) allow the determination of distances up to 6

nm or even larger [56]. Such distance measurements provide information about protein structure and conformational changes. Detailed information about the aforementioned EPR-applications will be given in chapter 3 and are also described in [74, 56].
Due to the flexibility of commonly used spin label side chains a model for the distribution of nitroxide orientations is helpful for reasonable interpretation of inter-spin distance distributions with respect to the protein structure. Methods to obtain this information are molecular dynamics (MD) simulations and rotamer analysis approaches. MD simulations provide insight into the spin label side chain motion over time, even under consideration of the movement of all protein atoms, thus, taking protein dynamics into account. In general, this well established method leads to reliable results [9, 23]. It is, however, very time-consuming and requires excessive computational resources. A rotamer library approach (RLA), developed by Jeschke and coworkers, predicts spin label conformations for a certain residue position by using a semi-dynamic structure model of the spin label and is computationally much less demanding [60].
Cw SDSL-EPR can also be used for the determination of spin label molecule orientations, for example with respect to a sample support. A wide spread method, applied since decades for this purpose, is the collection of EPR spectra, recorded at different sample orientations with respect to the external magnetic field, yielding the orientational information [66, 32]. Since a few years a new pulse EPR based method is advancing. This method, called *orientation selective* DEER spectroscopy, enables the determination of the mutual orientation of multiple spin label molecules or even the orientation between spin labels and paramagnetic ions [59, 67, 69]. The investigation of spin label (SL) orientations enables, for example, the traceability of structural changes within proteins, since changes of mutual SL orientations reflect reorientations of the labeled protein domains.
One of the advantages of EPR compared to other well established methods like X-ray crystallography is the fact that a crystallized state of the proteins is not necessary, hence, they can be investigated in a more physiological environment, such as aqueous buffer solutions. In summary, SDSL-EPR methods are powerful tools to investigate protein structures and dynamics.

2.4 Aim of this work

Although the crystal structure of vinculin is available, numerous questions about the function and role of the vinculin tail in cell adhesion processes are still unanswered. This work is supposed to contribute to the clarification of the following aspects. The frequently assembly and disassembly of vinculin in focal adhesion sites is accompanied by continuous transitions between different structural states of vinculin, which are strongly associated with and essential for its function. Here, the structural arrangement of vinculin tail bound to F-actin, to acidic lipids and in the absence of these binding partners under conditions close to the physiological ones constitute the focus of this work.
Various *cw*- and pulse EPR methods are used for the investigation of the vinculin tail structure in an aqueous solution and its structural changes due to interaction with acidic lipids and F-actin. The combination of the methods applied enable the construction of new structural models of Vt in the absence and the presence of F-actin and acidic lipids. In addition, the competition between the lipid and actin bound states of Vt is analyzed in dependence of different phospholipid types. The results are supported by laser excited fluorescence microscopy measurements.

Another purpose of this work is the investigation of the applicability of a rotamer library approach (RLA) for the analysis of spin label side chain motions and orientations. Therefore, a comparison between the experimentally obtained results of Vt in solution are used for comparison to the outcome of MD simulations and the computational much less demanding RLA.

A further main part of this thesis deals with orientation selective DEER spectroscopy. Since the methodology and applicability are still advancing and proper data analysis programs are still not available at present, this work shall contribute to their development. Here, this method is used at X-band frequencies, and a tool to determine mutual spin label orientations in proteins is presented and applied.

3 EPR Spectroscopy

EPR spectroscopic experiments are measurements on the electron spin, which is a quantum mechanical phenomenon. Therefore, the mathematical and physical description of EPR is based on quantum mechanics. The degenerated spin energy states (of unpaired electrons) are split in a static homogeneous magnetic field (Zeeman effect). The informations about the paramagnetic probe are derived from the absorption of microwave radiation, which energetically equals the energy difference between the split energy states. The total energy and time evolution of the system under investigation is described by the *spin Hamiltonian*. This quantum mechanical operator providing the theoretical basis for the understanding of the particular EPR methods will be introduced in the first parts of this chapter. Since in this work nitroxide spin labels (MTSSL) are used as spin carrying probes, only interactions between the unpaired electron and its environment relevant to this work, such as *electron Zeeman*, *nuclear Zeeman*, *hyperfine* and *electron-electron* (dipolar and exchange) interactions, are taken into account. Furthermore, the here applied EPR methods used to obtain the particular parameters occurring in the spin *Hamiltonian* are explained in more detail in the following chapters.

3.1 The electron spin

Considering a spin of a free electron in a static, homogeneous magnetic field of the form $\mathbf{B} = (0, 0, B_0)$ the components of the spin operator can be described by:

$$\hat{\mathbf{S}} = (\hat{s_x}, \hat{s_y}, \hat{s_z}) = \frac{1}{2}\left(\begin{pmatrix} 0 & 1 \\ 1 & 0 \end{pmatrix}, \begin{pmatrix} 0 & -i \\ i & 0 \end{pmatrix}, \begin{pmatrix} 1 & 0 \\ 0 & -1 \end{pmatrix}\right) \tag{3.1}$$

The electron spin is accompanied by a magnetic moment $\hat{\mu}_s$:

$$\hat{\mu}_s = -g_e \frac{e\hbar}{2m_e}\hat{\mathbf{S}} \tag{3.2}$$

$$= -g_e \mu_B \hat{\mathbf{S}} \tag{3.3}$$

Here, m_e is the mass of the electron and $g_e = 2.0023$ is the g-factor of the free electron. $\hbar$ describes the Planck constant divided by 2π and $\mu_B = 9.27400915 \cdot 10^{-24} JT^{-1}$ the Bohr magneton. The corresponding energy of a free electron in a magnetic field $\mathbf{B}$ is described by the *Hamiltonian* using the correspondence principle:

$$\hat{\mathbf{H}}_\mathbf{e} = -\hat{\mu}_\mathbf{s} \cdot \mathbf{B} = g_e \mu_B \cdot \hat{\mathbf{s}_\mathbf{z}} \cdot B_0 = \frac{1}{2} g_e \mu_B B_0 \begin{pmatrix} 1 & 0 \\ 0 & -1 \end{pmatrix} \tag{3.4}$$

The energy Eigenvalues and Eigenvectors can be calculated by solving the time independent Schrödinger equation (Eigenvalue equation):

$$\hat{\mathbf{H}} \mid \Psi_n \rangle = E_n \mid \Psi_n \rangle \tag{3.5}$$

, where E_n is the n-th Eigenvalue and $\mid \Psi_n \rangle$ the corresponding Eigenvector or electron wave function, respectively. In the here considered case of the free electron (spin S=1/2) the equation exhibits the following solution:

$$\mid \Psi_1 \rangle := \mid + \rangle = \begin{pmatrix} 1 \\ 0 \end{pmatrix} \qquad \mid \Psi_2 \rangle := \mid - \rangle = \begin{pmatrix} 0 \\ 1 \end{pmatrix} \tag{3.6}$$

$$E_1 = E_+ = +\frac{1}{2} g_e \mu_B B_0 \qquad E_2 = E_- = -\frac{1}{2} g_e \mu_B B_0 \tag{3.7}$$

This shows that an electron in a magnetic field can occupy two different energy states called *spin up* ($\mid + \rangle$) or *spin down* ($\mid - \rangle$) state. Consequently, the microwave frequency, inducing the transition from the *spin up* state into the *spin down* state after absorption, is given by:

$$\nu = \frac{\Delta E}{h} = \frac{E_+ - E_-}{h} = \frac{g_e \mu_B B_0}{h} \tag{3.8}$$

ν is also called Larmor frequency. The EPR resonance condition (equation 3.8) is the fundamental relation between the magnetic field strength B_0 and the incident microwave frequency ν. In *cw*-EPR spectroscopy (see chapter 3.3) the absorption of microwave radiation, exhibiting constant frequency (energy), is detected in dependence of the magnetic field strength. In the here considered theoretically case sweeping the magnetic field using a constant microwave frequency would lead to the observation of only one resonance position located at B_0.

3.2 The MTSSL and the total spin Hamiltonian

3.2.1 The MTS spin label

As it can be seen from equation 3.8 the resonance frequency or the position of B_0 depends on the *Hamiltonian* of the system under investigation. The systems investigated by EPR spectroscopy contain unpaired electrons, but in general they can not be treated as free like in the above considered case. The electrons under investigation are compounds of atoms or molecular structures, thus, they appear in atom or molecular orbitals interacting with their vicinity. In this work the commonly used (1-oxyl-2,2,5,5-tetramethylpyrroline-3-methyl) methanethiosulfonate spin label (MTSSL) is used as the spin carrying molecule. Figure 3.1 a) shows its chemical structure, its three-dimensional structure is depicted in b). It is convenient to define a molecular frame (MTSSL frame) for later considerations. Within this frame the x-axis is defined along the N-O bond of the nitroxide group, the z-axis is aligned parallel to the five-membered ring plane normal and the y-axis is perpendicular to both (see 3.1 b)).

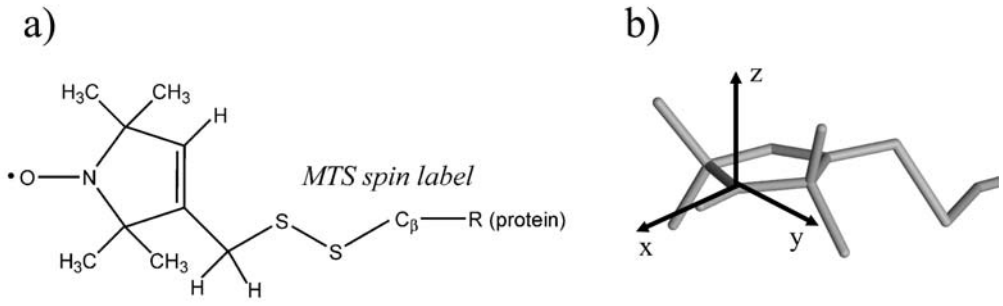

Figure 3.1: a): The chemical structure of the MTS spin label, b): The MTSSL eigensystem. The molecular frame axes are designated with x,y,z.

The electronic structure of the N-O-bond is schematically shown in figure 3.2. The unpaired electron giving the molecule its paramagnetic nature is located in the π-orbital resulting from the partially overlap of the $2p_z$ orbitals of the oxygen and the nitrogen atom.

Due to this fact, the electron underlies several internal interactions, hence, its properties are different from the free electron case. Additionally, Since the unpaired electron experiences other molecules and atoms in its environment, such as other protein atoms and/or atoms contained in the solvent, the spin label vicinity influences the electronic structure of the MTSSL, which it turn changes the electron spin properties. These interactions has to be considered in the EPR-theory in order to understand the EPR spectra shape.

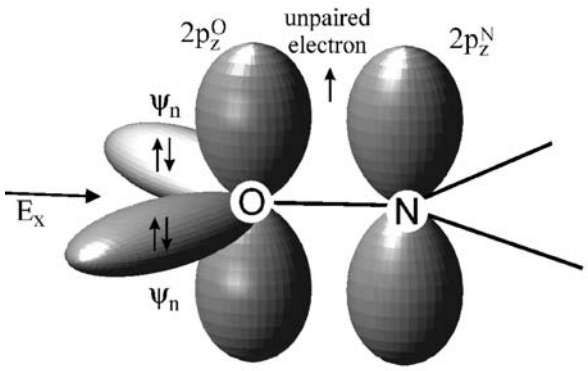

Figure 3.2: Electronic structure (schematic) of the MTSSL N-O bond. An electric field component E_x caused by the MTSSL environment is present. The non-bonding lone pair orbitals Ψ_n are a superposition of oxygen $2s, 2p_x$ and $2p_y$ orbitals: $\Psi_n = c_{ns}(2s) + c_{nx}(2p_x) + c_{ny}(2p_y)$. Graphic adopted and slightly changed from [58].

3.2.2 The total spin Hamiltonian

The most relevant interactions in SDSL-EPR are those between the electron spin and the external magnetic field (electron Zeeman interaction: EZ), magnetic moments from nuclear spins (hyperfine interaction: HF) and other electron spins (dipol-dipol and exchange interaction: DD and Ex). Another relevant interaction is the *nuclear Zeeman* interaction (NZ) describing the interaction between a nuclear spin and the external magnetic field.
Considering these interactions the total *spin Hamiltonian* is the sum of the particular energy contributions and of the form:

$$\hat{\mathbf{H}} = \hat{\mathbf{H}}_{EZ} + \hat{\mathbf{H}}_{NZ} + \hat{\mathbf{H}}_{HF} + \hat{\mathbf{H}}_{DD} + \hat{\mathbf{H}}_{Ex} \tag{3.9}$$

Here, the indices represent the above mentioned interactions. The aim of SDSL-EPR spectroscopy is to obtain information about the spin label and its environment by determination of the parameters occurring in the *Hamiltonian*. In order to understand the here applied EPR methods and analysis of EPR spectra, the terms of the particular interactions contributing to the total *spin Hamiltonian* will be discussed in the following chapters.

3.2.3 Electron Zeeman interaction and g-anisotropy

The electron Zeeman term describes the interaction between an electron and the external magnetic field. The magnetic moment of an electron spin bound to a molecule depends on its orientation with respect to the molecule or of the orientation of the molecule with respect to the magnetic field direction, respectively. This anisotropy arises from the fact that the electron exhibits an

orbital momentum $\hat{\mathbf{L}}$. The orbital momentum interacts with both the external magnetic field $\mathbf{B}$ and the momentum of the spin $\hat{\mathbf{S}}$ (spin orbit coupling):

$$\hat{\mathbf{H}} = g_e \mu_B \hat{\mathbf{S}} \cdot \mathbf{B} + \mu_B \hat{\mathbf{L}} \cdot \mathbf{B} + \lambda \hat{\mathbf{S}} \cdot \hat{\mathbf{L}} \tag{3.10}$$

The first term describes the interaction between the electron and the external magnetic field, and the second the interaction between the magnetic field and the orbital momentum. The third summand describes the spin orbit coupling. λ is the spin orbit coupling constant. The eigenvalues of this *Hamiltonian* can be obtained applying perturbation theory. A detailed calculation can be found in [5]. A *Hamiltonian* exhibiting the same eigenvalues as 3.10 is:

$$\hat{\mathbf{H}}_{EZ} = -\hat{\mu}_{\mathbf{s}} \cdot \mathbf{B} = \mu_B \, \mathbf{B} \, \mathbf{g} \, \hat{\mathbf{S}} \tag{3.11}$$

with:

$$\mathbf{g} = g_e \mathbf{1} + 2\lambda \mathbf{\Lambda} \tag{3.12}$$

and Λ a symmetric tensor with the following elements:

$$\mathbf{\Lambda_{ij}} = \sum_n \frac{\langle \Psi_0 | \, \hat{L}_i \, | \Psi_n \rangle \, \langle \Psi_n | \, \hat{L}_j \, | \Psi_0 \rangle}{E_0 - E_n} \, , n > 0; \; i, j = x, y, z \tag{3.13}$$

Equation 3.11 describes the electron Zeeman interaction and is analogous to the case of a free electron, but in contrast, here, $\mathbf{g}$ describes the g-tensor. The operator $\hat{L}_i$ describes the main axis components of $\hat{\mathbf{L}}$ (i=x,y,z). The function $|\Psi_0\rangle$ describes the singly occupied molecular orbital (SOMO) in the ground state and $|\Psi_n\rangle$ the n-th excited SOMO state. E_0 and E_n are the corresponding energy eigenvalues. The g-tensor has the general form:

$$\mathbf{g} = \begin{pmatrix} g_{xx} & g_{xy} & g_{xz} \\ g_{yx} & g_{yy} & g_{yz} \\ g_{zx} & g_{zy} & g_{zz} \end{pmatrix} \tag{3.14}$$

Within the eigensystem of $\mathbf{g}$ (or $\hat{\mathbf{H}}_{EZ}$ respectively) $\mathbf{g}$ can be diagonalized leading to the expression:

$$\mathbf{g} = \begin{pmatrix} g_{xx} & 0 & 0 \\ 0 & g_{yy} & 0 \\ 0 & 0 & g_{zz} \end{pmatrix} \tag{3.15}$$

This eigensystem is fixed in the system of the molecule exhibiting the spin and can be assigned to the above mentioned MTSSL frame. For a MTSSL label the main diagonal elements can be determined in first approximation according to [58]:

$$g_{xx} \approx g_e + 2\lambda(O)\frac{\rho_\pi^O c_{nx}^2}{E_\pi - E_n} \tag{3.16}$$

$$g_{yy} \approx g_e + 2\lambda(O)\frac{\rho_\pi^O c_{ny}^2}{E_\pi - E_n} \tag{3.17}$$

$$g_{zz} \approx g_e \tag{3.18}$$

, where $\lambda(O) = 151cm^{-1}$ describes the spin-orbit coupling of the oxygen atom. ρ_π^O is the π spin density on the oxygen $2p_z$ atomic orbital. c_{nx} and c_{nx} are molecular orbital coefficients describing the contribution of the $2p_x$ and $2p_y$ atomic orbitals to the oxygen lone pair orbital Ψ_n (see figure 3.2). $E_\pi - E_n$ is the excitation energy for a transition between $|\Psi_0\rangle$ and $|\Psi_n\rangle$ [58]. In order to express the g-tensor in the laboratory frame it has to be transformed into the laboratory system by the use of general *Euler* transformation matrices $D(\vartheta, \varphi, \psi)$. The g-tensor in the laboratory frame has the form:

$$\mathbf{g}_l = D(\vartheta, \varphi, \psi)\mathbf{g}D(\vartheta, \varphi, \psi)^{-1} \tag{3.19}$$

This leads to a g-factor depending on the orientations (ϑ,φ) of the spin carrying molecule with respect to the B-field direction, defining the laboratory z-axis:

$$g_{\vartheta,\varphi} = \sqrt{g_{xx}^2 sin^2\vartheta cos^2\varphi + g_{yy}^2 sin^2\vartheta sin^2\varphi + g_{zz}^2 cos^2\vartheta} \tag{3.20}$$

Figure 3.3 illustrates this transformation from the molecular frame of a nitroxide into the laboratory frame. Typical values for the g-tensor elements of a MTSSL are:

$$g_{xx} \approx 2.0089 \tag{3.21}$$

$$g_{yy} \approx 2.0067 \tag{3.22}$$

$$g_{zz} \approx 2.0023 \tag{3.23}$$

However, the B-field strengths used in this study (ca. 300 mT) are not sufficient to resolve the g-tensor anisotropy in the EPR spectra. Magnetic fields in the order of 3 T (W-band) or higher would be necessary.

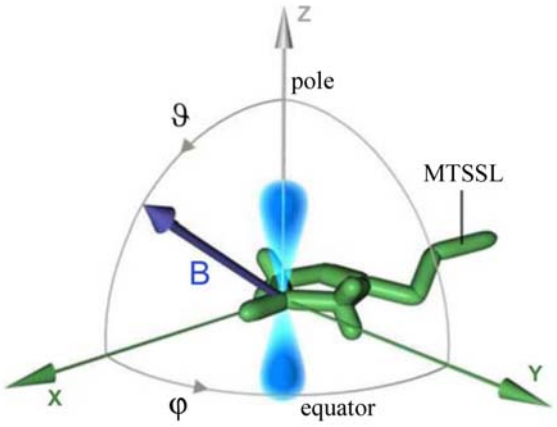

Figure 3.3: The transformation from the MTSSL frame (x,y,z) into the laboratory frame depends on two angle ϑ and φ. The B-field direction (blue arrow) coincides with the laboratory z-axis. The $2p_z$ orbital of the nitrogen atom of the MTSSL is illustrated in light blue.

3.2.4 Nuclear Zeeman interaction

In most EPR experiments the nuclear Zeeman interaction describing the coupling of a nuclear spin and the external magnetic field contributes insignificantly to the total *Hamiltonian*. However, it becomes relevant in several double resonance pulse EPR methods. Analogous to the electron Zeeman interaction it is described as:

$$\hat{\mathbf{H}}_{NZ} = \mu_n g_n \mathbf{B}\,\hat{\mathbf{I}} \tag{3.24}$$

, where g_n is the nuclear g-factor, μ_n describes the nuclear magneton and $\hat{\mathbf{I}}$ is the nuclear spin operator. In case of a nuclear spin of I=1 the components of $\hat{\mathbf{I}}$ can be described by 3x3 matrices.

3.2.5 Hyperfine interaction and A-anisotropy

A further relevant source of information in EPR is the hyperfine interaction. It characterizes the interaction between a nuclear spin $\hat{\mathbf{I}}$ and an electron spin $\hat{\mathbf{S}}$ and is described by:

$$\hat{\mathbf{H}}_{HF} = \hat{\mathbf{S}}\,\mathbf{A}\,\hat{\mathbf{I}} \tag{3.25}$$

Here, $\mathbf{A}$ is the hyperfine tensor characterizing the magnitude and anisotropy of the hyperfine coupling. $\mathbf{A}$ can be split in an *anisotropic* and an *isotropic* part leading to:

$$\hat{\mathbf{H}}_{HF} = \hat{\mathbf{H}}_{HF,aniso} + \hat{\mathbf{H}}_{HF,iso} \tag{3.26}$$

The isotropic part is also called Fermi contact interaction arising from the non vanishing probability of presence of the electron at the nucleus:

$$\hat{\mathbf{H}}_{HF,iso} = a_{iso}\hat{\mathbf{S}}\hat{\mathbf{I}} \tag{3.27}$$

with

$$a_{iso} = \frac{2\mu_0}{3\hbar}\, g_e\, \mu_B\, g_n\, \mu_n\, |\psi_{\mathbf{r}=0}|^2 \tag{3.28}$$

, where $|\psi_{\mathbf{r}=0}|^2$ describes the electron spin density at the nucleus. The anisotropic part of the hyperfine interaction originates from dipolar interaction between the nuclear and the electron spin. Using a point dipole approximation in the case of electron-nucleus interaction $\hat{\mathbf{H}}_{HF,aniso}$ is given by:

$$\hat{\mathbf{H}}_{HF,aniso} = \hat{\mathbf{S}}\, \mathbf{A}_{aniso}\, \hat{\mathbf{I}} \tag{3.29}$$

$$= -\frac{\mu_0\, g_e\, \mu_B\, g_n\, \mu_n}{4\pi} \left(\frac{\hat{\mathbf{S}} \cdot \hat{\mathbf{I}}}{r^3} - \frac{3\left(\hat{\mathbf{S}} \cdot \mathbf{r}\right)\left(\hat{\mathbf{I}} \cdot \mathbf{r}\right)}{r^5} \right) \tag{3.30}$$

with $\mathbf{r}$ as the connection vector between the point dipoles and r as its absolute. Furthermore, in presence of a strong external magnetic field the components perpendicular to the magnetic field direction can be neglected (high-field approximation) and one obtains:

$$\hat{\mathbf{H}}_{HF,aniso} = A(\Theta)_{aniso}\, \hat{\mathbf{S}}\, \hat{\mathbf{I}} = \frac{\mu_0\, g_e\, \mu_B\, g_n\, \mu_n}{4\pi} \left(\frac{1 - 3cos^2\Theta}{r^3} \right) \hat{\mathbf{S}}_{\mathbf{z}}\hat{\mathbf{I}}_{\mathbf{z}} \tag{3.31}$$

Θ is the angle between the connection vector $\mathbf{r}$ and the magnetic field direction. Considering a coincidence of the MTSSL z-axis and $\mathbf{r}$, equation 3.31 shows that the hyperfine coupling depends on the orientation of the molecule with respect to the magnetic field.
In the eigensystem of $\mathbf{A}_{aniso}$, which coincides with the g-tensor system, $\mathbf{A}_{aniso}$ can be written in tensor expression as follows:

$$\mathbf{A}_{aniso} = -\frac{\mu_0}{4\pi} \frac{g_e\, \mu_B\, g_n\, \mu_n}{r^3} \begin{pmatrix} -1 & 0 & 0 \\ 0 & -1 & 0 \\ 0 & 0 & 2 \end{pmatrix} \tag{3.32}$$

The total hyperfine tensor is then given by:

$$\mathbf{A} = \mathbf{A}_{aniso} + \mathbf{1}\, a_{iso} = \begin{pmatrix} A_{xx} & 0 & 0 \\ 0 & A_{yy} & 0 \\ 0 & 0 & A_{zz} \end{pmatrix} \tag{3.33}$$

The transformation from the molecular system into the laboratory frame is accomplished analogous to 3.19 leading to a hyperfine constant dependent of the orientation of the B-field with respect to the molecule:

$$A_{\vartheta,\varphi} = \sqrt{A_{xx}^2 sin^2\vartheta cos^2\varphi + A_{yy}^2 sin^2\vartheta sin^2\varphi + A_{zz}^2 cos^2\vartheta} \tag{3.34}$$

Typical values for the tensor elements of a nitroxide spin label, in which the unpaired electron interacts with the 14^N-nitrogen nucleus (I=1) of the N-O group, are:

$$A_{xx} \approx 0.5\, mT \tag{3.35}$$

$$A_{yy} \approx 0.5\, mT \tag{3.36}$$

$$A_{zz} \approx 3.5\, mT \tag{3.37}$$

In this case, a present hyperfine interaction leads to a splitting of the *spin up* and *spin down* states in three energy levels, respectively. This in turn causes the observation of three resonance positions in the EPR spectrum separated by the orientation dependent value of the hyperfine splitting (see 3.3 for a more detailed explanation). Moreover, the A_{zz} value is sensitive to the spin label environmental polarity (see chapter 3.3.3.1). The determination of the A_{zz} value, describing the polarity of the spin label environment, provide, beside others, the possibility to distinguish between R1 side chains, which are located in aqueous or lipid phases. Furthermore, the fact that the hyperfine anisotropy is partially resolved at X-band frequencies (A_{xx} and A_{yy} are well distinguishable from A_{zz}) enables the determination of spin label orientations with respect to the magnetic field direction or with respect to each other.

3.2.6 Electron-Electron dipolar interaction

Considering a system with two unpaired electrons, their interaction can be described by an exchange coupling (see below) and a dipole-dipole coupling analogous to 3.31.

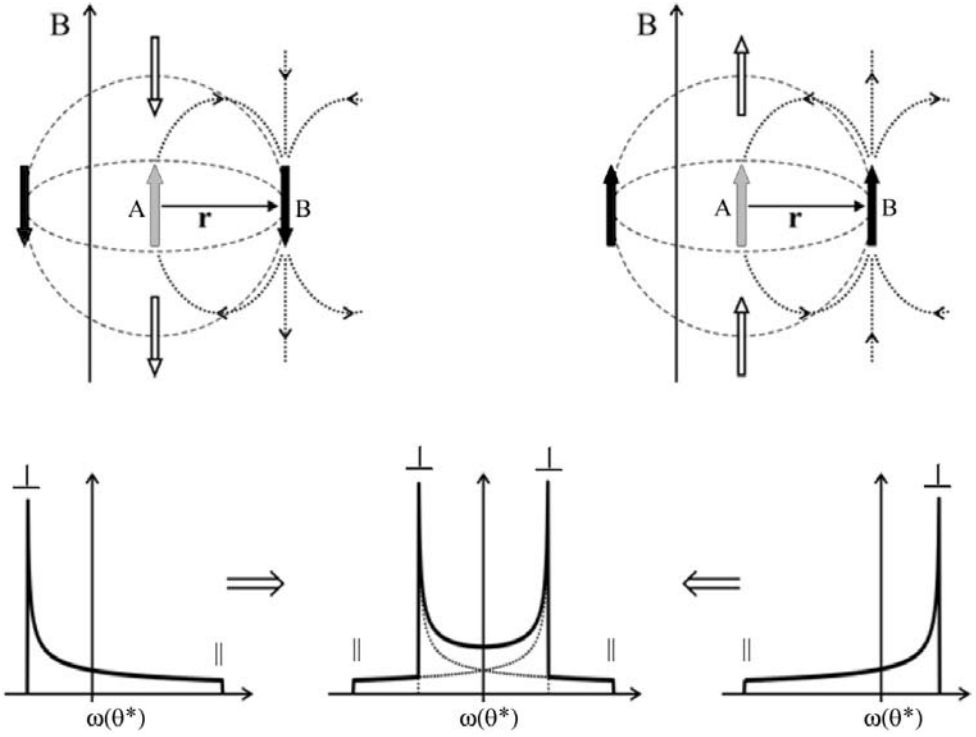

Figure 3.4: Elucidation of the Pake pattern. Top (left): The possible orientations of the dipolar axis of two interacting parallel aligned spins (A and B) with respect to an applied magnetic field **B**. Dipolar interactions between them are indicated as dotted lines. Within disordered samples the dipolar vector **r** can exhibit all possible orientations with respect to the magnetic field. Thus, its direction is statistically distributed over the unit sphere (indicated as dashed lines) and a powder average is performed by integration over Θ_{dd} using the weighting factor $\sin\Theta_{dd}$. The parallel case occurs when spin B is located at the poles (white arrows) ($\Theta_{dd} = 0°$), the perpendicular ($\Theta_{dd} = 90°$) case appears for spin B located on the equator (black arrows). Top (right): The inversion of spin B leads to the inversion of the transition distribution. Bottom: Shifts of resonance positions ω due to dipolar interaction according to the cases shown above. Transition distribution and corresponding intensities result from the average of ω over Θ_{dd} using the weighting factor $\sin\Theta_{dd}$. The resulting Pake pattern (center) is a superposition of the two cases. Picture modified from [26].

The dipole-dipole coupling contribution $\hat{\mathbf{H}}_{dd}$ to the hamiltonian is characterized by the dipole-dipole or also called zero field splitting tensor **D** and is given by:

$$\hat{\mathbf{H}}_{dd} = \hat{\mathbf{S}}_A \, \mathbf{D} \, \hat{\mathbf{S}}_B \tag{3.38}$$

, where $\hat{\mathbf{S}}_A$ and $\hat{\mathbf{S}}_B$ are the interacting electron spins. The use of the point dipole together with the high field approximation equation 3.38 leads to:

$$\hat{\mathbf{H}}_{dd} = \omega_{dd}\hat{\mathbf{S}}_{\mathbf{A},\mathbf{z}}\hat{\mathbf{S}}_{\mathbf{B},\mathbf{z}}\hbar \tag{3.39}$$

with:

$$\omega_{dd} = \frac{\mu_0\, g_e^2\, \mu_B^2}{4\pi\hbar}\left(\frac{1-3cos^2\Theta_{dd}}{r_{AB}^3}\right) \tag{3.40}$$

ω_{dd} is called dipolar frequency and depends on the angle Θ_{dd} between the magnetic field and the vector $\mathbf{r}_{AB}$ connecting spin A and spin B and the distance between those spins. The dipolar interaction causes a splitting of the resonance lines of $+\omega_{dd}$ and $-\omega_{dd}$. The connection vector between spin A and spin B is called dipolar vector or dipolar axis. In case of macroscopically disordered samples, in which a statistical distribution of dipolar axis orientations with respect to the magnetic field exists, equation 3.40 has to be averaged over the angle Θ_{dd} with the usual weighting factor $\sin\Theta_{dd}$. This leads to an observation of a Pake pattern (PP) (figure 3.4). The angle $\Theta^* \approx 54.7°$ leading to ω_{dd}=0 is known as the *magic angle*. A dipolar axis orientation exhibiting Θ^* causes no dipolar splitting and no dipolar interaction is detectable in this case. The largest splitting is obtained at $\Theta_{dd} = 0°$ (parallel component of the PP). $\Theta_{dd} = 90°$ (perpendicular component) gives the highest intensity contribution to the PP, due to the weighting factor of $\sin\Theta_{dd}$ used for averaging.
Since the shape of the Pake Pattern depends on $\mathbf{r}_{AB}$, the determination of ω_{dd} or the PP, respectively, enables e.g. the determination of interspin distances. A direct detection of the Fourier transform of the PP can be obtained by four pulsed DEER spectroscopy (see below). In low temperature cw-EPR measurements the dipolar interaction results in a considerable line broadening of the EPR spectra, detectable for distances below 2 nm.

3.2.7 Heisenberg spin exchange

The second electron-electron interaction, that has to be mentioned, is the Heisenberg spin exchange interaction or briefly exchange coupling $\hat{\mathbf{H}}_{Ex}$. Exchange coupling becomes significant for very small inter-spin distances ($\approx$ 0.8 nm [63]). In this situation the electron orbitals can partially overlap and the two electrons have a non-vanishing probability of presence at the same location. Thus, the Pauli exclusion principle lead to a weak binding (anti parallel spins) interaction. An extreme case would be the formation of an electron pair or a

covalent bond, but is not considered here, because this situation would not contribute to the EPR signal. The relevant interaction in this case, the Coulomb interaction between two electrons, leads to a weak anti-binding (parallel spins) interaction. The exchange coupling is represented by the Hamiltonian:

$$\hat{\mathbf{H}}_{Ex} = \hat{\mathbf{S}}_1 \mathbf{J} \hat{\mathbf{S}}_2 \tag{3.41}$$

J is a 3x3 tensor, which takes the coulombic interaction between the electrons into account. In general, only the most important part of the exchange-energy operator, the isotropic part, is considered:

$$\hat{\mathbf{H}}^0_{Ex} = J_0 \hat{\mathbf{S}}_1 \hat{\mathbf{S}}_2 \tag{3.42}$$

J_0 is the isotropic exchange coupling constant [80] describing the strength of the orbital overlap, which is given by the exchange integral:

$$J_0 = -2 \left\langle \Psi_a(1)\Psi_b(2) \right| \frac{e^2}{4\pi\epsilon_0 r} \left| \Psi_a(2)\Psi_b(1) \right\rangle \tag{3.43}$$

with Ψ_a and Ψ_b as different spatial molecular-orbital wave functions, evaluated considering the electrons to be non-interacting. ϵ_0 is the permittivity in vacuum and r is the electron-electron distance. Since the exchange coupling depends on the inter spin distance, it is possible to obtain information about r by determining J. Furthermore, the investigation of the exchange interaction can be used to determine spin label accessibilities to rapidly relaxing paramagnetic species exchanging with the unpaired electrons from the attached spin labels (see chapter 3.3.4).

3.3 Continuous wave (cw) EPR

In *cw*-EPR (cw=continuous wave) experiments the sample is placed in an external homogeneous magnetic field and is irradiated by microwave radiation exhibiting a constant frequency. The EPR spectrum is obtained by detecting the absorption of the microwave energy in dependence of the external magnetic field strength. In general, the first derivative of the EPR absorption spectrum is obtained due to technical reasons. The shape of the spectrum depends, as already mentioned, on the energetic nature, described by the *Hamiltonian* of the investigated system. This fact will be explained on a simple example (MTSSL single crystal). Furthermore, *cw*-EPR enables the determination of numerous parameters like spin label mobility and its accessibility towards specific substances. These measurements are usually carried out at room temperatures. The polarity of the spin label micro-environment and distances between two spin labels exhibiting distances below 2 nm can be investigated at low temperatures (below 200K). The influence of these parameters on the spectra shape, their determination and information provided thereby are explained in the following chapters.

3.3.1 Single crystal and powder spectra

Since the shape of the *cw* EPR spectrum depends on the energetic nature, described by the *Hamiltonian*, a short example is given to understand later discussions. Considering a MTSSL single crystal, in which all molecules are oriented in the same way, and the unpaired electron exhibits a hyperfine interaction with a nitrogen atom (I=1), the *Hamiltonian* has the form:

$$\hat{\mathbf{H}} = \hat{\mathbf{H}}_{EZ} + \hat{\mathbf{H}}_{HF} = \mu_B \, \mathbf{B} \, \mathbf{g} \, \hat{\mathbf{S}} + \hat{\mathbf{S}} \, \mathbf{A} \, \hat{\mathbf{I}} \tag{3.44}$$

With $\mathbf{B} = (0, 0, B)$ and disregard of the contributions containing x- and y-components of $\hat{\mathbf{S}}$ and $\hat{\mathbf{I}}$, as good approximation at high magnetic fields [26], the energy eigenvalues can be calculated to:

$$E_{m_s,m_I} \quad = \quad g_{\vartheta,\varphi}\mu_B m_s B + A_{\vartheta,\varphi} m_s m_I \tag{3.45}$$

$g_{\vartheta,\varphi}$ and $A_{\vartheta,\varphi}$ are the g factor and the hyperfine coupling constant in dependence of the magnetic field direction with respect to the MTSSL molecule (see equations 3.20 and 3.34). m_s and m_I are the magnetic electron and nuclear quantum numbers, respectively ($m_s = 1/2, -1/2$ and $m_I = 1, 0, -1$). Taking the quantum mechanical selection rules ($\Delta m_s = 1$ and $\Delta m_I = 0$) into account one obtains three resonance positions:

$$B_1 = \frac{\Delta E - A_{\vartheta,\varphi}}{g_{\vartheta,\varphi}\mu_B} \tag{3.46}$$

$$B_2 = \frac{\Delta E}{g_{\vartheta,\varphi}\mu_B} \tag{3.47}$$

$$B_3 = \frac{\Delta E + A_{\vartheta,\varphi}}{g_{\vartheta,\varphi}\mu_B} \tag{3.48}$$

Thus, the EPR spectrum consists of three lines centered at $g_{\vartheta,\varphi}$ and separated by $A_{\vartheta,\varphi}$ (figure 3.5).

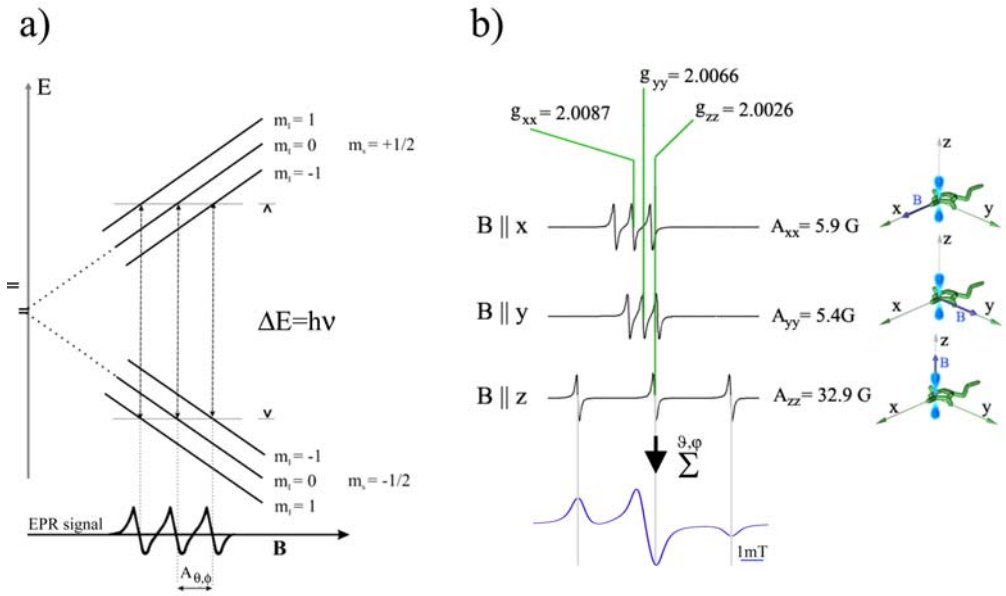

Figure 3.5: a): Schematic representation of the energy levels in a system exhibiting an unpaired electron (S=1/2) hyperfine coupled to a nucleus (I=1) in an external magnetic field B (top). The two energy states resulting from the electron Zeeman interaction are particularly split in three levels due two the hyperfine interaction. The presence of six energy levels leads to the observation of three EPR transitions (bottom) separated by the orientation dependent value $A_{\vartheta,\varphi}$. Picture was modified from [19]. b): B-field orientation dependence of single crystal spectra. The extreme cases are obtained for a magnetic field direction parallel to the spin label molecule's x-, y- and z-axis (black spectra). A powder like sample exhibiting all possible cases for the magnetic field direction with respect to the molecules (ϑ, φ) provides a powder spectrum (blue) composed as the sum of all single crystal spectra governed by the isotropically distributed values for ϑ and φ.

In the given example a single MTSSL crystal was considered, in which all spin labels exhibit the same orientation. In case of spin labeled proteins in water

solutions the EPR sample consists of numerous molecules with isotropic distributed orientations. At temperatures below 200K the proteins and attached spin labels are in a frozen state and the sample can be treated as a powder sample, in which the spin label orientations with respect to the magnetic field are randomly distributed. Three extreme cases occur, namely the magnetic field is parallel aligned to the spin label molecule's x-axis, y-axis or z-axis. The corresponding spectra are then governed by A_{xx} and g_{xx}, A_{yy} and g_{yy} or A_{zz} and g_{zz} (figure 3.5 b). All magnetic field orientations inbetween these extremes provide effective g and A values according to equations 3.20 and 3.34. The EPR powder spectrum (figure 3.5 b bottom) is the sum (superposition) of the single crystal spectra corresponding to all occurring magnetic field orientations (ϑ, φ), which are in this case assumed to be homogeneously distributed over the unit sphere.
However, the EPR spectra are not only influenced by the spin label orientations. Furthermore, they are sensitive to the spin label side chains motion. In liquid solution at room temperatures the orientations of the spin labels, and thereby the effective g- and A-tensors, become time-dependent. Molecular motion during microwave absorption, taking place on a nanosecond time scale, is the reason for a particular averaging of the tensors occurring in the Hamiltonian. This results in EPR line shapes, which differ from the powder sample case. Consequently, the protein movement, the spin label motional freedom, the viscosity of the solvent and temperature are significant parameters, which affect the EPR spectra shape. Additionally, electron-electron interaction is reflected in the EPR line shape as well. These effects can be used to obtain various suitable information about the spin label side chain environment and the protein itself. Numerous EPR applications were developed in the last years to gain diverse information about the samples under investigation. In the following chapters the here applied methods and the thereby available information are described.

3.3.2 Side chain dynamics and mobility measurements

3.3.2.1 Mobility regimes

The term *mobility* is employed to characterize the motion of the MTSSL side chain as extracted from general features of the EPR spectrum usually recorded at room temperatures [46]. The motion of a spin label side chain attached to a specific position of a protein depends on three important parameters. These are the entire protein motion, the segmental protein backbone motion and primarily the motion of the spin label molecule itself, defined by the possible rotations around the particular bonds connecting the nitroxide group with the protein backbone. The rotational and transversal motion of substances in aqueous

solution can be characterized as random diffusion processes, and their time scale can be quantified by the rotational correlation time τ, describing after which time the alignment of a molecules in a viscous solution is not anymore correlated to its initial orientation. Proteins are in general not spherical, but in most cases it can be assumed as a good approximation, and the value of τ can be extracted from the Stokes-Einstein relation:

$$\tau = \frac{4\pi\eta a^3}{3k_BT} = V\frac{\eta}{k_BT} \tag{3.49}$$

where η is the viscosity of the solution and a is the effective radius of the molecule. T is the temperature and k_B the Boltzmann constant. V describes the molecular volume, which is approximately proportional to the molecular mass M [13].
The effective τ is composed of the rotation correlation times of the three above mentioned motional contributions. The entire protein motion can be often neglected when considering vesicle[1]-bound proteins, soluble proteins with a molecular weight above 200 kDa or within a solvent exhibiting an appropriate viscosity. In these cases the rotational correlation time of the protein is beyond the sensitivity of the EPR time scale [13].
Regarding the spin label motion the effective correlation time τ can be understood as a measure for the average extent of the spectral anisotropies. In case of a spin labeled protein, this averaging depends for example on the motional freedom of the label attached to a specific site. A spin label located at a loop position exhibits a higher motional freedom than a buried label, whereby its motion is restricted by sterical contacts with other protein parts. Two representative examples are shown in figure 3.6 (top).
Generally, a distinction is made between four different τ regimes according to the spectral anisotropy $\Delta\omega$ (figure 3.6, see also [75] for an overview). The spectral anisotropy describes the maximal possible resonance frequency shift caused by anisotropy of the magnetic tensors. Using MTSSL at X-band frequencies the spectral anisotropy is governed by the hyperfine anisotropy, leading to $\Delta\omega/2\pi \approx 130$MHz.
The fastest motion regime is the *isotropic limit* ($\Delta\omega << \tau^{-1}$), where the anisotropies are completely averaged. In this case the positions of the spectral lines can be calculated with the isotropic g- and A-values:

$$g_{iso} = 1/3(g_{xx} + g_{yy} + g_{zz}) \tag{3.50}$$

[1]Lipids in water solutions form under certain conditions spherical bilayers called vesicles. They are often used to mimic artificial membranes.

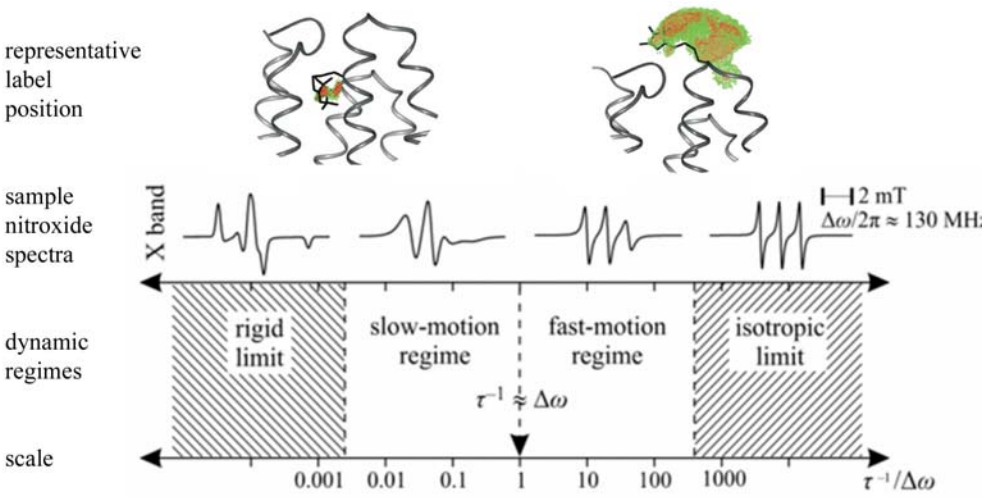

Figure 3.6: Dynamical regimes of nitroxide cw EPR spectra at X-band frequencies. The regimes are characterized by the rotational correlation time τ and the borders are specified by the ratio $\Delta\omega/\tau$, with $\Delta\omega/2\pi$ = 130MHz as the spectral anisotropy at X-band in frequency units. Two representative examples for specific spin labeled positions are shown (top). A spin label attached at a protein loop region (right) reveals a high mobility (probability of orientation highlighted in green) and a small value for the effective τ, whereas a label at a protein buried site (left) exhibits a larger effective τ due to its restricted motional freedom. Picture was modified from [41] and [39].

$$A_{iso} = 1/3(A_{xx} + A_{yy} + A_{zz}) \tag{3.51}$$

To account for the line width for spectra simulation the calculated stick spectrum, consisting of the resonance line positions, is convoluted with a Lorentzian line exhibiting a FWHM, which is proportional to $1/T_2$. T_2 is called the spin-spin relaxation time (see chapter 3.3.4). In the fast-motion regime ($\Delta\omega < \tau^{-1}$) differences in the line intensities can be observed. Simulation methods using the Redfield theory reflect the spectral shapes precisely (see [72]). In that case, the line broadening is determined by the following equation:

$$\frac{1}{T_2} = A_0 + A + Bm_I + Cm_I^2 \tag{3.52}$$

In A_0, effects such as natural line width or unresolved hyperfine splittings are considered, whereas the parameters A, B and C describe the broadening due to the motional averaging. It is noteworthy, that in the fast motion regime the line width depends on the nuclear quantum number m_I. This means that e.g. in case of a MTSSL ($m_I = -1, 0, 1$) the spectral lines located at high and low magnetic fields differ in width. Since the double integral of the EPR spectrum is proportional to the number of spins, a broader high field peak is accompanied by a decrease in intensity compared to the low field peak. The upper limit

for the fast motion regime is defined by a correlation time of approximately $\tau = 0.1$ns at X-band frequencies.
The *slow motion* regime ($\Delta\omega > \tau^{-1}$) still holds the biggest challenge according to spectra simulation, since the perturbation theory based method is not sufficient to describe the motional averaging anymore. Here, another formalism is necessary to achieve reasonable results for the agreement between the simulated and experimental EPR spectra. The basis of this method is the determination of the expectation value $\overline{\rho}$ of the time dependent density matrix, which can then be used for spectra calculations. It can be obtained from the stochastic Liouville equation (SLE) describing the time evolution of $\overline{\rho}$ [21]:

$$\frac{\partial}{\partial t}\overline{\rho}(\Omega,t) \quad = -i[\hat{\mathbf{H}}(\Omega(t)),\rho(\Omega,t)] - \Gamma[\rho(\Omega,t) - \rho_0(\Omega)] \tag{3.53}$$

where Γ is a Markoff operator describing the rotational diffusion, such as Brownian diffusion or jump diffusion, which are commonly used as models. ρ_0 is the equilibrium population of the density matrix. Ω is defined by a set of three Euler angles, which describe the spin label orientation with respect to the preferred orientation, also known as internal director frame. This frame originates from the SRLS (slowly relaxing local structure) model describing a specific way of the rotational diffusion of a MTSSL. For a detailed description see [10]. To solve the SLE it is convenient to introduce Wigner rotation functions as eigenfunctions of the Hamiltonian $\hat{\mathbf{H}}$ and Γ representing the orientation distributions.
For $\tau > 300ns$ the *rigid limit* ($\Delta\omega >> \tau^{-1}$) is reached and the spin label can be treated as completely immobilized. This is the case for powder samples or frozen solutions. The Hamiltonian is then time independent and the spectrum corresponds to a powder spectrum described in 3.3.1. The powder spectrum simulation will be discussed in 3.3.3.3.

3.3.2.2 Mobility parameters

The effective correlation time due to the reorientational motion of the spin label is assumed to be a complex function of secondary, tertiary, and eventually quaternary structure of the protein under investigation [13]. A quantitative description of the dynamic modes of the MTSSL side chain requires simulation of the EPR spectra, preferably at multiple frequencies.
However, two semi-empirical parameters extractable from certain spectral features can also be used for a spin label side chain mobility analysis. As can be seen from figure 3.6 the width of the central line ($m_I = 0$) increases with larger correlation times. Another effect coming along with the line broadening, is the distinct broadening of the lines corresponding to the $m_I = -1, 1$ transitions (low and high field peaks). The inverse line width of the central resonance

$(1/\Delta H_0)$ has proven to be a convenient experimental measure of the nitroxide mobility [47, 13]. The accompanying effect of the distinct broadening can be considered by the calculation of the inverse second moment $(1/\langle H^2 \rangle)$ of the spectrum defined as:

$$\left\langle H^2 \right\rangle = \frac{\int (B - \langle H \rangle)^2 S(B) dB}{\int S(B) dB} \tag{3.54}$$

with

$$\langle H \rangle^2 = \frac{\int B S(B) dB}{\int S(B) dB} \tag{3.55}$$

, where B is the magnetic field strength, and S(B) is the EPR absorption spectrum. Here it should be mentioned that these measures lead to problems when a two component spectrum is analyzed. The inverse line width overestimates the mobile component, whereas the inverse second moment overestimates the immobile component. Even if the contribution of the second component is small, one of the parameters will overestimate its contribution, e.g. the second moment of a spectrum, exhibiting predominantly mobile features, might be misleading due to a present minor immobile spectral component.

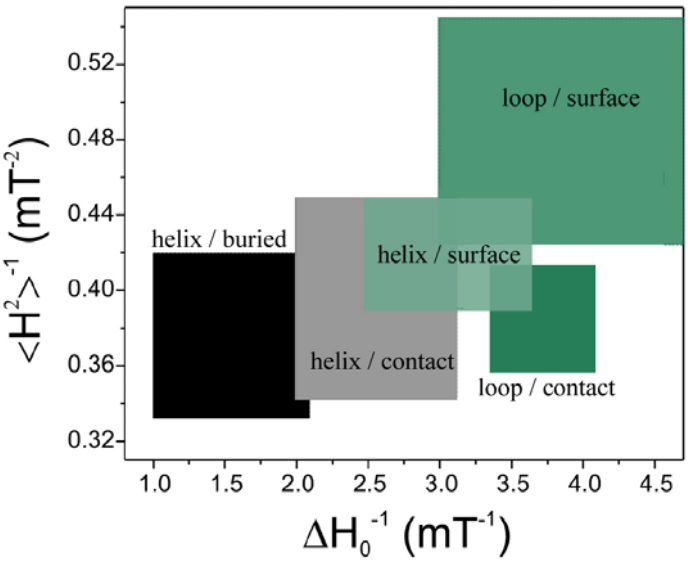

Figure 3.7: Classification of side chain localizations with regard to the protein structure by plotting the inverse spectral second moment $(1/\langle H^2 \rangle)$ versus the inverse central line width $(1/\Delta H_0)$ as semi empirical parameters calculated from cw X-band EPR spectra at room temperature. Picture modified from [13].

These semi empirical mobility parameters have been found to be even correlated with the structure of the protein attached spin label side chains vicinity

[47]. The plot of these mobility parameters versus residue number reveals the secondary structure element of the spin labeled site and its microenvironment in terms of exhibiting tertiary contact, being surface exposed or buried. This classification can be problematic, if a second component, governed by different mobility, is present, see above. Figure 3.7 shows a diagram containing the corresponding topological regions in such a plot. The main regions were determined by [47] and extended by [13]. Another advantage of a mobility analysis using the mentioned parameters is the fact that these parameters are directly extractable from X-band spectra, and that simulation approaches or measurements at multiple frequencies are not required.

3.3.3 Polarity and distance measurements

3.3.3.1 Polarity measurements

In frozen protein solutions at low temperatures (below 200 K) the spin labels are completely immobilized (vitrification). *Cw*-EPR measurements at these temperatures yield the so called powder spectra. One of the parameters, which primarily influences the spectral shape, is the hyperfine coupling.

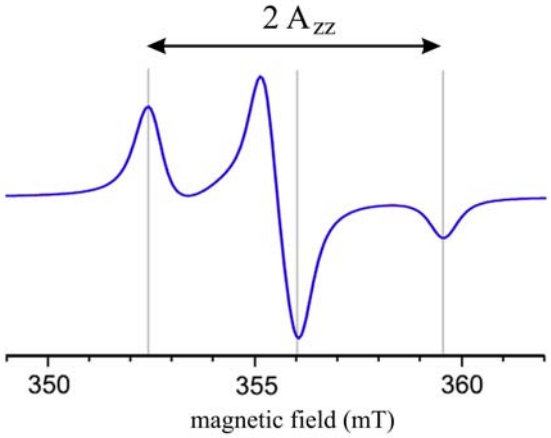

Figure 3.8: Simulated X-band *cw* EPR powder spectrum of a nitroxide spin label. The peak to peak distance of the low and high field equals $2 \cdot A_{zz}$. Figure modified from [15].

As already mentioned in 3.2.5 the hyperfine tensor element A_{zz} is sensitive to the polarity of the spin label environment, since a certain solvent induces a local electric field component E_x along the N-O bond direction (molecular x-axis) as shown in figure 3.2. This field causes a change of the π electron density distribution within the N-O bond. In polar solvents the density is shifted into the direction of the nitrogen atom, leading to a stronger hyperfine coupling with the N-atom (I=1). In contrast, an unpolar environment causes a density

shift into the direction of the oxygen (I=0). The electron density shift along the N-O bond leads either to a weaker or a stronger hyperfine coupling, well reflected in the A_{zz} value of the *cw* EPR spectrum, which is given by:

$$A_{zz} = Q\rho_{\pi}^{N} \tag{3.56}$$

Thus, A_{zz} is proportional to the π spin density in the $2p_z$ orbital of the nitrogen atom (ρ_{π}^{N}). The proportional constant Q=73 G (7,3 mT) was determined by Plato et al. [58].
The largest observed hyperfine splitting in the obtained powder spectrum arises from the hyperfine value governed by A_{zz}. Figure 3.8 shows a representative powder spectrum, simulated for the low temperature case using the typical g- and A-tensor elements of a nitroxide spin label. The A_{zz} value can directly be extracted from the low temperature *cw* X-band EPR spectrum as the half spacing between the low and the high field peak or can be obtained by spectra fitting (see chapter 3.3.3.3).

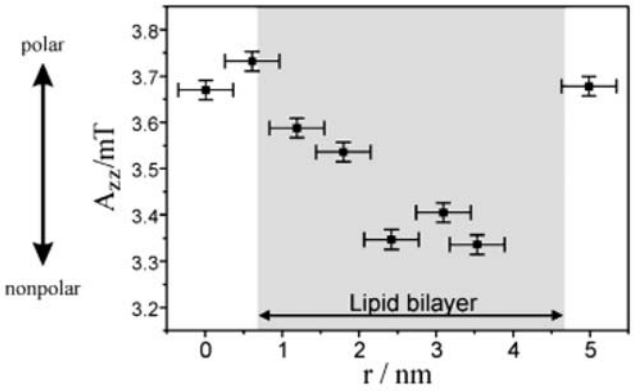

Figure 3.9: Plot of A_{zz} versus the spin label distance r from the lipid membrane surface. Spin labels located in the middle of the lipid membrane exhibit smaller A_{zz} values, whereas spin labels located near the lipid head groups reveal values larger values due to the polarity of the spin label environment. The data shown here where obtained from measurements on several spin labeled mutants of the membrane reconstituted transmembrane protein BR. Figure is taken from [68].

Polarity determination of the spin label environment enables for example the discriminability between protein domains, which are located within water or lipid membrane phases. The inner membrane regions differ immensely in polarity compared to lipid surface or solvent exposed regions. In figure 3.9 A_{zz} is plotted versus the distance r from the lipid membrane surface. Spin labels located in the middle of the lipid membrane exhibit A_{zz} values of approximately

3.35 mT, whereas spin labels located close to the lipid head groups (surface) reveal values larger than 3.60 mT. In this example several spin labeled mutants of the transmembrane protein bacteriorhodopsin (BR) reconstituted in lipid membranes have been investigated [68]. The particular values may differ by the use of different lipid and buffer types, but are in general comparable. A recalibration of the A_{zz}-behavior is in general convenient. Moreover, polarity investigations provide the traceability of structural changes of proteins on the molecular level and the means to obtain specific details of essential biological processes.

3.3.3.2 Distance determination

A further parameter, influencing the low temperature *cw* EPR spectral shape, is the dipolar interaction between two spins. In the distance range below 2 nm dipolar splitting, described by the Pake pattern, causes a significant line broadening (see chapter 3.2.6). The spectrum can be treated as a powder spectrum convoluted by the Pake pattern (PP) governed by the corresponding distance. Thus, smaller distances lead to broader EPR spectra, since the PP broadens along with smaller distances ($\omega_{dd} \propto r^{-3}$). This behavior is schematically shown in figure 3.10. In this case, the distance or distance distributions, respectively, can be obtained by fitting of simulated dipolar broadened powder spectra to the experimentally obtained spectra using a model of statistically oriented protein molecules. The determination of spin-spin distances is a further tool to investigate structural changes within proteins.

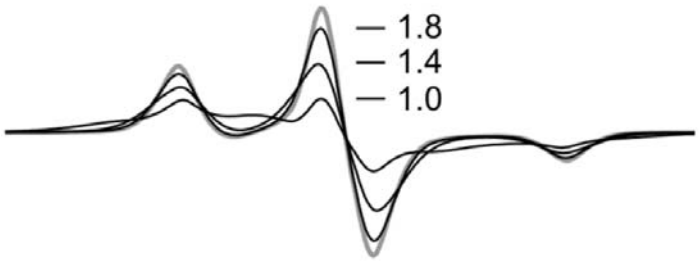

Figure 3.10: Elucidation of the influence of the dipolar interaction on low temperature X-band *cw* EPR spectra. The spectra were simulated with different inter-spin distances exhibiting a Gaussian distribution. Grey: $> 2nm$ (no visible dipolar interaction), black: 1.8, 1.4 and 1.0 nm. Picture taken from [13].

3.3.3.3 Low temperature cw-spectra fitting

For polarity (A_{zz}) and inter spin distance (r) determination powder spectra can be simulated and fitted to the experimental data. The powder spectra can be

calculated using equations 3.46, 3.47 and 3.48 (chapter 3.3.1). The calculation of the resonance positions is performed considering a homogeneous distribution of magnetic field directions (ϑ, φ) over an unit sphere. The sum of all calculated positions leads to a stick spectrum, which has to be convoluted with a pseudo-Voigt function to account for the respective line width. An additional convolution with a PP governed by the inter spin distance is done to consider the line broadening caused by dipolar interaction.
The spectral fitting is done by variation of the wanted parameters (e.g. A_{zz} and r) until the deviation between the simulated and the experimental spectrum is minimized. The quality of the agreement is in general judged by the calculation of the root mean square deviation χ^2 (RMSD). The EPR spectra simulation program DIPFIT (developed by Steinhoff and coworkers) considers a Gaussian distribution of inter spin distances, variable contributions of singly spin-labeled protein and employs automated routines to determine best-fit parameters [13, 64].
Another possible procedure for the determination of inter spin distances is implemented in the program *Short Distances* developed by Altenbach and coworkers. In this case, the distance distribution is obtained without explicit spectra simulation. Therefore, a spectrum composed of the sum of singly labeled species, exhibiting no dipolar broadening, is convoluted with PP according to an arbitrary shaped distance distribution. The shape of the distance distribution is varied in a way that the convoluted spectrum reveals the lowest deviation from the experimentally obtained spectrum, judged by χ^2. This is done using Tikhonov regularization as also used for DEER spectra analysis (see chapter 3.4.1 for more details).

3.3.4 Accessibility measurements

3.3.4.1 Collision reagents and relaxation times

The determination of the accessibility of paramagnetic quencher molecules to the protein bound spin label is a valuable tool in obtaining structural information for soluble and membrane proteins. Since specific paramagnetic quenchers possess characteristic access to the different phases of the sample, such as bulk water, lipid phase and protein interior, a distinction of the locations of the spin label sites regarding these phases can be done. Usual quencher compounds are the water soluble metal complex NiEDDA and molecular oxygen (O_2). In a membrane water system the NiEDDA presence is restricted to the aqueous environment and is excluded from the core of lipid vesicles and the membrane interior. In contrast, O_2 as a non-polar compound preferentially concentrates in hydrophobic regions, such as the inside of lipid bilayer membranes, with a well defined and lipid characteristically intra-membraneous concentration pro-

file [10].

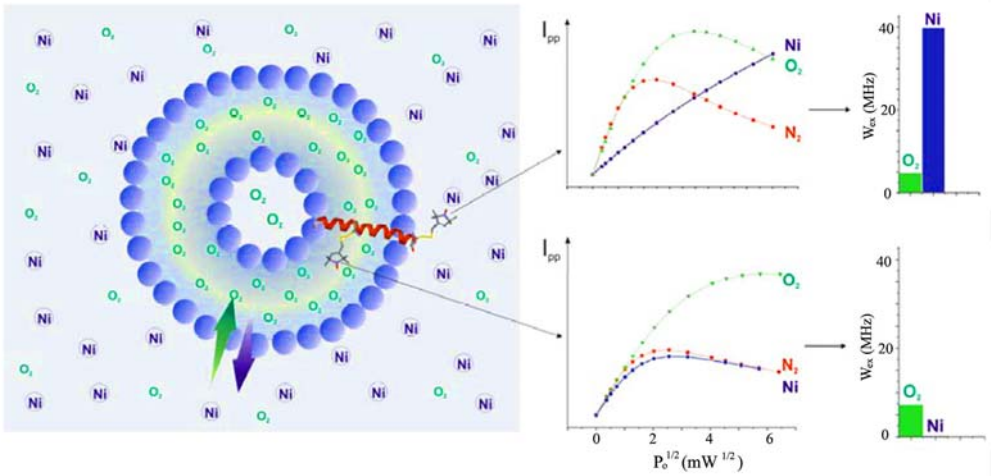

Figure 3.11: Left: Schematic illustration of the accessibility of the spin label side chain to the paramagnetic quenchers NiEDDA and O_2. O_2 exhibits a higher concentration within the lipid membrane, whereas the NiEDDA concentration is larger in the bulk water part of the sample. Right: examples of typical saturation curves are shown in presence of the reagents $NiEDDA$ (blue) and O_2 (green) according to equation 3.57. The red line indicates the saturation behavior in absence of a collision reagent (sample fluxed with N_2 (see *material and methods*)). Figure adapted from [62].

Consequently, a spin label located in the membrane interior reveals a larger accessibility to O_2 than compared to NiEDDA, whereas a water exposed site is associated with a high NiEDDA accessibility and a smaller O_2 accessibility (see figure 3.11). In case of a spin label localization within the protein interior, no or low accessibility for both, O_2 and NiEDDA, is generally observed.

The determination of the accessibility relies on the measurement of the collision frequency W_{ex} between the spin labels and the quencher reagents (NiEDDA and O_2). The collision frequency between a nitroxide and a paramagnetic quencher molecule is estimated from the change in spin-lattice relaxation time T_1 of the spin label involved in the collision event [54]. The spin-lattice relaxation is governed by energy transfer effects between electron spins and their environment, historically called *lattice*. The value of T_1 characterizes the relaxation of a spin system to thermal equilibrium, where the spin states (up and down) are populated according to a Boltzmann distribution. The rate $1/T_1$ describes how rapidly the spin system equilibrates, influenced by its environment.
In solutions, the relevant effects originate from fluctuating fields around the spin label caused by molecular motions, such as the Brownian diffusion of solubilized substances, or as in the here discussed case from molecular collisions. This effect is accompanied by an energy change of the system, since in case

of a collision the singly occupied orbitals of the two species overlap leading to Heisenberg spin exchange. This interaction in turn leads to an energy exchange pathway resulting in shorter life times of the microwave excited spin label states (spin up).
Another relaxation effect, which has to be mentioned, is the spin-spin relaxation characterized by the relaxation time T_2 or the relaxation rate $1/T_2$, respectively. This type of relaxation originates from the energy transfer between two electron spins (flip-flop processes). This electron flip-flop is an energy conserved process, thus the energy of the system remains unchanged, whereas phase information between the respective spins get lost. An introduction to spin relaxation processes can be found in [61].

3.3.4.2 Theoretical background and accessibility parameters

The relaxation times T_2 and T_1 determine the shape and the saturation behavior of *cw* EPR spectra. Since the collision frequency W_{ex} between a spin label and a quencher reagent has a more dramatic effect on T_1 as compared to T_2, a determination of T_1 leads to a good estimation of W_{ex}. T_1 or W_{ex}, respectively, can be determined by *cw* EPR power saturation measurements (see [13, 1, 54] for an overview).
Therein, the central line amplitude of the cw EPR signal is monitored as a function of the square root of the incident microwave power. The intensity rises to a maximum value followed by a decrease of the signal giving the so-called saturation curve, from which a parameter ($P_{1/2}$) related to the relaxation rates of the nitroxide can be determined (see figure 3.11 and 3.12). In the following a brief description of the theoretical background of the *cw* saturation method is presented.

The amplitude of the central line of a *cw* EPR spectrum in dependence of the microwave power is given by [54]:

$$Y' = \frac{I\sqrt{P}}{(1 + (2^{1/\epsilon} - 1)P/P_{1/2})^{\epsilon}} \tag{3.57}$$

, where ϵ is accounting for the homogeneity of the saturation. The extreme values are $\epsilon = 1/2$ for a complete inhomogeneous and $\epsilon = 3/2$ for homogeneous saturation. A detailed description and calculation can be found in [39]. I is a scaling factor and $P_{1/2}$ is the power, at which the signal amplitude is reduced to half of its theoretical unsaturated value. The saturation begins at a position, where the curve given by equation 3.57 significantly deviates from the linear

dependence of $\sqrt{P}$, valid for small microwave power values. Figure 3.12 shows a typical saturation curve and its theoretical behavior without saturation effects.

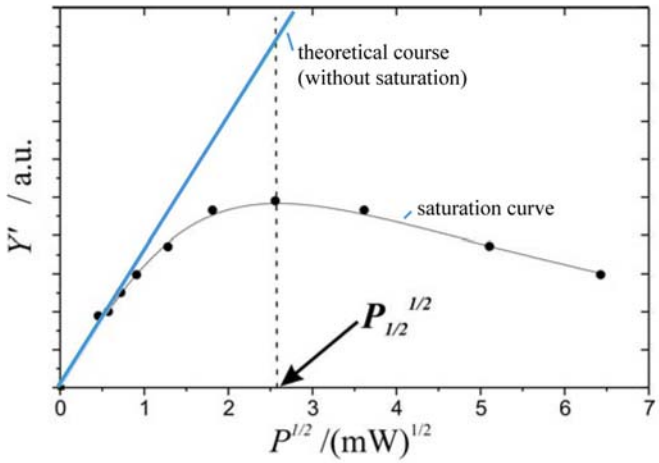

Figure 3.12: Plot of the experimentally obtained *cw* EPR signal amplitudes of the central line versus $\sqrt{P}$ (black dots). A fitting according to equation 3.57 is shown as black line. The blue line shows the theoretical behavior in the absence of saturation determined by extrapolating the linear region at small microwave power values. The value $P_{1/2}$ extractable from this plot is indicated. Figure adopted from [19].

The value $P_{1/2}$ can be extracted from a plot of Y' versus $\sqrt{P}$ and is a measure for the strength of the saturation effect, which are governed by the relaxation times T_1 and T_2. Consequently, the behavior of the saturation curve, thus the value of $P_{1/2}$ is a function of T_1 and T_2 with:

$$P_{1/2} \propto \frac{1}{T_1 \cdot T_2} \tag{3.58}$$

Since the peak-to-peak line width of the EPR central line (ΔH_{pp}) is inversely proportional to T_2, dividing $P_{1/2}$ by ΔH_{pp} leads to a parameter proportional to $1/T_1$. This can be done, if $W_{ex} << 1/T_2$. This is the case for room temperature measurements on spin labeled proteins, where T_1 is a few microseconds and T_2 is about 100 times faster [54, 1]. Thus a collision frequency in the MHz range will have a dramatic effect on T_1, whereas T_2 is not significantly affected. This holds for reagent concentrations, at which the spectral line width (governed by T_2) is not altered by adding the reagent compound to the sample. The accessibility Π [2] of a collision reagent to the spin label molecules nitroxide group can be

[2] In several works the accessibility parameter is normalized to a dimensionless parameter by division by a corresponding value of a reference sample to account for instrumental variability. Usually DPPH is used as reference. This is not the case here, since the determination of the proportional constant α leads to a direct calculation of W_{ex} as the measure for the accessibility.

determined by the change of $P_{1/2}$ in the absence and presence of the reagent. This change $\Delta P_{1/2}$ is proportional to the collision frequency W_{ex} and can be calculated according to [1]:

$$\Pi = \frac{\Delta P_{1/2}}{\Delta H_{pp}} = \frac{P_{1/2} - P^0_{1/2}}{\Delta H_{pp}} = \alpha W_{ex} \tag{3.59}$$

$P_{1/2}$ is the value in the presence and $P^0_{1/2}$ in absence of a collision reagent. The proportional constant α is a reagent and EPR spectrometer specific value, and has to be determined for each spectrometer individually. A detailed way to determine α is described in [19]. In figure 3.11 typical examples of saturation curves in presence of NiEDDA and O_2 are given, revealing different values for $P_{1/2}$ and W_{ex} with respect to the spin label location within the investigated system.
In general, values for W_{ex} can be determined by fitting simulated to the experimentally obtained saturation curves (see *Materials and Methods* 4.1.2.2).

3.3.4.3 The immersion depth parameter Φ

Another viable parameter, which can directly be calculated from the different W_{ex} values for NiEDDA and O_2, is the immersion depth parameter Φ.

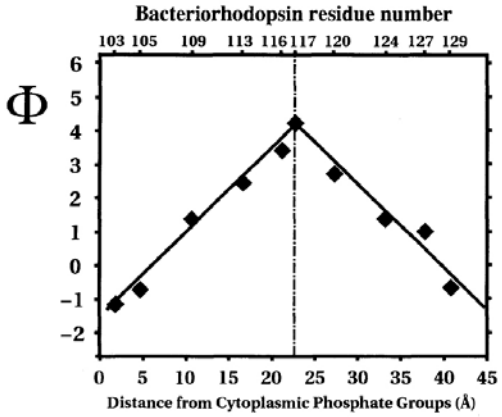

Figure 3.13: The immersion depth parameter Φ calculated from the collision frequencies between the paramagnetic reagents (NiEDDA, O_2) and a nitroxide spin label. The values were obtained from measurements on several BR mutants in a lipid bilayer. The dashed line indicates the bilayer center. The distances corresponding to the residue positions were determined from the BR structure. Figure adopted from [30].

Φ is a measure for the immersion depth of spin label with respect to a lipid bilayer membrane. According to [2] it is defined as:

$$\Phi = ln(W^{O_2}_{ex})/ln(W^{Ni}_{ex}) \tag{3.60}$$

, where $W_{ex}^{O_2}$ and W_{ex}^{Ni} are the collision frequencies determined in the presence of O_2 and NiEDDA, respectively. This parameter does not strongly depend on the lipid composition of the bilayer [30]. An extensive research regarding the immersion depth parameter was done by Hubbell and coworkers [30, 2] by calculating Φ for numerous spin labeled positions of the transmembrane protein BR reconstituted in a lipid bilayer. Figure 3.13 shows a plot of Φ versus the BR sequence positions, which are located along the transmembrane helix D of BR, spanning the whole bilayer. It is obvious that the depth parameter is a linear function of the distance from the bilayer head groups and reaches its maximum in the middle of the bilayer. This type of plot allows the determination of the distance of a nitroxide spin label from the lipid head groups by the calculation of Φ.

For more details about experimental conditions of *cw* EPR measurements regarding sample preparations, spectrometer setups and data analysis see chapter *Materials and Methods*.

3.4 Pulse EPR

Besides the fact that *cw*-EPR spectroscopy provides numerous information about spin labeled protein systems, the applicability of EPR spectroscopy is greatly increased by pulse EPR methods. In contrast to *cw* EPR, in which the sample is permanently irradiated with microwave radiation and the magnetic field is swept, in *pulse* EPR methods short microwave pulses on the nano-second time scale are applied using a constant external magnetic field strength. Various pulse sequences (2- and 3-pulse ESEEM, HYSCORE, Mims and Davies ENDOR, DEER, etc.) were developed in the last years, yielding different information about the spin system [78]. Especially the development of double electron-electron resonance (DEER) spectroscopy (also named pulsed electron double resonance (PELDOR)) contributes substantially to the investigations of biological systems. In contrast to *cw*-EPR methods, providing measurements of distances below 2 nm, DEER spectroscopy enables the determination of distance distributions in the 2-8 nm range. Another, still advancing but well applicable, method is orientation selective DEER spectroscopy. This method is based on DEER spectroscopy and yields orientation information about two dipolar coupled spins. In the following chapters a short theoretical background of both mentioned pulse EPR methods is given.

3.4.1 Distance measurements with DEER spectroscopy

The 4-pulse DEER method was developed in 2000 by Pannier et al. [56]. This method allows the determination of dipolar coupling frequencies (see section 3.2.6) of dipolar coupled spins, giving information about the inter spin distance. The basic idea behind a DEER experiment is based on the selective excitation of the particular partners A and B of a dipolar interacting spin pair. The selective excitation can be done by the use of two different microwave frequencies ν_A and ν_B. ν_A is called observer frequency and ν_B the pump frequency. These notations arise from the fact that in the experiment the behavior of a spin ensemble of species A excited at its resonance frequency ν_A is observed, whereas the polarization of the interacting spin species B is flipped by a so called microwave pump pulse, exhibiting the frequency ν_B. The resulting effects observed for the A spins arise from the dipolar coupling to the B spins. Monitoring this effect enables the determination of the dipolar coupling strength and thereby of the inter spin distance. How the effect can be observed and analyzed is described in the following.

First it has to be mentioned that the frequencies ν_A and ν_B have to be well separated from each other. The application of a microwave pulse of a finite length

always leads to a certain bandwidth of exciting frequencies. This excitation profile can be calculated as the Fourier transform of the applied pulse shape function, but can in good approximation be treated as a Gaussian. Its width can be approximated to $1/t_{pu}$, where t_{pu} is the pulse length. That means, the smaller t_{pu} the broader the exciting frequency range.

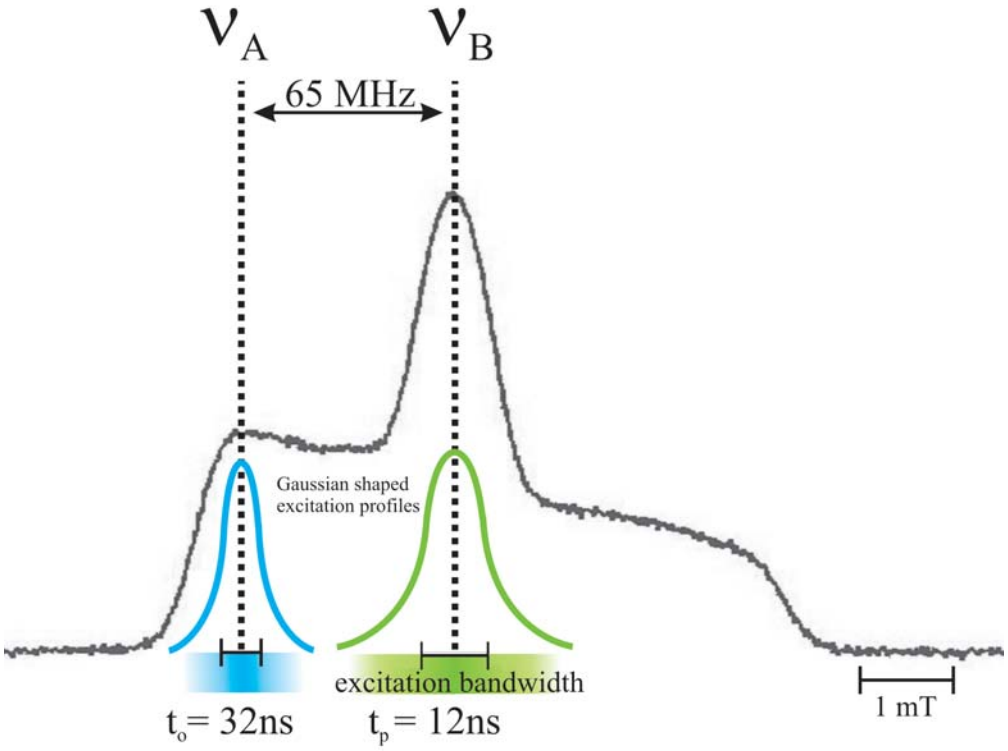

Figure 3.14: The positions of the pump pulse frequency ν_B and the observer frequency ν_A are shown with respect to the EPR absorption spectrum (black noisy trace) in a DEER experiment. The excitation profiles can be approximated as Gaussians. The different (typical) values for the π-pulse lengths of the observer pulse $t_o = 32ns$ (ν_A) and pump pulse $t_p = 12ns$ (ν_B) lead to different widths of the Gaussian shaped profiles indicated as black bars (FWHM). The color intensities in the colored bars represent the intensities of the Gauss-functions in a 1D manner. The magnetic field strengths (x-axis) can be translated into frequency units using the resonance condition 3.8.

In the DEER experiment it is convenient to adjust the respective pulse lengths and the frequency offset $\Delta\nu = \nu_B - \nu_A$ in a way that an overlap between the respective excitation profiles is excluded or minimized [3]. Thereby it is ensured that two different populations of spins are excited with ν_A and ν_B, respectively. On the other hand, it is favored to excite as much spins as possible to optimize

[3] The resonator efficiency $Q = \nu/\Delta\nu_m$ is a limiting factor for $\Delta\nu$, since it determines the bandwidth $\Delta\nu_m$ of microwave frequencies around its resonance frequency ν which can be coupled into the cavity.

the signal intensity and to increase the probability to excite coupled pairs. Therefore, an usual choice for the pump frequency ν_B is the frequency, which corresponds to the maximum of the EPR absorption spectrum [4] and the length of the π-pump pulse is usually set to $t_p = 12ns$. The observer frequency ν_A (π-pump length $t_o = 32ns$) is commonly set to the low field maximum, which corresponds to a value approximately 65MHz larger than ν_B (see figure 3.14) in case of nitroxide spin labels [60].
In order to understand the DEER signal the applied 4-pulse DEER sequence should be explained. Figure 3.15 shows a schematic representation of the applied pulse sequence. The first two pulses ($\pi/2 - \tau_1 - \pi$) applied with the observer frequency ν_A correspond to a common *Hahn-Echo* experiment, leading to a spin echo after the time $2\tau_1$, where τ_1 is the delay time between the two pulses.

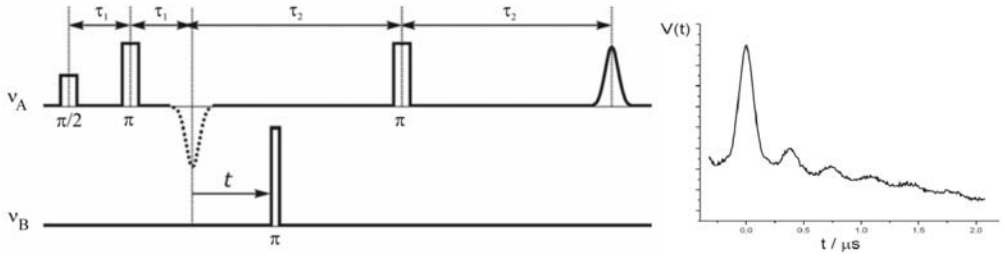

Figure 3.15: Left: Schematic representation of the 4-pulse DEER sequence. See text for details. Figure taken from [41]. Right: A typical DEER signal obtained by monitoring the echo intensity at position $2(\tau_1+\tau_2)$ in the DEER sequence in dependence of the pump pulse position t. The modulation arises from the dipolar interaction of the coupled spin pairs and the modulation frequency is the dipolar frequency ω_{dd} depending on the inter spin distance.

A second π pulse (ν_A) after the time τ_2 is applied to refocus the echo detectable at time $2(\tau_1 + \tau_2)$. This echo originates just from the A spins exhibiting the resonance frequency ν_A. The main part of this sequence is the application of an additional π pulse at time t after the second observer pulse, changing the polarization of B spins by excitation with ν_B. This causes a resonance frequency shift of the partial amount of the A spins, interacting with the B spins of $\pm 2\omega_{dd}$ (the dipolar frequency). Monitoring the echo amplitude at $2(\tau_1 + \tau_2)$ in dependence of the time t (the pump pulse position) yields the DEER signal (for a detailed description see for example [40, 71, 60, 27]).
The total DEER signal intensity $V(t)$ (figure 3.16 a) is composed of a damped

[4] The absorption spectrum is obtained by Echo detecting field sweep measurements, whereby the spin echo intensity (Hahn sequence) is detected as function of the magnetic field strength. The recorded spectrum corresponds to the *cw* EPR low temperature powder spectrum. Here the direct absorption spectrum is measured, not as in earlier discussions the 1. derivative.

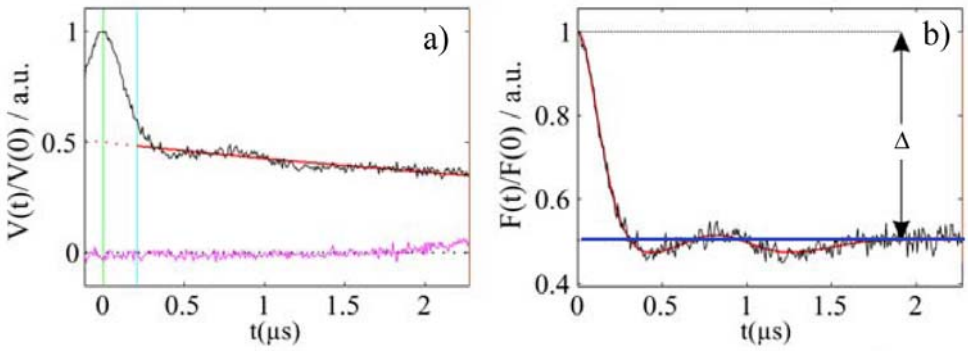

Figure 3.16: a): Experimentally obtained DEER spectrum $V(t)$ is composed of a damped modulated contribution $V^i(t)$ and an exponentially decaying background part $V^b(t)$. The simulated background part is highlighted as a red line. b): The form factor F(t) or also dipolar evolution function ($V^i(t)$) is obtained after background correction by division of $V^b(t)$. The modulation depth Δ is indicated. Figure adopted and slightly changed from [19].

ω_{dd} modulated part $V^i(t)$ (also called the intra molecular contribution) and an unmodulated background contribution $V^b(t)$ [71, 11]:

$$V(t) \quad = \quad V^i(t)V^b(t) \tag{3.61}$$

The background part arises from homogeneous distributed molecules within the sample exhibiting statistically distributed inter spin distances r to each other, and can be understood as a superposition of all $\omega_{dd}(r)$ modulated signals governed by these distances. Thus, it can be described as an exponential decay of the form:

$$V^b(t) = e^{-k^* t^{D/3}} \tag{3.62}$$

with

$$k^* = \frac{8\pi^2 \mu_B^2 g_A g_B}{9\sqrt{3}\hbar} C\lambda \tag{3.63}$$

where C is the spin concentration and λ the fraction of spins excited by the pump pulse. g_A and g_B describe the g-factors for the A and the B spins, respectively. D is the dimensionality of the background. In case of frozen protein solutions, where the spins causing the background contribution are three dimensionally homogeneously distributed, D=3 can be assumed [52, 60].
To separate the background part from the wanted intra molecular part, allowing the distance distribution calculation, a division of the experimentally obtained

DEER spectrum by V^b is done in general. This background correction leads to the wanted intra molecular contribution $V^i(t)$. The normalized signal intensity is theoretically [5] given by [34, 71, 11]:

$$V^i(t) = (1 - \lambda) + \lambda\tilde{V}^i(t) = 1 - \lambda(1 - \tilde{V}^i(t)) \tag{3.64}$$

with

$$\tilde{V}^i(t) = cos(\omega_{dd}t), \tag{3.65}$$

where ω_{dd} is the dipolar frequency (already introduced in 3.2.6) and λ the fraction of spins excited by the pump pulse, influencing the modulations depth Δ of the signal:

$$\Delta = 1 - (1 - \lambda)^{N-1}, \tag{3.66}$$

where N describes the number of interacting spins [36]. $V^i(t)$ is also known as *dipolar evolution function* or *form factor* $F(t)$ (see figure 3.16 b). This describes a with ω_{dd} oscillating function (shifted by 1-λ) beginning at $V^i(0) = 1$ with the amplitude λ. The damping of the background corrected function $V^i(t)$ has different reasons. On the one hand it can be explained by the presence of distance distributions exhibiting a certain width, leading to the superposition of different oscillating functions governed by the corresponding values for $\omega_{dd}(r)$. On the other hand the dependency of ω_{dd} on Θ_{dd} contributes to the signal damping as well, since a distribution of Θ_{dd} leads to a superposition of signals governed by the corresponding values for $\omega_{dd}(\Theta_{dd})$.
At this point it is anticipated that $V^i(t)$ also depends on various parameters, describing mutual spin label orientations [44]. In the case of full orientation correlation between two dipolar interacting spin labels their mutual orientation is given by a set of three Euler angles, described by a transformation matrix Ω, which transforms the spin label A molecular frame into the frame of spin label B (figure 3.17). As it can be seen from equation 3.66 ω_{dd} depends, besides on the inter spin distance r, on the angle Θ_{dd} between the dipolar axis D and the magnetic field direction. The magnetic field direction with respect to spin label frame A can be described by two angles ϑ and φ. In the here considered case the dipolar axis orientation (ψ,η) is fixed within the spin label frame A, thus

[5] In the here made considerations the Heisenberg interaction is neglected, considering distances beyond 1 nm. The dominating contribution of the Hamiltonian in this case is the dipolar interaction described by equation 3.39

the dependency of ω_{dd} on Θ_{dd} can be replaced by ϑ and φ, since the respective orientation information is with constant values for ψ and η also given by φ and ϑ.

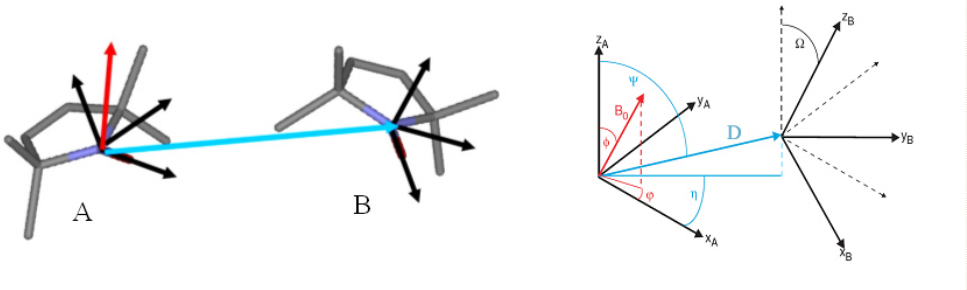

Figure 3.17: Representation of the orientations influencing the DEER signal shape. The mutual orientation between two spin label molecules A and B (black frames) is given by three Euler angles described by Ω. The dipolar vector D (blue) orientation with respect to the spin label molecule A frame is given by ψ and η and the magnetic field orientation B (red) in the same frame by ϑ and φ.

The pump efficiency λ depends, besides φ and ϑ, on the orientation Ω between the two interacting spin label molecules and on the pump frequency ν_B (see figure 3.14). To elucidate which parameters influence the shape of the DEER spectra the dependencies are summarized in the following formula [44]:

$$V^i(t, \nu_B, \Omega, \vartheta, \varphi, r) = 1 - \lambda(\nu_B, \Omega, \vartheta, \varphi)[1 - cos(\omega_{dd}(\vartheta, \varphi, r)t)] \tag{3.67}$$

The origin of the orientation dependence of $V^i(t)$ will be described in the next chapter.
To obtain the signal for a powder-like sample 3.67 has to be integrated over φ and ϑ using the weighting factor $sin(\vartheta)$, leading to:

$$V^i(t, \nu_A, \nu_B, \Omega, r) = \int\int V^i(t, \nu_A, \nu_B, \Omega, \vartheta, \varphi, r) sin(\vartheta) d\vartheta d\varphi \tag{3.68}$$

Considering the case of orientational full uncorrelated spin label pairs exhibiting a single fixed distance r, the relative orientations between spin A and B (Ω) as well as with respect to the vector D (ψ,η) will all be random. In these cases, integration over all Ω values will effectively average the magnetic field orientation dependence of the parameter λ [44], and the double integration in equation 3.68 can be converted into an integration over the dipolar angle Θ_{dd}, leading to:

$$V^i(t) = 1 - \lambda[1 - \int cos(\omega_{dd}(\Theta_{dd})t) d\Theta_{dd}] \tag{3.69}$$

In the considered case the background corrected dipolar evolution data would have the shape describable by equation 3.69. The Fourier transformation of this function into the frequency domain provides the Pake pattern (PP), described in 3.2.6, from which the inter spin distance can be calculated. In contrast, if an orientation correlation between the two spin pairs under investigation exists, a distorted Pake pattern (DPP) revealing shape differences compared to the undistorted Pake pattern (PP), is observed. The reason arises from the *orientation selectivity* of the applied pulses. Means to consider the orientation correlation between the spin label pairs in data analysis programs are still a challenge. One applied methodology, giving rise to the orientational situation of spin labels, is *orientation selective DEER*, what is presented in the next chapter.
However, in many systems the orientation correlation between the interacting spin labels is mostly unknown and the assumption of random orientations leads in general to reasonable results regarding inter spin distance determinations. Once the background contribution to the DEER signal has been removed, the resulting contribution $V^i(t)$ has to be analyzed in terms of a distance distribution.

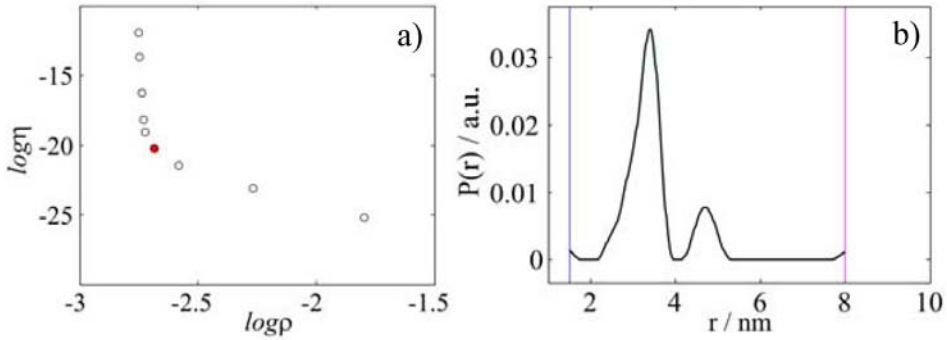

Figure 3.18: a): Example for a L-curve calculation ($\rho = \|S(t) - D(t)\|^2$ and $\eta = \left\|\frac{d^2}{dr^2}P(r)\right\|^2$) using the typical regularization parameter values of $\alpha = 0.001, 0.01, 0.1, 1, 10, 100, 1000, 10000, 100000$. The ideal value of α is extractable at the kink (red dot). b): Example for a distance distribution P(r) used for the simulation of the DEER spectrum (D(t)). Figure adopted and slightly changed from [19].

DEER data can be analyzed by fitting a distance distribution P(r) to $V^i(t)$. The computation of the distribution P(r) is an ill posed problem, meaning that the solutions are not unique or stable, since small variations in the DEER spectra (artifacts, signal-to-noise ratio, etc.) can cause large variations in the calculated distance distributions. A widely used approach for the analysis of DEER data is Tikhonov regularization, which has been implemented in the software *DeerAnalysis* developed by Jeschke and coworkers [35] and is used in

this work for the DEER data analysis. This approach relies on the minimization of the function:

$$G_\alpha(P) = \|S(t) - D(t)\|^2 + \alpha \left\| \frac{d^2}{dr^2} P(r) \right\|^2 \tag{3.70}$$

The first term on the right hand side represents the root mean square deviation (RMSD) between the simulated S(t) and the experimental background corrected DEER spectrum D(t). The second term is the regularization parameter α weighted square norm of the second derivative of P(r), which is a measure for the smoothness of the distance distribution. The calculation of the simulated spectrum is done according to:

$$S(t) = \int K(t,r)P(r)dr \tag{3.71}$$

The simulated signal S(t) (equation 3.71) is the superposition of all functions (K(t,r)), oscillating with the respective ω_{dd} governed by the contributing inter spin distances r. The intensities (amplitudes) of the particular contributions of K(t,r) are considered by a weighting with the corresponding intensities of the distance distribution P(r) (for a typical example for P(r) see figure 3.18 b). K(t,r) is the so called Kernel-function:

$$K(t,r) = \int_0^{\pi/2} cos(\omega_{dd}(\Theta_{dd})t)d\Theta_{dd} \tag{3.72}$$

Here, the similarity to equation 3.65 or to the modulated part in 3.69 should be pointed out. To consider the fact that ω_{dd} depends on the dipolar angle Θ_{dd} in a Pake pattern manner an integration over all angles from 0-$\pi/2$ is necessary to account for randomly distributed molecules. Additionally, it was found that the pump efficiency λ depends also on ω_{dd} and on the excitation bandwidth σ_{exc} of the whole 4-pulse DEER experiment. In general, the dependence of λ on ω_{dd} can be fitted quite satisfactorily by a Gaussian [8]. To account for this phenomenon, becoming significant at very small distances (below 2nm), equation 3.72 has to be expanded according to:

$$K(t,r) = \int_0^{\pi/2} exp\left(-\frac{\omega_{dd}^2}{\sigma_{exc}^2}\right) cos(\omega_{dd}(\Theta_{dd})t)d\Theta_{dd} \tag{3.73}$$

This arises from the fact that a B spin inversion shifts the resonance frequency of the A spins by twice the dipolar coupling frequency. Hence, the subsequent echo

refocusing by the final observer pulse can only take place, if both components of the dipolar douplet of A spins are located within the excitation range of the refocusing pulse. Consequently, in case of small distances (large dipolar splitting) a larger bandwidth is required.
Tikhonov regularization finds a compromise between smoothness and resolution of P(r) by the calculation of a regularization parameter α. A suitable value for α can be determined by the calculation of the so called L-curve, which is the plot of $\log(\|S(t) - D(t)\|^2)$ versus $\log(\left\|\frac{d^2}{dr^2}P(r)\right\|^2)$. This leads to a L-shaped curve and the most adequate value for α corresponding to the best above mentioned compromise is extractable at the kink (sharp bend) of the L-curve (figure 3.18 a).

3.4.2 Orientation selective DEER (OS-DEER) spectroscopy

As already mentioned, the shape of a DEER spectrum depends on various molecular orientations (see equation 3.67). In case of frozen protein samples the powder average, as calculated by equation 3.68, is always necessary to describe the DEER spectrum. However, the dependence of λ on the mutual spin label orientation Ω is not averaged out, if a strong orientation correlation between the two interacting spin label molecules exists. In this case, the obtained DEER spectrum differs from the shape described by 3.69. The assumption of statistically distributed spin label molecules with respect to the dipolar axis orientation, which all contribute to the DEER signal, is not true anymore and the usual weighting factor of $sin\Theta_{dd}$ can not be used for integration in case of an orientation correlation. This fact should be explained in more detail.

3.4.2.1 Orientation selectivity of the applied pulses

Coming back to the finite pulse lengths used in a DEER experiment, a certain bandwidth of exciting frequencies is generated by the application of short microwave pulses. In general, it can be well approximated to a Gaussian shaped profile (figure 3.14). The positioning of pump and observer pulses ($\Delta\nu = 65MHZ$) according to the EPR low temperature absorption spectrum leads to an excitation of spin label molecules exhibiting different orientations with respect to the external B-field. This fact is schematically shown in figure 3.19.
As discussed in 3.3.1, the EPR spectrum of a single nitroxide spin label molecule consists of three lines centered at the magnetic field orientation dependent value $g_{\vartheta,\varphi}$ and separated by the corresponding value $A_{\vartheta,\varphi}$ (hyperfine splitting). The g-anisotropy of nitroxide spin label is not resolved using X-band frequencies (9.5 GHz). That means, the $m_I = 0$ transitions of all molecules for all magnetic field

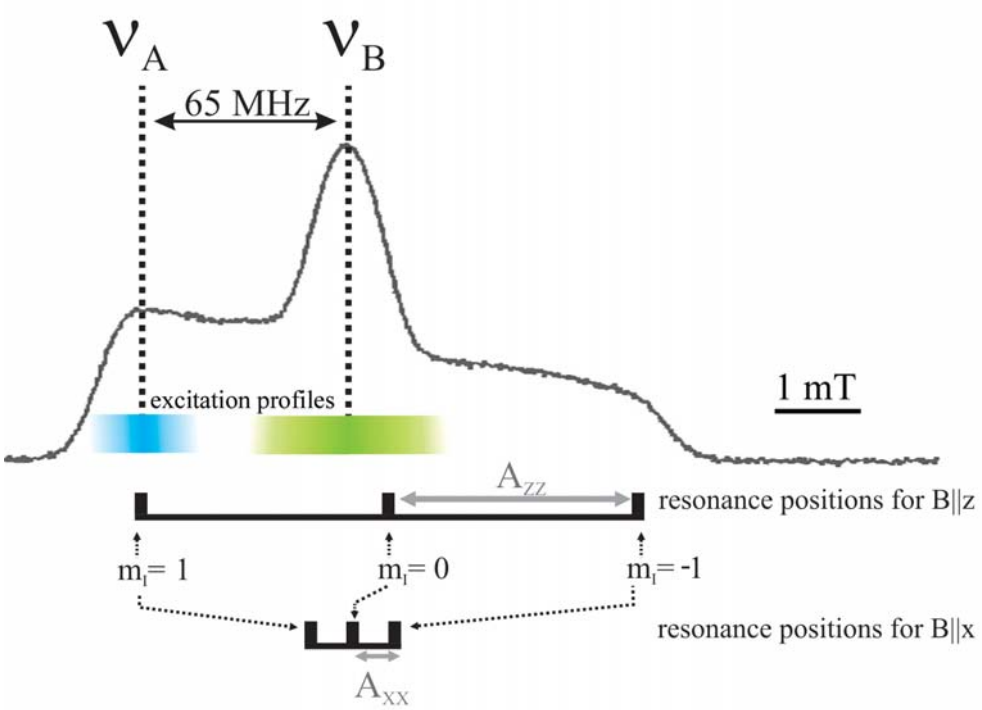

Figure 3.19: Orientation selectivity of the applied microwave pulses in a DEER experiment. The observer frequency ν_A separated by 65 MHz from the pump frequency ν_B primarily excites $m_I = -1$ transitions of spin labels, which z-axis is approximately parallel to the magnetic field direction. ν_B corresponding to the EPR absorption spectrum center excites spin label molecules exhibiting almost all possible orientations with respect to the magnetic field due to the unresolved g-anisotropy at X-band frequencies. As examples, the resonance positions of MTSSL exhibiting a molecular z-axis and x-axis parallel to the B-field direction ($B||z$ and $B||x$) are shown (black bars).

orientations (ϑ, φ) are located near the center (maximum) of the EPR absorption spectrum. Even the $m_I = +/-1$ transitions of the single molecule spectra exhibiting a respective magnetic field orientations governed by small values for $A_{\vartheta,\varphi}$ (such as A_{xx} or A_{yy}) are situated near the EPR spectrum center (figure 3.19).
Consequently, the molecules excited by the pump frequency ν_B (excitation profile centered at the EPR absorption spectrum center) exhibit all different orientations (ϑ, φ) with respect to the B-field. In contrast, the observer frequency ν_A excites primarily $m_I = -1$ transitions of molecules, which z-axis orientations are parallel aligned to the magnetic field, thus exhibiting hyperfine splitting values equal or close to A_{zz}. How this fact influences the DEER signal in case of the orientation correlation between two dipolar interacting spin labels should be explained in the following by two different examples.

3.4.2.2 Orientationally uncorrelated spin pairs

The first example describes the case in which no angular correlation between two interacting spin labels A and B exists, meaning all possible values and combinations of Ω, ψ, η are present within the sample (for definitions see 3.17). In case of frozen protein solutions, the magnetic field orientation (ϑ, φ) and thus the angles Θ_{dd} between the dipolar axis **D** and the magnetic field **B** are randomly distributed (figure 3.20 a). Furthermore, the pump pulse excites spin label B molecules, possessing all possible orientations with respect to the external magnetic field. Since no orientational correlation is present, in each group of excited B spins defined by a certain orientation with respect to the magnetic field (Ω, ϑ and φ), there will be the situation, in which an interacting spin partner (A spin) exhibits a molecular z-axis orientation, which coincides with the magnetic field. This situation appears for each arbitrary dipolar axis orientation Θ_{dd}. Consequently, all these cases can be observed using ν_A, exciting primarily $B||z$. That means that the observed interacting spin pairs contributing to the DEER spectrum exhibit statistically distributed values for their dipolar angle Θ_{dd} between 0 and $\pi/2$ (figure 3.20 b)). The DEER spectrum then contains all dipolar frequencies determined by $\omega_{dd}(\Theta_{dd})$ leading to the observation of a Pake pattern (PP). In this case the spectrum can be calculated using the weighting factor $sin\Theta_{dd}$ to account for the powder average as done in equation 3.69.

3.4.2.3 Fully correlated spin pairs and OS-DEER

The situation becomes more complicated if an orientational correlation between the two interacting spin label molecules exists. Considering the case of full orientation correlation, the orientation between the two molecules is given by fixed values for Ω, ψ and η. The molecules should be frozen in random orientations for Θ_{dd} or ϑ and φ, respectively. Also in this example, the pump pulse excites B spin carrying molecules exhibiting all possible orientations with respect to the magnetic field (figure 3.20 c)). However, the use of the observer frequency ν_A located at the low field maximum of the EPR absorption spectrum leads to the observation of just those molecules, which spin label A z-axis is parallel to the B-field. In case of full orientation correlation the number of the observed molecules (affecting the modulation depth Δ) is then decreased, and the observable range of Θ_{dd} is considerably restricted. Figure 3.20 d) shows a schematic representation for this case.
Here, the specific excitation bandwidth of the observer pulse always leads to the observation of spin label A molecules, which z-axes orientations exhibit small deviations relative to the magnetic field direction. Thus, the DEER spectrum is governed by a certain distribution of Θ_{dd} or ω_{dd}, respectively. However, the restriction for the observable dipolar frequencies is still strong and the fact that

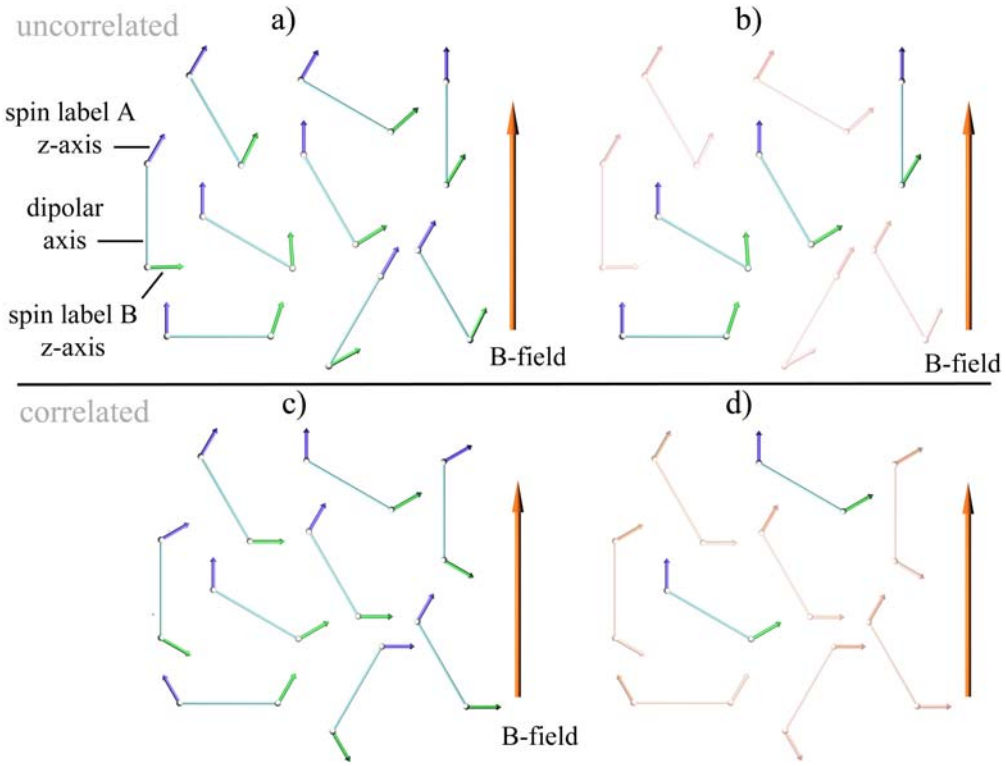

Figure 3.20: Schematic representation of the influence of the orientation selectivity of the pulses in a DEER experiment in case of frozen protein solutions, where the angle Θ_{dd} between the dipolar axis and the external magnetic field (red) is randomly distributed. The spin label pairs exhibit no (a)) or full (c)) orientational correlation. Thus, the mutual spin label orientations between spin label A (blue) and B (green) as well as the orientation of the dipolar axis (light blue) within their frames are completely random (a)) or fixed (c)). Shown are the molecules excited by the pump pulse exhibiting all possible orientations with respect to the magnetic field. For better visualization only the spin label z-axes are indicated. The orientation selectivity of the observer pulse ($\Delta\nu = 65MHz$) leads to the observation of spin pairs, whose A spin molecule z-axis is parallel to the B-field. Molecules which does not fulfill this conditions are blanked out (blurry red). In case of no orientational correlation (top) all possible values for Θ_{dd} are observed (b)) leading to the observation of a Pake pattern. In case of full orientational correlation case (bottom) the number the observed molecules is decreased compared to the uncorrelated case, and the observed values for Θ_{dd} are restricted. This leads to a distorted Pake pattern (DPP), which differs in shape in comparison with an usual PP.

only specific orientations are selected is leading to a frequency selection in the dipolar spectrum. This in turn causes a dependence of the DEER spectrum shape on the spin label orientation, affecting the Fourier transformation of the dipolar evolution function. The Fourier transformation does not anymore lead to the PP described above, but to a distorted Pake pattern (DPP), which may differ significantly in shape.

In order to calculate the DEER spectrum in case of orientational correlation between the spin labels, the integration over Θ_{dd} from 0 to $\pi/2$ can not be done anymore using a weighting factor of $sin\Theta_{dd}$. The pump efficiency λ will depend on the mutual orientation of the two molecules A and B. Additionally, it is obvious from figure 3.19 that the respective pulse positions influence the DEER spectrum shape, since ν_A defines the observed orientations, which contribute to the signal. Moreover, the pulse lengths (t_o, t_p) determine the width of the excitation profile and, thereby, the orientation selectivity of the pulses. This orientation selectivity will lead to a distribution function $P(\Theta_{dd}, \nu_A, \nu_B, t_o, t_p)$ of dipolar angles, which differs from the $sin\Theta_{dd}$ distribution of a PP. A weighting factor has to be introduced to account for the orientation dependence. The echo normalized signal intensity for a given pump and observer frequency can, in such cases, be described by [44, 11]:

$$V^i(t) = 1 - \int P[1 - cos(\omega_{dd}(\Theta_{dd})t)d\Theta_{dd}] \tag{3.74}$$

where P is the above mentioned distribution function. Jeschke and coworkers [59] calculated the excitation profile for a total DEER experiment and the weighting factor for the on Θ_{dd} depending positions in the Pake Pattern can be approximately described by:

$$w = exp\left(-\left(\frac{\nu_{A,res} - \nu_{B,res} - \Delta\nu}{\Delta\nu_{exc}}\right)^4\right) \tag{3.75}$$

Thus the corresponding function P would be described by:

$$P = exp\left(-\left(\frac{\nu_{A,res} - \nu_{B,res} - \Delta\nu}{\Delta\nu_{exc}}\right)^4\right) sin\Theta_{dd} \tag{3.76}$$

where $\nu_{A,res}$ and $\nu_{B,res}$ are the resonance positions (in frequency units) of spin label A and B, respectively. Here, it should be again referred to figure 3.19. $\Delta\nu = \nu_A - \nu_B$ is the frequency offset between the pump and the observer frequency, and $\Delta\nu_{exc}$ describes the the effective excitation bandwidth of the experiment.
However, if the geometry of the system (the orientation correlation between the molecules A and B) is unknown, the determination of the weighting function P is difficult and still a challenge for researchers at present. The significance of this problem is clear, considering the case of spin labeled proteins, where the spin label motion and spacial freedom is restricted by interactions with the protein backbone and side chain atoms. This leads in the most cases to an

angular correlation between two spin labels attached to a protein, and thus to a dependence of the DEER spectral shape on their mutual orientation. In turn, the spectral shape influences the shape of the distance distributions calculated from the DEER spectra, if the angular correlation of the spin labels are omitted. This can easily lead to misinterpretation of the experimental data. The determination of spin label orientations on spin labeled proteins, therefore, would support the analysis and interpretation concerning the obtained distance distributions.
A innovative method for this purpose is *orientation selective DEER spectroscopy*. Therein, the pump and observer pulse frequency positions are shifted within the corresponding EPR absorption spectrum range. A typical choice is the variation of the observer pulse frequency (ν_A), whereas the pump pulse frequency stays located at the EPR absorption spectrum center. In this way the orientations selected by ν_A are systematically scanned and the behavior of the spectra in dependence on the frequency offset $\Delta\nu = \nu_A - \nu_B$ give rise to the orientational situation of the investigated system. If the spectra recorded at different $\Delta\nu$ reveal differences in shape, this is a first indication for an orientation correlation between the spin pairs, and one has to assume that distance distribution calculated from DEER measurements are affected by this fact.
However, the resulting weighting function P can for instance be calculated, if a molecular model of the investigated system exists [11, 59]. In this case all possible orientations with regard to the model are considered by a set of different conformers. For each of these conformers, the resonance positions of spins A and B are calculated for all orientations of the magnetic field vector. Their individual contribution to the signal or to the PP, respectively, (defined by P) is calculated by the $\Delta\nu$ depending weighting with the intensities of the excitation profile, corresponding to the respective resonance position. Simulated spectra can be compared to the experimental results to validate the accuracy of the model. If the molecular model is adequate, the calculated spectra using the corresponding function P (calculated for the model), reflect the behavior of the experimental spectra along with $\Delta\nu$ well.

To the best of my knowledge, up to now only this strategy has been used. The vice versa procedure, meaning the calculation of P from the experimental results without any knowledge about the orientational correlation between the spin pairs seems to be problematical. Especially, if orientational distributions of the investigated molecules or even different molecular conformations are present, a fitting of P to the experimental data is computational intensely demanding.

4 Material and Methods

4.1 EPR measurements and procedures

4.1.1 Sample preparations

4.1.1.1 Vt preparation

Cloning and expression procedures, described in the following, were carried out by Franziska Dietrich (IZKF Leipzig).

Cloning and mutagenesis of vinculin tail constructs Vinculin encoding cDNAs used in this study are described in [16]. Vinculin tail (Vt) constructs in pQE-30 (Qiagen) encoding amino acids 858-1066 are equipped with an N-terminal FLAG and His tag. The Quick Change® Method (Stratagene) was used to replace the three wild type cysteines at positions 950, 972 and 985 by alanines. Subsequently, the triple alanine mutant of Vt was used to generate eight mutants carrying a single cysteine (Vt-(A901C), Vt-(A922C), Vt-(A950C), Vt-(A957C), Vt-(V984C), Vt-(S1033C), Vt-(A1062C) and Vt-(A1067C)) as well as four double cysteine mutants (Vt-(A901C/A957C), Vt-(A901C/S1033C), Vt-(A922C/A957C), Vt-(V984C/C985V/S1033C)). All mutant constructs were verified by DNA sequencing.

Protein expression, purification and characterization Recombinant cysteine mutants were expressed and purified as described in [83]. Labeling with the MTS spin label ((1-oxy-2,2,5,5-tetramethyl-pyrrolinyl-3-methyl) methanethiosulfonate) was carried out overnight by incubating the proteins bound to Ni-NTA beads (Qiagen) with 1mM MTSSL, for single cysteine mutants, or 2 mM MTSSL, for double cysteine mutants. Free label was removed by washing the Ni-NTA beads several times with 50mM phosphate buffer, pH 7.2. Labeled protein was eluted according to the manufacturer's instructions (Qiagen) and transferred into 20 mM phosphate (pH 7.2) buffer using PD10 desalting columns (GE Healthcare). Protein integrity was confirmed using SDS-PAGE and circular dichroism spectroscopy. Concentrations were determined using a BCA assay (Thermo Fischer Scientific).
The MTS labeled single cysteine (R1) mutants are termed Vt901R1, Vt922R1, Vt950R1, Vt957R1, Vt984R1, Vt1033R1, Vt1062R1, Vt1067R1 and the double

cysteine mutants Vt901/957R1, Vt922/957R1, Vt901/1033R1, Vt984/1033R1 in following discussions. R1 positions under investigation are illustrated in terms of their location in the Vt crystal structure (and Vt amino acid sequence) in figure 4.1.

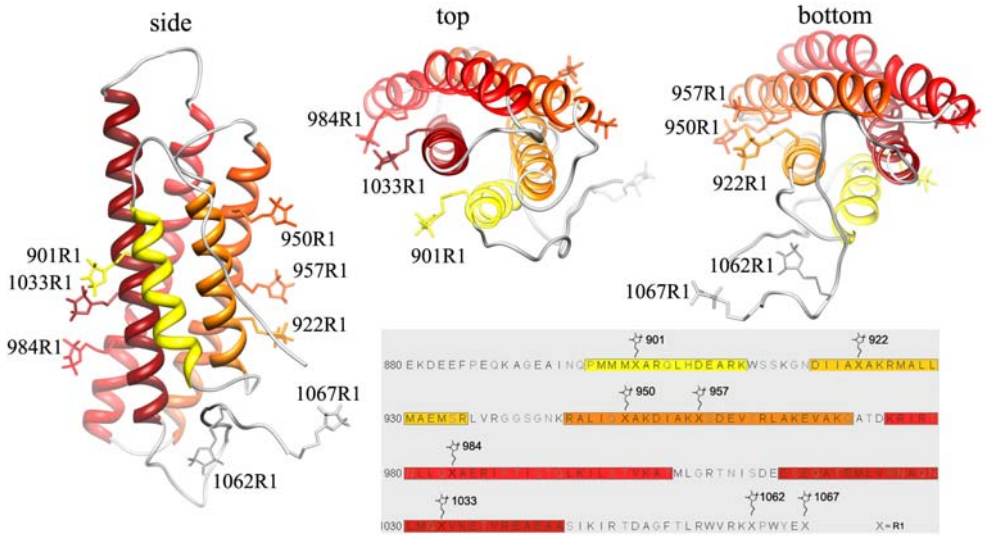

Figure 4.1: R1 locations after spin labeling are illustrated on the Vt crystal structure (PDB-code:1ST6) from different views (side, top, bottom) and on the Vt amino acid sequence. Spin labeled positions are indicated.

4.1.1.2 Vt in lipid vesicle solutions

Preparation of lipid vesicle solutions Lyophilized phospholipid powder (3-sn-Phospatidyl-serine (PS) and 1-palitoyl-2-Oleoyl-sn-3-Phosphocholine (PC)) was purchased from Sigma Aldrich. In each case the powder was dissolved in liquid chloroform (10 mg/ml final lipid concentration). For experiments with solutions containing different lipid mixtures the lipid/chlorophorm solutions were mixed in the respective ratios. To obtain vesicle solutions containing spin labeled lipids, 1 mg spin labeled 5/16-doxyl-stearic acid (SA) powder was dissolved in 1 ml chloroform, and added to the respective lipid/chloroform solution to a final lipid:SA molar ratio of 100:1. 100 μl of the final lipid/chloroform solution was filled in a 2 ml Eppendorf vial, and the solvent was evaporated under continuous gaseous N_2 flux for at least 1.5 hours. 1.5 ml of 20 mM Tris-HCl-buffer (150 mM NaCl, pH 7.5) was added and the solution was incubated at 42 °C for 3 hours, permanently shaking in an incubation shaker. After incubation, the vesicles were pelleted down by centrifugation at room temperature with 12000 rpm for 1 hour in a tabletop centrifuge. The supernatant was discarded and the pellet was resuspended in 100 μl of the same buffer leading to a giant vesicle

(GV) solution (ca. 10 mg/ml). Small unilamellar vesicle (SUV) solutions were obtained within at least two minutes of sonication using a dip-sonifier (Branson 250).

Preparation of Vt in lipid vesicle solutions Protein solutions containing 2-3 mg/ml Vt were mixed with the GV lipid vesicle solution, exhibiting a volume ratio of 1:4 (lipid:Vt). The protein/lipid solution was incubated for at least 30 min, permanently mixing at 42°C in an incubation shaker. For DEER measurements, 10% deuterated gylcerol was added to increase relaxation times. In following discussions the respective samples are termed as mentioned before with the appendix *PS*.

4.1.1.3 F-actin binding assay

For sample preparations of Vt bound to filamentous actin (F-actin) an actin toolkit, purchased from Hypermol (Ulrike Hinssen, Bielefeld), was used.

Preparation of G-actin solutions To obtain 1 mg/ml (globular) G-actin stock solution, 1 ml H_2O was added to the vial, containing 1 mg lyophilized actin powder. After vortexing for 30 sec, the protein solution was kept at room temperature for 2 min for rehydration.
The actin solution was dialyzed for at least 12 hours against 25-50x volume of dialysis buffer, containing 2mM Tris-Cl pH 8.2, 0.4 mM ATP, 0.01 mM DTT and 0.1 mM CaCl2 (MonoMix), using ZelluTrans dialysis tubes (MWCO:8000-10000). The same was done for 1 ml of the solution, containing the respective spin labeled Vt mutant (2 mg/ml), simultaneously. To obtain solutions containing mixtures of Vt single mutants the Vt solutions were mixed in a molar ratio of 1:1. After dialysis a low speed cosedimentation of both solutions was carried out for 45 min in a tabletop centrifuge (13000 rpm, at 4 °C). The pellets were discarded. After cosedimentation the supernatants exhibit experientially a concentration of around 1 mg/ml Vt due to the loss of protein by aggregation during the dialysis process. All stock solutions were stored on ice.

Preparation of F-actin solutions 1.25 ml H_2O was added to the vial containing the lyophilized actin polymerization buffer (Polymix; 0.1 M KCl, 2 mM MgCl2, 1 mM ATP, 10 mM Imidazol, pH 7.4) and vortexed until the powder was fully dissolved. The resulting solution is termed 10xPolyMix in the following. 40 μl 10xPolyMix was added to 1 ml G-actin stock solution and was mixed using a pipette. The polymerizing actin solution was kept at room temperature for approximately 30 min without agitation. To verify the polymerization the

visible change in viscosity was tested by turning the vial upside down. In contrast to the aqueous G-actin solution, (filamentous) F-actin is a gel like matrix. F-actin solution was stored on ice.

F-actin bundling by Vt In order to prepare sample mixtures of the ligand protein Vt and F-actin 50 μl 10xPolyMix was added to 450 μl H_2O leading to 1xPolyMix solution. Thereafter, 360-400 μl of the dialyzed Vt solution (1 mg/ml) was added to 500 μl F-actin solution (molar ratio 1:1). To obtain 1 ml of solution with a final actin concentration of 0.5 mg/ml 100-140 μl of 1xPolyMix was added. After cautiously mixing with a pipette, the mixtures were incubated for 60 min at room temperature. To remove unbound Vt the solutions were centrifuged for 60 min in a tabletop centrifuge (13000 rpm at room temperature) and the supernatant was carefully discarded. The residual gel like pellet, containing the Vt bundled F-actin filaments, was resuspended in 500-1000 μl 1xPolyMix and the procedure was repeated. Afterwards, the pellet was resuspended in 50-80 μl 1xPolyMix. For DEER experiments, 1xPolyMix was prepared with D_2O and samples were resuspended in 50-80 μl deuterated 1xPolyMix. Finally 10% deuterated glycerol was added. The sample was immediately filled in the DEER capillary and frozen in liquid nitrogen. In following discussions the samples containing actin bound singly and doubly labeled Vt are termed as mentioned before with the appendix A. Samples containing mixtures of two different Vt single mutant are nominated with Vt901R1/Vt957R1A and Vt901R1/Vt1033R1A.

4.1.1.4 Lipid and F-actin competition measurements

For lipid and F-actin competition measurements, SUV vesicle solutions containing different lipid types (PC and PS) were prepared according to 4.1.1.2. Vt957R1A solutions were prepared according to the F-actin bundling assay described above. Vt concentration after acting bundling was determined by spin number determination using a 100 μM MTSSL solution as reference. Lipid solutions were added to Vt957R1A, resulting in final Vt:lipid ratios of ca. 1:30, 1:100 and 1:200, respectively. After adding lipid solutions the samples were immediately transfered into an EPR quartz capillary (inner diameter 0.9 mm). Room temperature EPR spectra were recorded and stored in 1 min steps.

4.1.2 Cw-EPR measurements

4.1.2.1 Mobility measurements

Room temperature *cw*-EPR measurements were carried out on a MiniScope benchtop EPR spectrometer (MS200; Magnettech GmbH, Berlin, Germany)

equipped with a rectangular TE102 resonator fluxed with gaseous nitrogen for temperature stabilization. The microwave power was set to 10 mW and the B-field modulation to 0.15 mT. To solutions containing Vt in absence of binding partners, 40 % (m/v) sucrose was added to reduce protein rotational diffusion. 10 μl of sample volume with protein concentrations of 80 - 120 μM (2-3 mg/ml) were filled in EPR glass capillaries (0.9 mm inner diameter). As semi-empirical mobility parameters the width of the central line and the spectral second moment (see 3.3.2.2) were used for the analysis of spin label mobility. The central line width was extracted directly from the EPR spectrum, whereas the second moment was calculated using the program *unispec* written by Christian Beier. For lipid and F-actin competition measurements a Varian spectrometer (Standard E-109, X-band) was used. Room temperature measurements on Vt in presence of PS-vesicles were repeated to verify results obtained by Klaus Peter Vogel (University of Osnabrueck, unpublished).

4.1.2.2 Accessibility measurements

Accessibilities were determined for the collision reagents gaseous oxygen and NiEDDA (Ni(II)ethylenediamine diacetate). Measurements were carried out on a homebuilt *cw* EPR spectrometer equipped with a loop gap resonator. The B-field modulation was set to 0.15 mT. The applied microwave power was varied in the range from 0.1 to 65 mW. In order to change the main attenuator during the measurement a motor, controlled by the measuring software, was used. Gas permeable TPX (Polymethylpenten) capillaries (RototecSpintec GmbH, Biebesheim, Germany) were filled with 5 μl of sample solution and placed into the resonator.
For reference measurements the sample was deoxygenated by fluxing the resonator permanently with nitrogen gas. In order to obtain accessibilities for oxygen, the nitrogen was replaced by air (21 % O_2). For Ni-accessibility determination, 1 μl of 200 mM NiEDDA solution was added to 9 μl sample solution, leading to a final concentration of 20 mM. During the measurement the nitrogen gas flux was preserved. Before each experiment the sample was fluxed with the respective gas for at least 15 min.
W_{ex} was calculated using the program *powerfit* written by Martin Kühn [39]. Therein, a set of EPR spectra recorded at different microwave powers P are analyzed. The peak-to-peak line widths of the EPR central line (ΔH_{pp}) and the corresponding amplitudes Y' were obtained by fitting of a pseudo-Voigt function to the EPR central line. Thereafter, the calculated amplitudes Y' were plotted versus the square root of the power P, automatically done by the program *satfit*. To these data points a curve according to equation 3.57 was fitted, where I, ϵ and $P_{1/2}$ are adjustable parameters. The parameter $P_{1/2}$ was

calculated from the resulting best fitting curve as the power value, at which the central line amplitude is reduced to half of its theoretical unsaturated value. The accessibility parameter Π or W_{ex}, respectively, was determined using equation 3.59. Under the here applied experimental conditions the value for α, needed for the calculation of W_{ex}, amounts $\alpha = 1,91 +/- 0,20$ (derived by M. Doebber, personal communication). Φ was calculated using equation 3.60.

4.1.2.3 Polarity and distance measurements

Low temperature *cw*-EPR measurements were carried out at 160 K using a homemade X-band EPR spectrometer equipped with an AEG H103 rectangular cavity. The microwave power was set to 0.2 mW and a B-field modulation amplitude of 0.24 mT was used. 40 μl of sample solution with a final protein concentration of 80-120 μM was filled into an EPR quartz capillary (3 mm inner diameter). A continuous flow cryostat Oxford ESR 900 allowed stabilization of the sample temperature. Measurements on Vt in absence and presence of PS-vesicles were repeated to verify results obtained by Klaus Peter Vogel (University of Osnabrueck, unpublished).
Inter spin distances and A_{zz} were determined from a detailed line shape analysis using the program *Dipfit* (see 3.3.3.3). Parameters for the hyperfine coupling, g-tensor and line width parameters were obtained by fitting simulated EPR spectra to the experimental data of the corresponding singly labeled protein samples. For analysis of distances below 1 nm the program *Short Distances* was used (see also 3.3.3.3), kindly provided by Christian Altenbach (UCLA, CA). All fits were performed assuming an isotropic distribution of mutual nitroxide orientations, disregarding Heisenberg exchange interaction.

4.1.3 Pulse EPR measurements

4.1.3.1 DEER spectroscopy

DEER experiments were performed at X-band frequencies (9.4 GHz) with a Bruker Elexsys 580 spectrometer equipped with a Bruker Flexline split ring resonator ER 4118XMS3. 40 μl of sample solution with a final protein concentration of 80-120 μM containing 10% of deuterated glycerol was filled into an EPR quartz capillary (1 mm inner diameter). A continuous flow helium cryostat (ESR900; Oxford Instruments) and an Oxford Instruments ITC 503S were used for temperature controlling. All measurements were performed using the four-pulse DEER sequence: $\pi/2(\nu_A) - \tau_1 - \pi(\nu_A) - t' - \pi(\nu_B) - (\tau_1 + \tau_2 - t') - \pi(\nu_A) - \tau_2 - echo$. For the DEER pulses at the observer frequency the $\langle x \rangle$ channels were used. A two-step phase cycling (+ $\langle x \rangle$, - $\langle x \rangle$) is performed on $\pi/2(\nu_A)$. Time t is varied, whereas τ_1 and τ_2 are kept constant, and the dipolar evolution

time is given by t = t' - τ_1. Data were analyzed only for t $\geq$ 0. The resonator was overcoupled to Q $\approx$ 100; the pump frequency ν_B was set to the center of the resonator dip and coincided with the maximum of the nitroxide EPR absorption spectrum, whereas the observer frequency ν_A was 65 MHz higher and coincided with the low field local maximum of the absorption spectrum. All measurements were performed at a temperature of 50 K with observer pulse lengths of 16 ns for $\pi/2$ and 32 ns for π pulses and a pump pulse length of 12 ns. Deuterium modulation [1] was averaged by adding traces at eight different τ_1 values, starting at $\tau_{1,0}$ = 400 ns and incrementing by 56ns. This corresponds to an averaging over one modulation caused by deuterium. Background correction and determination of interspin distance distributions were carried out using the programm DEERAnalysis (2006) using a model of randomly oriented spins with respect to the dipolar axis and Tikhonov regularization (see chapter 3.4.1).

4.1.3.2 OS-DEER spectroscopy

Orientation selective DEER measurements were done using the four pulse DEER sequence as described before. The length of the pump pulse was set to 32 ns to minimize overlaps of the particular excitation bandwidths, especially for measurements at small frequency offsets. DEER spectra were recorded at five different frequency offsets $\Delta\nu = \nu_A - \nu_B$. The frequency offset was varied from +40 to +80 MHz in steps of 10 MHz (figure 4.2).
The experiments were carried out with the double mutant Vt901R1/957R1 mixed with unlabeled wild type Vt in a molar ratio of ratio 1:2 (Vt:Wt) in order to suppress contributions of intermolecular distances to the DEER traces. The obtained dipolar spectra were analyzed using a modified simulation program kindly provided by Y. Polyhach and G. Jeschke (ETH Zürich), and a home written matlab script as described in the next chapter.

4.1.3.3 OS-DEER data analysis

The program DEERsim Simulations of distorted Pake pattern (DPP, see chapter 3.4.2.3) were done in order to obtain orientational information about the system. Orientation dependent DPP simulations were performed using a

[1] Adding deuterium to the sample leads to an increase of the relaxation times, since the magnetic moment of a deuterium nucleus is significantly smaller than that of a proton. Thus, the dipolar interaction, influencing the effective relaxation time, between the magnetic moments of an electron and a deuterium nucleus is smaller than compared to protons. This in turn enables the use of larger τ_2. Longer time traces are thus recordable meaning that the determination of larger distances is possible. However, hyperfine interaction between the deuterium and the nitroxide label can lead to an additional unwanted modulation within the DEER time trace.

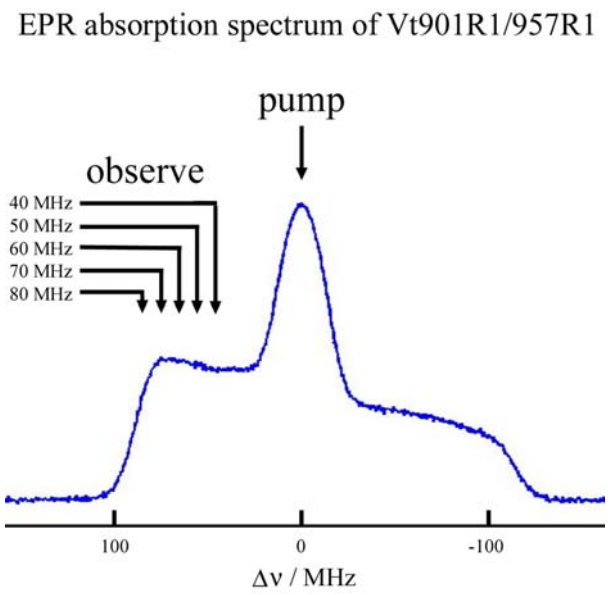

Figure 4.2: EPR absorption spectrum of Vt901R1/957R1 (blue line). For orientation selective DEER measurements spectra were recorded using five different frequency offsets $\Delta\nu = \nu_{pump} - \nu_{obs}$. The frequency offset $\Delta\nu$ was varied from +40 to +80 MHz in steps of 10 MHz.

modified Matlab script kindly provided by G. Jeschke and Y. Polyhach (ETH Zürich). The simulation program enables calculation of DPP for fixed orientations of two nitroxide spin labels, exhibiting a fixed distance between the spins. In order to describe the mutual spin label orientations within the system it is convenient to introduce a common reference frame D [59]. The dipolar axis is fixed in this reference frame aligned along the y-axis (Y_D). The orientation of the two spin labels, A and B, in this frame are given by the Euler angles $(\vartheta_A, \varphi_A, \chi_A)$ and $(\vartheta_B, \varphi_B, \chi_B)$, respectively. The B-field direction with respect to the dipolar axis is then defined by two angles (ϑ, φ)[2] (see figure 4.3). Averaging is performed by taking a random distribution of the protein orientations within the sample into account. Thus, the DPP depends on six different angles $(\vartheta_A, \varphi_A, \chi_A, \vartheta_B, \varphi_B, \chi_B)$ and the interspin distance r.
The program was modified according to a geometrical model described in the following. First, the presence of distance distributions is neglected, and all calculations were done using a defined value for r. Furthermore, an axial symmetry of g- and A-tensors, which is a good approximation at X-band frequencies ($A_{||} = A_{zz} \gg A_{\perp} = A_{yy} = A_{xx}$ and $g_{||} = g_{zz} < g_{\perp} = g_{yy} = g_{xx}$), is assumed. In this case, the orientation of A with respect to the dipolar axis Y_D can be

[2]Here ϑ and φ do not anymore describe the angle between the spin label molecule frame and the magnetic field directly as discussed before (chapter 3.4.1), but the same informations are included in these parameters.

described by only one angle ϑ_A, and the orientation of B with respect to A or D is given by the two angles ϑ_B and φ_B. A frame rotation around the spin labels z-axis (using χ) does not change the situation in case of axial symmetry. In other words, here it is sufficient to describe the spin label molecules z-axis orientation with respect to the dipolar frame D. The number of orientation variables is then reduced to three.
The B-field direction with respect to the dipolar axis is still given by ϑ and φ. After performing the powder average (see below) for a single orientation (and defined distance r) the Fourier transform of the dipolar evolution function would reveal the shape of a DPP($\vartheta_A, \vartheta_B, \varphi_B$, r) depending on only one set of angles describing the mutual spin label orientation ($\vartheta_A, \vartheta_B, \varphi_B$).

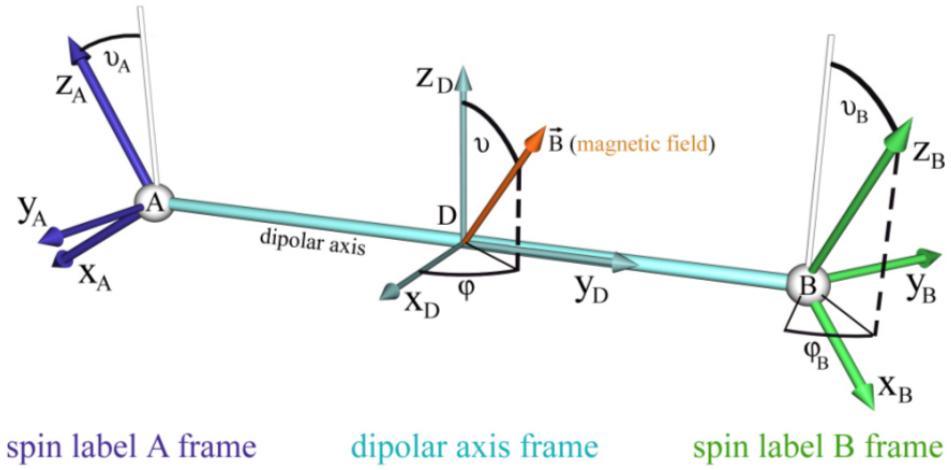

Figure 4.3: Angle definitions used in the program *DEERsim* after modification. ϑ_A is the angle between the spin label A (blue frame) z-axis and the z-axis of the reference frame D (light blue). The dipolar axis is fixed in D and aligned along Y_D. φ_B and ϑ_B describe the orientation of the spin label B (green frame) z-axis with respect to the dipolar axis, or Z_D respectively. The magnetic field orientation (red) is given by φ and ϑ.

The dipolar angle Θ_{dd} is defined as the angle between the magnetic field orientation and the dipolar axis (y_D) and can be calculated by:

$$\Theta_{dd} = arcos\,(\mathbf{y_D} \cdot \mathbf{B}) \tag{4.1}$$

where $\mathbf{y_D}$ is the unit vector along the y-axis of frame D (the dipolar axis), and $\mathbf{B}$ the normalized magnetic field vector. The dependency of ω_{dd} on the B-field direction is averaged out by assuming a random distribution of protein orientations within the sample. To consider this powder average a set of homogeneously distributed magnetic field orientations is generated using the grid function provided by Easyspin (written by Stefan Stoll, www.easyspin.org) (for

a schematic representation see figure 4.4). For each magnetic field orientation the resonance frequencies (according to 3.46, 3.47 and 3.48) for both spin label molecules and the corresponding dipolar frequencies ω_{dd} ((according to 3.66) are calculated. For a given frequency offset $\Delta\nu$ the respective doublet intensity contributing to the the DPP is then determined as the sum of the weightings calculated by equation 3.75, where both spin label molecules are treated as pump and as observer spins, respectively. The superposition of all calculated values for ω_{dd} (frequency doublets) with the corresponding weightings in a histogram manner lead to the DPP(ϑ_A, ϑ_B, φ_B). Note, that to achieve a PP (for a single distance) as expected for the uncorrelated case would require the calculation of the superposition of such calculated DPPs for all orientations (ϑ_A, ϑ_B and φ_B). Moreover, in case of a present distance distribution, the spectra are composed by the superposition of the distance dependent DPPs weighted by the corresponding intensities of this distribution, what is not considered in the approach presented here.

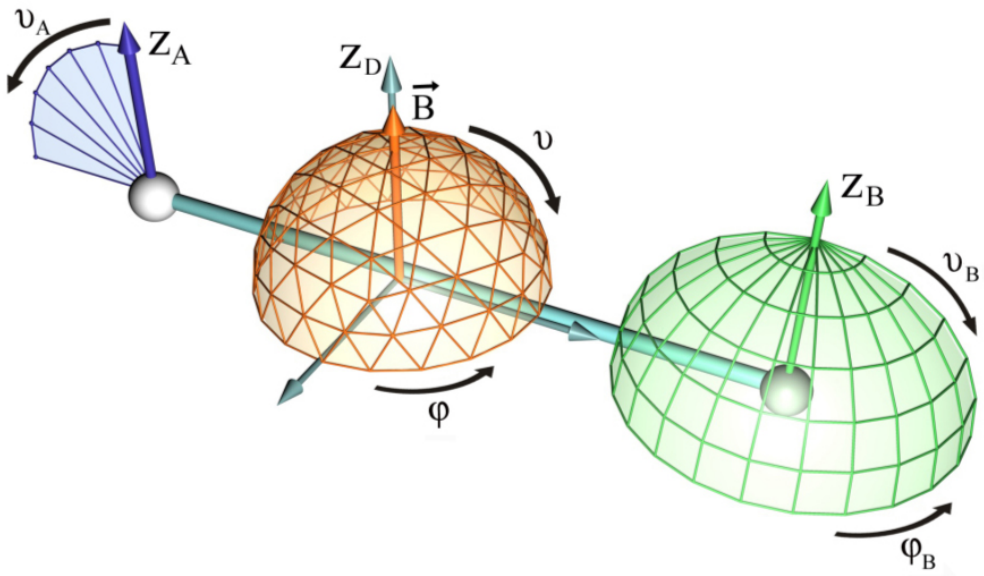

Figure 4.4: Schematic representation of the coarse orientational grid iteration used for DPP calculations. The knots on the grids indicate the calculated orientations. The angle ϑ_A was varied from -90 to 0°. For each ϑ_A value φ_B was varied from 90° to 270° and ϑ_B from 0° to 90°. In each case the variation was carried out in steps of 15°. The chosen orientation ranges are sufficient to sample all occurring combinations of z-axis orientations between A and B due to the assumed axial symmetry.

Simulation procedure To investigate the orientation correlation of the spin label pairs of Vt901R1/957R1, DPPs(ϑ_A, ϑ_B, φ_B) were calculated over orientation grids using two iterations. The first iteration was done using a coarse

orientational grid (figure 4.4). The angle ϑ_A between the spin label A z-axis and the D z-axis was varied from -90 to 0° in steps of 15°. For each ϑ_A value, φ_B was varied from -90° to 90° and ϑ_B from 0° to 90° in steps of 15°, respectively. The orientation ranges chosen are sufficient to sample all occurring combinations of z-axis orientations between A and B, assuming axial symmetry of the tensors g and A. This is because the investigated system exhibits a mirror symmetry, wherein the plane spanned by Y_D (dipolar axis) is a mirror plane, and a point symmetry due to the reversibility of the z-axis orientations. Thus, the sampling of Z_B directions located only in one octant (of frame D) is required, leading in turn to a shorter computation time. The calculations were done for different frequency offsets between pump and observer pulse frequencies according to the experiments (40-80MHz, see figure 4.2) using the experimentally obtained mean distance of 2.65 nm (see chapter 5.1.4). This leads to a number of more than 3000 DPPs.

Data analysis Further Data analysis was done using a self made Matlab script (DEERsimAnalysis.m). All obtained DPPs(ϑ_A, ϑ_B, φ_B) were convoluted with a narrow Gaussian to account for small distance and angle distributions. This approximation is adequate, if the DPP broadening due to distributions in distance and orientation are small and of similar extent in the frequency domain. Furthermore, the RMSD (root mean square deviation) for each convoluted DPP(ϑ_A, ϑ_B, φ_B) with respect to the corresponding experimental spectrum was calculated. As a measure for the agreement between simulation and experimental data the RMSD of each single orientation for the five investigated frequency offsets $\Delta\nu$ were summed up. The minimum of this overall RMSD reveals the orientation, at which the DPP shows the best agreement with the experimental data. In order to refine the results, a second iteration was done by repeating the procedure introduced above with a small range of orientations around the best fitting orientation obtained, using a finer orientational grid (5° steps for ϑ_A, ϑ_B and φ_B).

4.2 Other computational methods

4.2.1 MD simulation

The experimentally obtained distance distributions for Vt in an aqueous buffer solution were compared to the results of MD-simulations. The MD simulations were carried out by Prasad Gajula (University of Osnabrueck). The resulting distance distributions used for further comparisons were taken from [22]. However, a small introduction into the topic MD simulations is be given in the following, and the simulation parameters are described.

Molecular dynamic (MD) simulations provide insight into the spin label side chain's motion over the course of time, considering the movement of all wanted protein atoms. Generally, in molecular dynamics simulations a system is modeled out of individual atoms. For Vt for example the X-ray structure is obtainable containing the 3D informations about the positions of all protein atoms. For this model, the dynamics are calculated based on a MD force field. The force field is a model of the interactions between the individual atoms and gives rise to forces, which turn the static model into a dynamic system. The force fields contain libraries of pre-calculated terms of force constants or potential energies (E) on all atoms. The total potential energy is composed of the potentials of bonded and non-bonded atoms. Potentials due to inter atomic bonds, angles and dihedrals together form the bonded potential, whereas potentials due to the van der Waals and the electrostatic interaction together form the non-bonded potential. MD simulations are generally calculated in a classical way using Newtons equations of motion, combined with the use of force constants, generally calculated in a non-classical way, provided by the force field:

$$\mathbf{F} = -\frac{\partial}{\partial \mathbf{r}} E = m\mathbf{a} = m\frac{d\mathbf{v}(t)}{dt} = m\frac{d^2\mathbf{r}(t)}{dt^2} \tag{4.2}$$

with $\mathbf{a}$ as the acceleration of the mass m. $\mathbf{r}$ describes the 3D-coordinates of an atom as part of the system. Additionally, it is possible to couple the system to a thermal bath to control the temperature. The time evolution in MD simulations is provided by an algorithm, which calculates successively the velocities $\mathbf{v}$ and coordinates $\mathbf{r}$ of the system. The integration for all atoms in discrete time steps yields the dynamics in a stepwise manner. However, it is very time-consuming and demands high computational resources. For more detailed literature about MD simulations see for example [70].

The dynamics of a spin label attached to a specific protein site can be calculated in this way leading in general to appropriate results [23, 9]. The MD simulations used for comparisons in this work were done in the following way:

The R1 side chain was modeled and attached to each of the investigated residues in the crystal structure of Vt (PDB-code: 1ST6) and reoriented manually to avoid steric overlaps with neighboring residue side chains. All MD simulations were performed with the GROMACS simulation suite. The force field ffG43b1 from GROMOS, which is integrated into GROMACS, was used for the simulations in vacuum. Energy minimization to obtain an initial model was performed by using steepest descent and conjugate gradients algorithms for

1000 steps. Several MD simulations were performed with different spin labeled sites according to the experiments at 600K in vacuo with position restraints on the backbone atoms. The final production MD runs were carried out for $5 \cdot 10^6$ steps with a time increment of 2 fs. The current structure was saved every 0.2 ps giving a 10 ns trajectory file with 50000 frames. Distances between nitroxide N-O group centers were extracted from each frame of the trajectory files and used for inter spin distance calculations, leading to distance distribution histograms.

4.2.2 The rotamer library analysis

To predict possible orientations of R1 side chains and distances between these side chains attached to different helix positions a semi-dynamic structure model of the spin label can be used. In this model the dynamics of the R1 side chain is represented by a discrete set of possible rotational isomers (rotamers).
The program used in this work, performing the rotamer analysis, was kindly provided by Y. Polyhach and G. Jeschke (ETH Zürich) and is well described in [60]. In this case conformational structures of the MTSSL (R1) were provided by a so called rotamer library, containing 98 R1 rotamer structures. The structures of the library had been generated by systematic variation of dihedral angles of R1 attached to a single cysteine residue and geometry optimization using the DFT package ADF2002.
The thus determined structures of R1 can be attached to a specific position in a protein structure, such as X-ray structure files, obtainable from the protein data bank (PDB). The set of possible rotamers on the selected position is determined by calculating the probability of each particular rotamer of the library to occur in the protein structure. These probabilities are influenced by spatial restrictions of the R1 chain due to its local environment defined by other protein atoms. Therefore, the free energy for each rotamer is computed as the scoring function considering the interactions between atoms of the label and atoms of the protein using a Lennard-Jones potential parameterized by an OPLS (optimized potentials for liquid simulations) force field. The Lennard Jones potential takes the repulsion (clashes) and van-der-Waals attraction of spin label and protein atoms into account. The energy E_k for the k-th rotamer of the library attached to the protein is therefore calculated by:

$$E_k = \sum^{i} \sum^{j} 4\epsilon_{ij} \left(\left(\frac{\sigma_{ij}}{r_{ij}} \right)^{12} - \left(\frac{\sigma_{ij}}{r_{ij}} \right)^{6} \right) f_{ij} \tag{4.3}$$

Here, r_{ij} is the distance between the i-th atom of the spin label side chain and the j-th protein atom. $\epsilon_{ij} = (\epsilon_i \epsilon_j)^{1/2}$ is the interaction coefficient from

the individual atom coefficients (extractable from the used force field), and $\sigma_{ij} = (\sigma_i \sigma_j)^{1/2}$ describes the effective radius from the van der Waals radii of the respective atoms. f_{ij} is an energy scaling factor, which originally was set to 1 in the OPLS force field. Reducing the scaling factor in this case would reduce the energy penalty, which defines atomic clashes. In this way a certain amount of protein structure flexibility is mimicked. The grade of flexibility is in general unknown. Hence here, the scaling factor, also called forgive factor, is an adjustable parameter.
Furthermore, the population (probability) P_k for the k-th rotamer in the library attached to a certain protein position is then calculated by weighting the determined energy E_k according to a Boltzmann distribution normalized by division by the partition function Z:

$$P_k = \frac{exp\left(-\frac{E_k}{k_B T}\right)}{Z} = \frac{exp\left(-\frac{E_k}{k_B T}\right)}{\sum^k exp\left(-\frac{E_k}{k_B T}\right)} \tag{4.4}$$

Rotamers are considered, if their calculated population exceeds a certain threshold value (e.g. $P_t = 0.001$). From the rotamer sets of two different residual positions all possible distance combinations were calculated and their intensities were weighted by the product of the populations of the considered rotamers. Small spatial fluctuations around the conformational state of each rotamer are taken into account by convoluting the calculated distances with a non significant Gaussian (0.05nm width).
The rotamer analysis was done using the Vt crystal structure (PDB-code: 1ST6) for all positions according to the experiments.

4.2.3 Determination of the molecular alignment within the Vt-dimer

To obtain information about the mutual orientation between two Vt molecules, forming a dimer in aqueous solution, a self made Matlab script (*OrientSol.m*) was used. As input, the measured distances together with the corresponding width of the distance distribution, and a protein structure file are required. Here, the Vt crystal structure (PDB:1ST6) was used. To this structure the spin label side chains were attached to the six investigated positions (901, 922, 950, 957, 984, 1033), exhibiting the structural conformations of the rotamers revealing the highest population obtained from the rotamer library approach. The corresponding experimental values for distances and distance widths were extracted from the results of DEER measurements of singly labeled Vt in solution.
First, the protein structure is duplicated to obtain two equal molecules 1 and 2. A translation vector $\mathbf{t}$ has to be considered connecting the centers of mass

of both molecules, which shifts molecule 2 away from molecule 1. The orientations of $\mathbf{t}$ were generated with the above mentioned grid function provided by Easyspin. Since Easyspin generates an array of unit vectors over a half sphere, the second half of the sphere was considered by rotation of a copied set of orientations by 180° to obtain unit sphere vectors homogeneously distributed over an entire sphere (number of grid points = 362). The grid point orientations then are defined by a pair of two angles ϑ_t and φ_t. The absolute value of the vector $\mathbf{t}$ was varied from 1.6 nm (corresponding to a value smaller than the diameter of Vt) up to 3.8 nm (no possible contact between molecule 1 and 2 for all orientations) in steps of 0.2 nm. At each grid point of $\mathbf{t}$ an orientational grid search for the orientations between molecule 1 and 2 is performed. The orientation of molecule 2 with respect to molecule 1 is given by a set of three Euler angles (α, β, γ). α and γ has to be varied from 0°-360° and β from 0°-180° to sample all possible mutual orientations. Therefore, α, β and γ were varied in 5°-steps. The rotations of molecule 2 were carried out around its center of mass.

For each calculation step inter-spin distances as the distance between the N-O group centers of the investigated R1 chains of molecule 1 and 2 are calculated. The deviation between the modeled r_{mod} and the experimentally obtained distance r_{exp} was calculated considering a tolerance for r_{exp} by taking the respective distribution width Δr_{exp} into account. A modeled distance is in agreement with the experimentally obtained one, if the following condition for the judge parameter s is fulfilled:

$$s = |r_{mod} - r_{exp}| - \Delta r_{exp} \leq 0 \tag{4.5}$$

Therefore, the modeled distance is calculated by:

$$r_{mod} = |(\Omega(\alpha, \beta, \gamma)\mathbf{r_2} + \mathbf{t}) - \mathbf{r_1}| \tag{4.6}$$

where $\mathbf{r_1}$ and $\mathbf{r_2}$ are the coordinates of the N-O group center of the R1 side chain attached to the investigated position of molecule 1 and 2, respectively. Ω is the Euler rotation performed on molecule 2, determined by the three Euler angles. The condition for s has to be fulfilled for all six investigated positions. Therefore, a scoring function was introduced to judge the grade of agreement of the respective distances for all investigated positions giving the value s_{tot} as a measure for this agreement:

$$s_{tot} = \sum_{i=1}^{6} s_i^2 \tag{4.7}$$

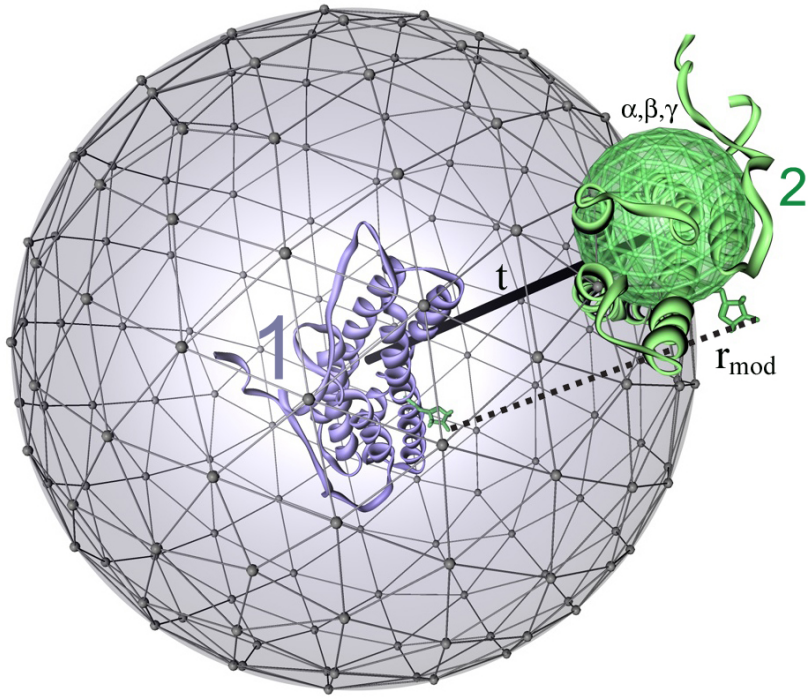

Figure 4.5: Schematical representation of the strategy used in the self made script *OrientSol*. The translation vector **t** (solid black) connects the center of mass of both molecules 1 (blue) and 2 (green). Its orientations were varied on a grid (black) lying on a sphere with the radius of its absolute, wherein the center of mass of molecule 1 defines the origin. The knots on the grids represent the calculated orientations schematically. The absolute of **t** (radius of the sphere) was varied during the calculations. Here, only one example (no possible clashes) is shown for reason of better visualization. At each grid point the orientation (α, β, γ) of molecule 2 with respect to molecule 1 was varied as described in the text. The orientational variation of molecule 2 is indicated by the green grid. After each calculation step all distances r_{mod} (dashed line) between the N-O centers of the corresponding attached R1 side chains were calculated and judged by comparison with the experimental data. Additionally, molecular clashes between the two molecules were checked as well.

where s_i is the judge value for the i-th investigated position. The smaller the value for s_{tot} is, the better is the agreement of all modeled distances. In each calculation step protein clashes were checked using the scoring function:

$$r_{m,n} \geq 2 \cdot r_{vdW,C} \tag{4.8}$$

Here, $r_{m,n}$ is the distance between atom m of molecule 1 and the n-th atom of molecule 2. $r_{vdW,C}$ is the van der Waals radius of the carbon atom (170 pm). A

more accurate way would have been the use of the corresponding van der Waals radii of each respective atom or even the calculation of the molecular energies in each step, but was not chosen here because of computational effort reasons. An adequate check for clashes is also given by equation 4.8, since C-atoms and N-atoms are besides (smaller) H-atoms the primarily part of protein backbones or even side chains. Moreover, the vdW radius of C is slightly larger than the vdW radius of N.
If a clash-free solution is found for a combination α, β, γ and $\mathbf{t}$ these values together with the corresponding value for s_{tot} are stored. A plot of the wanted values versus s_{tot} reveals the most probable orientation of the two Vt molecules (see chapter 5.1.5.2 for details).

4.3 Fluorescence laser scanning microscopy

Sample preparation For fluorescence laser scanning microscopy, PS-SUV solutions were prepared as described above. For F-actin preparations the *Actin-Toolkit Fluorescence Microscopy* purchased from Hypermol (Ulrike Hinssen, Bielfeld) was used. Rhodamine-actin (Rh-actin) labeled at Cys374 with tetramethylrhodamine was mixed with Actin in a ratio of 1:1. Vt957R1A(Rh) was prepared in accordance to the F-actin bundling assay described in 4.1.1.3.
Experiments were done with solutions containing actin bound Vt in the absence (Vt957R1A(Rh)) and in the presence of lipids (Vt957R1A(Rh)+PS). In case of Vt957R1A(Rh)+PS, Vt957R1A(Rh) was mixed with PS-SUV solutions leading to a final Vt:PS ratio of 1:200, and was incubated for at least 20 min at room temperature. Additional control measurements were done with pure F-actin (Rh) solutions. In all cases 3.5 μl of sample solution were applied on a glass slide and fixed by a cover glass. Measurements were performed using a confocal laser scanning microscope (CLSM) type TCS SL (Leica Microsystems Heidelberg GmbH) equipped with an 40x immersion oil objective (NA=1.25, resolution: 160x160x200 nm) and an Ar-laser. The excitation wave length was set to 514 nm. Fluorescence light was detected at ca. 610 nm using a beam splitter DD 458/514. Pinhole size was set to 82 μm.

5 Results and Discussion

R1 labeled Vt was investigated in terms of side chain dynamics, accessibilities, polarities and inter spin distances in the presence and absence of acidic PS-lipid vesicles and F-actin. The results, leading in each case to the construction of new molecular models for Vt, are presented in the first part of this section.
The second part deals with the results obtained from orientation selective DEER measurements on the double mutant Vt901R1/957R1. A tool is presented to determine the mutual spin label orientation of R1 labeled proteins.

5.1 Vinculin Tail structure in aqueous buffer solution

For the structural elucidation of Vt in aqueous solution the above mentioned EPR methods were applied on singly and doubly labeled Vt. For comparison with the mobility and distance measurements, a rotamer analysis was carried out on the Vt crystal structure. Moreover, the results discussed in the following are used as reference for further investigations on Vt in the presence of binding partners.
Furthermore, DEER measurements on singly labeled Vt reveal a small fraction of dimeric Vt present in aqueous solutions in absence of binding partner. These results were used in order to determine the structural arrangement of two Vt molecules forming the dimer.

5.1.1 Mobility measurements

Room temperature spectra of the singly labeled Vt variants in 40 % sucrose are shown in figure 5.1 (right). The analysis was done in terms of the classification of R1 side chain localizations with regard to the protein structure. Therefore, the semi empirical mobility parameters $1/\langle H^2 \rangle$ (inverse spectral second moment) were calculated and plotted versus the inverse central line widths $(1/\Delta H_0)$ (as described in chapter 3.3.2.2)(figure 5.1).
Remarkably, Vt901R1 reveals two spectral components. Under the assumption that the protein exhibits just one single conformation in the sample, this result would indicate the presence of two motional states for the spin label attached at position 901 [57]. On the other hand, the different observed mobility states of Vt901R1 could arise from two different Vt conformations existing in the

sample. Here, it can not be distinguished between those two cases. However, the spin label (or protein) conformation, contributing to the immobile spectral component, is dominating.
However, the value of the inverse line width is dominated by the mobile component, which individually reflects a loop or surface exposed site. In contrast, the value of the inverse second moment is governed by the (dominating) immobile spectral component and refers to a tertiary contact or protein surface related position, which might describe the situation here more likely. However, in this case, the presence of two spectral components complicates an exact interpretation in terms of protein atoms and R1 interaction, and the results for Vt901R1 should be treated with caution.

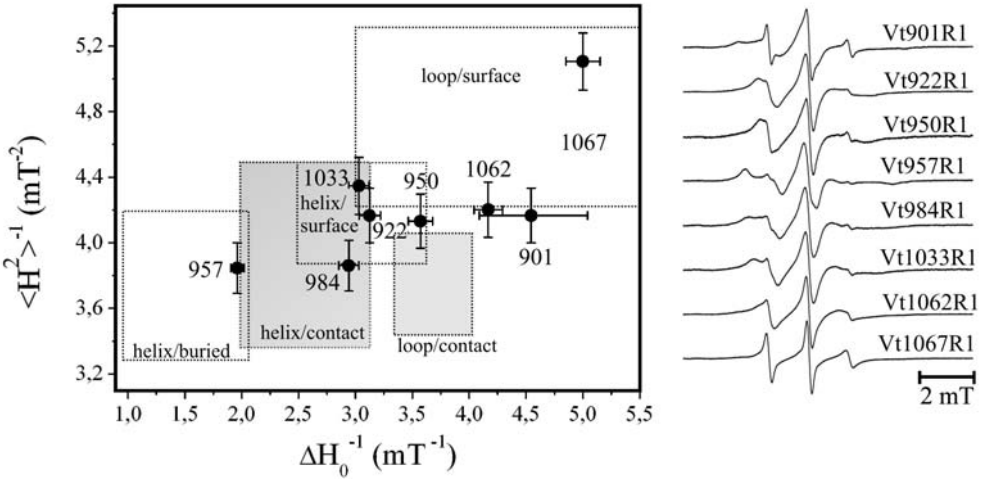

Figure 5.1: Mobility analysis of R1 side chains attached to Vt in aqueous solution containing 40 % sucrose. Left: Plot of the semi empirical mobility parameters $1/\langle H^2 \rangle$ (inverse spectral second moment) versus the inverse central line width ($1/\Delta H_0$). The topological regions were drawn according to [47] and [13] (see figure 3.7). Right: Cw-EPR room temperature spectra of the singly labeled Vt variants.

The results of the other investigated positions are more definite. The results indicate that the R1 side chains attached to Vt922R1, Vt950R1, Vt957R1 , Vt984R1, Vt1033R1 and most likely also Vt901R1 are attached to helical secondary structure elements and might exhibit tertiary contacts to other helices. In terms of the topology regions, marked in figure 5.1, Vt922R1, Vt984R1 and Vt1033R1 are located at the border between areas, representing surface exposed and helix contact sites. In contrast, Vt957R1 shows clear features of a side chain yielding strong tertiary contact, and might even be buried in the protein interior. This is difficult to distinguish here. Accessibility measurements will give rise to an answer concerning this question (see next chapter). These

results are consistent with the Vt crystal structure, where the $C_\alpha - C_\beta$ bonds of the above mentioned positions are oriented towards neighboring helices. This applies also for Vt950R1, however the EPR results indicate that position 950 is surface exposed, or, under consideration of the experimental error be classified as being attached to a loop region exhibiting tertiary contact. The latter is in line with the fact that position 950 is located two helical turns below 957 close to the N-terminal end of helix three (H3) (cf. figure 5.4). It could be shown by the analysis of the root mean square fluctuations of C_α-atom locations during MD simulations as a function of the Vt residue number [22] that Vt exhibits a larger flexibility at helical ends than compared to regions close to the middle of the helix, where residue 957 is situated. Thus, in case of Vt950R1 the higher flexibility of the H3 N-terminal end might lead to a higher observed mobility of the attached spin label and in turn to an EPR spectrum, reflecting a higher R1 mobility as compared to Vt957R1.
The results for Vt1062R1 and Vt1067R1 indicate that spin labels bound to these respective positions can be classified as sites, which are located at surface exposed loop regions. These findings agree with the crystal structure as well, in which position 1062 is situated at the accessible C-terminal random coil domain of Vt and 1067 on the very end of the C-terminus, which is therefore supposed to exhibit a higher mobility compared to position 1062.

5.1.2 Polarity and accessibility measurements

In order to specify the relative alignment of the R1 side chains with respect to the Vt structure in solution, polarity and accessibility measurements were carried out on spin labeled Vt variants. Accessibility measurements were performed to distinguish between residues exposed to the bulk water (buffer) or buried in the protein interior. Polarity determination of the R1 side chains environment provides a further mean to affirm the findings obtained from the accessibility investigations.

5.1.2.1 Accessibility measurements

Measurements were performed as described in 4.1.2.2 and data analysis was done using the program *powerfit* (explained in 4.1.2.2). From the thus obtained W_{ex} values (NiEDDA and 0_2) the immersion depth parameter Φ was derived (see chapter 3.3.4).

Φ values obtained for all investigated positions are in the range $-2.5 < \Phi < -1$ (see figure 5.2). The reference data obtained from spin labeled BR mutants (figure 3.13) reveals that values below $\Phi = -1$ refers to completely water ex-

posed sites, indicating that all investigated positions in Vt are exposed to the bulk water. This is in accordance with the mobility analysis (5.1.1). The possibility that Vt957R1 might be a protein buried site, as proposed by mobility measurements, can thus be excluded. This implies that the R1 side chain of Vt957R1 points into the direction of the bulk water, but nevertheless shows the strongest immobilization due to neighboring side chains compared to other positions.

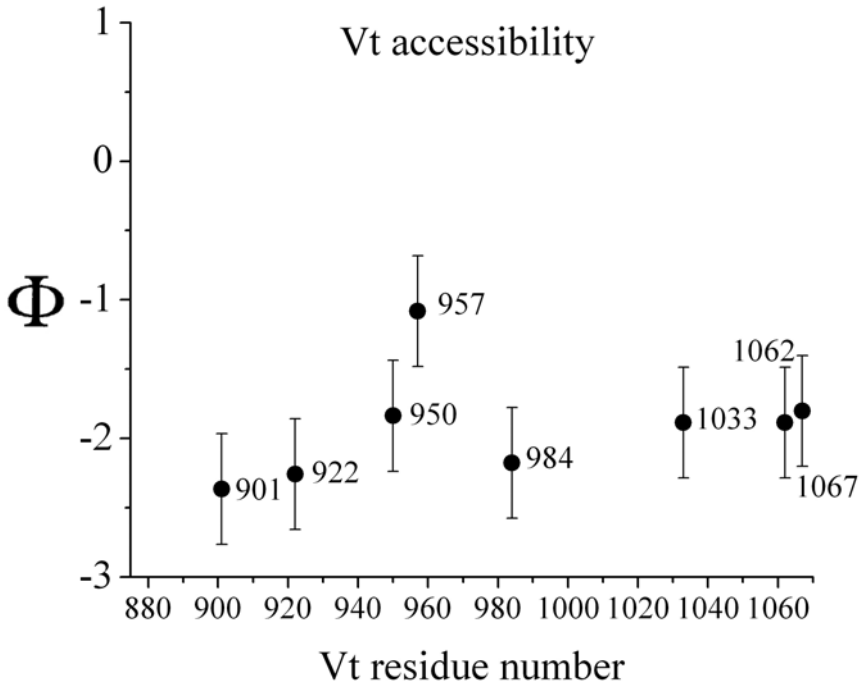

Figure 5.2: Accessibility measurements: Plot of the immersion depth parameter Φ versus the Vt residue number.

The strong interaction between the R1 side chain attached to residue 957 and neighboring helices and/or other protein atoms is likewise accompanied by a partial shielding of the R1 side chain from the molecules contained in the solvent. This fact is also reflected in the results obtained from accessibility determination. Vt957R1 reveals the largest Φ value ($\Phi = -1.1$) compared to other positions, indicating that the accessibility of the collision reagents (NiEDDA and O_2) to Vt957R1 is slightly decreased, most likely due to surrounding protein atoms. Nevertheless, the spin label attached to Vt957R1 is still water exposed. In case of Vt901R1, Vt922R1, Vt950R1, Vt984R1, Vt1033R1, Vt1062R1 and Vt1067R1 the obtained Φ values are similar and around $\Phi = -2 \pm 0.4$. This refers in each case to water exposed R1 side chains, which are more accessible,

and thus, exhibiting less contacts to neighboring protein atoms than in case of Vt957R1.

5.1.2.2 Polarity determination

The hyperfine coupling tensor element A_{zz} is obtained from low temperature (160 K) *cw*-EPR spectra and is a measure for the polarity of the R1 side chain's environment. Thereby, high A_{zz} values reflect the presence of a polar solvent, whereas the presence of an apolar environment leads to the observation of significantly smaller A_{zz} values (see chapter 3.3.3.1 for details). Experimental conditions are described in 4.1.2.3. The spectra analysis (A_{zz} determination) was performed with the program *Dipfit* as described in 3.3.3.3.

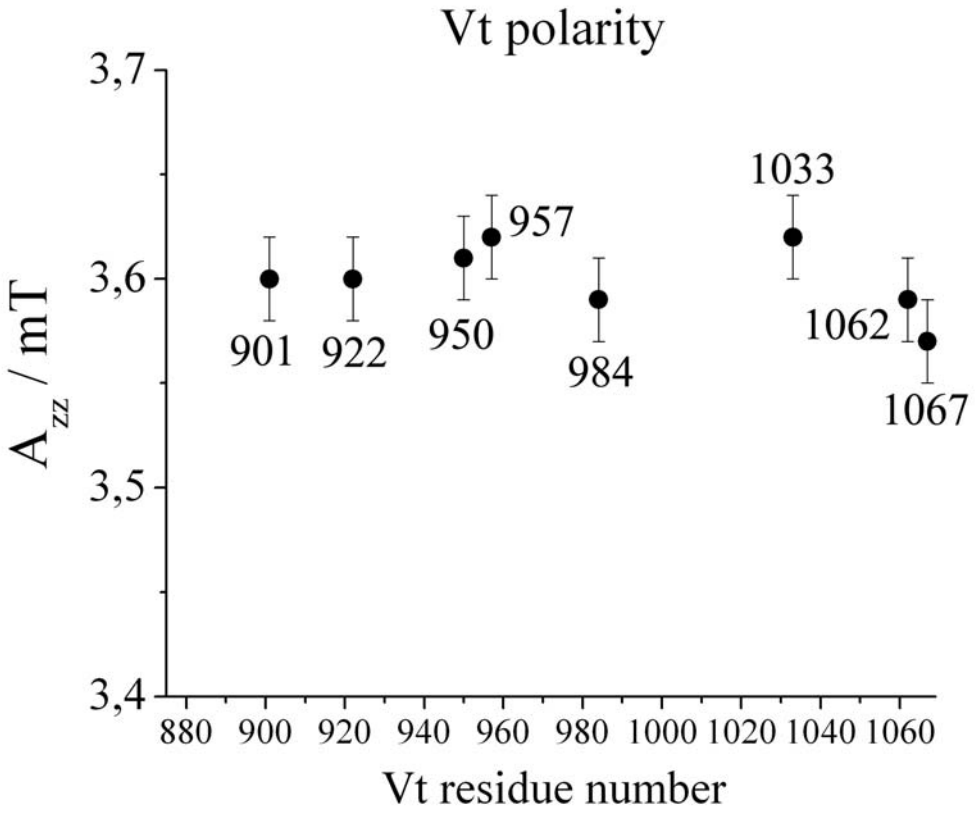

Figure 5.3: Polarity measurements: Plot of the hyperfine tensor element A_{zz} as a measure for the R1 environments polarity versus the Vt residue number.

In figure 5.3 A_{zz} is plotted as a function of the Vt residue number. All positions reveal A_{zz} values within a range of 3,6 mT $\pm$ 0.03 mT (for detailed numbers see table 5.6), referring in each case to a highly polar R1 environment. This is an additional evidence that the nitroxides are accessible to water [58, 68, 13]. Inter-

estingly, Vt957R1 exhibits the highest polarity value. As the R1 chain attached to this position exhibits the lowest solvent accessibility (highest Φ), a smaller polarity value compared to the other R1 side chains, exhibiting higher solvent accessibilities, is expected. Consequently, the high A_{zz} value for Vt957R1 could result from the polarity provided by surrounding protein side chains. According to the Vt crystal structure several hydrophilic residues (polar and capable of hydrogen bonding) are in the closer vicinity of residue 957. These are amino acids ASP(953, H3), LYS(956, H3), ASP(959, H3), GLU(960, H3) and ARG(925, H2). These protein side chains might have the observed increasing effect on A_{zz} in case of Vt957R1. Moreover, considering all investigated positions the deviations from 3,6 mT are ± 0.03 mT at maximum, which is inconsiderable small and comparable to the experimental error of 0.02 mT. In summary, the results are in line with the results obtained by accessibility measurements.

5.1.3 Rotamer analysis

A rotamer analysis was carried out to obtain additional information about the possible structural alignment, as well as about the motional freedom of R1 side chains, attached to Vt. The rotamer analysis was performed on the Vt crystal structure (pdb: 1ST6) using a *Matlab* script, kindly provided by Yevhen Polyhach (ETH, Zürich). The rotamer library contains 98 rotamer structures, which were analyzed in terms of their probability to occur in the protein structure at the particular position (see chapter 4.2.2 for details). The analysis was done for each position separately, except for position 1067, which is not provided by the Vt crystal structure (last residue: 1066). A manual attachment of this residue to the Vt structure would be inaccurate, because a qualitative investigation would require the consideration of the complete FLAG and HIS-tag structure, which is attached to this residue in the experimental case.
The RLA results are presented in figure 5.4. The R1 rotamers populated above the given threshold for each investigated position attached to the Vt crystal structure are shown. The numbers of possible rotamers for each case are listed in the table shown in figure 5.4 (bottom, right).

For position 922 (H2) and 1033 (H5) only one possible rotamer is obtained, indicating that the spatial freedom of R1 side chains attached to these positions are highly restricted due to surrounding protein atoms (figure 5.4 a)-c)). The same applies to positions 950 (H3) and 957 (H3), which reveal two populated rotamers, exhibiting very similar structures in terms of the ring position and their R1 z-axis orientation (figure 5.4 c)).
Position 901 (H1) reveals three possible rotamers, still indicating a spatial and

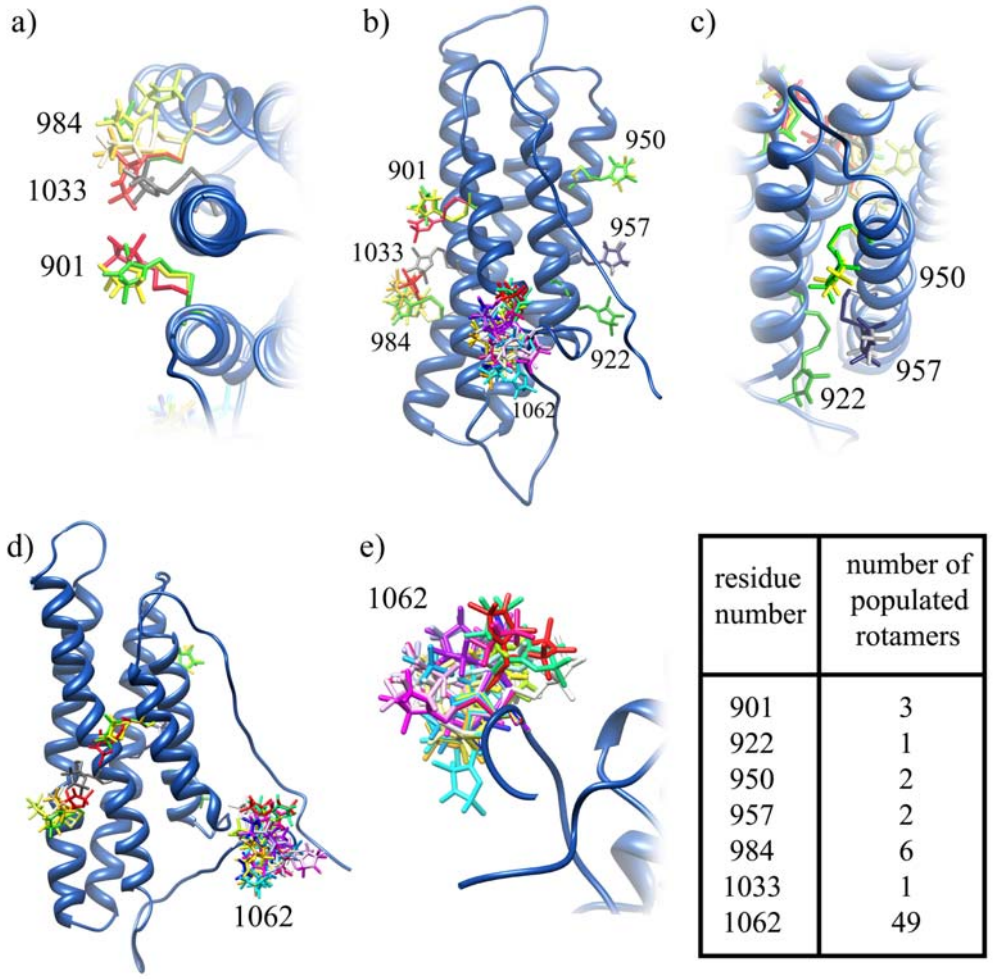

residue number	number of populated rotamers
901	3
922	1
950	2
957	2
984	6
1033	1
1062	49

Figure 5.4: RLA results, a)-e): Populated R1 rotamers for each investigated position are shown attached to the Vt crystal structure (pdb: 1ST6). The numbers of possible rotamers for each case are listed up in the table (right bottom). Except for position 1062 (e), the number of possible rotamers is considerable small indicating highly restricted spatial freedom of R1, whereas the high number of rotamers for residue 1062 reflects a high mobility of R1 at this position.

motional restriction of a R1 side chain at this position (figure 5.4 s)). However, two of the three rotamers have similar structures and populations [1], whereas the third rotamer has a slightly different conformation and exhibits the smallest population value (ca. 4%). In case of position 984 (H4), six possible rotamers are obtained, suggesting that R1 attached to this position is more flexible as compared to the aforementioned cases. For position 1062, which is located on the C-terminal end (random coil domain) of Vt, the highest number (49)

[1]Population for the three rotamers obtained for position 901: rotamer 1 $\approx$ 52 %, rotamer 2 $\approx$ 44 %, rotamer 3 $\approx$ 4 %.

of populated rotamers was obtained (figure 5.4 d), e)), indicating a very high degree of motional freedom for the attached R1. Taken together, in all cases, exept for position 1062, the number of populaterd rotamers is small, referring in each case to spatial and motional restrictions caused by strong secondary and tertiary interactions. Due to this fact, the EPR spectra should reveal in each case very immobile features. However, this is only the case for Vt957R1. It has to be mentioned that the movement of protein side chains and backbone atoms are completely neglected in the RLA. This is most likely the reason for the observation of higher R1 flexibilities in the experiments, as expected from the RLA results. Furthermore, regarding the assigned topology regions, the RLA results for positions 922, 957, 984, 1033 are in line with the mobility measurement results, since all these positions could be characterized as helix attached sites exhibiting tertiary contacts. Likewise, the large conformational space of the R1 side chain attached to position 1062, as predicted by RLA, is reflected in the EPR results as well.
In contrast, position 950 could be assigned as a helix/surface related site, which is not in agreement with the RLA result, since here a strong tertiary contact is revealed. As already mentioned in chapter 5.1.1, the location of position 950, namely at the more flexible end of helix H3, might explain this deviation. Furthermore, the obtained two different rotameric states for 901 might explain the two spectral components observed in the EPR spectrum, whereby the additional mobile component could emerge from the reorientation of surrounding side chains, providing more space for one of both conformational states (defined by the less and the two highly populated rotamers).
Another important fact can be extracted from the RLA results. The rotamer structures obtained for each position are aligned in a way that the nitroxides are located on the water exposed protein surface and pointing away from the protein interior (figure 5.4 b)), which is in accordance with the results obtained from accessibility and polarity measurements.
In summary, the RLA results are in line with the experimentally obtained EPR results, indicating that the structure of Vt in an aqueous solution agrees largely with the Vt crystal structure.

5.1.4 Distance determination on Vt double mutants

5.1.4.1 EPR distance measurements

Inter spin distances were determined, testing four different Vt double cysteine mutants: Vt901R1/957R1 with spin labels at distant helices (H1 and H3) and three Vt variants, Vt922R1/957R1 (H2/H3), Vt901R1/1033R1 (H1/H5) and Vt984R1/1033R1 (H4/H5) to analyze distances between neighboring helices. Low temperature *cw*-EPR and DEER spectra were recorded as described in

4.1.2.3 and 4.1.3.1. The crystal structure, where investigated spin label positions are indicated, and the corresponding *cw*-EPR low temperature spectra (T = 160K) are shown in 5.5.

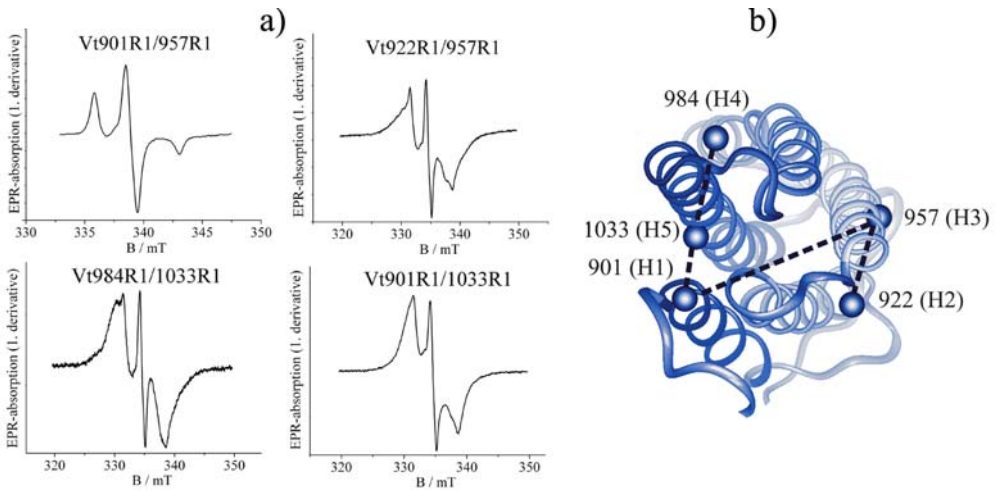

Figure 5.5: a): Low temperature *cw*-EPR spectra of the four investigated doubly labeled Vt variants. b): Schematic representation of the labeled positions (balls) in the Vt crystal structure. Residue numbers and numbers of corresponding helices are indicated. The measured distances are highlighted by dashed lines.

The spectra of Vt922R1/957R1 (H2/H3), Vt901R1/1033R1 (H1/H5) and Vt984R1/1033R1 (H4/H5) display a significant broadening [2], indicating close proximity between the respective spin labeled side chains. In contrast, no dipolar broadening is observed for Vt901R1/957R1 (H1/H3), revealing an inter spin distance larger than 2 nm, which is not detectable using *cw*-EPR. The spectra analysis of the *cw*-EPR spectra in terms of distance distributions was done using the two different programs *Dipfit* and *Short Distances* (see 3.3.3.3). The fitting using *Dipfit* leads in case of Vt922R1/957R1 (H2/H3), Vt901R1/1033R1 (H1/H5) and Vt984R1/1033R1 (H4/H5) to unsatisfactory results. The experimentally obtained spectral shape could not be reflected by the spectra simulated by *Dipfit*. A possible reason might be that in the algorithm implemented in *Dipfit* a single Gaussian shaped distance distribution is assumed. Furthermore, Heisenberg spin exchange becomes relevant for interspin distances below 0.8 nm [63]. This fact might also affect the spectral shape, but is not considered in *Dipfit*. Thus, in the cases of Vt922R1/957R1, Vt901R1/1033R1 and Vt984R1/1033R1 the results obtained by *Dipfit* were discarded and are not shown. In contrast, the results obtained with the program *Short Distances* using Tikhonov regularization are more reasonable. The fitting results and the obtained distance distributions for Vt922R1/957R1, Vt901R1/1033R1 and

[2] The narrow central lines arise from ca. 20 % of singly labeled species in each case.

Vt984R1/1033R1 are shown in figure 5.6. Mean distances and widths of the resulting distributions are summarized in table 5.1.

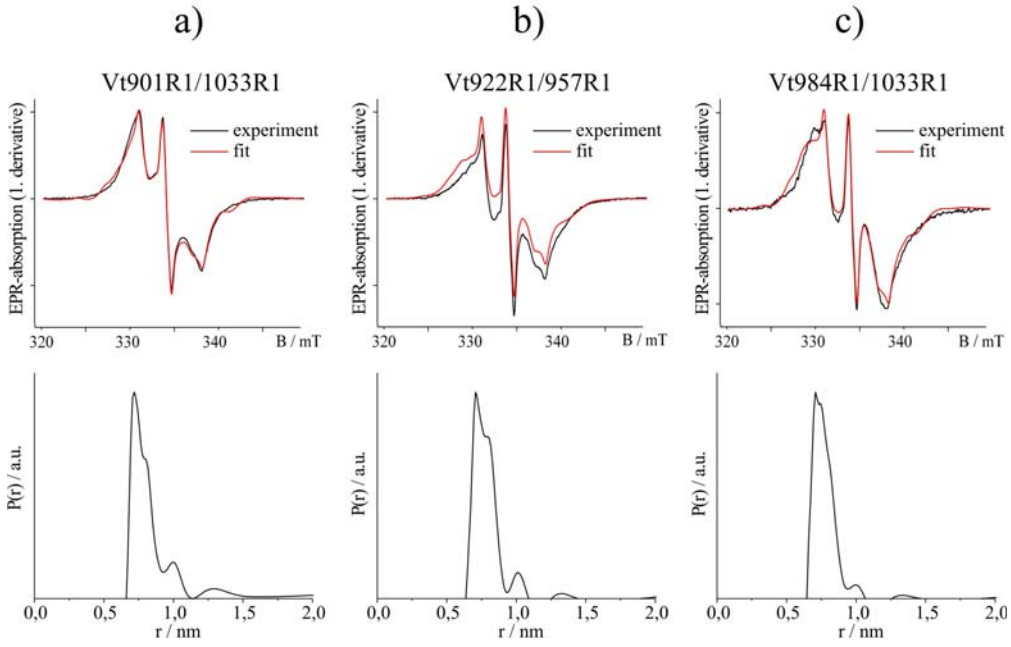

Figure 5.6: Experimentally obtained low temperature *cw*-EPR spectra (black) of Vt922R1/957R1 (H2/H3), Vt901R1/1033R1 (H1/H5) and Vt984R1/1033R1 (H4/H5) are overlaid with the fits calculated with the program *Short Distances* (red), obtained by the fitting procedure using Tikhonov regularization. The corresponding distance distributions are shown below.

In case of Vt901R1/1033R1 the Tikhonov-fit reflects the experimentally obtained spectrum well. The mean distance extracted from the corresponding distance distribution is 7.2 nm ± 0.08 nm (HWHM). Additionally, a small contribution around 1 nm is present in the distribution. The simulated spectrum of Vt984R1/1033R1 reveals small deviations in the region of the low field maximum. The mean distance, extracted from the calculated distance distribution (0.74 nm ± 0.07 nm) is similar to the result obtained for Vt922R1/957R1 (0.76 nm ± 0.08 nm).
The intensity of the first minimum of the experimental spectra (low field minimum) differs in all cases from each other, whereas the obtained mean distances are comparable. In case of Vt901R1/1033R1 and Vt984R1/1033R1 these particular different intensities are even reflected by the simulations. Interestingly, this affects the obtained mean distances insignificantly and results only in minor deviations of the distribution shapes. However, in case of Vt922R1/967R1 the highest deviations between simulation and experiment is achieved. Spectral regions, where the low field minimum intensity reaches values below zero, can not be reflected by the simulations, leading to further deviations at the wings.

The shapes of the individual parts of the low field maximum, the central line region and the high field minimum, separately, are however well reflected by the simulations.
A possible explanation for the deviations between simulations and experimental data might be the fact that in the here discussed distance range the point-dipole approximation (a reasonable approximation in the distance range 1 - 2 nm, allowing the Pake pattern calculation as described in 3.2.6), might not be valid anymore. Furthermore, since the fitting procedure (convolution with Pake patterns) is based on an isotropic distribution of R1 orientations, deviations between simulation and experimental data may arise from present correlations of the relative orientations of the nitroxides. Mobility measurements and RLA, indicating motionally restricted and thus orientationally correlated spin label pairs, support this assumption.
Additionally, in the here discussed distance range Heisenberg spin exchange becomes relevant, and the disregard of this interaction in the here applied analysis may account for further deviations. Moreover, Heisenberg exchange coupling depends, besides the interspin distance, on the mutual R1 orientation as well. This is obvious, since the respective strength of the coupling depends on the extent of the electron orbital overlap. Considering the case of a fixed distance in which the R1 z-axis of both spin label are parallel to each other, the orbital overlap would be of more extent as compared to the case, where their x-axes are parallel to each other (here it should be referred to figure 3.2). This means, the mutual spin label orientation in case of Vt901R1/1033R1, Vt922R1/957R1 and Vt984R1/1033R1, respectively, might differ, whereas the nitroxide distances are similar. The influence of the R1 orientation on the spectral shape in case of a present Heisenberg exchange interaction is (to the authors knowledge) still unknown, thus no exact predictions in terms of spin label orientations can be made at this point.
However, the fact that the deviations are small in each case, and the overall broadening of the EPR spectra is well reflected in the simulations, leads to the assumption that the obtained mean distances are reasonable and a more precise analysis by a consideration of Heisenberg spin exchange is assumed to change the results insignificantly.
The short distances determined for Vt922R1/957R1, Vt901R1/1033R1 and Vt984R1/1033R1 indicate that the spin labeled positions are located in close vicinity. In comparison to the $C_\alpha - C_\alpha$ distances extracted from the Vt crystal structure, the results imply that the inter helical distances between H1-H5, H2-H3 and H4-H4 of Vt in aqueous solution agree with the helical alignment revealed by x-ray crystallography (see table 5.1). The deviations between inter spin and $C_\alpha - C_\alpha$ distances are smaller than expected, considering an

C_α-nitroxide distance of approximately 0.65 nm [3] and the structural diversity of R1 chains. Since in the case of Vt922R1/957R1, Vt901R1/1033R1 and Vt984R1/1033R1 the R1 side chains are attached to neighboring helices, this leads to the conclusion that the vector connecting C_α and the nitroxide center of the two attached R1 side chains, in each particular investigated case, have similar orientations (aligned in parallel) with respect to the respective helix long axis. This result is supported by the RLA results (see figure 5.4). The nitroxide distance distributions resulting from the RLA will be discussed in the next paragraph.

Mean distances obtained from *ShortDistances* [nm]			
sample	$Vt901R1/1033R1$	$Vt922R1/957R1$	$Vt984R1/1033R1$
EPR	0.72 ± 0.08	0.76 ± 0.08	0.74 ± 0.07
$C_\alpha - C_\alpha$	1.08	0.58	0.69

Table 5.1: Mean distances extracted from the distance distributions for Vt901R1/1033R1, Vt957R1/957R1 and Vt984R1/1033R1 obtained from *Short Distances* using Tikhonov regularization. For comparison the $C_\alpha - C_\alpha$ distances extracted from the Vt crystal structure are given.

As mentioned above, in case of Vt901R1/957R1 no dipolar broadening was observed in *cw*-EPR measurements, indicating a distance larger than 2 nm. The dipolar evolution function obtained by DEER spectroscopy overlaid with the fits obtained by DEERAnalysis is shown in figure 5.7 (left). Within the time domain of 2200 ns six well resolved modulation maxima are detected. Fourier transformation into the frequency domain generates the Pake pattern, shown in figure 5.7 (middle). The distance distribution calculated by Tikhonov regularization (figure 5.7 (right)) shows a major distance of 2.65 nm ± 0.10 nm. Additional low-populated contributions at different distances are visible in the distribution, which correspond to frequency features in the Pake patterns, which most probably arise from inter molecular distances due to Vt dimerization (see chapter 5.1.5). However, the main peak at 2.65 nm is dominating and the additional contributions are small. The HWHM of the main distance peak of 0.1 nm reflects a strong restriction of the reorientation of both of the spin label side chains. The inter spin distance is larger than the $C_\alpha - C_\alpha$ distance (1.7 nm in this case). Considering the R1 chain length of around 0.65 nm the experimentally obtained distance of 2.65 nm is in the range between 1.7 nm

[3] An analysis of all 98 rotamer structures of the library used in this work reveals a range of 0.5 nm - 0.8 nm for the nitroxide-C_α distance.

and the maximal reachable distance of $1.7 + 2 \cdot 0.65$ nm = 3.0 nm, being in line with the crystal structure.

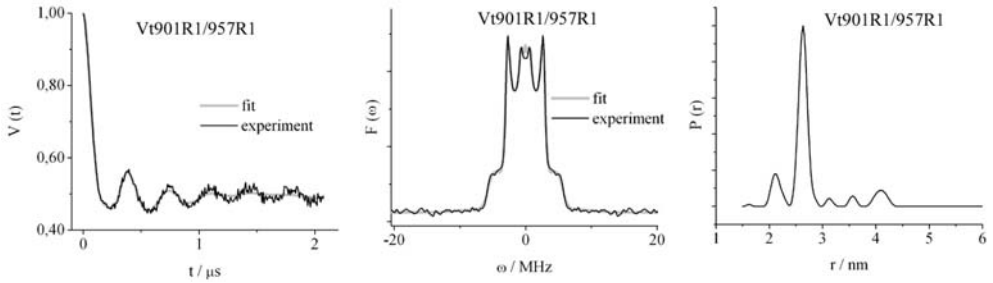

Figure 5.7: Results of DEER distance measurements on Vt901R1/957R1 (H1/H3). Left: Dipolar evolution function (black line) overlaid with the fit obtained by DEER-Analysis (gray line). Center: The Pake pattern obtained by Fourier transformation of the dipolar evolution function and the corresponding fit (gray line). Right: Distance distribution calculated by DEERAnalysis using Tikhonov regularization, revealing a mean distance of 2.65 nm with a HWHM of 0.10 nm.

5.1.4.2 RLA and MD distance distributions

Theoretical distance distributions based on the Vt crystal structure for the investigated double mutants were calculated by RLA and MD simulations as described in 4.2.2 and 4.2.1. The resulting distance distributions will be compared to the outcome of EPR experiments and discussed in the following.

The RLA yields only one significantly populated spin label rotamer for positions 1033 and 922, whereas up to six different rotamer conformations can be found for the other mutated positions (see chapter 5.1.3). The distance distributions were calculated considering all possible rotamer combinations, weighted according to the product of the respective populations.
In case of very small distances, the investigation of each individual position separately can lead to rotamer combinations, in which two spin label side chains exhibit steric clashes. Therefore, these rotamer combinations are excluded by the following procedure. The computations for double mutants Vt901R1/1033R1, Vt922R1/957R1 and Vt984R1/1033R1, where the close vicinity of the respective labeled positions can lead to clashes or overlaps between R1 side chains, were also done using the Vt crystal structure, to which the previously found (unique) R1 rotamer structures of positions 1033 and 922 were attached. In this way, atoms of these rotamers are considered in the population calculation and combinations of clashing rotamers are not anymore considered in the calculated distance distributions.

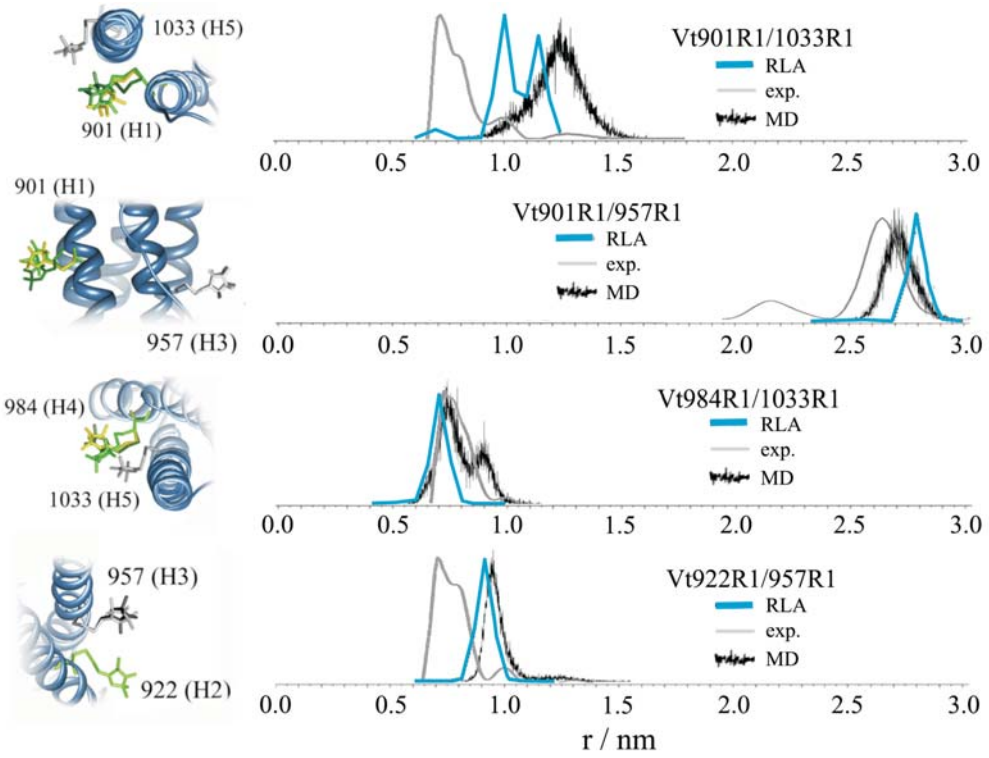

Figure 5.8: Distance distributions for Vt901/957R1 (H1/H3), Vt984/1033R1 (H4/H5), Vt922/957R1 (H2/H3), Vt901/1033R1 (H1/H5) obtained by EPR-spectroscopy (gray lines), Rotamer Library Approach (dotted lines) and MD-simulations (noisy traces) are shown. Populated rotamers of the respective positions used for distance distribution calculations are shown attached to the Vt crystal structure. By attaching the previously obtained unique rotamers of position 922 and 1033 at the crystal structure for the analysis, the number of populated rotamers in case of Vt984/1033R1 is reduced from six to three. This indicates that three of the previously obtained rotamers at position 984 reveal clashes with the only obtained R1 attached to position 1033. Only the displayed rotamers were considered in the distribution calculation.

In the presence of the R1 rotamer at position 1033 in the structure file, for residue 984 (H4) the number of populated rotamers is reduced from six to three, indicating that the R1 side chain bound at position 1033 (H5) restricts the spatial freedom of R1 bound at position 984 (H4). For Vt901R1 (H1) three significantly populated rotamers were found in absence and presence of R1 at position 1033 (H5). The number of populated rotamers (two) for Vt957R1 (H3) does also not change in dependence of presence of the R1 rotamer 922 (H2) in the crystal structure file of Vt. This indicates that the motional and spatial freedom of R1 at positions 957 (H3) and 901 (H1) are not influenced by a R1 side chain at position 922 (H2) or 1033 (H5), respectively.
The rotamers exhibiting the highest population (> 0.1 %) are shown in figure

5.8 (left panel). The calculated distance distributions for the double mutants under investigation are shown in figure 5.8 together with the experimental EPR data and the results from the MD simulations. Mean distances and distributions widths are summarized in table 5.2.

Mean distances obtained from RLA and MD simulation			
residues	EPR	RLA	MD
901/1033	0.76 ± 0.08	$1.00(1.15) \pm 0.05$	1.27 ± 0.11
901/957	2.65 ± 0.10	2.80 ± 0.05	2.73 ± 0.08
984/1033	0.74 ± 0.07	0.70 ± 0.05	$0.73(0.9) \pm 0.05$
922/957	0.76 ± 0.08	0.90 ± 0.05	0.95 ± 0.11

Table 5.2: Mean distances and distribution widths extracted from the distance distributions obtained from RLA and MD simulations. For comparison the experimental EPR results are shown in the left column.

The experimentally obtained distance of 2.65 nm for Vt901R1/957R1 is in line with the computational results taking experimental errors into account. For Vt922R1/957R1 and Vt984R1/1033R1 the distributions determined by MD simulation and RLA show mean distances < 1 nm. In this distance regime Heisenberg exchange coupling might contribute to the EPR spectra shape, what is assumed to be a reason for the deviations of low temperature cw-EPR spectra and the corresponding simulations of the two double mutants.
The obtained distance distribution for mutant Vt901R1/1033R1 (H1/H5) yields the highest distribution width, indicating a higher motional flexibility of 901 and 1033 compared to the other cases, where the smaller distance distributions widths reflect restricted flexibilities of the attached spin label side chains. Furthermore, this mutant reveals small deviations in the distance distributions obtained by MD and RLA. The center of the distance distribution obtained by MD is located at 1.27 nm, RLA exhibits 1.1 nm. Moreover, the RLA shows two distinct components, corresponding to two different rotamer structures, whereas the MD simulation yields a single Gaussian shaped distribution. However, the distance range obtained by RLA is covered by the MD simulations, indicating that the MD simulation samples more R1 orientations compared to RLA. During MD simulations and RLA calculations the protein backbone atoms were fixed. Therefore, the deviations between RLA and MD results in case of Vt901/1033R1 (H1/H5) could be explained by the fact that in MD simulations protein side chains are able to reorient due to interactions with other residues or R1 side chains. In contrast, all protein atoms were fixed in the RLA, leading to a smaller accessible space for R1 compared to the MD simulation results.

The distributions obtained by MD simulations show even larger distances than the RLA results, indicating that the distances between MTSSL on helix H1 and H5 are larger than 1 nm in the Vt crystal structure. In contrast, EPR measurements on Vt901R1/1033R1 (H1/H5) reveal a mean distance of 0.76 nm, indicating that the helical arrangement of helix one and five of Vt in solution differs from the crystal structure. One possible explanation of the results could be the fact that helix one and five of Vt in an aqueous solution are able to converge, whereupon the spin label side chains at positions 901 (H1) and 1033 (H5) might come slightly closer to each other.
For Vt984R1/1033R1 (H4/H5) two distinct populations centered at 0.73 and 0.90 nm were found by MD simulations, indicating that at least for one of the R1 two dominating conformations exist, whereby the most dominant conformation results in a mean distance of 0.73 nm. In fact, the MD trajectories suggest two distinct orientation ranges for position 1033 (data not shown), but no indication for two conformational components is apparent in the distance distribution of Vt901R1/1033R1, indicating that the presence of 984R1 affects 1033R1 in a way that mainly two different conformations in case of 1033R1 are preferred. However, the second component is not visible in the distance distribution obtained by RLA. Also here, the possible side chain movement in case of MD could explain this result. The more dominant peak of the MD distance distribution is well reproduced by RLA and the experimentally obtained distances for the mutant Vt984R1/1033R1 (H4/H5) are in very good agreement with the computational results, indicating that in the experimental case the helical arrangement between H4 and H5 is similar to the Vt crystal structure case. This means that mainly helix H1 is involved in the above mentioned structural rearrangement of Vt in solution. The helix movement is assumed to be a combination of both, a slightly rotation of helix H1 and a small shift in the direction of helix H5, enabling the convergence of R1 side chain attached to position 901 to 1033. However, since Heisenberg exchange interaction is neglected in the analysis the interpretation in terms of the proposed small conformational change should be treated with caution.
Furthermore, the computational results of mutants Vt922R1/957R1 (H2/H3) (MD: 0.95 nm; RLA: 0.9 nm) and Vt901R1/957R1 (H1/H3) (MD: 2.73 nm; RLA: 2.8 nm) are in very good agreement. In case of Vt901R1/957R1, the deviation of the experimentally obtained distances of around 0.1 nm could also be an indication for a small reorientation of corresponding helices of Vt in solution, but the effect is assumed to be insignificant small, as the observed deviation is in the range of the experimental error.

In summary, the experimentally determined inter helical distances between H1-H3, H1-H5, H5-H4 and H2-H3 are in line with the crystal structure. Further-

more, assuming an *antiparallel* five-helical bundle (as predicted by the crystal structure), meaning that all helices are parallel aligned to each other and one helix is connected to its neighboring helices on opposite sites, the individual distances in the investigated two-helical bundle parts depending strongly on each other. Consequently, a small conformational change of Vt in solution with respect to the crystal structure involving even only one helix would effect several inter helical distances of the here chosen combinations, which could not be observed here. Taken together, the results provided by EPR distance measurements for the here investigated doubly labeled Vt variants indicate that the complete five helical bundle arrangement proposed by the crystal structure of Vt is preserved in an aqueous environment.

5.1.5 Distance measurements on Vt single mutants reveal dimerization

In crystals Vt was found to be a dimer [7]) leading to the question, if this is an artificial result arising from the crystallization conditions (high protein concentrations, low pH etc.) or if the dimerization also occurs under physiological conditions. This question could be answered by previous NMR spectroscopy results [55], which reveal a dissociation constant of $K_d \approx 300\mu M$ under similar conditions as applied in this work, leading to a Vt dimer fraction of approximately 10 %. This percentage of Vt dimers is minor, but is likely to be crucial for the F-Actin bundling function of Vt. Knowledge about the mechanism of the self association could support investigations of Vt dimerization, which is observed for Vt in the presence of F-actin.
Here, the dimerization of Vt in an aqueous solution is investigated by DEER distance measurements on singly labeled molecules [4]. The results obtained for helix attached sites (positions 901 (H1), 922 (H2), 950 (H3), 957 (H3), 984 (H4) and 1033 (H5)) are used to propose a model for the conformation of the Vt dimer, regarding the relative orientations of two Vt molecules and their interactions surfaces. The labeling positions chosen are evenly distributed over the α-helical core of the protein, leaving out loop regions and the N- and C-terminal ends. DEER and computational results for the Vt alignment are discussed in the following chapters.

5.1.5.1 DEER measurements on Vt single mutants

DEER measurements were performed as described above. The DEER dipolar evolution functions are shown in figure 5.9 (left panel) together with the resulting distance distributions (right panel).

[4] *Cw*-EPR distance measurements were carried out in addition revealing no indication for a dipolar interaction (distances below 2 nm) in each case.

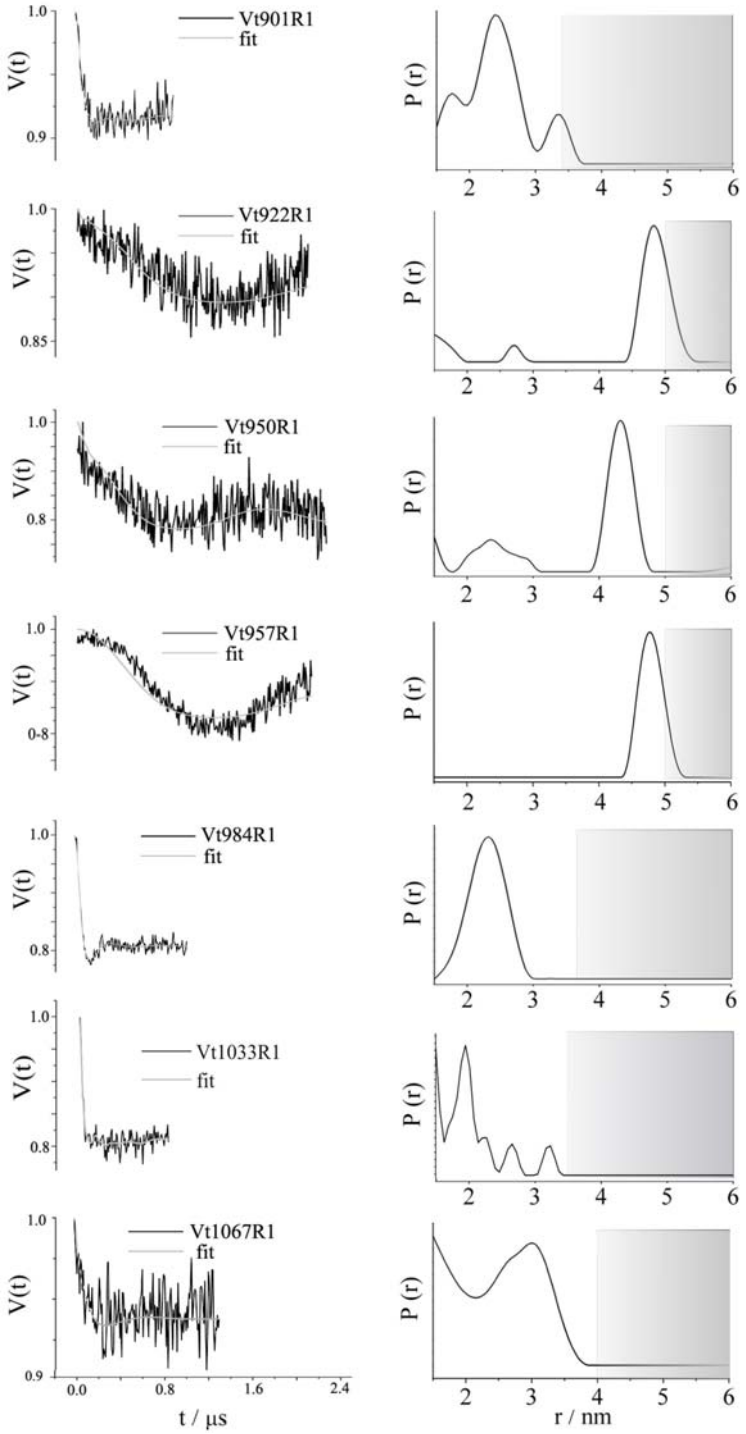

Figure 5.9: DEER spectroscopy results of Vt single mutants. Left: Dipolar evolution functions are shown as black lines and the corresponding fits calculated with DEER-Analysis are indicated as gray lines. Right: Resulting DEER distance distribution obtained from DEERAnalysis.

Dipolar oscillation could not be observed in case of Vt1062R1 (data not shown), indicating that either the modulation frequency is too low to be traced within the applied dipolar evolution time (1200 μs), corresponding to distances larger than 4 nm or the absence of dimerization. The latter would be an indication for the fact that the mutation of position 1062 effects the dimerization behavior of Vt and thus, it plays an important role for the dimerization.
However, except for Vt1062R1, in each case dipolar modulations are observed in the DEER time traces, indicating a dipolar interaction caused by Vt dimerization. The particular modulation depths vary between < 0.1 and 0.2. This corresponds to a number of interacting spins of ca. 1.1 - 1.3 (determined using DEERAnalysis), which reflects the percentage of dimers in the sample (10% - 30%). A reason for the variation of the modulation depth among different samples might be that some mutations affect the grade of the self dissociation, and thus the percentage of dimers within the sample. Slight variations in protein concentration in different experiments might also contribute to this fact. However, in each case the Vt dimer fraction is $\leq$ 30 %, indicating small fractions of dimers present in the sample, which are comparable to the above mentioned results obtained by NMR spectroscopy.

Mean distances of Vt single mutants (helix attached sites)					
$Vt901R1$	$Vt922R1$	$Vt950R1$	$Vt957R1$	$Vt984R1$	$Vt1033R1$
2.3 ± 0.3	4.8 ± 0.2	4.3 ± 0.2	4.8 ± 0.2	2.3 ± 0.4	2.0 ± 0.2

Table 5.3: Mean distances and HWHM extracted from the DEER distance distributions obtained for Vt single mutants.

Vt1067R1 reveals a very broad distance distribution covering the range between 2 nm and 4 nm. Due to the used dipolar evolution time in this case, distances above 4 nm are not detectable, but might be present. The contributions below 2 nm present in the distribution arise most likely from noisy parts in the beginning of the DEER trace. However, the distribution width reflects a high mobility of the R1 attached to Vt1067R1, and is in line with the mobility measurements. In contrast, the resulting distance distributions of the helix attached sites (Vt901R1-Vt1033R1) reveal well defined dominating distances. Mean distances and corresponding HWHH are summarized in table 5.3. Additional small contributions occur most likely as consequence of the low signal to noise ratio, especially in case of Vt922R1 (H2), Vt950R1 (H3) and Vt1033R1 (H5). The same applies for the contribution below 2 nm in case of Vt901R1 (H3). The contribution above 3 nm is not reliable, since the dipolar applied evolution time is too short to judge distances above 3 nm. Uncertain-

ties concerning the distance determination might also be taken into account for Vt922R1 and Vt957R1, where the applied dipolar evolution time allows reliable distance quantification up to approximately 5.0 nm. Thus the distances in the cases Vt922R1 and Vt957R1 might be slightly larger than those obtained by Tikhonov regularization.
The distances of Vt901R1, Vt984R1 and Vt1033R1 are considerable smaller compared to Vt922R1, Vt950R1 and Vt957R1, indicating that helix one, four and five might be involved in, or close to the dimerization interface. This fact was investigated in more detail by the computational analysis of the here obtained DEER results in terms of the Vt dimer configuration, as described in the following chapter.

5.1.5.2 Determination of the molecular alignment within the Vt dimer

NMR studies [55] as well as DEER measurements on singly labeled Vt performed in this study provide evidence for the presence of dimeric Vt in aqueous solution even in the absence of interaction partners. Here, the DEER data of the helix bound R1 side chains exhibiting well defined mean distances are used in order to answer questions concerning the dimerization interface and the relative alignment of two Vt molecules. For the orientation determination between two Vt molecules forming the dimer, the self written Matlab script *OrientSol* (explained in 4.2.3) was used. Since the above discussed results for Vt reveal its structure to be largely in accordance with the structure obtained by X-ray crystallography, the computational analysis was performed using the Vt crystal structure file. To this structure, the R1 side chains, exhibiting the structural conformations of the highest populated rotamers (obtained by RLA), were attached to positions 901, 922, 950, 957, 984 and 1033, respectively.
The experimental mean distances and distance widths were obtained from DEER experiments on Vt901R1 (H1), Vt922R1 (H2), Vt950R1 (H3), Vt957R1 (H3), Vt984R1 (H4) and Vt1033R1 (H5) (see chapter 5.1.5). All calculations were also done by omitting the N- and C-terminal domain atoms for the clash determination, since a rearrangement of the strap and the C-terminus after Vt dimerization can not be excluded. The thereby obtained results show insignificant differences compared to the case discussed in the following, where all protein atoms were considered.
Using the orientational grids as defined in 4.2.3, the calculations lead to approximately 1000 clash-free solutions. The quality of the agreement with the DEER data for each of these 1000 structures was judged by the parameter s_{tot} (see 4.2.3). All structures were analyzed by plotting the Euler angles α, β and γ versus the corresponding s_{tot} for each solution in order to find adequate values for the Euler angles, reflecting the most probable relative orientation of two Vt

molecules (figure 5.10). In each case, the plot reveals two characteristic regions. The regions between $s_{tot} = -14$ (best agreement) and $s_{tot} = -9$ show minor variances of the respective Euler angles. In contrast, in the region $s_{tot} > -9$ the values for α, β and γ begin to disperse. This was expected, considering the fact that the more an Euler angle value differs from the best solution (smaller s_{tot}) the worse is the agreement with the experimental data (larger s_{tot}).

The appearance histograms in the left panel of figure 5.10 reveal the most frequent occurring values for each Euler angle considered. In each case a dominant peak is visible corresponding to a certain value for α, β or γ, respectively.
At this point it has to be mentioned that no orientational correlation between the peaks with similar intensities of the particular histograms have to exist. That means for example that the best obtained solution does not necessarily correspond to the Euler angle combination extracted from the histogram maxima. But here, the centers of the dominant peaks in the histograms coincide approximately with the maxima, corresponding in each case to the value, around which the particular Euler angle values in the *good agreement* region vary. Additionally, the variances around each maximum (or center) are small, indicating that a certain value for α, β and γ is preferred and that the desired orientation does not differ significantly from the orientations determined by the histogram maxima. However, it is extractable from both plots that a second area within the *bad agreement* region emerges, in which some of the solutions accumulate, indicating a second possible conformation for the two Vt molecules. Also obvious from figure 5.10 is the fact that the additional, less dominant, peaks in the histograms arise from those solutions exhibiting the worst agreement with the DEER data. Samples taken from this area also reveal a structural alignment, in which the actin binding sites (primarily helix three [33]) are masked by at least one of the two Vt molecules. Consequently, dimer molecules exhibiting the conformations extracted from the *bad agreement* area would not be able to bind and bundle actin filaments.
Due to these facts, solutions exhibiting $s_{tot} \geq -9$ were not considered, and the average orientation (α, β, γ) was extracted from the histograms centers, corresponding to the best 20 % of all solutions. This leads to $\alpha = 120° \pm 20°$ $\beta = 95° \pm 10°$ and $\gamma = 40° \pm 10°$ (figure 5.11). As uncertainties the HWHM of the respective histograms are given.
The same analysis was done with the orientation (ϑ_t and φ_t) of the translation vector $\mathbf{t}$ and its absolute. The center of mass distance (defined by the absolute value $|\mathbf{t}|$) between molecule one and two could be determined to 2.8 nm ± 0.2 nm as the well defined maximum in the histogram plot shown in figure 5.12 (left) reveals. The plots for ϑ_t and φ_t show a very defined orientation for ϑ_t ($\vartheta_t = 150° \pm 10°$), whereas the distribution of φ_t ($\varphi_t = 325° \pm 40°$) is broader

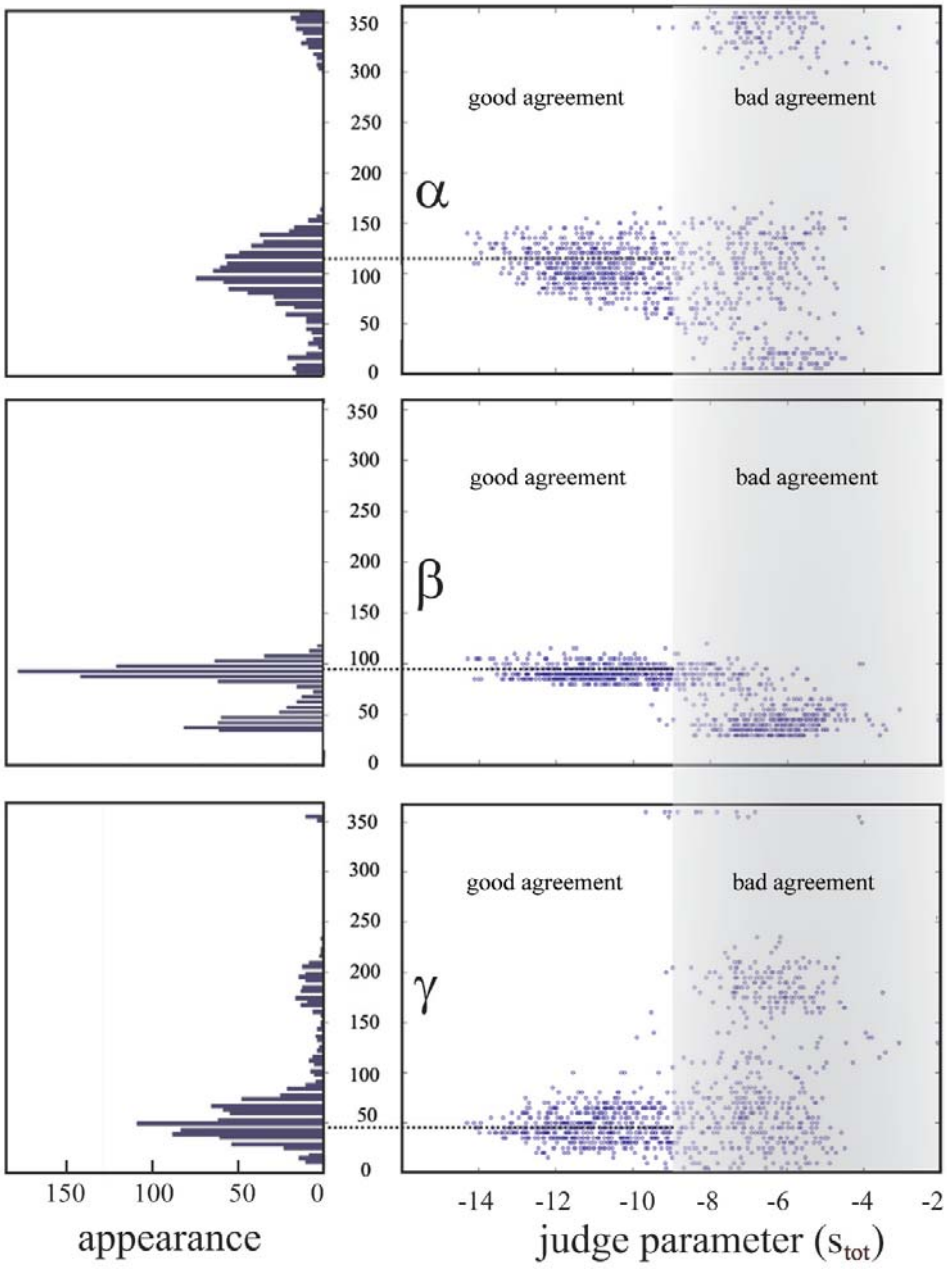

Figure 5.10: Euler angles α, β and γ were plotted versus the corresponding s_{tot} for each solution in order to find adequate values for the Euler angles reflecting the most probable relative orientation of two Vt molecules (right). Smaller values for s_{tot} reflects better agreement with the experimental results. Appearance histograms (left) reveal the most frequent occurring values for the Euler angles and were further used for determination of the relative Vt alignment.

compared to ϑ_t.

Here, it has to be mentioned that in this analysis all spin label molecules were

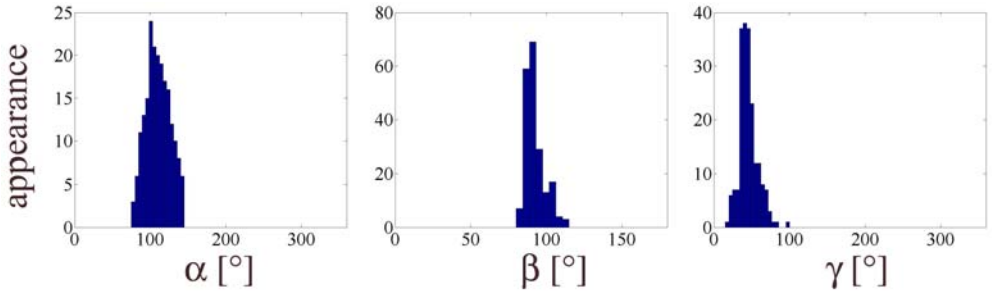

Figure 5.11: Appearance histograms resulting from a consideration of the best fitting 20 % of all solutions. Determined mean values are $\alpha = 120° \pm 20°$ $\beta = 95° \pm 10°$ and $\gamma = 40° \pm 10°$. The HWHM of the respective histograms are given as uncertainties.

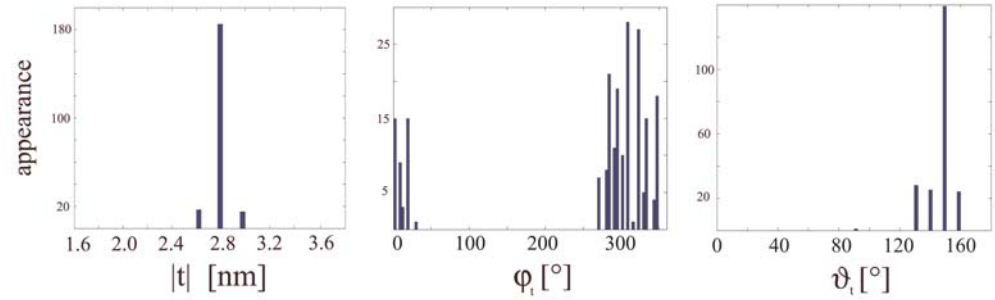

Figure 5.12: Appearance histograms for ϑ_t, φ_t and the absolute of the translation vector **t** are presented. The exctracted mean values are $\vartheta_t = 150° \pm 10°$, $\varphi_t = 325° \pm 40°$ and abs(**t**)=2.8 nm ± 0.2 nm.

treated as fixed with respect to the protein structure. In reality, the spin labels perform a re-orientational motion. The width of the DEER distance distributions arise on the one hand from orientational distributions between the two molecules, but also from the mentioned R1 motion. Here, by the use of the DEER data, the distribution widths are translated into pure protein orientational distributions and the R1 side chain movement is neglected. Thus, the here determined orientational distributions for the Euler angles and for the translation vector are assumed to be smaller than indicated here.
The fact that the φ_t uncertainty is larger compared to ϑ_t could be explained with the anisotropy of the spin label side chain motion. All R1 side chains are attached to helical domains and at each position the nitroxide groups are located between two helices (see chapter 5.1.4.2). The R1 motion along the helix or protein long axis, respectively, is favored compared to a motion perpendicular to that, because the freedom of movement into this direction is restricted by two helices. Hence, this analysis would reveal a larger orientation distribution along the protein long axis. This might be reflected by the larger distribution of φ_t. In order to confirm this assumption, two extreme cases (φ_t= 280° and 360°

with similar values for α,β and γ) were chosen for comparison. It is obvious from figure 5.13 that the shift caused by φ_t is approximately into the direction of the long axis of molecule two, corresponding to the main direction of motion of all attached spin labels. In this case, ϑ_t is 150° and the difference in φ_t of both examples 80°. Hence, the angle ϕ between the respective translation vectors can be calculated to $\phi = 80° \cdot sin(\vartheta_t) = 80° \cdot sin(150°) = 40°$, which is also assessable from figure 5.13. This indicates that the obtained large uncertainty of the value φ_t is most likely governed by the R1 chain motion, which is not considered in this analysis.

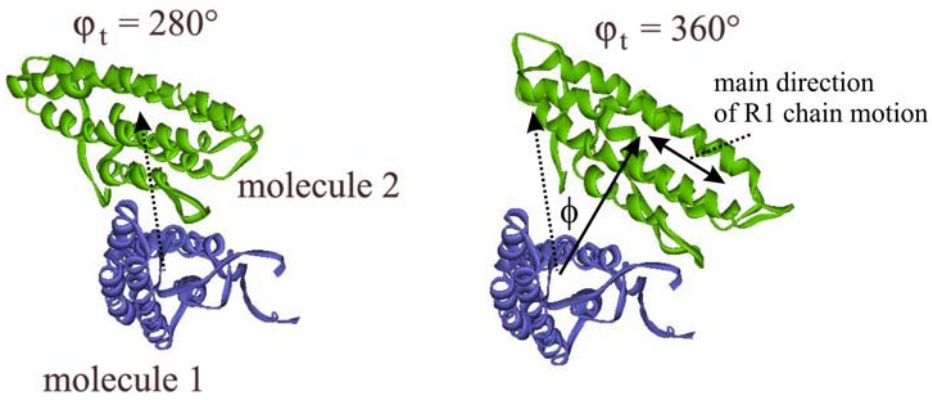

Figure 5.13: Two extreme cases exhibiting the values φ_t= 280° and 360°, respectively, with comparable values for α,β and γ are shown for comparison. A shift of $\Delta\varphi_t = 80°$ results predominantly in a shift into the direction of the Vt long axis, which coincides with the main direction of R1 motion indicating that the large uncertainty determined for φ_t is most likely governed by the not considered R1 chain motion.

However, all parameters determining the relative orientation between the two Vt molecules are well defined. A solution exhibiting the average values obtained could be found within the best fitting 2.5% of all solutions. This average structure represents the most probable alignment of two Vt molecules and is shown in figure 5.14). It reveals a cross-like upside-down alignment of the two molecules. Two regions can be identified, where the two Vt molecules come very close together, indicating that these regions constitute the contact interface (figure 5.14, front view).

More precisely, one Vt molecule (here: molecule one) reveals primarily helix five to be involved in the main interaction surface together with parts of helix H1 (second half) and a small part of helix four. Additionally, a small fraction of the middle C-terminal end is assumed to be part of the dimerization interface. The second smaller interface region of this molecule can be assigned to the N-terminal end of helix five (figure 5.15 a) and c)). For the second binding partner (molecule two) the main contact region can be specified as parts of the

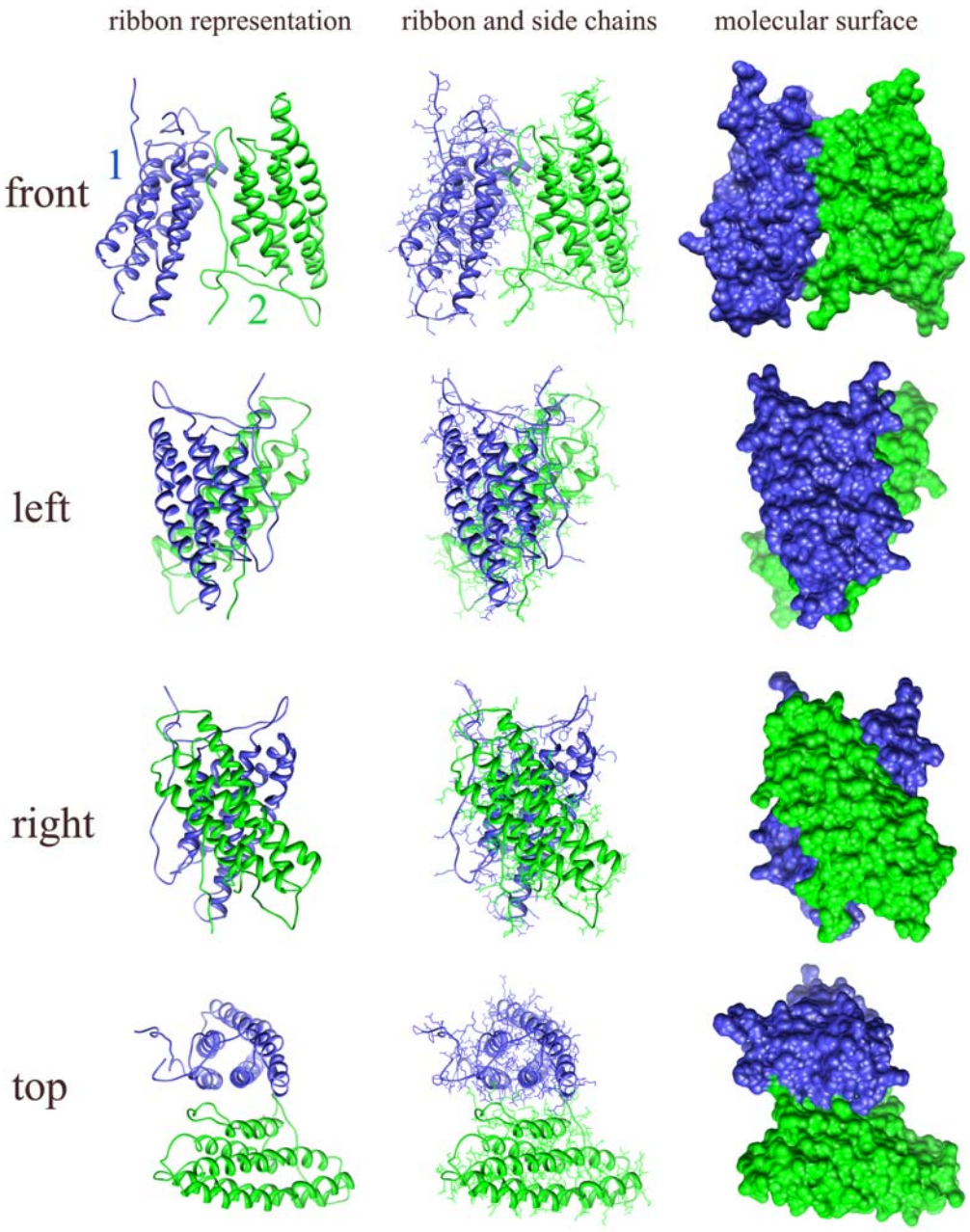

Figure 5.14: The resulting molecular model is shown from different perspectives. Vt molecules one (blue) and two (green) exhibit a cross-like upside down alignment. Left: ribbon representation, middle: ribbon and side chains are shown, right: surface representation.

N-terminal strap, which is adjacent to helix H1 and a major part of helix H1. The end parts of the C-terminal end and likely of the N-terminal strap define the counter part of the second smaller contact region (see figure 5.15 a) and b)).

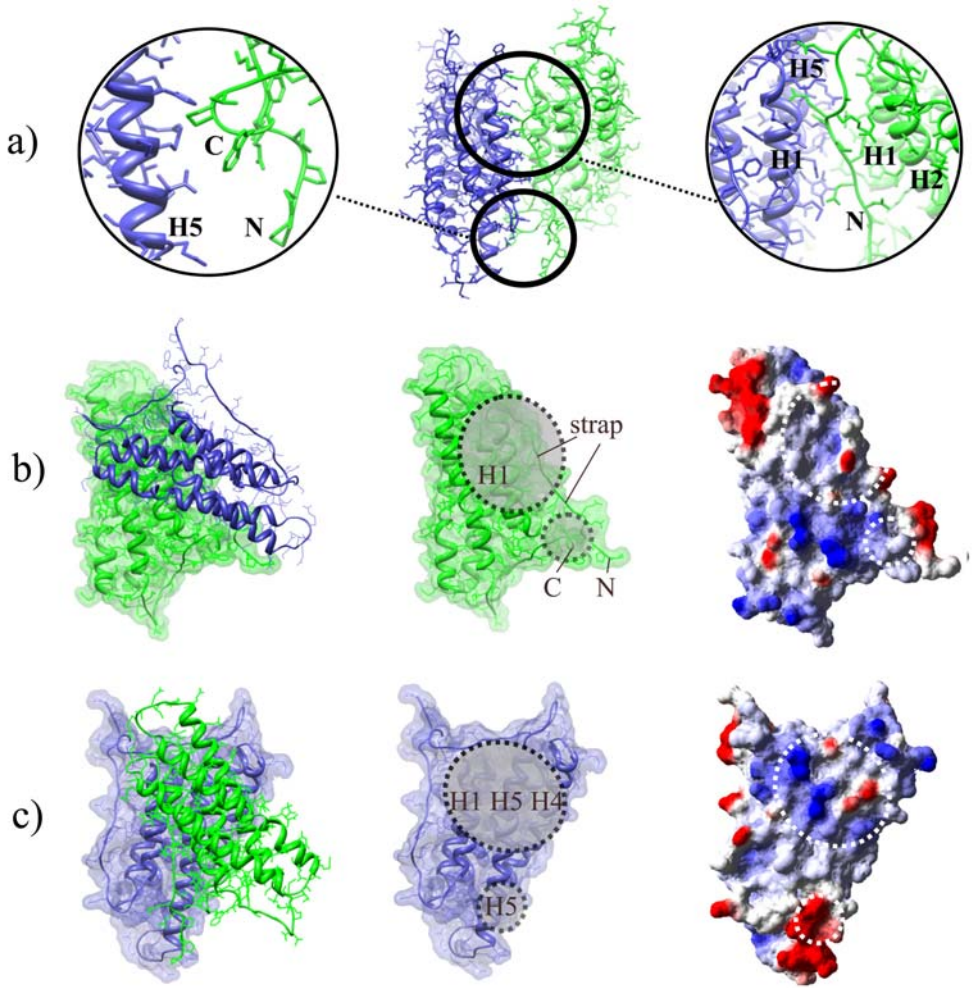

Figure 5.15: Detailed view on the Vt dimer model. a): Zoom in the two different assumed dimerization sites. Helix numbers, N- and C-termini are indicated. b): View on the dimerization region of molecule two (green). Left: Vt dimer model. Middle: Assumed dimerization surfaces are shown as black dotted circles. Right: Positively charged surface areas are highlighted in blue, negative charges in red. The assumed surfaces involved in the dimerization are circled with dotted white lines. c): View on the dimerization region of molecule one (blue). Left: Vt dimer model. Middle: Two different dimerization surface areas (black dotted circles). Right: Positively charged surface areas are highlighted in blue, negative charges in red. The assumed dimerization surfaces are shown as white dotted circles.

A surface charge analysis of the proposed contact regions in the Vt dimer show that the respective counter parts reveal predominantly contrary charges (figure 5.15 b) and c), right panel). The large region of molecule one (5.15 c)) reveals positive charges located in the helix one/five regions and a small region with negative charges situated at helix H4 and at the C-terminal end. The corresponding counter part of molecule two (5.15 b)) (helix H1), which

is supposed to bind to the negatively charged part of helix H4 of the other molecule, is positively charged. Additionally, the negatively charged regions of the molecule two strap are assumed to bind to the positively charged region composed of the respective parts of helices H1 and H5 of its binding partner. Furthermore, the small binding interface domain of molecule one is completely negatively charged, whereas the corresponding part of molecule two exhibits primarily positive charges. The opposing charges of the interface regions lead to the assumption that the binding might be supported or even regulated by the molecular surface charges, i. e. being primarily of electrostatic nature.

As an additional evaluation of the computational results, a rotamer analysis was carried out on the obtained dimer model. The resulting distance distributions are shown in figure 5.16, overlaid with the experimental DEER data.

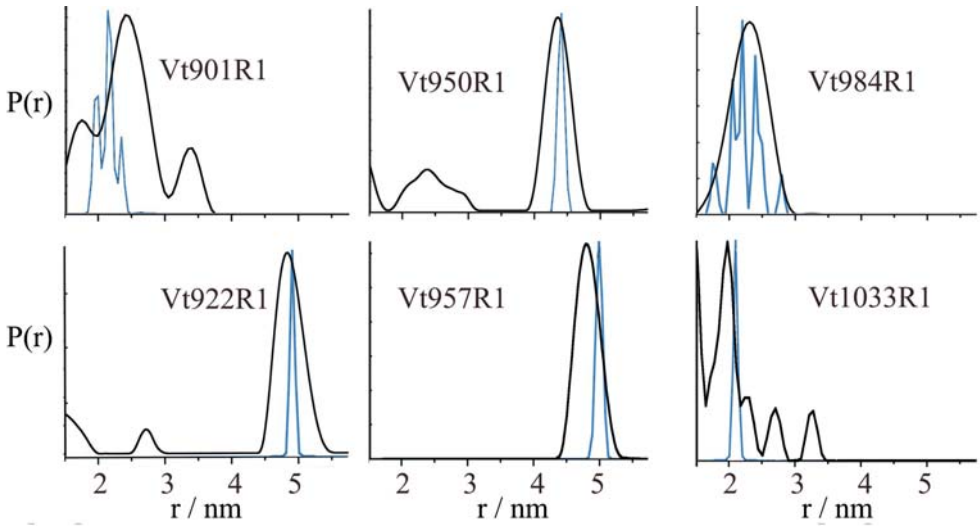

Figure 5.16: Comparison of the DEER distance distributions (black lines) with the outcome of the RLA (blue lines) carried out on the Vt dimer model structure.

In each case, the mean distances of the distributions calculated from RLA are in good agreement with the experimental results, even under consideration of a tolerance value (experimentally obtained distributions width) for the distance agreement used in the calculations for the Vt alignment determination. In case of Vt984R1 even the width of the experimentally obtained distribution is reflected by the RLA result. The largest deviations are obtained for positions 901 and 957. However, for position 901 a less dominating contribution of the distribution obtained by RLA coincides with the mean distance obtained by DEER experiments. The low populated rotamer conformation leading to this contribution might be more dominant in the experiment (as already proposed for Vt901R1 in 5.1.4.2), since rearrangements of neighboring protein side

chains, influencing the rotamer populations, are not considered in RLA. This is most likely also the reason for the fact that the RLA distributions are in each case narrower as compared to the experimental results. The flexibility of the protein side chains lead to a larger conformational space of the spin label side chain, which in turn increases the distance distribution width. Additionally, a small distribution of the orientational arrangement between two Vt molecules building up the dimer, as well as the flexibility of the whole protein structure contribute to the widths of the experimentally obtained distance distributions. However, all deviations are minor, consolidating the fact that the dimer structure of Vt in aqueous solution is well represented by the here presented model. In summary, the surface charge analysis and the RLA results support the above made specification for the binding domains. The assumption of the preservation of the crystal structure of Vt in an aqueous solution is also confirmed, since the here made analysis was performed on the Vt crystal structure.

It has to be mentioned that the crystal structure of Vt was solved as a dimer with helix H1 distal from the site of dimerization. In that case helix four and five of both molecules are located within the interaction surface. Thus, the here obtained structural model contradicts these findings. It is possible that under the conditions used for crystallization (e.g. pH=5.0, see [7]) the mode of dimer formation differs from that under more physiological conditions.
Previous NMR results reveal parts of helix five and helix four to be solely involved in the dimerization sites leading to the assumption that the interaction site is similar to that observed for the Vt dimer crystal structure [55]. That parts of helix H5 and H4 belong to the dimerization interface is in agreement with the results found in this work. Unfortunately, signals from residues 904-914 (helix one) were not detectable in the mentioned NMR study, which are here assumed to be important parts of the dimerisation interface of one binding partner. Without this information, the dimerization sites found in the NMR study have necessarily to be assigned to both molecules leading to the similarity to the crystal structure. However, here it could be concluded that the in the NMR study found dimerization sites apply only for one of the molecules.
Furthermore, the involvement of helix H1 and the N-terminal strap in the dimerization interface proposed in this work is supported by another fact, which is visible from the full length vinculin crystal structure. Vt in its inactivated state is grabbed by the head domain. The strap and parts of helix H1 are not masked by the head domain, so the dimerization binding sites of at least one Vt molecule are accessible. Thus, the results obtained here could give also new insights into the activation pathway of vinculin, considering that another activated vinculin molecule can bind an inactivated Vt, which in turn is activated.

5.2 Structure of Vinculin Tail bound to acidic lipids

Acidic phospholipids, such as PIP_2 and PS, play an essential role in cell migration. They regulate the assembly and disassembly of focal adhesions and assist the linking of the actin-cytoskeleton with the cell membrane [45, 7]. Although the propositions of the role of acidic lipids are discussed diversely in literature, and numerous details remain largely unknown, the importance of the interaction of acidic lipids and vinculin for its function in cell migration is beyond dispute. Structural changes of Vt in presence of acidic lipids were reported [7, 6], which are accompanied by a dimerization and/or higher oligomerization of Vt [28]. However, detailed structural models of the Vt conformation bound to acidic lipids are still unavailable. In order to answer questions concerning structural changes of Vt in the presence of acidic lipids, various EPR methods were applied in this work. The results of mobility, polarity, accessibility and distance determinations of singly and doubly labeled Vt variants allow the construction of a molecular model of Vt bound to PS-lipid membranes. The results are presented and discussed in the following chapters.

5.2.1 Mobility measurements

Sample preparations and measurement procedures for singly labeled Vt in presence of PS-lipid vesicles (Vt901R1PS, Vt922R1PS, Vt950R1PS, Vt957R1PS, Vt984R1PS, Vt1033R1PS, Vt1062R1PS and Vt1067R1PS) are described in chapter 4. The mobility parameters $1/\langle H^2 \rangle$ and $1/\Delta H_0$ are plotted in figure 5.17 (green) together with the results obtained for Vt in aqueous solution (black) for direct comparison. The corresponding EPR spectra are shown in figure 5.17 (right).
A minor fraction of mobile components is present in case of Vt901R1PS, Vt950-R1PS, Vt984R1PS and Vt1067R1PS, leading to higher uncertainties in terms of the determination of the central line width. These spectral features additionally complicate the second moment calculations especially for Vt901R1PS, Vt984R1PS and Vt1067R1PS, since in these cases the value of the second moment has shown to be very sensitive to the considered magnetic field range and baseline corrections. Thus, the error for the calculations is assumed to be considerably higher compared to the other cases. The inverse line width $1/\Delta H_0$ in case of Vt901R1PS refers to a loop/surface, loop/contact and also to a helix/surface related site, whereas the value for $1/\langle H^2 \rangle$ excludes the loop/contact case. Considering the experimental error, in case of Vt901R1PS, here it can not be precisely distinguished between loop/surface and helix/surface related sites. However, assuming a preservation of the secondary structure elements, Vt901R1PS (H1) can most likely be assigned to a helix attached site exhibiting

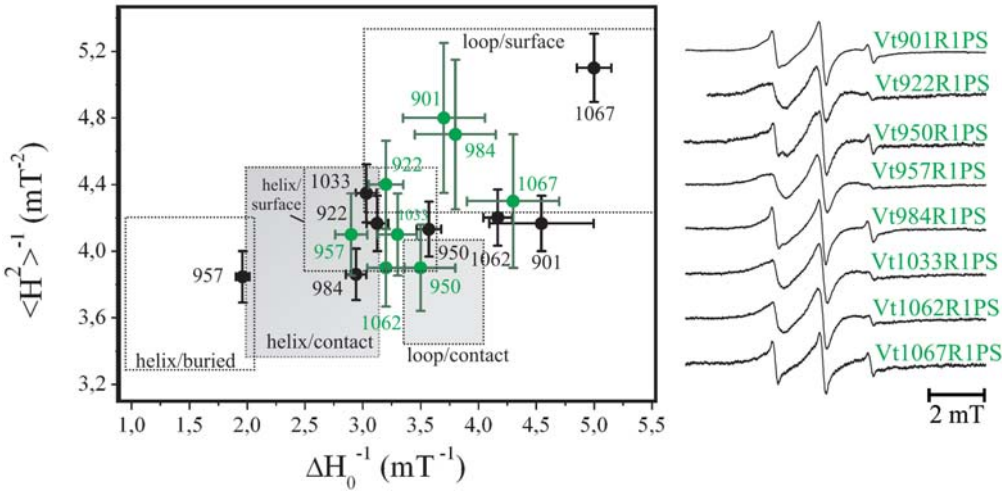

Figure 5.17: Mobility analysis of R1 side chains attached to Vt in presence of PS-lipid vesicles. Left: Plot of the semi empirical mobility parameters $1/\langle H^2 \rangle$ versus $1/\Delta H_0$. The topological regions were drawn according to [47] and [13] (see figure 3.7). Results for Vt in presence of lipids (green) are shown together with the results obtained for Vt in absence of lipids containing 40 % sucrose (black). Right: Cw-EPR room temperature spectra of the investigated singly labeled Vt variants in presence of PS-lipids.

no significant tertiary contacts. The same applies for Vt984R1PS. However, due to the large error the results for Vt901R1PS and Vt984R1PS should not carry significant weight.

The result obtained for Vt1067R1PS to be a loop attached site is more explicit, whereas also here, taking the experimental error into account, it can not be clearly indicated if a R1 attached to this position is surface exposed or exhibit contact with surrounding atoms. Note, contact related positions might not only refer to a tertiary contact to protein atoms in this case, but might also reflect contact with atoms, which are part of the lipid bilayer, either the lipid head groups or fatty acid chains. Positions, which reveal molecular contacts are furthermore Vt950R1PS, Vt957R1PS and to a small extent also Vt922R1PS, Vt1033PS and Vt1062PS. The result for position 1062 located at the C-terminal end of Vt leads to the assumption that Vt1062R1PS is related to a loop/contact site. In contrast, R1 side chains of Vt922R1PS and Vt1033R1PS are situated on helix two and five, respectively, thus, Vt1033R1PS is most likely assigned to a helix/surface related site, whereas Vt922R1PS can be both, a helix/contact or helix attached surface exposed site. Vt950R1PS (H3) and Vt957R1PS (H3) show clear features of surface related positions, whereas position 957 reveals also the possibility to exhibit molecular contacts. The deviations in these cases might be traced back to their respective position with respect of helix three. The mobility of the R1 side chain bound to Vt950R1PS might be higher than

compared to Vt957R1PS, because the R1 is attached close to the end of helix three, where a higher mobility of the helix (backbone) is assumed as compared to residue 957, which is situated in the middle of helix three.
Compared to the result in absence of PS-lipids the helical end located Vt950R1 (H3) reveal insignificant changes. Similarly, the mobilization of R1 at position 922 (H2) in presence of lipids is small. However, several positions show considerable changes in presence of lipids. Vt957R1 (H3) becomes clearly more mobile in the presence of PS-lipids, indicating that the previously observed strong tertiary contact is reduced or even not present in case of Vt957R1PS. An increase of mobility is also observed for R1 at position 984 (H4), in presence of lipids, clearly indicating that the tertiary contact in presence of PS is largely abolished. The same applies for Vt901R1PS (H1), which shows an increase especially in the inverse second moment. Vt1033R1 (H5) in terms of the topology region plot is shifted towards the center of the area corresponding to helix/surface related sites after adding lipid vesicles. The increase of $1/\Delta H_0$ indicates that the interaction between Vt and PS lipid lead to a weakening of tertiary contact in this case as well. The position of Vt1062R1 and Vt1067R1 are shifted into the direction of the loop/contact related region, indicating that these position are also affected by the presence of acidic lipids, thus, an interaction of R1 at positions 1062 and 1067 with the lipid vesicles.

Taken together, the EPR mobility measurement results indicate a conformational change in Vt in presence of PS-lipid vesicles, leading to higher spatial freedom of R1 attached to residues 901 (H1),957 (H3), 984 (H4) and 1033 (H5) and most likely also 922 (H2). Since all helices are involved, this indicates that the compact five-helical bundle structure might be particularly or even completely released, meaning a considerable reorientation or separation of all helices. One possibility would be an opening of the helix bundle upon binding of Vt to a lipid vesicle, what was also be proposed in previous works [7, 6]. In this case, Vt957R1PS (H3), and probably also Vt922R1PS (H2) would exhibit contact to the phospholipids, whereas other helix attached R1 (901, 950, 984, 1033) might exhibit no or weaker interactions with lipid atoms. Additionally, the EPR results indicate that positions 1062 and 1067 are affected by the Vt-lipid interaction. A direct interaction of the C-terminal end of Vt with the lipids would explain the decrease of mobility.
However, detailed insight into the structural change and questions concerning the relative locations of helices and R1 side chains with respect to the lipid bilayer can not be extracted from the mobility measurements results. In order to answer these questions polarity, accessibility and distance determinations were carried out and are discussed in the following chapters.

5.2.2 Polarity and accessibility measurements

In order to characterize the relative location and alignment of the Vt attached R1 side chains with respect to the PS-lipid bilayer, polarity and accessibility measurements were performed. Accessibility measurements were carried out to distinguish between residues exposed to the bulk water and those which penetrate the bilayer. The calculation of the parameter Φ from the collision frequencies of the paramagnetic reagents (NiEDDA, O_2) with nitroxide spin labels provide information about the immersion depth. The results should be affirmed by polarity measurements. Since the parameters Φ and A_{zz} for different immersion depths may depend on the lipid types used, measurements on spin labeled stearic acids, incorporated into the lipid bilayer, were done in absence of Vt in order to obtain reference values for investigations on Vt. Using this calibration, the expected values for Φ and A_{zz} for a certain immersion depth of R1 attached to Vt can be indicated.

5.2.2.1 System calibration

Accessibility and polarity measurement procedures, data analysis and preparations of PS-lipid vesicle solutions containing ca. 1% 5- or 16-doxyl-stearic acids (SA5PS and SA16PS) are described in chapter 4. Here, the nitroxide spin label is bound to the 5th or 16th C-atom of the stearic acid alkyl chain, counted from the head (carboxyl group). Sketches of the stearic acid and PS-lipid molecular structures are shown in figure 5.18 a). The distances between the labeled positions and the head group are approximately 0.5 nm and 1.8 nm for positions 5 and 16 respectively. In case of PS-lipid, the fatty acid chain length is ca. 2 nm, thus the PS-lipid-bilayer is assumed to exhibit a thickness of $\approx$ 4 nm, disregarding headgroups. Consequentliy, after the incorporation of stearic acids into the bilayer, position SA16 is located close to the middle of the bilayer, whereas SA5 is expected to be ca. 0.5 nm apart from the lipid head groups.

sample	Φ	A_{zz} / mT
SA5PS	0.6 ± 0.4	$3,46 \pm 0.02$
SA16PS	3.9 ± 0.4	3.24 ± 0.02

Table 5.4: Table containing the results obtained from accessibility (Φ)and polarity (A_{zz}) measurements for SA5PS and SA16PS.

The results obtained from accessibility measurements are listed up in table 5.4 and plotted in figure 5.18 b) in order to compare the results with the findings for the membrane spanning protein bacteriorhodopsin BR. Regarding the BR example the here obtained results indicate that SA16PS is located close to the

center of the lipid membrane and SA5PS approximately 0.8 nm apart from the lipid head groups. Considering the experimental error ($\Delta\Phi = \pm 0.4$) the values are in reasonable agreement with the above mentioned theoretical values, thus, for further discussions a direct comparison of the immersion depth Φ for spin labeled Vt in the presence PS-lipids with the BR results is reliable.

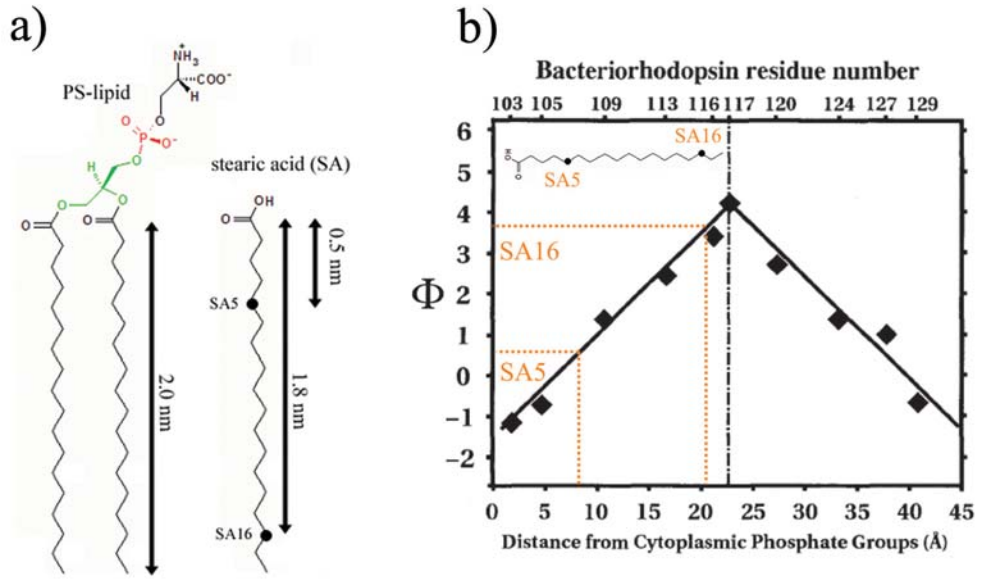

Figure 5.18: a): Molecular structures of a stearic acid (SA) and a PS-lipid. Distances from the lipid head groups are illustrated as green lines, distance values are indicated. b): Immersion depth parameter Φ and corresponding distances from the lipid head groups obtained for SA5PS and SA16PS (orange dotted lines) are plotted into the graph adopted from [30]. The values (black squares) were obtained from measurements on various BR mutants reconstituted in a lipid bilayer. The black dashed line indicates the bilayer center. The structure of a stearic acid molecule is shown (top) and the labeled positions indicated as orange dots.

Furthermore, the determined polarity values for SA5PS and SA16PS (table 5.4) support these findings. An A_{zz} value of ca. 3,6 mT is expected for a completely water accessible R1 side chain. Here, in case of SA5PS, the polarity is clearly decreased ($A_{zz} = 3,46$ mT) indicating that SA5PS exhibits a reduced environmental polarity due to its immersion into the apolar region of the lipid bilayer. The A_{zz} value in case of SA16PS is significantly smaller (3,24 mT), indicating a highly apolar environment. Such a situation is given in the middle of the bilayer. These values obtained for SA5PS and SA16PS are used as reference values for further investigations on Vt in the presence of PS-lipids.

5.2.2.2 Accessibility measurements

For each position, the value of the immersion depth parameter Φ is increased in presence of PS-lipids (see figure 5.19 and table 5.5). This indicates that the presence of PS-lipids affects the respective paramagnetic quencher molecule accessibilities to R1. Vt950R1PS (H3), Vt957R1PS (H3) and Vt1062R1PS show the highest obtained Φ values. A comparison to the calibration measurements using SA5PS, SA16PS and BR (figure 5.18 b)) enables the assignment of the respective Φ values to corresponding immersion depths into the lipid bilayer. The highest immersion depth obtained (approximately 1 nm) is exhibited by Vt950R1PS (H3). Similar values are determined for Vt957R1PS (H3) and Vt1062R1PS ($\Phi = 0.3 - 0.4$), indicating that the corresponding nitroxide groups are located ca. 0.7 nm apart from the lipid head groups, similar to the findings for SA5PS (0.8 nm).

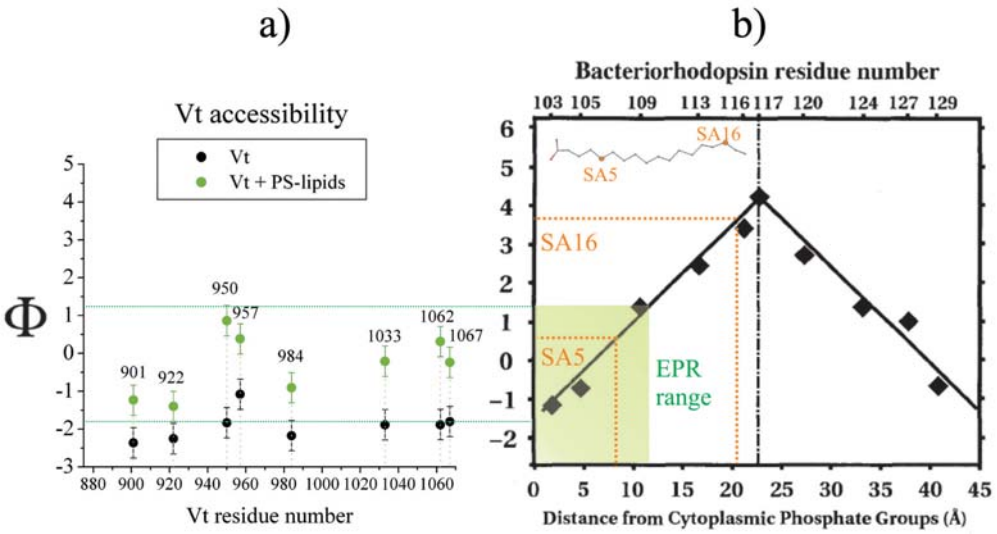

Figure 5.19: a): The immersion depth parameter Φ determined by accessibility measurements for Vt and Vt in presence of PS-lipids. b) Comparison to the results of spin labeled stearic acids incorporated into PS-lipid vesicles (SA5/16PS). The results are plotted into the graph determined by [30] (orange dotted lines). The range of obtained Φ values in case of Vt+PS is indicated (green rectangle).

In general, two possibilities for the alignment of the respective helices with respect to the lipid bilayer are assumed. Either, the helices span the whole bilayer (helix long axis parallel to the bilayer surface normal) or the helices lie on the lipid membrane surface (long axis perpendicular to the surface normal). The longest helices of Vt are helices H3, H4 and H5 with a length of ca. 4.3 nm. In the first mentioned case, these helices would penetrate the whole bilayer and positions 957 and 1033, located on helix centers, would be situated close to the bilayer center. However, the values obtained for Vt957R1PS and Vt1033R1PS

indicate that the nitroxides are situated closer to the lipid head groups than to the bilayer center, where $\Phi = 3.9$ (SA16PS) is expected. Furthermore the distance between positions 950 and 957 (two helical turns: ca. 1 nm) would lead to a larger difference in Φ than obtained here, leading to the conclusion that helix three is associated to the lipid membrane surface. The penetration depth of around 0.7-1.0 nm (950 and 957) would in this case result from the R1 side chain length of approximately 0.65 nm.

labeled position	$\Phi(Vt)$	Φ (Vt+PS)
901	-2.4 ± 0.4	-1.2 ± 0.4
922	-2.3 ± 0.4	-1.4 ± 0.4
950	-1.8 ± 0.4	0.9 ± 0.4
957	-1.1 ± 0.4	0.4 ± 0.4
984	-2.2 ± 0.4	-0.9 ± 0.4
1033	-1.9 ± 0.4	-0.2 ± 0.4
1062	-1.9 ± 0.4	0.3 ± 0.4
1067	-1.8 ± 0.4	-0.2 ± 0.4

Table 5.5: Table containing the results obtained from accessibility measurements (Φ) in presence (Vt+PS) and absence (Vt) of PS-lipids.

This conclusion is also in line with mobility measurement results. The higher mobility observed for Vt950R1PS compared to position 957 could again be explained by the higher mobility of the helical end. Moreover, the topology regions in figure 5.17 are determined in terms of tertiary contact with protein atoms. Here, the contact might be governed by interaction with phospholipid atoms, which most likely reveal a higher mobility than secondary/tertiary structure elements of proteins. Especially in the immersion depth range discussed here, phospholipid fatty acid chains exhibit a considerable depth depending mobility (the deeper within the membrane the higher the mobility), which also could be shown by EPR measurements (data not shown, see also [48]).

The results for Vt901R1PS (H1), Vt922R1PS (H2), Vt984R1PS (H4) and Vt1033R1PS (H5) clearly indicate that these positions are located in close vicinity to the lipid head groups, leading to the assumption that helices H1, H2, H4 and H5 do also not penetrate the membrane, but lie on its surface. The reduced accessibilities for all investigated positions in the presence of lipids could then be explained, if the respective helices slightly immerse into lipid head group region and displace them marginally. Thus, in case of Vt901R1PS, Vt922R1PS, Vt984R1PS and Vt1033R1PS the spin label side chains would be located close

to the lipid head groups. Additionally, the slight deviation between the R1 side chain length (0.65 nm) and the penetration depth for Vt950R1PS and Vt957R1PS (0.7 - 1.0 nm) could be explained by this fact. Taken together, the Φ values obtained for each position are similar or smaller than that of SA5PS, leading to the assumption that a bilayer penetration of the entire helices can be excluded. An association of all helices to the lipid membrane surface requires a conformational change within Vt in presence of lipids, since a simultaneous association of all investigated positions would not be possible if the helical bundle is preserved.
In the helical bundle structure the hydrophobic faces of the amphipatic helices are oriented towards the protein interior. An acidic lipid induced conformational change, such as the bundle opening proposed here, could lead to an alignment of the respective helices, in which the hydrophobic parts interact with the lipid bilayer surface. Since the polar lipid head groups are hydrophilic, a slight immersion into the lipid head group region is assumed, which in turn facilitates the convergence of hydrophobic helix parts to the apolar fatty acid region of the lipid molecules. This kind of arrangement would also be energetically more favorable than the case, in which hydrophobic helical parts interact with either the polar head group region or the bulk water phase.
Furthermore, this conformational change might be triggered by the interaction of the positively charged *basic ladder* (H3), the hydrophobic hairpin (C-terminal residues 1062-1066) and the *basic collar* (including amino acids 910, 911, 1049, 1060, and 1061, see figure 2.4) with the acidic lipid head groups (predominantly negatively charged) as already proposed by [7, 6]. Evidence for the hydrophobic hairpin being involved in this pathway, is given by the clear increase of Φ for Vt1062R1PS and Vt1067R1PS upon addition of lipids. A possible explanation might be that parts of the C-terminal end of Vt binds to the membrane surface. This is in agreement with the assumptions made by Bakolitsa et al. [7, 6] that, beside others, the hydrophobic hairpin mediate the first contact to the lipid membrane.

5.2.2.3 Polarity measurements

In accordance with the accessibility measurement results, the hyperfine coupling tensor element A_{zz} is decreased upon addition of PS-lipids for each investigated position (figure 5.20 and table 5.6) by about 0.1 mT, indicating a polarity change of the respective R1 side chain environment due to the presence of a lipid membrane. These results support the above discussed possibility of an association of the particular helices on the membrane surface and a slight immersion into the lipid head regions.
Compared to the slightly smaller A_{zz} value found for SA5PS the results for

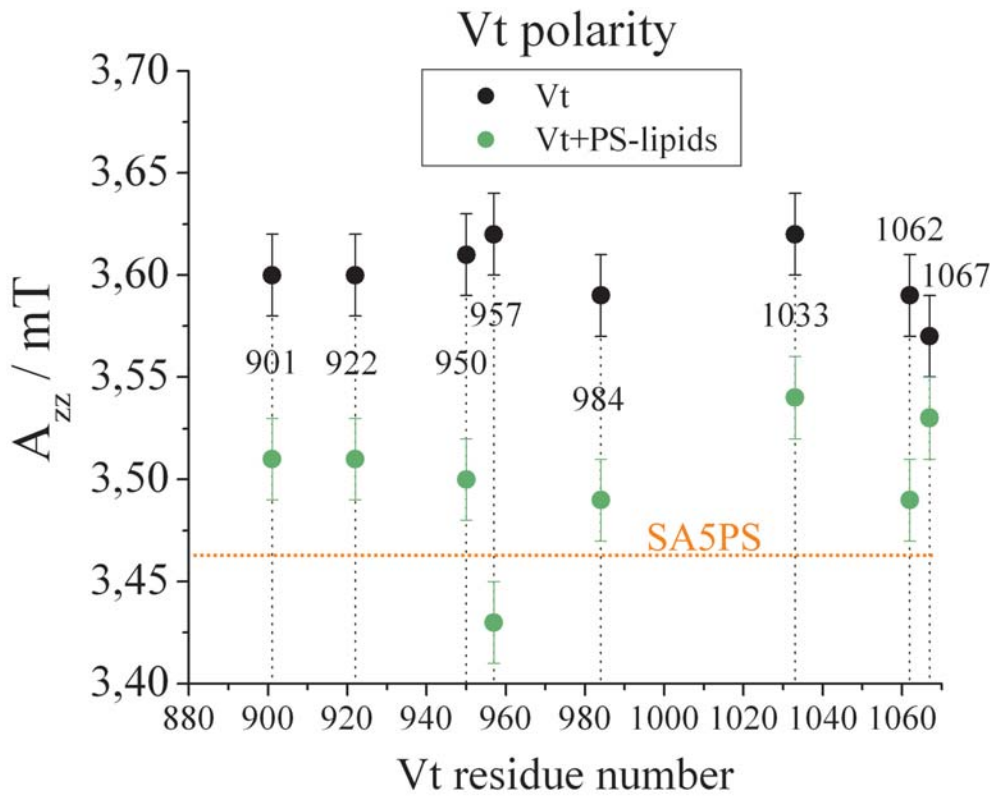

Figure 5.20: a): Hyperfine coupling tensor elements A_{zz} determined by polarity measurements for Vt (black) and Vt in presence of PS-lipids (green). The A_{zz} value obtained for SA5PS is drawn for comparison (orange dotted line).

Vt901R1PS, Vt922R1PS, Vt984R1PS, Vt1033R1PS, Vt1062R1PS, Vt1067R1-PS are in agreement with accessibility measurement results, namely that these positions are located in closer vicinity to the lipid head groups than SA5PS. Since the A_{zz} values for the investigated labeled positions resemble that of SA5PS, and the expected A_{zz} value for a membrane center located site is close to 3.22 mT (SA16PS, see above), this supports the proposition that the corresponding helices are associated to the lipid bilayer surface and do not penetrate the whole bilayer.

Unexpectedly, for position 950, which reveals a comparable or slightly larger immersion depth than Vt957R1PS, a higher polarity compared to 957 is observed. This could be explained by the fact that the accessibility of the quencher molecules to Vt950R1PS might be shielded by helical parts situated between R1 (pointing into the lipid bilayer direction) and the bulk water. This situation could affect the corresponding Φ value, leading to the impression of a slightly deeper immersion depth than actually present. However, the A_{zz} value in case of

Vt957R1PS (3.43 mT) is smaller compared to that of SA5PS (A_{zz} = 34.6 mT) and all other positions, indicating a deeper immersion depth for Vt957R1PS with respect to SA5PS. This is in agreement with the results found by accessibility measurements, leading to the assumption that R1 at position 957 (H3) is located deeper within the PS-lipid membrane compared to other investigated cases, indicating also here that H3 might be associated to the lipid membrane in a way that residue 957 is pointing into the direction of the lipid bilayer center. In summary, the polarity measurement results suggest an association of Vt to the lipid vesicle surface and are in line with the accessibility results.

labeled position	A_{zz} / mT (Vt)	A_{zz} / mT (Vt+PS)
901	3.60 ± 0.02	3.51 ± 0.02
922	3.60 ± 0.02	3.51 ± 0.02
950	3.61 ± 0.02	3.5 ± 0.02
957	3.62 ± 0.02	3.43 ± 0.02
984	3.59 ± 0.02	3.49 ± 0.02
1033	3.62 ± 0.02	3.54 ± 0.02
1062	3.59 ± 0.02	3.49 ± 0.02
1067	3.57 ± 0.02	3.53 ± 0.02

Table 5.6: Table containing the results obtained from polarity measurements (A_{zz}) for Vt in absence (Vt) and presence of PS-lipids (Vt+PS).

5.2.3 Distance determination

In order to trace the assumed acidic lipid induced conformational change within Vt, distance measurements with doubly labeled Vt constructs were carried out using *cw*-EPR and pulsed EPR (DEER) techniques. Additionally, to investigate the proposed dimerization and/or higher oligomerization of Vt distance measurements were performed on singly labeled Vt in the presence of acidic lipids.

5.2.3.1 Singly labeled Vt

DEER dipolar evolution functions obtained for singly labeled Vt in presence of PS are presented in figure 5.23 (left). In each case dipolar modulations are detected, clearly indicating a dimerization (or higher oligomerization) of Vt in presence of PS-lipids. The modulations depth are equal or higher compared to Vt in aqueous solution, indicating that a similar (10% - 30%, see above) or slightly higher dimer fraction is bound to lipids. The corresponding distance

distributions are shown in figure 5.23 (right). Contributions below 2 nm are treated as artifacts, since *cw*-EPR results show no indication for distances below 2 nm (data not shown). Contributions above 3.0 nm or 3.5 nm, respectively, are most likely present, but can not be judged in more detail due to the limited dipolar evolution times. Moreover, these contributions could be artifacts arising from uncertainties in the background corrections of the DEER spectra, which in turn also result from the limited evolution times.
The distance distribution for Vt1067R1PS reveals a dominating peak at 2.5 nm, thus, a preferred inter molecular distance might exist in this case. However, distances covering the whole detectable range are present, indicating on the one side a high flexibility of Vt1067R1PS and on the other side that the C-terminal ends of Vt after lipid binding are still eminently disordered. This is also and even better reflected by the distribution obtained for Vt1062R1PS.
The distribution obtained for Vt901R1PS reveals a dominating contribution at r = 2.1 nm, and is similar to the value obtained for Vt901R1 in the absence of lipids (r = 2.3 nm), indicating that the dimerization interface involving helix H1 might be maintained after membrane association. The peak at 3 nm is assigned to the not reliable distance range, due to the above mentioned reasons.
However, assuming that only Vt dimers contribute to the distance distributions the dimer structure determined for Vt in solution is not preserved, since most of the dipolar evolution functions and the resulting distance distributions differ significantly between the two preparations. This applies especially for the helix attached sites Vt922R1PS, Vt950R1PS and Vt957R1PS, revealing (in contrast to the lipid absence case) clear distance contributions in the range between 2 and 3 nm. This clearly refers to a conformational change within Vt. Furthermore, also Vt984R1PS and Vt1033R1PS show broader distance distributions in the presence of PS-lipids, indicating a conformational change as well.
In case of Vt950R1PS, Vt957R1PS and Vt984R1PS preferred average inter spin distances might be 2.4 nm, 2.3 nm and 2.2 nm, respectively, whereas the distributions revealed by Vt922R1PS, Vt1033R1PS, Vt1062R1PS and Vt1067R1PS cover the whole detectable range with similar intensities.
All distance distributions are remarkably broad. This should result from a higher R1 mobility due to helical rearrangements after lipid surface association of Vt, in line with mobility measurements. In addition, an orientational distribution of both, the mutual alignment of two dimer forming Vt molecules associated to the membrane and mutual helix alignments within a single molecule with respect to each other, might contribute to the distance distribution widths. This leads to two possible conclusions. First, the helical bundle is completely released and the tertiary structure of Vt is abolished, enabling the convergence of equivalent parts of two Vt molecules to each other in a parallel manner, leading to distances in the range of 2-3 nm in each case. Or, second, the con-

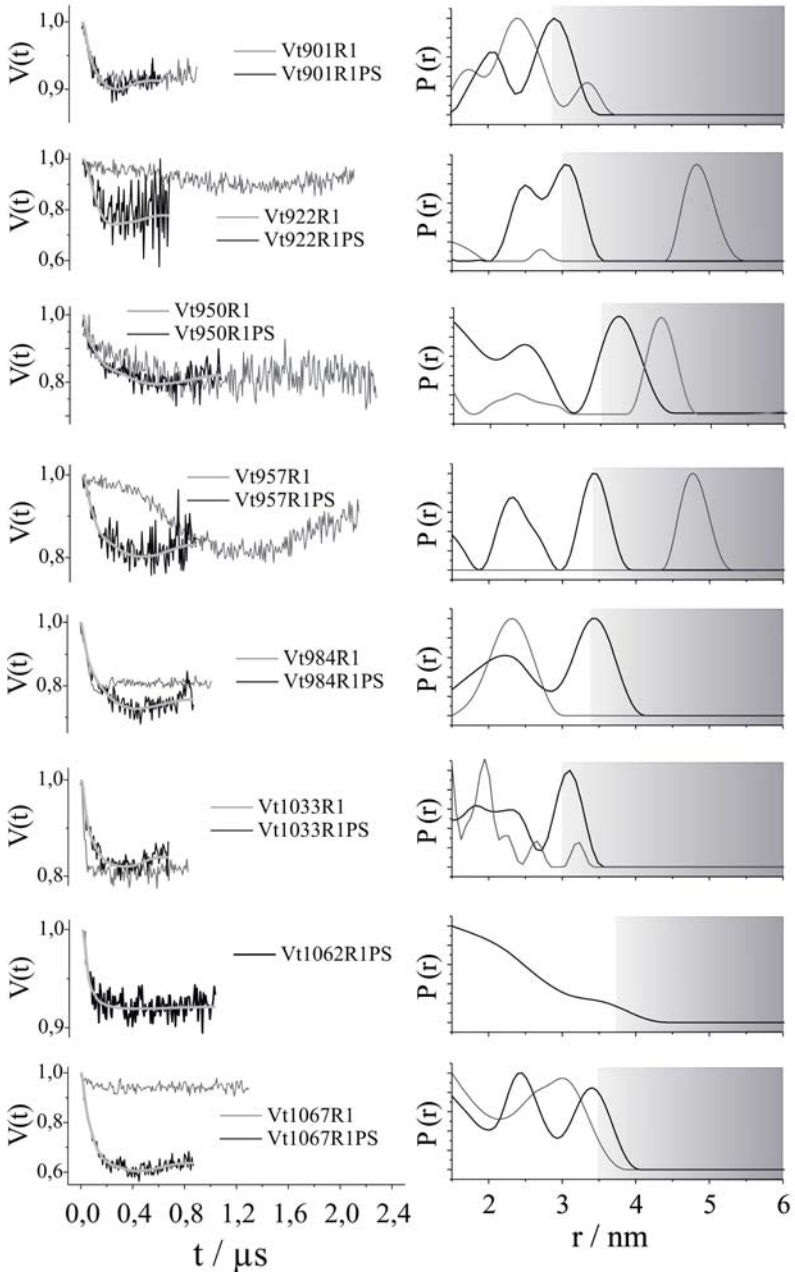

Figure 5.21: DEER spectroscopy results of Vt single mutants in presence of PS-lipids. Left: Dipolar evolution functions are shown as black lines and the corresponding fits calculated with DEERAnalysis are indicated as gray lines. The data is overlaid with the results obtained for Vt in absence of PS (gray noisy traces). Right: Resulting DEER distance distributions of Vt in presence of PS (black) overlaid with the distributions obtained for Vt in absence of PS (gray lines). The gray area represents the range of not reliable distances due to the short dipolar evolution times used in the experiments in case of Vt+PS.

formational change of Vt leads to an unmasking of additional putative binding sites, enabling the formation of higher oligomers, in which equivalent helical parts of the involved Vt molecules can come closer to each other, but do not deceed distances of 2.0 nm. It has to be mentioned that in each case indications for distance contributions larger than 3.5 nm do exist, which could be caused due to the formation of higher oligomers.
Based on the results presented here, it is not possible to determine the degree of oligomerization, especially to distinguish between Vt dimers or higher oligomers. However, the data unambiguously indicate the association of at least two Vt molecules.

5.2.3.2 Doubly labeled Vt

Cw-EPR spectra detected for the investigated doubly labeled Vt mutants exhibit no significant dipolar broadening (figure 5.22).

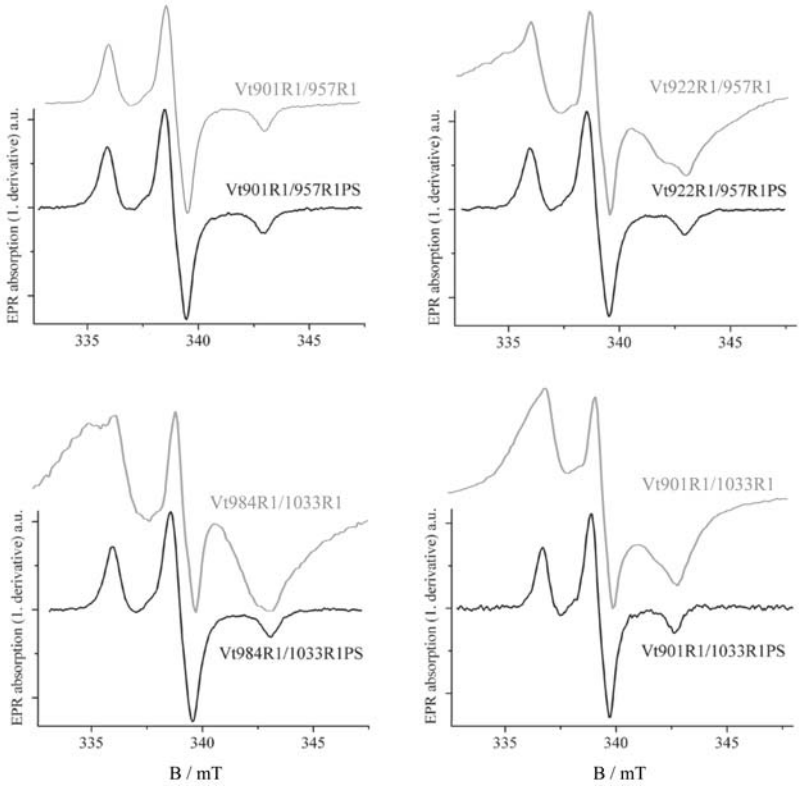

Figure 5.22: Low temperature *cw*-EPR spectra of the four investigated doubly labeled Vt variants in the presence (black) and in the absence (gray) of PS-lipid vesicles are shown. In the presence of lipids no line broadening due to dipolar interaction could be observed, indicating inter spin distances above 2 nm.

Compared to Vt901R1/957R1 in absence of acidic lipids (r = 2.65 nm) no conformational change can be traced in the presence of lipids using low temperature

cw-EPR. In contrast, the intense line broadening reflecting very small distances, present in the low temperature spectra of Vt901R1/1033R1, Vt922R1/957R1 and Vt984R1/1033R1 vanishes in presence of PS-lipids. Thus, in each case the intra molecular distances increase from below 1 nm to above 2 nm, indicating a considerable acidic lipid induced conformational change within the Vt structure, in which all helices might be involved. Furthermore, it can be extracted that the fraction of unbound Vt is insignificant small, since a small contribution of the spectra obtained for Vt901R1/1033R1, Vt922R1/957R1 and Vt984R1/1033R1, exhibiting a huge line broadening in absence of lipids, would considerably effect the overall EPR spectra shape. Moreover, the fraction of intermediate structural stages of the binding process eventually frozen during sample preparations is assumed to be small.
In order to gain more detailed informations about the respective distances DEER measurements were performed on doubly labeled Vt in presence of PS-lipids.
The results are shown in figure 5.23. *Cw*-EPR distance measurements have shown that the intra molecular distances of Vt901R1/957R1PS, Vt901R1/1033-R1PS, Vt922R1/957R1PS and Vt984R1/1033R1PS are beyond 2 nm (see above), thus contributions below 2 nm can be attributed to noise close to t = 0 μs. For dimeric doubly labeled molecules also inter molecular distances are in general detectable. These distances contribute to the signal obtained for doubly labeled Vt. Thus, the determined distance distributions contain intra molecular as well as all combinations of inter molecular distances. In order to illustrate where the inter molecular distances at least between equivalent residues are expected to be located within the distance distributions, the corresponding results of singly labeled Vt are overlaid with the results obtained for Vt double mutants (see figure 5.23 (right)).
In each case broad distance distributions covering a range between 2 nm - 3.5 nm or larger are obtained. In case of Vt922R1/957R1PS (H2/H3) two dominating contributions at ca. 2 nm and 2.6 nm can be observed. These contributions are less dominant in the distributions obtained for singly labeled Vt. This means, considering a Vt dimer that these contributions arise from intra molecular distances or inter molecular distances between R1 combinations, involving non-equivalent positions of two Vt molecules (e.g. 922R1 of Vt molecule one and 957R1 of Vt molecule two and vice versa). In the latter case, these combinations would contribute with the same magnitude as those from equivalent combinations, except for the very unlikely case that all distances are equal. However, even in such a case the intra molecular distances dominate, since not all molecules in the sample are supposed to oligomerize (10% - 30% of the Vt molecules, see 5.2.3.1). Moreover, the significant increase in modulation depth in each case (from $\approx$ 0.2 (single mutants) up to $\approx$ 0.5 (double mutants)), com-

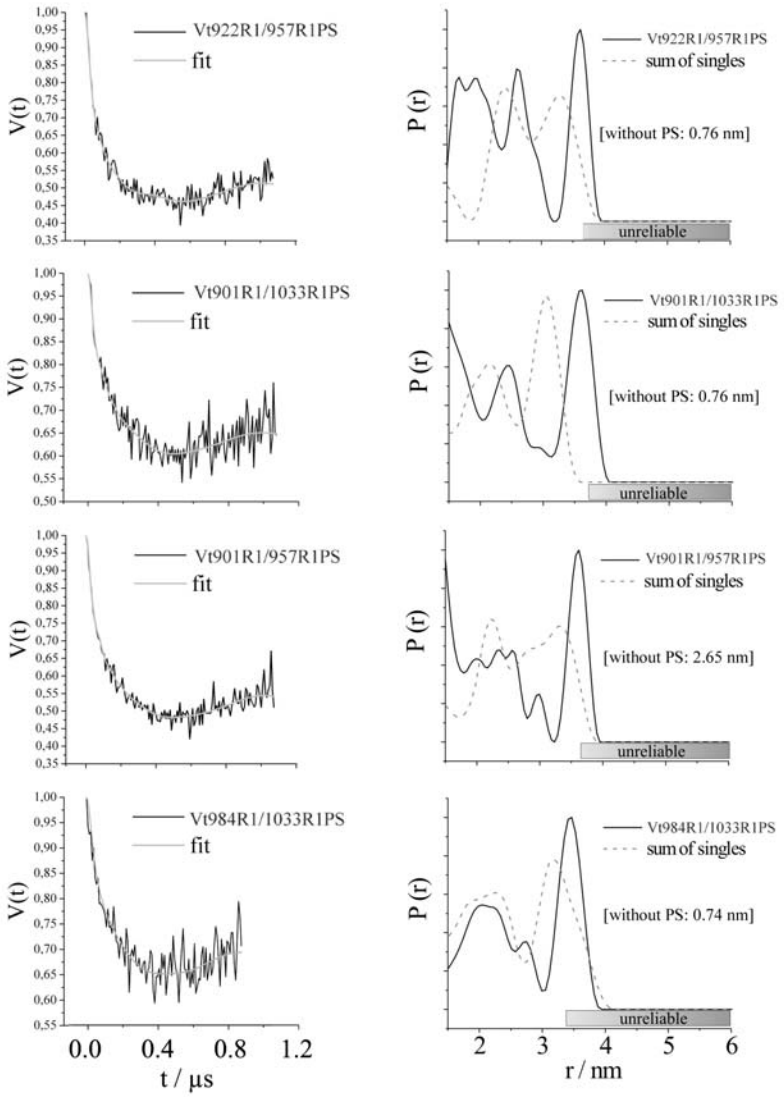

Figure 5.23: DEER spectroscopy results of Vt double mutants in presence of PS-lipids. Left: Dipolar evolution functions (black lines) are overlaid with the corresponding fits calculated with DEERAnalysis (gray lines). Right: Resulting DEER distance distributions of Vt double mutants (black) are overlaid with the corresponding results obtained for singly labeled Vt contributing to the here discussed DEER traces. The gray dashed lines are the normalized and summed distance distributions of singly labeled Vt. The gray bars represent the area of not reliable distances due to the limited dipolar evolution times. Well defined mean distances obtained for Vt in solution (in the absence of PS-lipids) are given in brackets for comparison.

pared to the results obtained for Vt single mutants, indicates that the distance distributions are dominated by intra molecular distances.
For Vt922R1/957R1PS the presence of small distances around 2 nm is obvious,

but the extent is indefinable, since additional contributions to this peak can also arise from the spectral fit of noise features as mentioned above. Thus, the dominant peak close to 2 nm has to be treated with caution. The peak at 2.6 nm is assumed to be an intra molecular distance between the R1 chains attached to helices H2 and H3. Moreover, intra molecular contributions of distances larger than 3.5 nm are most likely present as well, indicating that more than one favored mutual alignment between H2 and H3 might exist. Both facts indicate a separation of H2 and H3 after Vt lipid association. Beside this, the obtained distance distributions show distances distributed over the complete detectable range. Both, higher R1 mobilities due to helical rearrangements after lipid binding and a distribution of the H2 and H3 orientation with respect to each other might contribute to the large distribution width. Additionally, minor contributions of inter molecular distances are assuredly present.
Within the detectable range of 2 nm - ca. 3.5 nm Vt901R1/1033R1PS (H1/H5) reveals a broad distribution with a dominant peak centered at ca. 2.4 nm. Due to the fact that the distribution maxima obtained by the sum of corresponding singly labeled mutants does not coincide with this peak, no significant contributions from equivalent or non-equivalent inter molecular distances to this peak are expected, meaning that the contribution at 2.4 nm in case of the double mutant is most likely an intra molecular distance. Also here, indications for distances larger that 3.5 nm do exist. These findings imply on one side a separation of H1 and H5 and on the other side a bi- or multimodal situation as well. The large distance width might originate from the same reasons as discussed for Vt922R1/957R1PS.
Considering the mentioned results for Vt901R1/1033R1PS and Vt922R1/957R1-PS, it can be inferred that helix H1 separates from H5 and helix H2 from H3, leading to the assumption that the bundle part H1/H2 separates from the rest of the bundle (H3/H4/H5). This would in turn affect the distance between H1 and H3. This is supported by the results obtained for Vt901R1/957R1PS (H1/H3). In contrast to the lipid absent case, in which a well defined distance at 2.65 nm is obtained, Vt901R1/957R1PS (H1/H3) reveals a very broad distance distribution covering the range between 2 and 3.5 nm. This indicates that the structural change of Vt in presence of PS-lipids affects the helical arrangement of H1 and H3 and is in line with the above made assumption.
In case of Vt984R1/1033R1PS a very broad peak exhibiting a maximum at ca. 2.2 nm is obtained. The distribution shape is similar to the distribution obtained from the sum of the results for corresponding singly labeled Vt, leading to the impression that the obtained distribution results only from inter molecular distances, and that the intra molecular distances is beyond 3.5 nm. However, the significantly increased modulation compared to the case of the singly labeled Vt indicates that the DEER traces are dominated by intra molecular distances.

Thus, the intra molecular distances are, at least partly, between 2 and 3.5 nm. Consequently, a separation of position 984 (H4) and 1033 (H5) up to at least 2.2 nm takes place in the presence of lipids.

Taken together, the proposed opening of the helix bundle is further supported by these results. The well defined intra molecular distances of doubly labeled Vt in the absence of lipids are converted into broad distributions after addition of PS-lipids, indicating that a defined helix-helix contact does not exist anymore. Furthermore, the results show that a significant conformational change takes place in Vt in which H1/H2 is assumed to separate from H3/H4/H5. A further separation of H5 from H3/H4 is supposed. The respective separated helices exhibit most likely orientational distributions rather than defined orientations, with respect to each other. Moreover, the indications for intra molecular distances beyond 3.5 nm observed in all cases lead to the assumption that Vt exists in more than one conformational state.

5.2.4 Molecular model of Vt bound to PS-lipids

The above discussed results of *cw*-EPR and pulsed EPR measurements on singly and doubly labeled Vt were used for the construction of a molecular model [5] of Vt bound to acidic PS-lipids (schematically shown in figure 5.24). Accessibility and polarity measurements show that all investigated positions interact with the lipid membrane surface. This is only possible if all helices are associated to the lipid membrane, where the hydrophobic parts of the respective helices point into the direction of the lipid bilayer. Consequently, Vt has to undergo a significant structural change, since in the case of a preserved helix bundle only specific sites would be able to contact the vesicle membrane. Distance measurements on Vt double mutants reveal a separation of the helix bundle away H1/H2 from H3/H4/H5. Furthermore, indications for a movement of H5 apart from H4 exist. The conformational change is assumed to be an opening of the bundle at the side of the N-terminal strap and the C-terminal end domain of Vt (figure 5.24 a). In this way, the domains H1/H2, H3/H4 and H5 are able to separate directly from each other. This is in line with the propositions made by [7, 6] that the hydrophobic hairpin and the *basic collar* of Vt regulate the first contact to the lipid membrane.

[5] The model was constructed using the Vt crystal structure and the molecular modeling tool YASARA. Loops were deleted and rebuild after helix alignment. R1 side chains were connected to the investigated positions and reoriented by changing dihedral angles corresponding to allowed rotations around linker atom bonds.

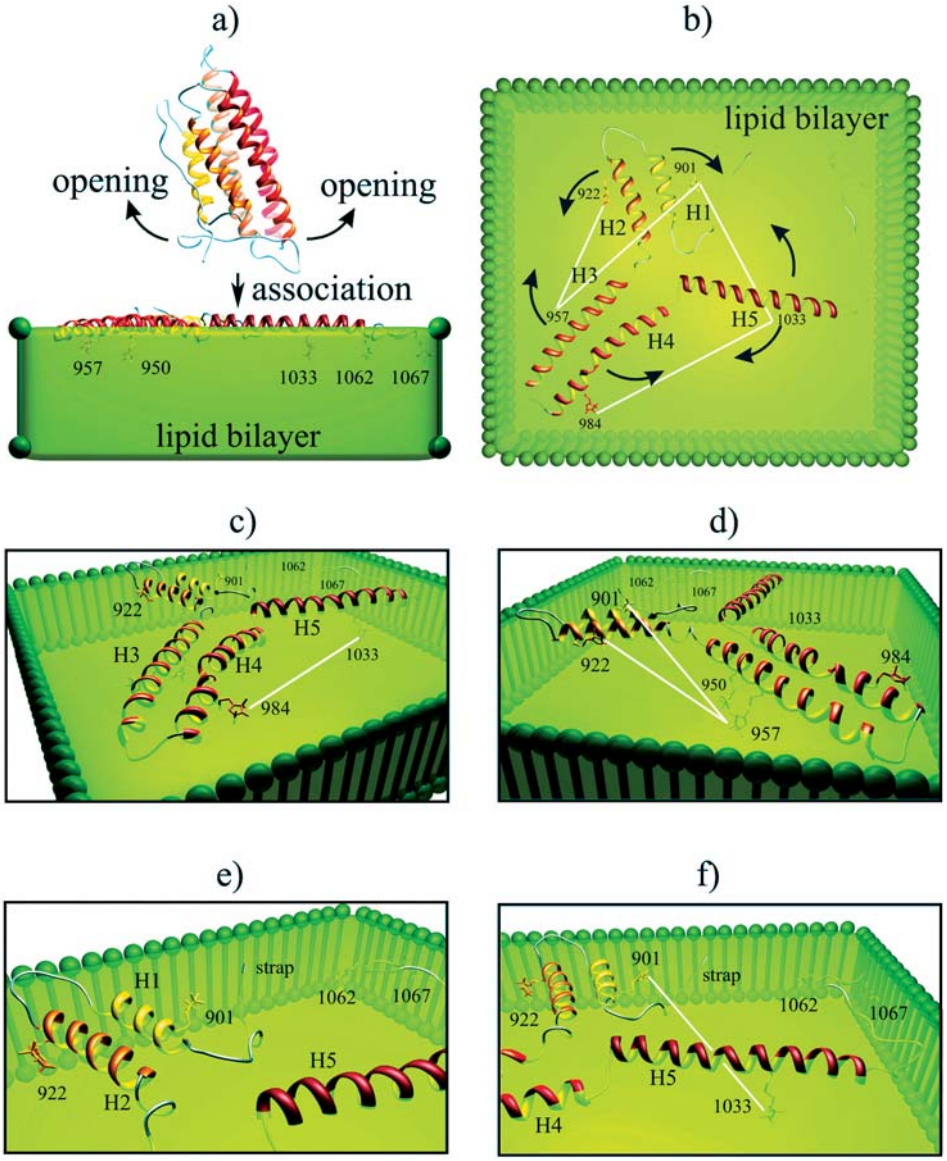

Figure 5.24: Molecular model of Vt bound to a PS-lipid membrane. An opening of the Vt helix bundle at the side of the N-terminal strap and the C-terminal end domain of Vt and a subsequent association to the lipid bilayer (green) is assumed (a). b): Average structure of possible Vt conformations. The bundle parts H1/H2 (yellow/orange), H3/H4 (light red/red)) and H5 (dark red) are supposed to separate. The respective separated domains exhibit an orientational distributions with respect to each other (black arrows). Favored conformational states of Vt might exist in which corresponding helices are associated weakly in the respective extreme cases regarding the assumed orientational distributions. Hydrophobic helix sides point towards the lipid bilayer center. Orientations of R1 side chains and locations of nitroxide groups with respect to the lipid bilayer are consistent with accessibility measurement results (c-f). Measured interspin distances are indicated (white lines).

The broad and/or bi/multimodal distribution obtained from DEER measurements on doubly labeled Vt do not allow exact determinations of defined intra molecular distances, but indicate in all cases distances within the range between 2.0 nm - 3.5 nm and probably larger distances. Consequently, orientational distributions between the respective separated helices, and high flexibilities of the attached R1 side chains can be assumed. The high R1 mobilities, most likely resulting from the helix separation, could also be traced by EPR mobility measurements. The orientational distribution might arise from rotations of the respective separated bundle parts around the center of the associated Vt molecule (see figure 5.24 b), indicated by black arrows). It has to be mentioned that the structure shown in the figure exhibit intra molecular distances beyond 3.5 nm and has to be interpreted as an average structure. The assumed orientational distribution of the separate domains can lead to conformations, in which the distances between R1 chains attached to H1-H5, H4-H5, H2-H3 or H1-H5, respectively, reach values located within and covering the distance range detectable in the DEER experiments, leading to the observed broad distance distributions. However, the bimodal distributions obtained for Vt901R1/1033R1PS (H1/H5) and Vt922R1/957R1PS (H2/H3) suggest that different preferred conformations of Vt are frozen in the experiment, in which either the bundle part H1/H2 is close to or weakly associated to H3/H4 or to H5, leading to the dominating distances present in the corresponding distributions. Moreover, conformational states in which H5 is associated to H3/H4 are supposed, since dominating contributions around 2.2 nm are present in the distance distribution obtained for Vt984R1/1033R1PS.

It has to be mentioned that no information about the alignment between H1 and H2 could be obtained from the Vt variants investigated here, thus a separation of H1 and H2 can not be excluded. This might lead to an additional orientational distributions between H1 and H2, contributing to the corresponding distances to H3 and H5, respectively. A separation of H4 and H3 can also not be excluded, but is very unlikely, since H4 and H3 are connected *via* a very short and inflexible loop consisting of three amino acids (CYS972, THR973 and ASP974).

Furthermore, the results obtained from accessibility and polarity measurements suggest that Vt950R1, Vt957R1, Vt1033R1, Vt1062R1 and Vt1067R1 exhibit contact to phospholipid fatty acid chains, but are located closer to the lipid head groups than to the lipid membrane center. The results for Vt901R1, Vt922R1 and Vt984R1 on the other hand indicate that the attached R1 chains are located near the lipid head groups. These findings are also consistent with the proposed structural model shown in 5.24 (a-f). In addition, in the case of the above made assumption of a partially helix association (extreme cases of the assumed orientational distributions of helices), the proposed alignments of

the respective R1 side chains do not lead to intra molecular distances below 2 nm, which is in agreement with the results obtained from *cw*-EPR, where no indications for distances below 2 nm were found.

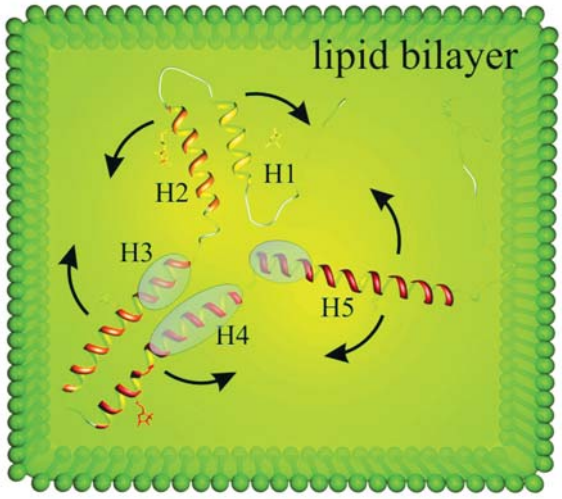

Figure 5.25: Molecular model of Vt bound to an acidic lipid membrane (top view). Approximate D1 binding sites are schematically shown by grey ovals and were extracted from figure 2.6.

The presented model describes the structural alignment of Vt in presence of acidic lipid membranes. In nature, membrane associated Vt must be released from the membrane bound state in order to provide the possibility for Vt to fulfill its function in cell migration, such as a subsequent actin binding. The vinculin head domain is assumed to play an important role in the release process, since, according to the full length vinculin crystal structure, Vt is masked by several head domains (D1-D3), where D1 provides most of the Vt binding sites (see section 2.2 and 2.2.2.2). Thus, one possibility for the Vt release may be the interaction between D1 and Vt. In figure 5.25 the approximate Vt-D1 interaction regions according to the vinculin crystal structure are indicated. It can be clearly seen that these regions are located in the center of the model presented here. A binding of D1 to the regions highlighted in figure 5.25, accompanied by an application of a pulling force acting on the middle of the membrane bound molecule could in turn lead to a release of Vt from the membrane, followed by a reformation of the antiparallel helical bundle. This process might furthermore lead to a vinculin head bound inactivated state, which after reactivation is then again competent for ligand binding. Mohl et al. have shown that Y1065 phosphorylation of Vt enhances vinculin exchange in focal adhesions, which might support this process [49].

5.3 Structure of Vinculin Tail bound to F-actin

In cell migration, adhesion protein complexes link the cell cytoskeleton (consisting, among other components of actin filaments) with the substrate. Vinculin creates a linkage between these adhesion protein complexes and the actin filaments, stabilizing the focal contacts by binding *via* its head domain to talin and its tail domain to actin. The binding of Vt to filamentous actin (F-actin) promotes Vt dimerization and thereby actin cross-linking [82]. Conformational changes are supposed for Vt upon F-actin binding [7, 33], but detailed information regarding the structural rearrangement of Vt are still missing. Here, various EPR methods, such as mobility, polarity and inter spin distance determinations, are applied on Vt bound to actin filaments. *Cw*- and pulsed EPR techniques were used in order to trace the conformational changes within Vt. The results, enabling the construction of a new molecular model of the actin bound Vt dimer, are presented and discussed in the following chapters. Sample preparations, measurement and data analysis procedures are described in chapter 4.

5.3.1 Mobility measurements

Cw-EPR room temperature spectra of the investigated singly labeled Vt constructs in presence of actin and the corresponding mobility parameters, overlaid with the reference data of Vt in solution containing of 40 % sucrose, are presented in figure 5.26. In all cases, except for Vt901R1A and Vt1062R1A, an immobilization of the respective R1 side chain is revealed. A small contribution to the observed immobilization, affecting all positions in a similar manner, is to be expected by the prevented protein tumbling motion of Vt after binding to the comparable large actin filaments. However, this effect is assumed to be small, since 40% sucrose was present in the solutions, used in the absence of actin, which increases the rotation correlation time of the reorientational motion of Vt [4]. Thus, especially the minor R1 immobilization observed for helix attached sites Vt922R1A, Vt957R1, Vt1033R1A, Vt1067R1A, and most likely the decrease of inverse linewidth for Vt1062R1A, might be caused by this fact. However, the changes observed for Vt901R1A, Vt950R1A and Vt984R1A are considerable, indicating structural changes within the respective R1 side chains vicinities.
Vt901R1A reveals a significant R1 mobilization after actin binding. Moreover, the mobility plot shown in figure 5.26 suggest that Vt901R1A is located at a loop/surface region, indicating that Vt901R1A does not exhibit contacts to tertiary or secondary structure elements anymore. This result could be explained by a separation of H1 and H5. A subsequent higher mobility of helix H1 might

contribute to the mobility of the R1 attached to Vt901R1A. A partially unfolding of H1 after Vt dimerization and actin binding can also not be excluded [42].

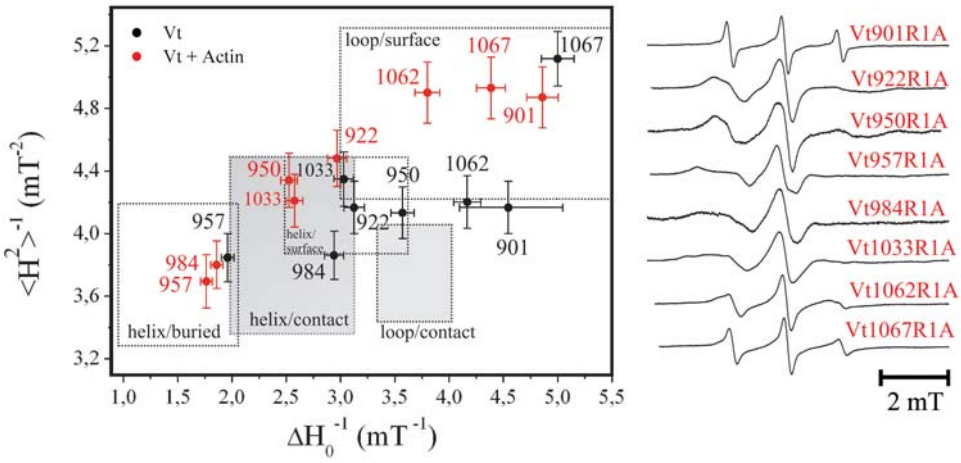

Figure 5.26: Mobility analysis of R1 side chains attached on Vt bound to F-actin. Left: Plot of the semi empirical mobility parameters $1/\langle H^2 \rangle$ versus $1/\Delta H_0$. The topological regions were drawn according to [47] and [13] (see figure 3.7). Results for Vt in presence of actin (red) are shown together with the results obtained for Vt in absence of ligands (black). Right: Cw-EPR room temperature spectra of the investigated singly labeled Vt variants bound to F-actin.

The immobile spectral component observed for Vt901R1 is significantly reduced in the presence of actin and a spectrum reflecting a very high R1 mobility is obtained (see figure 5.27). For Vt in the absence of ligands it was found that a small fraction of dimers (ca. 20 %) exists in the solution (see 5.1.5.1). The mobile component, present in the room temperature spectrum of Vt901R1, may arise from dimeric Vt, whereas the immobile component originates from monomeric Vt. The equilibrium between the structural conformtations (monomeric/dimeric Vt) might be shifted into the direction of the conformation corresponding to the mobile spectral feature (dimeric Vt) in the presence of actin. This is supported by the fact that the binding of Vt to F-actin promotes Vt dimerization, thus the percentage of Vt dimers in the presence of actin is assumed to be higher compared to Vt in the absence of ligands. Furthermore, this would mean that the structure of helix H1 is affected in the same manner after Vt dimerization leading to the assumption that the dimerization interface domain in the case of F-actin induced dimerization might be very similar compared to the interface found for Vt in solution, involving H1 (chapter 5.1.5.2).
Regarding the topology regions shown in the mobility plot, Vt950R1A is shifted into the region corresponding to helix/contact related sites, reflecting the im-

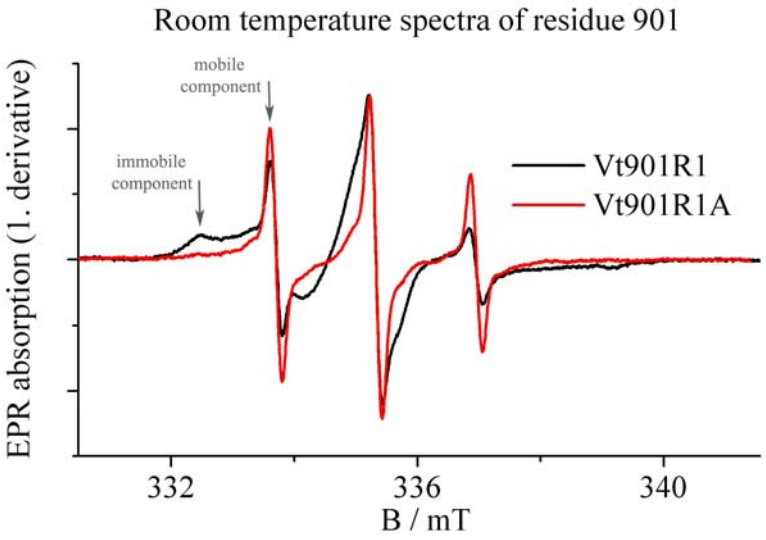

Figure 5.27: Room temperature spectra of Vt901R1 (black) and Vt901R1A (red). The immobile spectral component (low field peak) present in case of Vt901R1 is considerably reduced upon F-actin binding.

mobilization of the attached R1 upon actin binding. A slight immobilization was also observed for Vt957R1A, revealing the most immobile features compared to other positions, and indicating that the R1 attached to position 957 remains motionally highly restricted. Also, in case of Vt984R1A a significant immobilization can be observed. Compared to the actin absent case, in which the R1 side chain attached to position 984 is supposed to be a helix bound site exhibiting tertiary or secondary contacts, Vt984R1A clearly reveals features of a helix/buried site, similar to Vt957R1A. In case of Vt950R1A (H3), Vt984R1A (H4) and most likely also Vt957R1A the R1 immobilization might be caused by a combination of both, a stabilization of the corresponding helices after actin binding, and contacts to actin molecules. However, also a major structural rearrangement of these helices can not be excluded. Helix H3 is assumed to be mainly involved in actin binding by providing most of the binding sites (including residue 950) [33]. Thus, the R1 side chains attached to H3, especially Vt950R1A, as well as on the neighboring helices H2 (position 922) and H4 (position 984) might exhibit contacts to the ligand, decreasing the spatial freedom of the respective R1 and thus their mobility, as it could be observed for Vt984R1A. Actin binding sites are also proposed for the C-terminal end of H2 [33]. However, residue 922 is located at the N-terminal end of H2, thus the R1 side chain of Vt922R1A does not necessarily exhibit sterical contacts to actin. The insignificant change observed for Vt922R1A compared to vt922R1 supports this assumption.
The spectrum of Vt1033R1A shows features of slightly more immobilized R1

chains compared to the actin absent case. The change regarding the location within the corresponding topology plot is small, and the slight immobilization could be caused by the above mentioned effect of protein motional restriction after F-actin binding. For Vt1062R1A, the inverse second moment is significantly increased, reflecting a R1 mobilization, what indicates that parts of the C-terminal end of Vt might be affected by actin binding. Besides H3 and parts of H2, also the C-terminal end of Vt is assumed to be involved in actin binding (residues 1050-1056 [33]). Binding of these domains to actin could lead to a dissociation of the residual C-terminal domain from Vt including Vt1062R1A, consequently leading to a higher R1 mobility. However, the deviation between Vt1067R1A and Vt1067R1 is small, and the slight immobilization might also be explained by the reduced Vt tumbling motion after F-actin binding. The fact that the R1 on Vt1067R1A is still more mobile than that on Vt1062R1A leads to the conclusion that the structural nature of the environment of residue 1067 is largely preserved after Vt dimerization and actin binding.

5.3.2 Polarity measurements

Hyperfine tensor elements (A_{zz}) extracted from low temperature *cw*-EPR spectra of singly labeled Vt are shown in figure 5.28 and summarized in table 5.7. The data is overlaid with the results of Vt without binding partner. It has to be mentioned that a direct comparison of the values obtained for Vt in absence and presence of actin is not possible, since the polymerization buffer composition used for the measurements in presence of actin filaments differs from the buffer used for Vt reference measurements (see chapter 4). Additional ions and different ion concentrations, present in the buffer, most likely influence the electric field (E_x) around the nitroxide N-O bond of R1 (see also 3.3.3.1) and thus the overall polarity compared to the buffer used for Vt in solution.

Here, a slight shift (ca. 0.05 mT) to higher polarities can be observed, which might be due to this fact. Considering this shift, the behavior of the A_{zz} values (excluding Vt922R1A) of Vt bound to actin is similar to the actin absent case, indicating that the polarities of the micro-environment are unaffected by actin binding. The increase of the A_{zz} value observed for Vt922R1A indicates a slightly higher environmental polarity of this position. However, in general no significant shielding of respective R1 chains from the solvent by any actin or Vt domains is revealed, and all positions are assumed to be accessible to the solvent (bulk water).

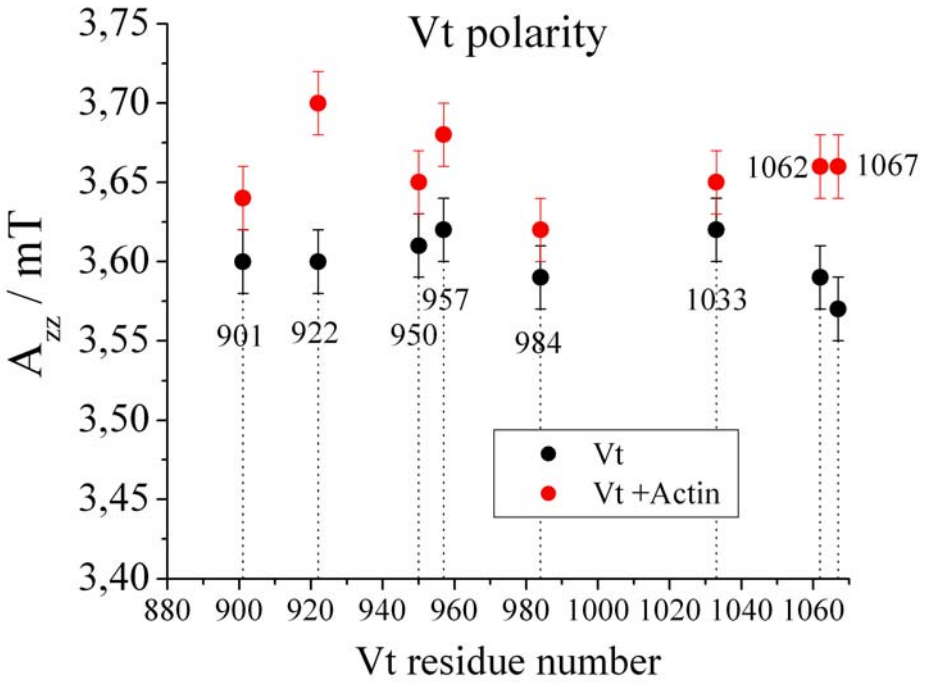

Figure 5.28: Hyperfine tensor elements (A_{zz}) extracted from low temperature *cw*-EPR spectra of singly labeled Vt bound to F-actin (red) overlaid with the data obtained from Vt in absence of actin (black). Due to the differing buffer compositions no direct comparison between Vt and Vt+A is possible. Values of Vt+A might be shifted by ca. 0.05 mT to larger A_{zz} values.

labeled position	A_{zz} /mT (Vt)	A_{zz} / mT (Vt+A)
901	3.60 ± 0.02	3.64 ± 0.02
922	3.60 ± 0.02	3.70 ± 0.02
950	3.61 ± 0.02	3.65 ± 0.02
957	3.62 ± 0.02	3.68 ± 0.02
984	3.59 ± 0.02	3.62 ± 0.02
1033	3.62 ± 0.02	3.65 ± 0.02
1062	3.59 ± 0.02	3.66 ± 0.02
1067	3.57 ± 0.02	3.66 ± 0.02

Table 5.7: Table containing the results obtained from polarity measurements (A_{zz}) for Vt in absence (Vt) and presence of F-actin (Vt+A).

5.3.3 Distance measurements

5.3.3.1 Cw-EPR distance measurements

Dipolar line broadening was not observed in the low temperature *cw*-EPR spectra (not shown) of the investigated singly labeled Vt constructs bound to actin. The *cw*-EPR spectra obtained for doubly labeled Vt mutants under investigations are shown in figure 5.29.

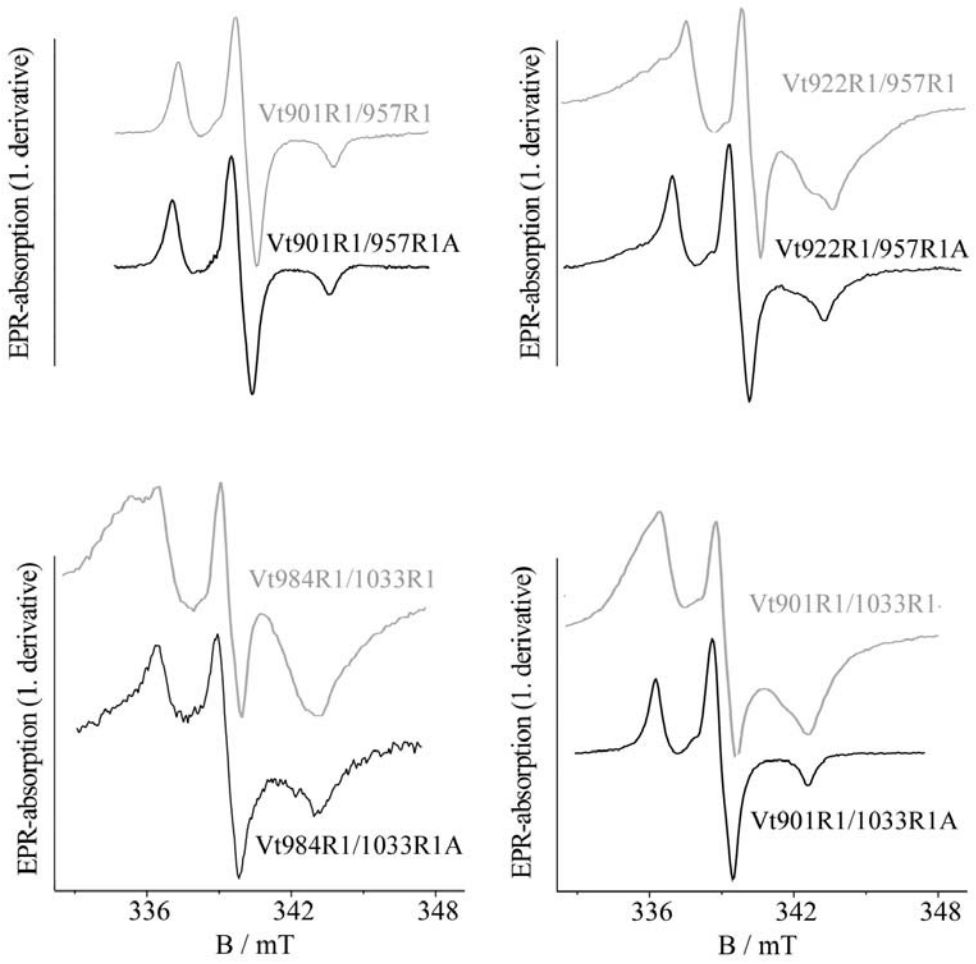

Figure 5.29: *Cw*-EPR spectra obtained for doubly labeled Vt bound to F-actin (black) are shown together with the results for Vt in the absence of actin (gray).

Considerable line broadening was observed for Vt922R1/957R1A and Vt984R1/1033R1A, as also obtained in the absence of actin for these cases. A higher fraction of non interacting spin labels (fitting reveals ca 30% singly labeled species) is present for Vt922R1/957R1A. This unbroadened spectral component can be traced back to a low spin labeling efficiency in this batch of double mutants. However, the presence of two different Vt conformations can not be

excluded. The spectral fits and distance distributions calculated with *Short Distances* are shown in figure 5.30. The spectral line shapes are well reflected by the simulations. The distance distributions obtained for Vt922R1/957R1A and Vt984R1/1033R1A reveal dominating peaks centered at 0.76 nm and 0.70 nm, respectively (summarized in table 5.9).

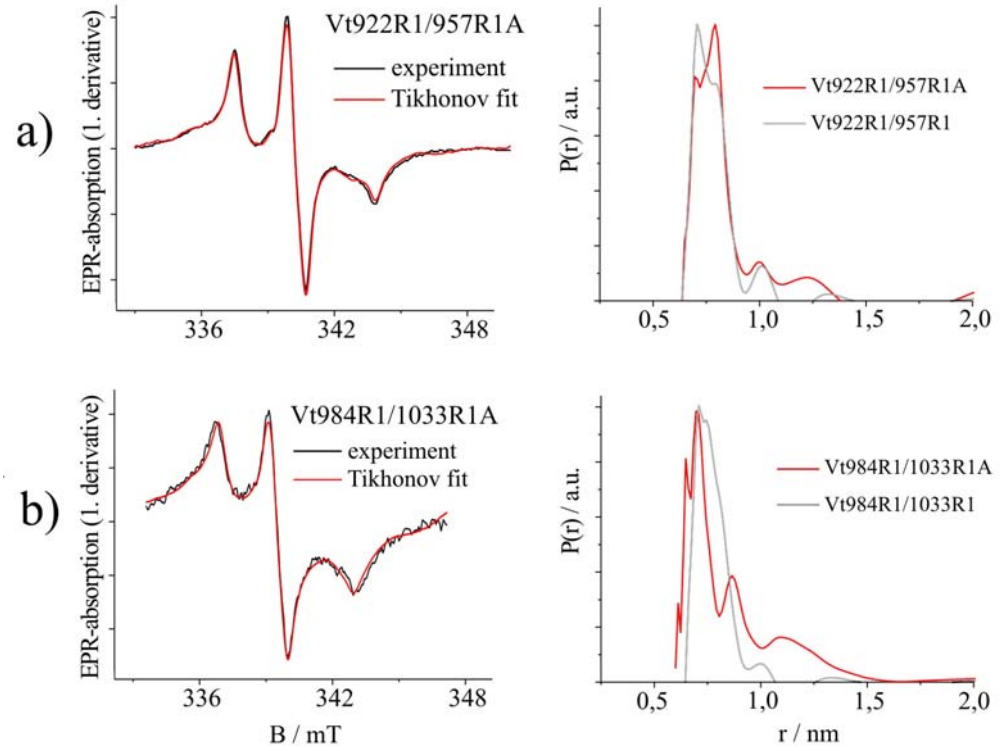

Figure 5.30: Experimental spectra (black), fits and distance distributions (red) calculated with *Short Distances* using Tikhonov regularization for Vt922R1/957R1A (a)) and Vt984R1/1033R1A (b)) are shown. Distance distributions are overlaid with the results obtained for corresponding doubly labeled Vt in aqueous solution (gray).

These values are similar to the distances obtained from measurements without F-actin (0.76 and 0.74 nm), leading to the conclusion that the helical arrangements H2/H3 and H4/H5 are largely preserved upon F-actin binding. Vt984R1/1033R1 in the presence of actin shows an additional contributions at ca. 1.1 nm in the distance distribution. A slight rearrangement of helix H4 and/or H5, or of R1 surrounding side chains, could lead to a situation, in which the respective R1 side chains exist in different rotameric conformations, leading to the observed contributions with different inter spin distances. Alternatively, Vt might exhibit two different conformations after dimerization, whereby the helical arrangement of H4/H5 in one Vt molecule differs slightly from the other Vt molecule within the dimer. However, indications for two different mobility components are not visible in the room temperature spectra of the correspond-

ing single mutants. Consequently, if two different conformations are present, the respective R1 side chains exhibit a similar restricted motional freedom. Furthermore, the contribution below 1 nm dominates, and the deviations between the particular components in terms of the inter spin distance are minor, indicating that the helical arrangement of H4/H5 in Vt bound to F-actin is similar to the structure of Vt in the absence of actin.
Vt901R1/957R1A does not reveal any dipolar broadening, indicating an inter spin distance beyond 2.0 nm (in absence of actin r = 2.65nm). The same applies to Vt901R1/1033R1A. In contrast, for Vt901R1/1033R1 (without actin) an extensive line broadening, yielding a distance of ca. 0.76 nm, was obtained. This result shows on the one hand that the fraction of unbound monomeric Vt is insignificantly small within the samples, supporting the above made conclusion that the line broadening in case of Vt922R1/957R1A does not arise from unbound Vt. On the other hand, the vanishing line broadening of Vt901/1033R1A indicates that a conformational change within Vt takes place upon F-actin binding, involving H1 and/or H5. Considering the result for Vt984R1/1033R1 (H4/H5), the separation of helices H1 and H5 takes place in a way that H1 moves away from the bundle part H4/H5 or vise versa. However, also the above made proposition of a partial unfolding of H1 could lead to the observed distance increase between R1 chains attached on residues 901 and 1033.

5.3.3.2 DEER distance measurements

DEER measurements on Vt bound to F-actin were performed in order to trace the conformational changes within dimeric Vt after F-actin binding. Measurements on Vt single mutants were carried out to determine inter molecular distances and are compared to the results obtained for Vt in absence of actin. Moreover, intra molecular distances beyond 2.0 nm which can not be detected with *cw*-EPR (Vt901R1/957R1A and Vt901R1/1033R1A) are determined. DEER measurements and data analysis were performed as described above.

Singly labeled Vt Dipolar evolution functions for singly labeled Vt bound to F-actin are shown in figure 5.31 (left panel) together with the resulting distance distributions (right panel). For Vt1062R1A and Vt1067R1A no traces with a sufficient signal to noise ratio could be obtained (data not shown). No dipolar oscillation was observed for Vt950R1A. Considering the applied dipolar evolution time of t=2.4 μs this indicates that the inter molecular distance has to be larger than 5 nm.
However, dipolar oscillations could be observed for the helix attached sites Vt901R1A, Vt922R1A, Vt957R1A, Vt984R1A and Vt1033R1A. For these cases

well defined distances are obtained. The modulation depths, reflecting the percentage of interacting spins and thus, the percentage of dimers, are similar to these of Vt in the absence of ligands. Since dimerization should be promoted by the presence of actin, a large modulation depth was expected. However, this could not be observed here. Possible reasons for this fact can, in general, be low label efficiencies or a small fraction of dimers present. In the latter case, single Vt molecules would be bound to the actin filaments as well, contributing only to the background signal. However, the dimerization of Vt upon actin binding could be observed.

The small contributions at shorter distances obtained for Vt901R1A, most likely arise from fits of noisy spectral features. A small fraction of unbound Vt dimers leading to these contributions can not be excluded, but is very unlikely due to the removal steps in the sample preparations. However, a small contribution of one-sided bound dimers, thus not cross linking and exhibiting partially the same structure as found for Vt in solution might also be present for a small extent in this case. However, the DEER traces and distance distributions for position 901 in the presence and absence of actin show clear differences. The distance distribution obtained in the presence of actin reveals a dominating peak at 4.6 nm, indicating that the inter molecular distance increases significantly compared to Vt in solution, where the major distance peak is at 2.3 nm. Consequently, the structure of dimeric Vt bound to actin differs significantly from the structure determined for Vt in the absence of actin[6].

The result for position 922 has to be treated with caution. The distance obtained for Vt922R1 (Vt in solution) is close to the border of the reliable range, meaning that the intermolecular distance could be slightly larger than the obtained value of 4.8 nm (see also 5.1.5.1). In case of Vt922R1A (in the presence of actin) the longer dipolar evolution time, as compared to Vt922R1, could lead to the observed shift of the mean distance to larger values, since background correction might be more accurate in this case. Although a slight increase of the inter molecular distance can not be excluded, detailed predictions in terms of a change in the inter molecular distance can not be made in this case. However, the fact that Vt950R1A does not reveal any detectable dipolar oscillation,

[6]The applied dipolar evolution time in the experiments used for distance determination of Vt901R1 and Vt1033R1 was set to lower values in order to improve signal to noise ratio, especially in the beginning of the DEER trace. The possibility that a large distance, similar to that observed for Vt901R1A and Vt1033R1A, might be present in case of Vt901R1 and Vt1033R1 is excluded by repeating the experiments, using a comparable dipolar evolution times as applied for Vt901R1A and Vt1033R1A. Indications for the presence of dipolar modulation arising from larger distances could not be observed in both cases (see appendix).

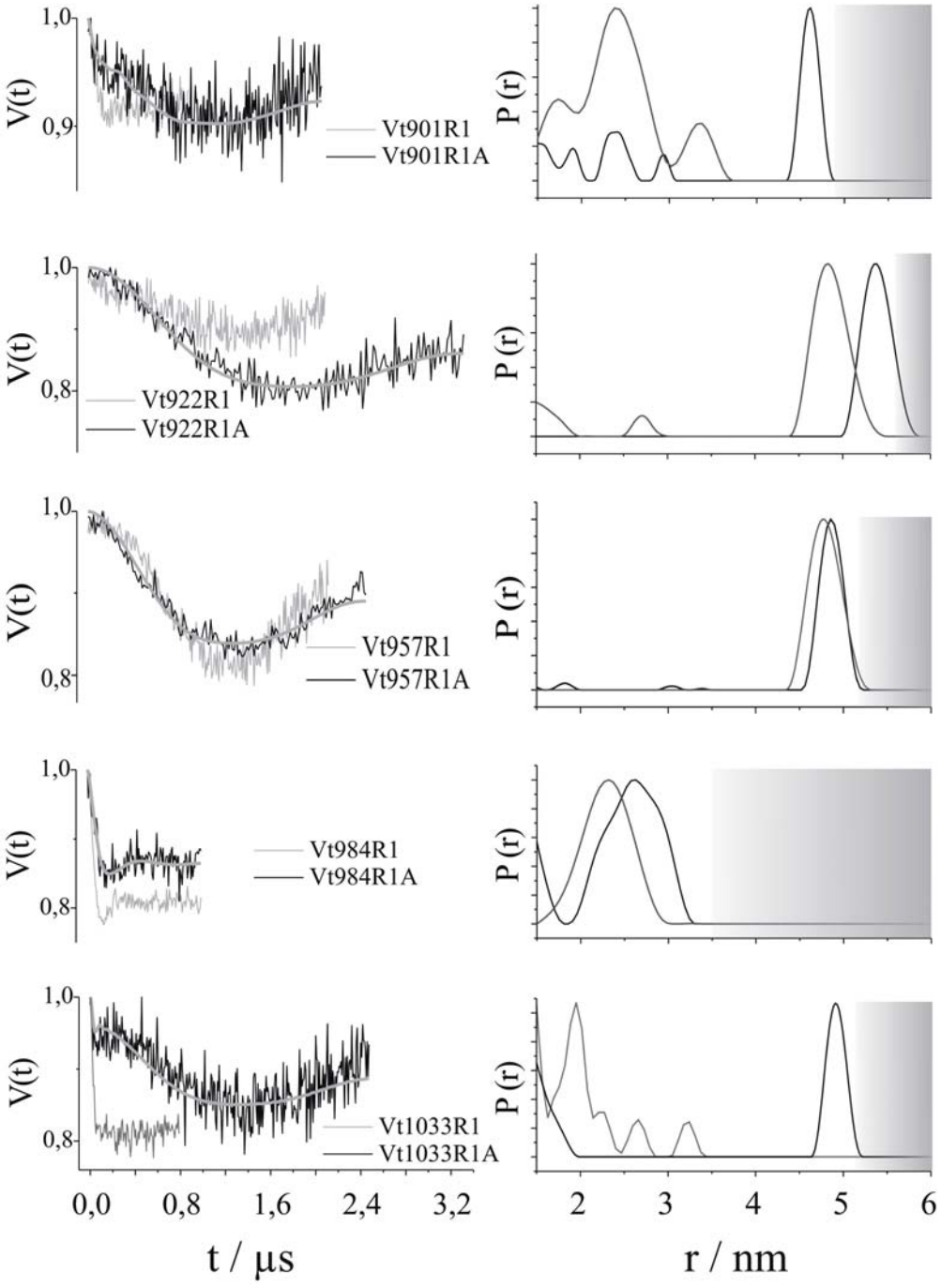

Figure 5.31: Left: Dipolar evolution functions of singly labeled Vt bound to F-actin black) and corresponding fits (gray lines) are presented and overlaid with the results obtained for Vt in solution (gray). Right: Distance distributions calculated with DEERanalysis of Vt bound to F-actin (black) overlaid with the distributions obtained for Vt in absence of actin (gray).

suggesting an inter molecular distance larger than 5.0 nm, indicates a structural rearrangement of dimeric Vt after actin binding, which could also lead to an increased distance for position 922. In contrast, a significant change could not be observed for position 957. The results for Vt984R1 reveal a distribution centered at 2.6 nm. The deviation from Vt984R1 is small, but also visible from the dipolar evolution functions, indicating that the arrangement of H4 might also be slightly affected upon actin binding of Vt. The initial fast decay of the dipolar evolution function obtained for Vt1033R1A might lead to the impression that small distances are present. However, no indication for distances below 2 nm could be observed in *cw*-EPR measurements. Thus, the fast decay of the dipolar evolution function of Vt1033R1A is most likely artificial and the contribution in the distance distribution below 2.0 nm can be traced back to noise. But also here, an insignificant small fraction of unbound Vt present in the sample can not be excluded. However, the inter molecular distance is increased from 2.0 nm up to ca. 4.9 nm, clearly indicating a large rearrangement of helix H5 upon Vt actin binding.

In summary, the results clearly show that the structure of the Vt dimer bound to F-actin differs from the structure obtained for Vt in solution. Assuming that the crystal structure of Vt would be preserved within a single molecule upon actin binding, the results would indicate that the mutual orientational alignment between the two Vt molecules differs in presence and absence of actin. However, this case is very unlikely, because of the following reasons. Vt984R1 reveals the smallest distance of 2.6 nm, leading to the assumption that H4 is still involved in the dimerization or located near the dimerization interface. The small deviation from the value found for Vt in solution (2.3 nm) indicates that parts of the dimerization interface of Vt involving H4 are similar in the presence and absence of F-actin. Consequently, in case of the helix bundle preservation at least one inter molecular distance between R1 attached to neighboring helices (next to H4), namely H3 or H5 is expected to be comparable to the distance obtained for Vt984R1A. However, in all other cases inter molecular distances around 5 nm are obtained leading to the conclusion that a conformational change has to take place within the particular Vt molecules forming the dimer.
The deviations between Vt in solution and Vt bound to F-actin are mainly reflected by the inter helical distances for helices H1 and H5, respectively, indicating that H1 and H5 are involved in the structural changes. This is in line with the above made assumption of a H1-(H4/H5) separation. Such kind of conformational change also lead to an increase of the intermolecular molecular distance of Vt901R1A and Vt1033R1A. A partial unfolding of the first helical turn of H1 seems unlikely, as in this case the distance distribution ob-

tained for Vt901R1A would have to be broader as observed here, since the conformational space of the R1 attached to an unstructured protein domain is significantly larger than compared to R1 attached to a helix. However, since the distribution width also depends on the mutual R1 orientation, the partially unfolding can still not be completely excluded.
The inter molecular distance for position 984 remains less affected by the proposed H1-(H4/H5) separation. A slight rotation of the bundle part H4/H5 around H4, leading to slight increase of the inter molecular distance of Vt984R1A and a larger increase of the inter molecular distance between positions 1033 could explain the results. Moreover, this motion could affect the intra molecular distance between residues 901 and 1033 in a way that its value is shifted from below 1.0 nm to beyond 2.0 nm, as it could be determined by the *cw*-EPR measurements.

Mean distances of singly labeled Vt		
residues	without actin	with actin
901	2.3 ± 0.3	4.6 ± 0.2
922	4.8 ± 0.2	5.3 ± 0.10
950	4.3 ± 0.2	> 5.0
957	4.8 ± 0.2	4.85 ± 0.15
984	2.3 ± 0.4	2.6 ± 0.4
1033	2.0 ± 0.2	4.9 ± 0.1

Table 5.8: Mean distances and HWHM of singly labeled Vt bound to F-actin. Results obtained for Vt in solution are given for comparison.

Doubly labeled Vt The structural change within Vt upon F-actin binding involving helices H1 and H5 is obvious from the results obtained with singly labeled Vt. In order to gain more detailed information about the structural changes, DEER measurements on doubly labeled Vt constructs Vt901R1/957R1-A (H1/H3) and Vt901R1/1033R1A (H1/H5) were performed. As already mentioned, in case of doubly labeled proteins equivalent and non-equivalent inter molecular distances contribute to the distance distributions. Therefore, to distinguish the contributions from doubly labeled Vt from those of equivalent and non-equivalent inter molecular distances, additional DEER measurements were carried out on samples containing mixtures of different singly labeled constructs. In this case, no intra molecular distances are present, whereas all combinations of equivalent and non-equivalent inter molecular distances exist. Additionally,

measurements were done using mixtures of doubly labeled Vt and unlabeled wild type Vt. Thereby, inter molecular distances can be suppressed (spin dilution). Comparisons with the distance distributions of pure doubly labeled Vt then gives rise to the identification of the intra molecular distances.

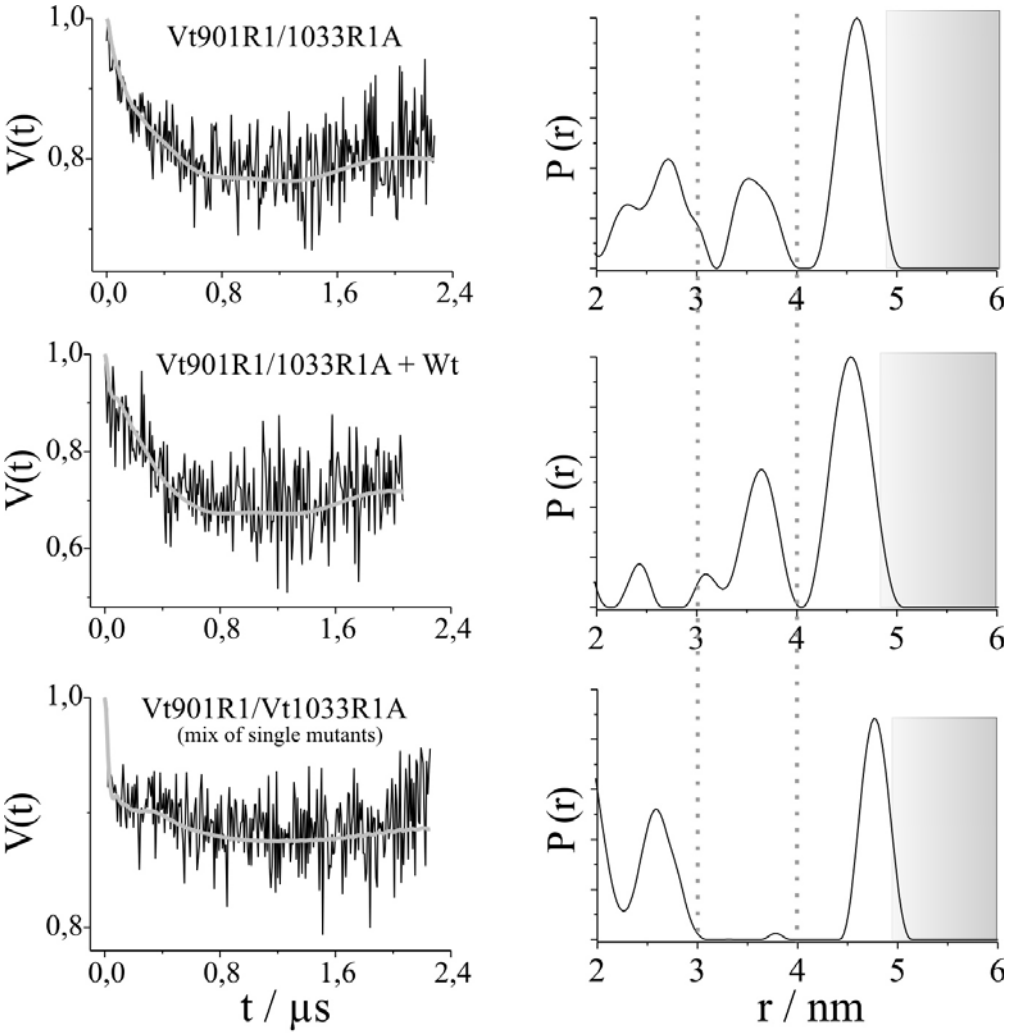

Figure 5.32: Intra molecular distance determination of Vt bound to F-actin. Top: DEER spectra and distance distributions obtained for pure doubly labeled Vt901R1/1033R1A, middle: spin diluted sample of Vt901R1/1033R1A mixed with unlabeled wild type Vt, bottom: mix of singly labeled Vt901R1 and Vt1033R1 in presence of actin. Fits are indicated as gray lines.

The results for Vt901R1/1033R1A are shown in figure 5.32. The distance distribution reveals dominating peaks centered at ca. 2.6 nm, 3.55 nm and 4.6 nm. In the distance distribution obtained for the spin diluted sample, the contribution between 2 and 3 nm is significantly reduced. This indicates that the peak

centered at 2.6 nm is governed by inter molecular distances. The ratio between the peak intensities of the mean distances at 4.6 and and 3.55 nm changes in favor of the distance located at 3.55 nm, indicating that this contribution arises from the desired intra molecular distance between positions 901 (H1) and 1033 (H5). The results obtained by the measurement on the mixtures of singly labeled Vt901R1 and Vt1033R1 bound to actin (Vt901R1/Vt1033R1A) (no intra molecular distances) support this assumption, since the contribution at 3.55 nm vanishes completely. These results suggest that the intra molecular distance of Vt901R1/1033R1A is 3.55 nm ± 0.5 nm, thus, supporting the proposed separation of H1 and H5 after F-actin binding.

The same procedure was applied for the double mutant Vt901R1/957R1A. The distance distribution shown in figure 5.33 reveals a dominating peak at 2.65 nm, minor contribution below 3 and 4 nm, and a peak at approximately 5 nm. These small contributions are reduced in case of Vt901R1/957R1A+Wt, indicating that the dominant peak at 2.65 nm constitutes the wanted intra molecular distance. Measurements on the mixture of respective singly labeled Vt (Vt901R1/Vt957R1A) yields a single peak located at 4.8 nm, which clearly arises from inter molecular distances (equivalent cases: 4.6 nm (Vt901R1A), 4.85 nm (Vt957R1A)). Thus, the intra molecular distances can be assigned to 2.65 nm, which agrees with the case of Vt in absence of F-actin (see figure 5.33 top and table 5.9). This means that the helical arrangement between H1 and H3, and most likely also the connecting helix H2, remains largely unaffected by actin binding. The fact that the distance distributions obtained for Vt901R1/957R1A and Vt901R1/957R1 reveal a similar shape, further argue against the above mentioned possibility of a partially unfolding of H1, since also here the distance distribution would be expected to exhibit a broader width, if 901R1 would be located in an unstructured domain.

Mean distances of doubly labeled Vt		
residues	without actin	with actin
901/1033	0.76 ± 0.08	3.55 ± 0.25
901/957	2.65 ± 0.10	2.65 ± 0.10
984/1033	0.74 ± 0.07	0.70 ± 0.05
922/957	0.76 ± 0.08	0.76 ± 0.08

Table 5.9: Mean distances obtained by *cw* and pulse EPR measurements of doubly labeled Vt in presence and absence of F-actin.

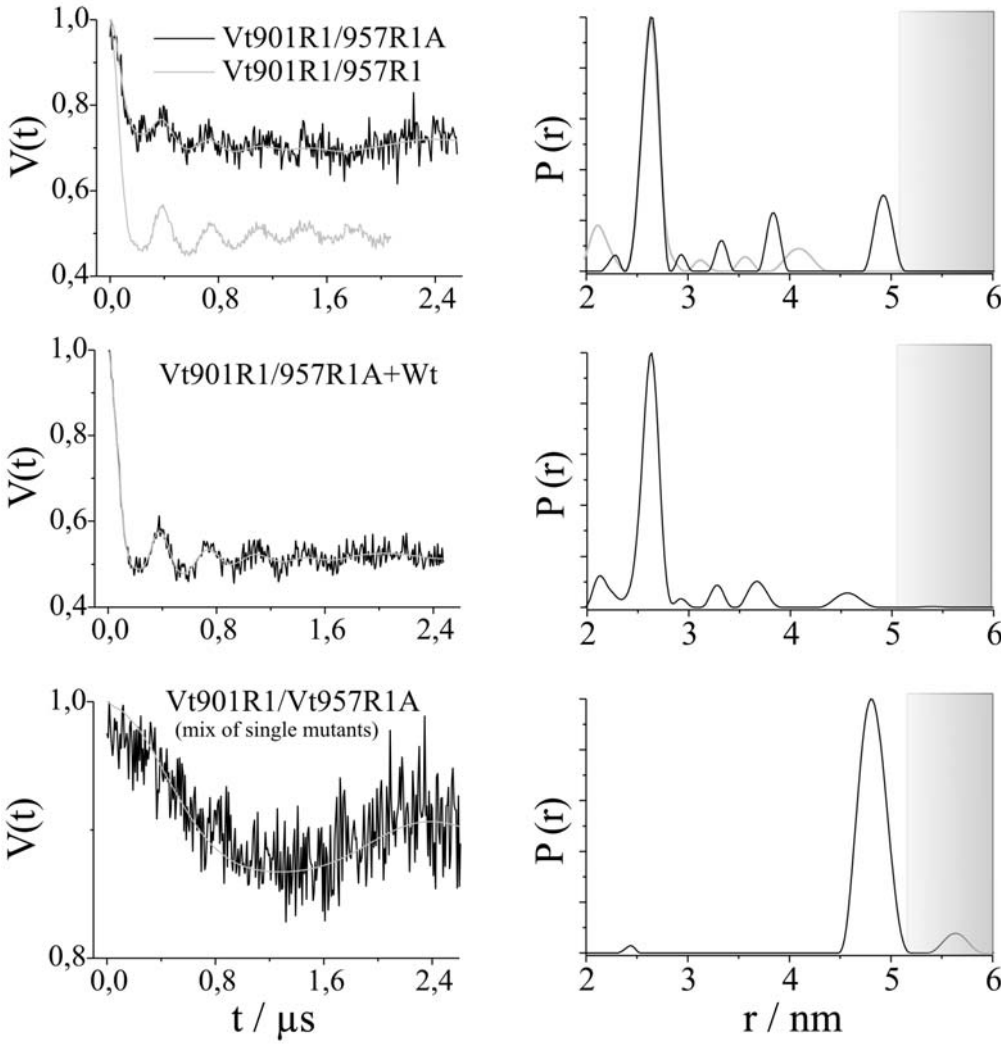

Figure 5.33: Intra molecular distance determination of Vt bound to F-actin. Top: DEER spectra and distance distributions obtained for pure doubly labeled Vt901R1/957R1A (overlaid with results of Vt901R1/957R1), middle: spin diluted sample of Vt901R1/957R1A mixed with unlabeled wild type Vt, bottom: mix of singly labeled Vt901R1 and Vt957R1 in presence of actin. Fits are indicated as gray lines.

5.3.4 Molecular model of Vt bound to F-actin

For the construction of the structural model presented below, the following assumptions are made. The dimerization process of Vt in absence of ligands is supposed to constitute an initial step within the dimerization pathway induced by actin. To the authors knowledge, the detailed dimerization pathway, whether Vt dimerizes before or as a consequence of actin binding, is not known at present. Both cases might occur in nature. Furthermore, in this work it could be shown that a small fraction of dimeric Vt is present within the samples un-

der investigation. Thus, F-actin induced dimerization of monomeric Vt as well as already dimerized Vt molecules are supposed to lead to the observed actin cross linking. Here, it is assumed that the resulting structures of dimeric Vt bound to F-actin are similar (or even identical) in both cases. Therefore, for the construction of the model, the structure of dimeric Vt in solution determined in this work, is used as the initial structure, which is assumed to undergo conformational changes upon F-actin binding. This assumption implies that the dimerization interface, found for Vt in aqueous solution, is largely preserved in the presence of F-actin. This is supported by the results obtained by mobility measurements on Vt901R1 and Vt901R1A (see 5.3.1).

The EPR spectroscopy results indicate that the relative helix alignment within the bundle domains H1/H2/H3 and H4/H5 of both Vt molecules within the actin bound dimer are virtually unaffected. Furthermore, the observed increase of the intra molecular distance between positions 901 (H1) and 1033 (H5) (from below 1 nm up to 3.5 nm) is supposed to be caused by a separation of these domains. This is accompanied by an increase of the inter molecular distances from 2.3 nm to 4.6 nm (901) and 2.0 nm to 4.9 nm (1033), respectively.
In figure 5.34 (top) a schematic illustration of the assumed initial situation (Vt dimer in solution (see for 5.1.5.2 details)) is shown. Starting from this structure, exhibiting an antiparallel Vt alignment, three different possibilities of a structural rearrangement of Vt upon actin binding should be discussed.
The first two yield a symmetric conformational change, meaning that the final structures of the particular Vt molecules are identical. In the first case (shown in figure 5.34 a)) an opening of the Vt helix bundle caused by a relative outward movement of H1/H2/H3 with respect to H4/H5 is assumed. Such movement leads to the observed increase of the intra and inter molecular distance between positions 901 and 1033, whereas inter molecular distances of residues 922 and 957 remain largely unaffected[7].
The distances obtained for Vt901R1 and Vt1033R1 both changes from ≈ 2 nm to ≈ 5 nm upon actin binding. Such simultaneous distance increase is possible, if non-equivalent protein parts perform a reorientation within an antiparallel Vt alignment as illustrated in figure 5.34. This supports the assumption of an arrangement similar to Vt in solution, and the preservation of the dimerization

[7] It has to be mentioned that figure 5.34 illustrates the helical movement schematically. Here, a top view of both Vt molecules was chosen for clarity. Due to the assumed flexibility of the Vt dimer complex, the respective Vt molecules might exhibit a declination with respect to each other (see 5.1.5.2 or 5.35), which leads in case of the illustrated helical rearrangement to a slight increase of the inter molecular distance of Vt950R1A up to beyond 5 nm, whereas the distances between 922 and 957 are largely preserved, which is in better agreement with EPR spectroscopy results.

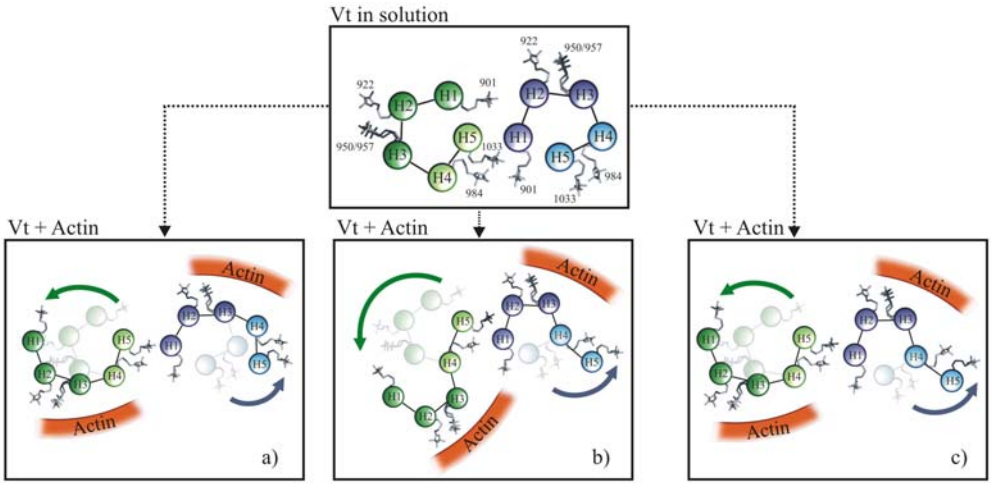

Figure 5.34: Schematic illustration of the assumed rearrangement within the Vt dimer bound to F-actin. Top views of the respective Vt molecules are shown for clarity, helices corresponding to two different Vt molecules (green and blue) are indicated as colored circles. Top: Sketch of the assumed initial structure corresponding to the above determined structure of dimeric Vt in solution. Upon actin binding a conformational change of dimeric Vt is assumed. Three different possibilities for the helix movement are shown (bottom). a): The opening of the helix bundle takes place by a relative outward movement of H1/H2/H3 with respect to H4/H5 (symmetric conformational change). b): The structural rearrangement is governed by a rotation of bundle domain H4/H5 around helix H4 (symmetric conformational change). c): The Asymmetric conformational change as combination of both presented cases (a) and b)) reflects the experimental obtained results at best. The sides at which F-actin is proposed to bind are indicated in red.

interface. Moreover, in model a) the assumed actin binding sites (predominantly H3 and parts of H2 and H4) are located on opposite sides of the Vt dimer and are completely accessible, enabling the bundling of actin filaments. This model is in agreement with the experimental data. However, regarding the proposed helical movement, the inter molecular distance of position 984 reaches values > 3 nm, thus being not completely in line with the experimental results obtained for Vt984R1 (2.3 ± 0.4 nm) and Vt984R1A (2.6 ± 0.4 nm), which suggest that helix H4 is only slightly affected upon F-actin binding.
A second possibility for the structural alignment of Vt in presence of actin might be that the separation of H1 and H5 in both Vt molecules results from a rotation of domain H4/H5 around helix H4 (figure 5.34 b)). This symmetric alignment is also in agreement with the findings by EPR distance measurements, however, the actin binding sites of at least one Vt molecule are not completely accessible, since they are partially shielded by the other Vt molecule, complicating a bundling of actin filaments.

Due to these facts, a combination of the aforementioned symmetric conformational changes is assumed, in which one molecule undergoes the conformational change according to possibility a) (outward movement of H1/H2/H3) and in the second involved Vt molecule a rotation of H4/H5 around helix H4 (case b) is taking place. The resulting model (figure 5.34 c)) is in good agreement with the experimental results, and the actin binding sites are completely accessible. However, the existence of the former two (symmetric) cases can not be excluded and might also occur in nature. Here, the latter (asymmetric) case, describing the experimental data at best, is assumed to be the favored structure, describing the helical arrangement within Vt bound to F-actin most likely.
Furthermore, a dynamic flexibility of the dimer complex is suggested, slightly affecting the mutual alignment of two Vt molecules in a similar way as assumed for dimeric Vt in solution. This means that a small orientational distributions between two Vt molecules is assumed, in which a complete antiparallel alignment (in terms of helix long axis orientations) of two Vt molecules and also a small declination between them might exist. In figure 5.35 (a) a sketch of the assumed average structure of dimeric Vt bound to F-actin is illustrated. The approximate actin binding regions proposed by Janssen et al. [33] are highlighted in b) and c). It is obvious that the proposed actin binding sites are well accessible and in close vicinity in the presented model.
A reason for the observed Vt opening might be that thereby a larger contact surface for actin filament binding is provided, which could facilitate and have a stabilizing effect on the filament bundling. In this way, the contact regions might be enlarged from H3 to areas including parts of H2 and H4 [33]. As a consequence, R1 side chains attached to these regions, and located between the Vt and the F-actin interaction surface, are most likely affected by Vt actin binding. This could be observed for Vt950R1A (H3), Vt957R1A (H3) and Vt984R1A (H4), revealing the most significant decrease in R1 mobility, and is in line with the model of Vt bound to actin filaments here presented. A further contribution to the observed R1 immobilization of Vt984R1A might be caused by the assumed rotation of H4/H5, taking place in one of the Vt molecules. This might lead to a situation, in which the motional freedom of R1 attached to position 984 is hindered by H5 and additionally by H3. Taken together, the presented model is in line with the results obtained by EPR distance and mobility measurements.

Two possibilities for the relative orientation of the Vt dimer with respect to the bundled actin filaments are suggested in the following. The first possibility exhibits a parallel alignment between Vt helix long axes and the actin filament long axis (figure 5.36 a), b), c)). If a binding of the particular Vt molecules to equivalent regions of the actin filaments is assumed (see also [33]), this case

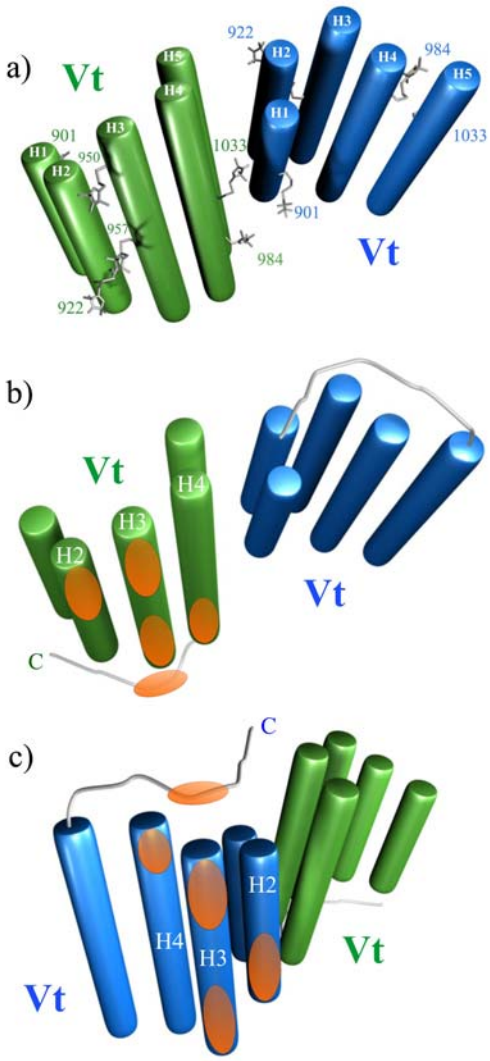

Figure 5.35: Model of dimeric Vt bound to F-actin. a): Schematic representation of the assumed helix alignment within the Vt dimer. Helices of one Vt molecule are displayed as green cylinders, helices corresponding to the second Vt molecule are shown in blue. The shown model corresponds to the asymmetrical helical rearrangement illustrated in figure 5.34 c). The Vt molecules exhibit a slight declination with respect to each other. A minor mutual orientational distribution due to motional flexibility of the dimer complex is assumed. The dimerization interface is suggested to constitute H1 and parts of the N-terminal strap of one Vt molecule (blue) and H5 (and eventually parts of H4) of the other Vt molecule (green). Approximate localizations of label positions are indicated. b) and c): Approximate helix regions, exhibiting the in [33] proposed actin binding sites, are highlighted by orange ovals. Beside smaller parts of H2 and H4, H3 yields most of the actin binding sites. Moreover, the C-terminal end of Vt reveals to be partially involved in the actin binding as well (gray). Information extracted from figure 2.6.

would imply that the two cross linked actin filaments are aligned in an antiparallel manner, since the two Vt molecules exhibit an antiparallel alignment. However, Vt is able to cross link parallel actin filaments as well. This would only be possible, if the Vt binding sites in both cross linked filaments are not equivalent, or if the orientation of Vt with respect to the filaments differs from the discussed case. The former can not be excluded, and could explain the observed asymmetric conformational change within Vt. A Vt dimer, exhibiting a perpendicular orientation of Vt helix long axes with respect to the filament long axis (as shown in figure 5.36 d), e), f)), might be able to cross link parallel actin filaments by binding equivalent filament regions. Due to this fact, and further taking the assumed flexibility of the Vt dimer complex into account, an adaptability of Vt to the orientational situation of to be linked actin filaments is suggested. This is supported by the following fact. Using the applied bundling assay, Vt is able to cross link actin filaments, which are randomly orientated with respect to each other. The case, in which two filaments exhibit a parallel or anti parallel orientation occur more rarely compared to all other cases. This would mean that statistically almost all of the filaments would not be cross linked, what could not be observed here.

It should be noted that the actin binding sites and the proposed interaction surface of Vt and acidic lipids (see 5.2.4) are located on opposite sides of the respective Vt molecules. Thus, the model, exhibiting partially opened Vt molecules, would facilitate also lipid binding (to both hydrophobic helical parts and C-terminus of Vt) and does not contradict the reported interplay between acidic lipid and F-actin binding of Vt.
However, it has to be mentioned that the structural alignment and the observed conformational change of Vt upon actin binding contradicts the findings of Janssen et al [33], where no large scale conformational changes within Vt after actin binding could be observed. Furthermore, the therein assumed dimerization interface differs from the one presented here. However, the applied tomography method (3D-cryo electron microscopy) is restricted in resolution. Janssen et al. report a resolution of 2 nm or lower of their determined reconstruction, which was used for alignment determination of two Vt crystal structures forming the dimer. In terms of the crystal structure the diameter of Vt is approximately 2.5 nm, which is similar to the obtained resolution. This might complicate the determination of the relative Vt alignment and the traceability of structural rearrangements within the molecules, which could be observed here using EPR spectroscopy.
The work of Janssen et al. reveals a distance of 10 nm between the centers of two parallel aligned actin filaments (diameter ca. 7nm). The distances between the molecular surfaces, pointing towards each other, of two parallel aligned actin

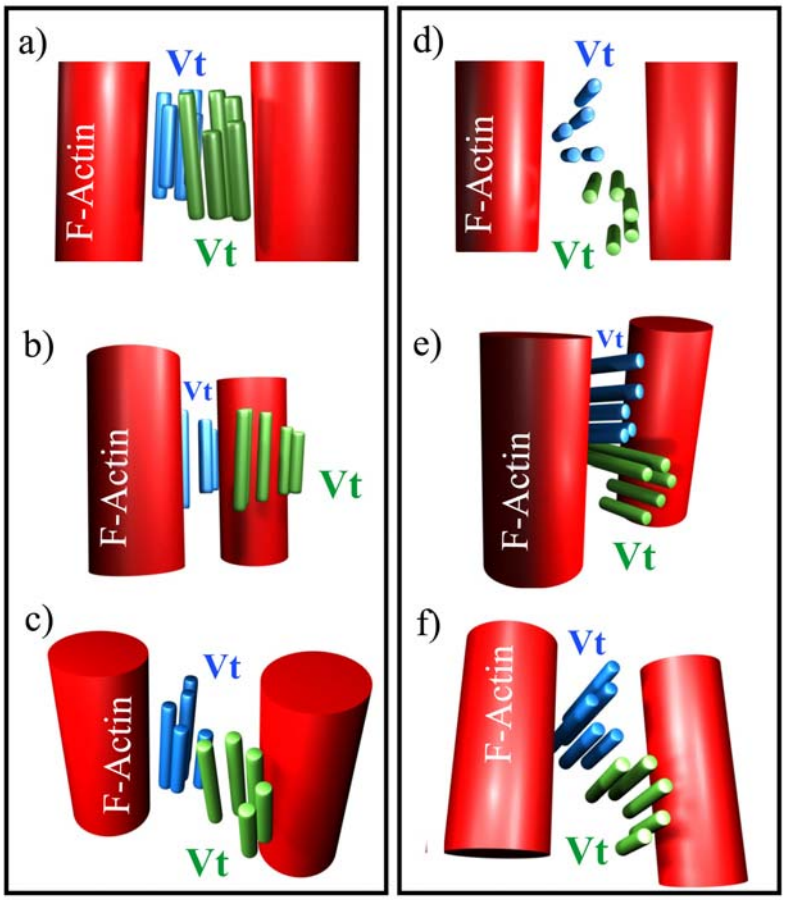

Figure 5.36: Two discussed possibilities for the relative orientation of the Vt dimer with respect to the bundled actin filaments. a), b) ,c): Different views of the parallel alignment between Vt helix long axis (green and blue molecules) and the actin filament long axis (indicated as red cylinder). d), e), f): Perpendicular orientation between Vt helix and actin filament long axis.

filaments is between 2.5 and 4.5 nm (information extracted from the resulting structure file of Vt bound to actin filaments, kindly provided by Dorit Hanein (Burnham institute, La Holla, CA)). The here presented model of dimeric Vt provides the possibility to link actin filaments exhibiting the mentioned distance range.

Furthermore, it has to be mentioned that asymmetric conformational changes within protein dimers are infrequently reported, but could be proven for example for GPCR and Hsp90 dimers [43, 65]. Here, the proposed asymmetric conformational change of two different Vt molecules might be explained by the non-equivalent protein parts, involved in the dimerization interface. The interface is supposed to comprise H1 (and most likely also the N-terminal strap) of one molecule and H5 (and eventually parts from H4 and C-terminus) of the respective binding partner. This means that different molecular parts within

particular Vt molecules are bound to each other and are thus differently motionally restricted in terms of performing structural rearrangements. Consequently, this asymmetric alignment might in turn trigger asymmetric structural changes within the particular Vt molecules. A further possibility might be that non-equivalent parts of actin filaments can be bound by two different Vt molecules, which might induce asymmetric conformational changes as well.

5.4 Competition between F-actin and acidic lipids

In cell migration, F-actin and acidic phospholipids together control Vt interaction in adhesion sites and allow regulation of assembly and disassembly of focal contacts. A competition between F-actin and acidic phospholipid binding exists, which induces a release of vinculin from focal contacts and consequently disassembly of these contacts at high lipid concentrations [25, 16]. How this process is controlled in cells is only poorly understood at present.
Here, time dependent room temperature *cw*-EPR and confocal laser scanning microscopy measurements were performed on actin bound Vt in the presence of PS-lipids in order to investigate the influence of acidic lipids on the Vt-actin assembly.

5.4.1 EPR spectroscopy

The EPR spectrum of Vt957R1A reveals a dominating immobile component, meaning the low field peak maximum is shifted into the direction to lower field strengths (figure 5.37 right). In contrast, the more mobile R1 side chain in case of Vt957R1PS (dominating mobile component) leads to an EPR spectrum, in which the low field peak maximum is shifted to larger fields (figure 5.37 right). Since EPR spectra of Vt957R1A and Vt957R1PS show the largest differences regarding the inverse second moment and line width compared to other Vt constructs, this construct was used here to trace time depended spectral changes upon addition of PS-lipids.
Sample preparations and time dependent EPR measurements were performed as described in 4.1.1.4. The elapsed time between adding SUV (small unilamellar vesicle) solution to Vt957R1A and the storage of the first EPR spectrum was $\approx$ 3 min. Afterwards, EPR spectra for different Vt:PS ratios (1:30, 1:100 and 1:200) were recorded and saved in 1 min steps for 40 min. Representative EPR spectra of Vt957R1A+PS are shown in figure 5.38 in dependence of time. As a control, measurements were done using PC-lipid solutions. Using negatively charged PS lipids, it can be seen that the spectra of Vt957R1A+PS reveal time dependent alterations. Already in the first minutes the spectra clearly differ from Vt957R1A. At higher SUV concentrations the spectral deviations are even more pronounced and the EPR spectra becomes more similar to the spectral shape of Vt957R1PS, especially after larger incubation times. In contrast, for Vt957R1A+PC no significant changes can be observed within 30 min. These results indicate that acidic PS-lipids induce a conformational change within actin bound Vt. The similarity of the spectra obtained for Vt957R1A+PS and Vt975R1PS for large incubation times leads to the assumption that Vt is released from F-actin and turns over into the PS-lipid membrane bound state.

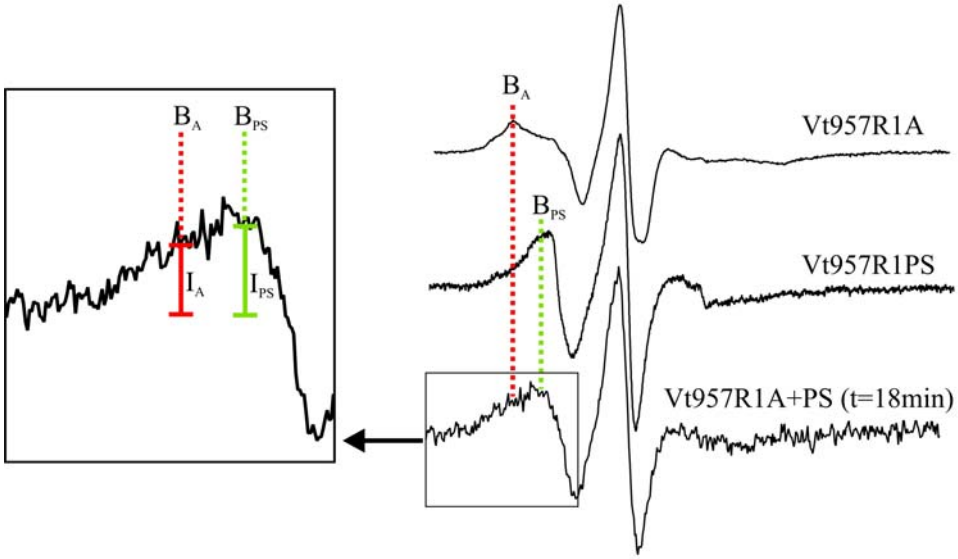

Figure 5.37: Right: The EPR spectrum of Vt957R1A, Vt957R1PS and Vt957R1A after 18 min after addition of PS-lipids (Vt957R1A+PS) (sweep width 12 mT). The position of the low field peak maximum of Vt957R1A is located at the field strength B_A (red). The low field peak maximum in case of Vt957R1PS is shifted to a higher field B_{PS} (green). Left: Enlarged view of the low field peak of the representative Vt957R1A+PS spectrum. For the analysis from each spectrum the signal intensities I_A and I_{PS} at B_A and B_{PS} were extracted. The time dependent ratio R(t)=$I_A(t)/I_{PS}(t)$ was used as a measure for the kinetics of the conversion progress from the actin into the lipid bound state of Vt.

In order to characterize the turn over process in more detail, EPR spectra were analyzed as described in the following.

The position of the low field peak maximum (immobile component) of Vt957R1A in absence of PS-lipids is located at the field strength B_A. The low field peak maximum in case of Vt957R1PS in absence of F-actin is shifted to a higher field B_{PS}. It is assumed that the spectrum of Vt957R1A+PS at a certain time t is a superposition of the spectra obtained for Vt957R1A and Vt957R1PS at a certain ratio. Thus, from each Vt957R1A+PS spectrum the signal intensities I_A and I_{PS} at B_A and B_{PS}, respectively were calculated (see figure 5.37 left for illustration) and the time dependent ratio R(t)=$I_A(t)/I_{PS}(t)$ was used as a measure for the conversion progress from the actin bound state into the lipid bound state of Vt.
The R value, obtained for the spectrum of Vt957R1A, is R_A=2.45. Since the first 3 minutes of the progress could not be traced a start value of R(t=0)=R_A=2.45 was chosen. From the spectrum of Vt957R1PS a value of R_{PS}=0.35 can be extracted. That means, a value R(t)=0.35 would describe the case in which all Vt molecules prior bound to actin would be bound to PS-SUVs.

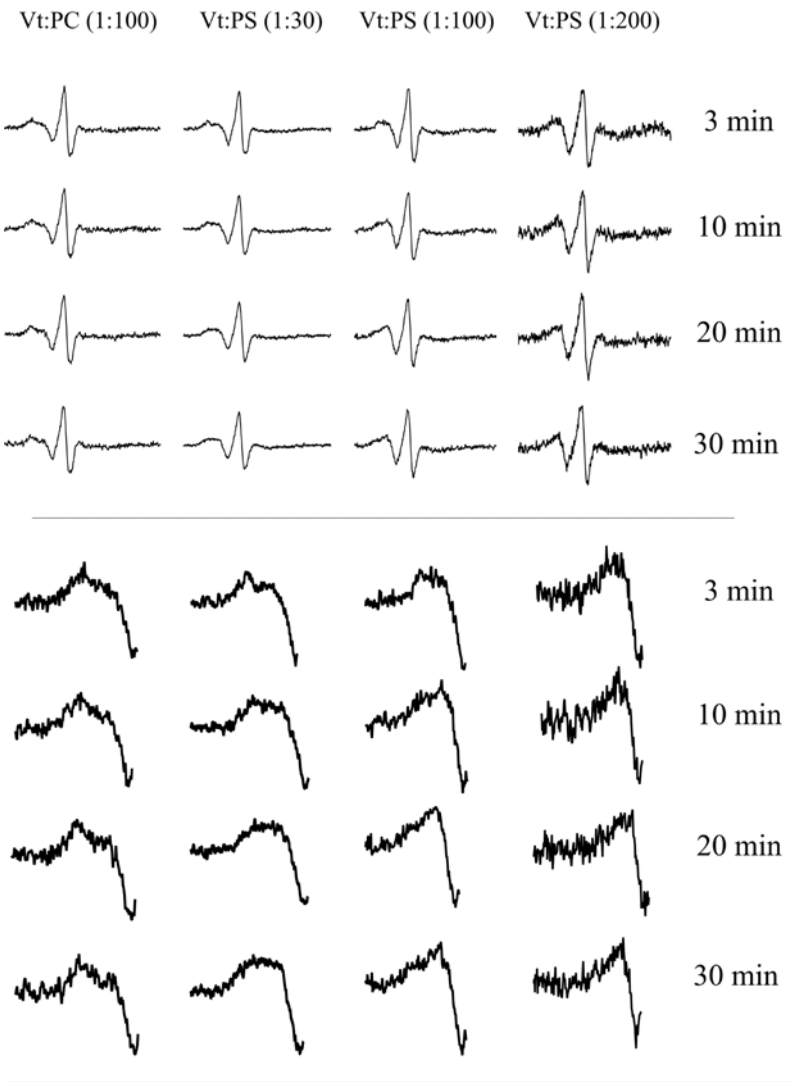

Figure 5.38: Top: EPR spectra for different Vt:lipid (PS/PC) ratios were recorded for 40 min (32 min in case of Vt:PC) and saved in 1 min steps. EPR spectra of Vt957R1A in the presence of lipids recorded after 3, 10, 20 and 30 min are shown as representative spectra. Bottom: Enlarged low field peaks of the corresponding EPR spectra shown above.

R(t) for Vt957R1A+PC fluctuates around R_A, indicating that Vt remain in the actin bound state in the presence of PC lipids (figure 5.39), thus, PC does not influence the Vt-actin assembly. In contrast, the plots of R(t) for Vt957R1A+PS versus time reveal time dependent decays, illustrating the conversion process of Vt from the actin to the PS-lipid bound state. These traces were fitted assuming an exponential decay. Fit parameters are summarized in figure 5.40.
The obtained decay times (t_0) are in the range of 1.3 min - 5.3 min, and decrease upon increasing lipid concentrations, indicating that the turn over kinetics de-

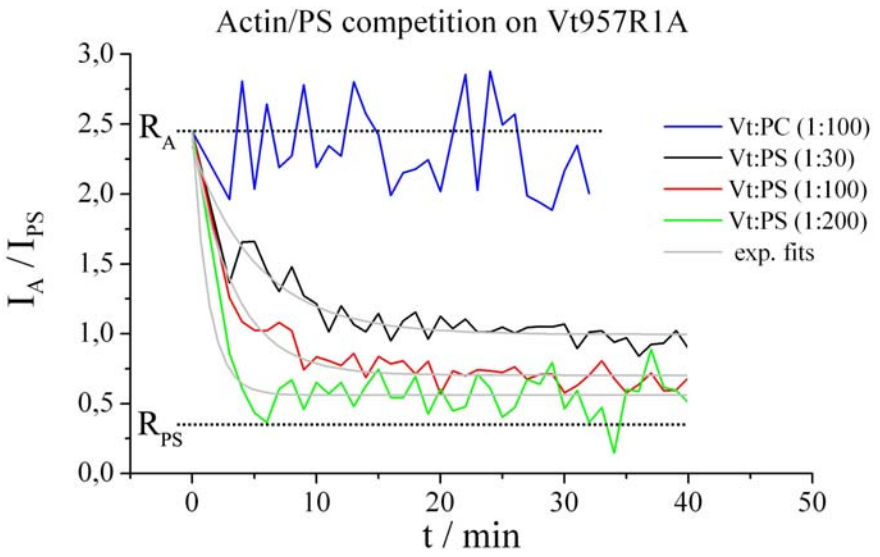

Figure 5.39: Plot of R(t)=$I_A(t)/I_{PS}(t)$ versus time t for Vt957R1A+PS in dependence of different lipid types and concentrations. The obtained exponential decays illustrate the conversion process of Vt from the actin into the PS-lipid bound state. Reference values R_A and R_{PS} are indicated (dotted lines).

pends on the PS-lipid concentration. In case of 1:200 (Vt:PS) the decay could not be resolved, since R(t) has already decayed to a constant value within 3 min. Thus, t_0 is most likely smaller than the here obtained value of t_0=1.3 min. As expected, the rate $1/t_0$, quantifying the speed of the reaction (process), increases along with the lipid concentration (see figure 5.40, right). This is obvious, considering that the probability for a Vt-SUV contact increases with higher lipid concentrations.

Exponential fit parameters			
Vt:PS	t_0 / min	A	y_0
1:30	5.3 ± 0.6	1.3 ± 0.1	0.99 ± 0.02
1:100	3.3 ± 0.3	1.7 ± 0.9	0.70 ± 0.02
1:200	1.3 ± 0.4	1.9 ± 0.1	0.56 ± 0.02

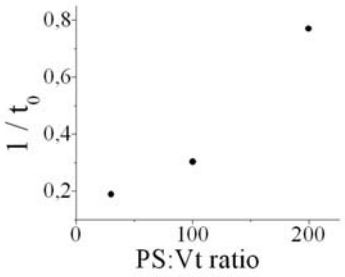

Figure 5.40: Left: Parameters obtained from fitting of experimentally obtained data (R(t)) using a mono-exponential decay, $F(t) = y_0 + A \cdot e^{-\frac{t}{t_0}}$. $1/t_0$ is the decay (or reaction) rate, which can here be understood as reaction speed. The shift y_0 was introduced to account for an equilibrium state, which might differ from and can be compared to R_{PS}, describing a complete turn over. The sum of y_0 and the amplitude A describes the starting point F(t=0)≈R(t=0)=R_A.

However, the results show that all traces do not decay down to the value R_{PS}, and the values of y_0 obtained by the fits (see 5.40) are larger than R_{PS} in each case. Furthermore, y_0 is smaller using higher lipid concentrations. This indicates that an concentration dependent equilibrium between the F-actin bound and PS-lipid bound states of Vt exists. A permanent transition from one state to another is most likely present, and the equilibrium might be shifted into the direction of the PS-bound state by increasing the lipid concentration, leading to lower y_0 values. Possibly, a small fraction of Vt molecules, masked by actin filaments in a such a way that these Vt molecules are not accessible to SUVs, may also be present in the sample and might contribute to y_0.
In summary, the results show that PS-lipids affect the Vt-actin assembly directly. Furthermore, these findings support the fact that the lipid binding sites of Vt are not shielded by F-actin, thus no or only minor overlaps of the respective binding sites are present, confirming the above presented model of Vt bound to filamentous actin (5.3.4). Finally, the assumption that the release of Vt from focal adhesion contacts might be regulated by acidic lipids, could be substantiated by EPR spectroscopy.

5.4.2 Fluorescence laser scanning microscopy

To investigate the effect of PS-lipid vesicles on the Vt-actin assembly, confocal laser scanning microscopy (CLSM) experiments were performed on filamentous Rhodamine-actin (F-actin(Rh)) and on Vt bound to F-actin(Rh) (Vt957R1A(Rh)) in the absence and in the presence of PS-SUV. Images obtained by CLSM are shown in figure 5.41.

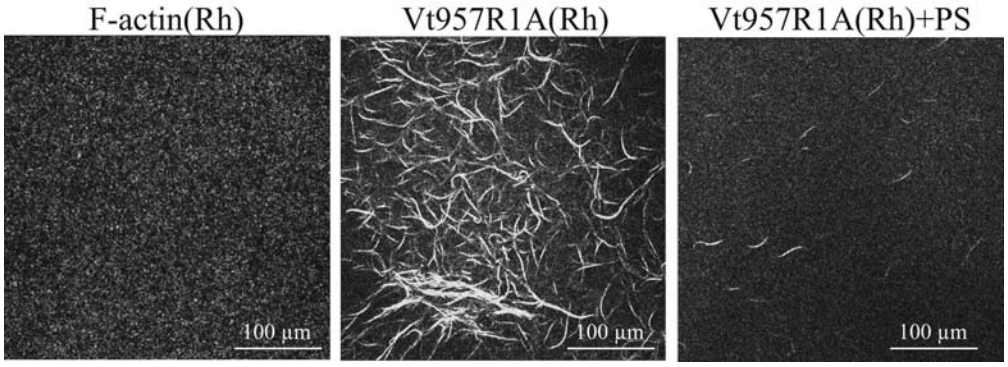

Figure 5.41: Confocal laser scanning microscopy images of samples containing pure F-actin(Rh), Vt957R1A(Rh) and Vt957R1A(Rh)+PS. In case of Vt957R1A(Rh) (middle) F-actin bundles are clearly visible (white), whereas the number of intact bundles is significantly decreased upon addition of PS-lipids (right).

F-actin bundling can not be observed in the sample containing pure F-actin(Rh) (figure 5.41 left). This is obvious, since no binding partner for F-actin is present.

Furthermore, the unbundled actin filaments exhibit a diameter of approximately 8 nm and the resolution of the used microscope is not sufficient to resolve the F-actin structure, as expected. However, upon Vt induced F-actin crosslinking, the resulting F-actin bundles can be observed by CLSM. In the image shown in figure 5.41 (middle) huge bundles of F-actin are visible in case of Vt957R1A(Rh). After incubation with PS-SUV the number of intact bundles is significantly decreased (figure 5.41 right), indicating that Vt is released from the Vt-actin assembly, subsequently leading to a disassembly of F-actin bundles. The results support the above made conclusion that the observed changes of the EPR spectral shapes are caused by the Vt release and consolidate the results found by EPR spectroscopy.

5.5 Orientation selective DEER measurements

Pulse electron paramagnetic resonance using the four pulse DEER sequence has established as a valuable method to determine inter spin distances between spin labels attached to protein molecules [60, 56]. DEER spectra depend on the mutual orientation of the bound spin label molecules [44, 59], complicating data analysis. On the other hand, knowledge of the mutual spin label orientations would provide additional information about the structure and conformational changes of proteins.
A new method to investigate spin label orientations is orientation selective DEER. The hyperfine coupling anisotropy of the commonly used nitroxide spin labels enables orientational selectivity by shifting pump and observer pulse frequencies within the corresponding EPR absorption spectrum range. Here, X-band orientation selective DEER measurements using five different frequency offsets between pump and observer pulses were applied on the double mutant Vt901R1/957R1, revealing motionally highly restricted R1 side chains. The obtained DEER spectra were analyzed by calculating the corresponding Pake patterns in dependence of mutual spin label z-axis orientations and relating them to the experimental data by means of the root mean square deviation (RMSD) between the simulated and experimental Pake spectra for all orientations. The thus obtained orientation profile reveals the most probable orientations of the spin label side chains. In this approach it is assumed that the two R1 side chains, separated by a defined distance, exhibit a single mutual orientation. No further assumptions about the orientational situation of the spin labels are required to obtain their relative mutual orientations. Spin label orientations predicted by a rotamer library approach were compared to the experimental results.

5.5.1 Experimental results

The dipolar evolution functions in dependence of the frequency offsets are shown in figure 5.42 a). The modulation depth increases with increasing frequency offset between pump and observer pulses. Clear differences in the shapes of the dipolar evolution functions are visible, especially in the region of the first minimum. Accordingly, the intensity ratios between the perpendicular and the parallel components of the corresponding Pake patterns increase with increasing frequency offsets (b). The spectral features at low dipolar frequencies close to 0.6 MHz most likely arise from a small contribution of dimers still present in the sample. The dipolar frequency corresponding to the inter molecular distance (4.8 nm) between positions 957R1 is located in this frequency range. However, the observed depending of the dipolar traces on the frequency offset

indicates that different orientations between the dipolar axis and the magnetic field direction were selected in the particular experiments. As described in 3.4.2, this is only possible, if an orientation correlation between the spin labels and the dipolar axis exists.

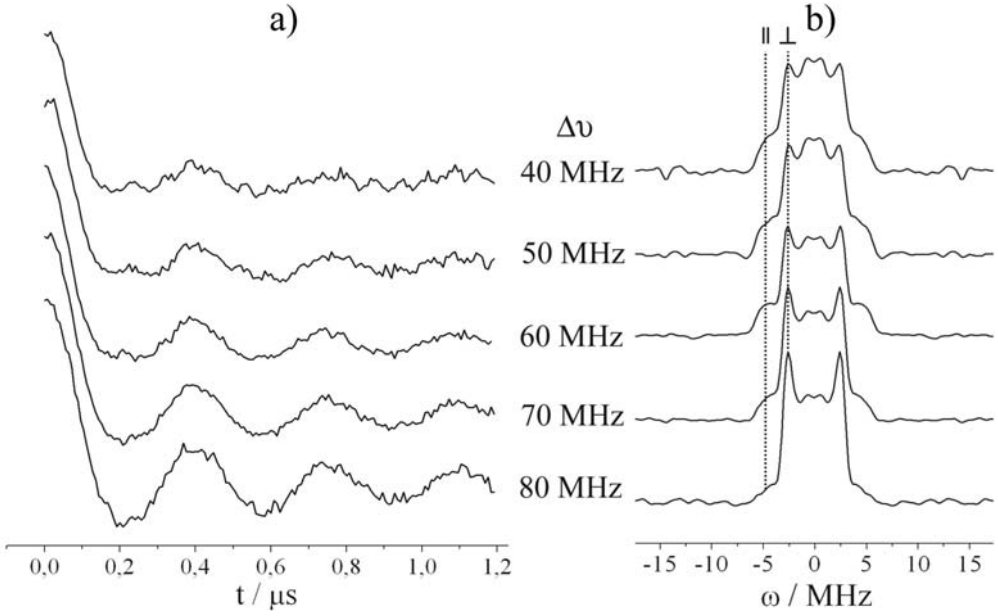

Figure 5.42: The background corrected DEER traces for different frequency offsets $\Delta\nu$= 40, 50, 60, 70 and 80 MHz show clear differences in the first minimum and in modulation depth (a). Corresponding spectra in the frequency domain (b) were obtained by Fourier transformation of the data shown in a). Parallel and perpendicular components are indicated.

In X-band the g-anisotropy of nitroxides is not resolved. Consequently, the Zeeman transitions of the nitroxides with the nitrogen nuclear quantum number m_I=0 are located near the center of the EPR absorption spectrum regardless of the nitroxide orientation with respect to the magnetic field. Thus, a pump pulse with the central resonance frequency leads to an excitation of B spin molecules exhibiting all possible orientations with respect to the magnetic field direction. The modulation of the DEER signal arises from the interaction between these spins and the A spins excited by the observer pulse. Depending on the observer pulse frequency only specific A spins exhibiting a corresponding nitroxide orientation with respect to the magnetic field and nitrogen nuclear quantum number (m_I=-1) are selected. Consequently, in the case of an orientational correlation a certain orientation Θ_{dd} between the dipolar axis and the magnetic field orientation is selected leading to a frequency selection in the dipolar spectrum. By the variation of the observer pulse position (from 40 MHz to 80 MHz) the orientations selected by ν_A are systematically scanned, leading to signal contributions of molecules exhibiting different dipolar axis orientations

with respect to the magnetic field direction, thus yielding different dipolar frequencies. This results in changes of the evolution functions' Fourier transform depending on the observer pulse position, as it could be observed here. In addition, the modulation depth, which depends besides the number of interacting spins on the mutual spin label orientation, increases along with the frequency offset. Taken together, these results indicate that an orientational correlation between the interacting spin labels exists. Beside the fact that the intensity ratios between the perpendicular and the parallel features change by the use of different frequency offsets, it is obvious that the perpendicular features in all patterns are located at the same dipolar frequency value. This shows that the mean distance (2.65 nm) extracted from the DEER trace measured at $\Delta\nu$=65 MHz is not affected by orientation selection effects in this case. The distance was validated by its determination from the dipolar frequency at the dominating peaks (perpendicular features) of the Pake pattern and the use of equation 3.66 with Θ_{dd}=90° (2.66 nm). Thus, the use of this experimentally obtained distance value for further simulations is justified.

5.5.2 Pake pattern simulation and spectra analysis

The narrow width of the DEER distance distribution indicates highly restricted spin label motions for both positions, 901 and 957, which is confirmed by mobility and the rotamer analyses (see chapter 5.1.1 and 5.1.4.2 or below). Since the highly populated rotamers obtained by RLA reveal similar spin label Z-axis orientations, it is further assumed that a single rotamer is populated at each site, exhibiting a single orientation with respect to each other, which can be describes by three angles ϑ_A, φ_B and ϑ_B. (see chapter 4.1.3.3 and figure 5.43). Furthermore, it is assumed that the observed EPR spectra are dominated only by intra-molecular spin-spin interactions. Thus, the DPP calculations in dependence of ϑ_A, φ_B, ϑ_B and $\Delta\nu$, using the approach described in chapter 4.1.3.3, were done using a single inter spin distance of 2.65 nm.
After convolution with a narrow Gaussian distribution the RMSD from the experimental Pake pattern was calculated for all orientations. The contributions at small frequencies observed in the experimentally obtained spectra, which most likely arise from inter molecular distances and are very sensitive to the background correction, were excluded from the spectra analysis by excluding the frequency range between -1.5 MHz and +1.5 MHz from RMSD calculations (see also figure 5.46).
For each value of angle ϑ_A between the nitroxide z-axis of the A spins (Z_A) and the dipolar axis a two dimensional pattern of RMSD values in dependence of φ_B and ϑ_B is obtained. The first iteration using a coarse orientation grid leads to lowest RMSD values for ϑ_A= -15°. For this ϑ_A, angles of φ_B=15° and ϑ_B=75°

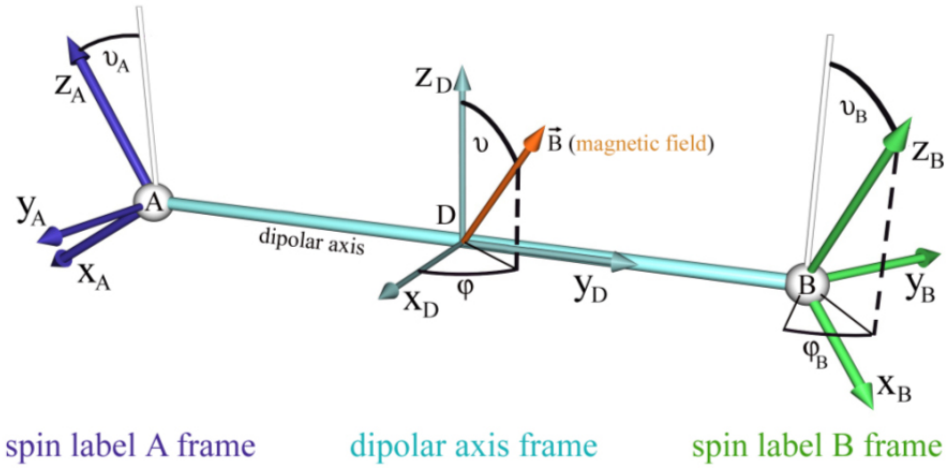

Figure 5.43: Angle definitions. ϑ_A decribes the angle between the spin label A (blue frame) z-axis and the z-axis of the reference frame D (light blue). The dipolar axis is aligned along Y_D. φ_B and ϑ_B describe the orientation of spin label molecule B (green frame) z-axis with respect to Z_D. The magnetic field orientation (red) is given by φ and ϑ.

between the dipolar axis and the nitroxide z-axis of the B spins (Z_B) exhibit the lowest RMSD (figure 5.44 a)), thus, the most probable orientation with respect to the dipolar axis. A second minimum emerges at φ_B=-15° and ϑ_B=90° and, exhibiting a slightly larger RMSD value compared to the aforementioned orientation.

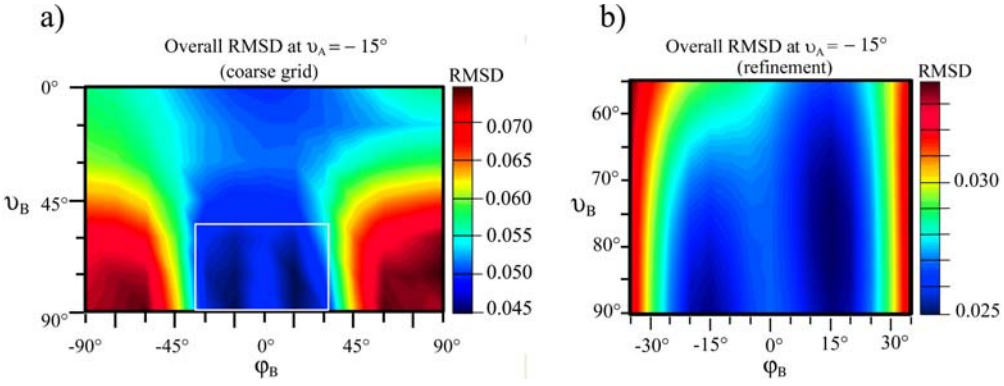

Figure 5.44: a): RMSD values in dependence of φ_B and ϑ_B at ϑ_A=-15° (coarse grid). The RMSD values are displayed in a color code using dark red as highest and dark blue for the lowest RMSD value. The colors (representing the RMSD value) between the 91 calculated knots on the orientational grid were interpolated. The lowest RMSD was obtained at φ_B=15° and ϑ_B=75° (φ_B=-15°, ϑ_B=90°) between the dipolar axis and Z_B. b): Result of the 5°-step refinement calculated in the white framed section in a) (and ϑ_A=0°-30°). The refinement leads to the more accurate values ϑ_A=-15°, φ_B=15° and ϑ_B=80°. The patterns obtained for other ϑ_A values (coarse grid and refinement) are shown in the appendix.

A refinement was done in the range of ϑ_A=0° - 30°, φ_B= -35° - 35° and ϑ_B=55° - 90° in steps of 5°, leading to a RMSD minimum centered at ϑ_A=-15°, φ_B=15° and ϑ_B=80° (see figure 5.44 b)). Figure 5.44 b) shows that the second minimum mentioned before (at φ_B=-15° and ϑ_B=90°) corresponds to the equivalent orientation resulting from the assumed symmetry of the system[8] (see chapter 4.1.3.3). Figure 5.45 shows the pattern from figure 5.44 a) mapped on a sphere, considering the above mentioned mirror symmetry, displaying the RMSD for the spin label B molecular z-axis orientations with respect to the dipolar axis and the best fitting orientation of Z_A.

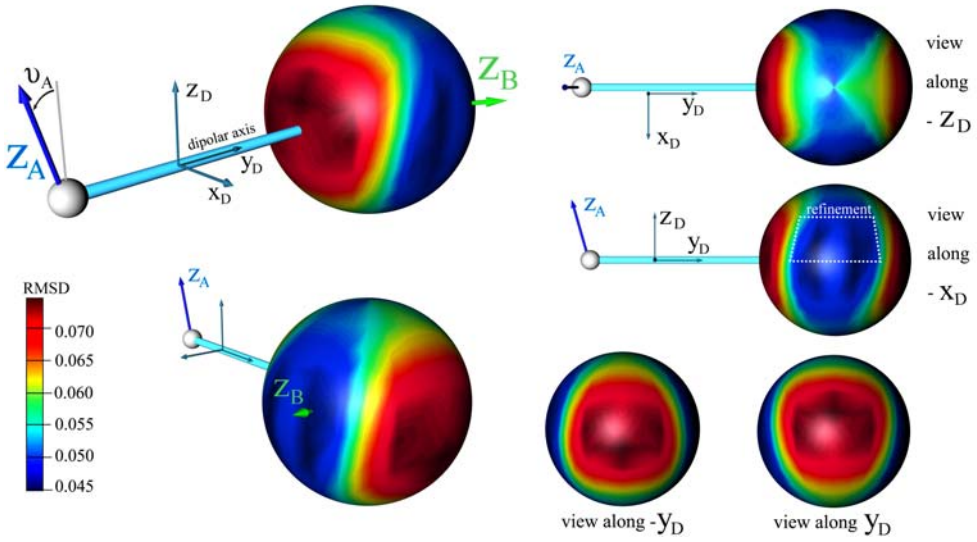

Figure 5.45: The RMSD profile from figure 5.44 a) (coarse grid), providing the color coded RMSD values in dependence on φ_B and ϑ_B describing the orientation of Z_B with respect to D, is mapped on a sphere under consideration of the symmetry of the system. Shown is the dipolar axis and the reference frame D in cyan, the spin label B z-axis (green arrow) and the spin label A z-axis (blue) exhibiting the angle -15° with D_Z. Different perspectives are shown on the right. The region, in which the refinement was done, is indicated (white dashed frame).

The simulated DPPs for the best fitting overall orientation are overlaid with the experimental data for each $\Delta\nu$ in figure 5.46.
The simulated and experimental spectra in the considered frequency range are

[8] An inversion of the z-axis orientation at φ_B=15° and ϑ_B=80° would lead to φ_B=-165° and ϑ_B=100°. Due to the mirror symmetry with the plane spanned by D_y and D_z as mirror plane, the value set φ_B=-15°, ϑ_B=100° is equivalent to φ_B=15° and ϑ_B=80°. Moreover, a second set of ϑ_A, φ_B and ϑ_B, which is equivalent to the here found best fitting orientation, was expected, since the orientation resulting from an exchange of molecule A and B z-axes describes the same orientational situation, but differ in ϑ_A, φ_B, ϑ_B. Here, the orientation, which is equivalent to the found best fitting values is calculated to ϑ_A=-20.8°, φ_B=15.7° and ϑ_B=80.03°, approximately coinciding with the here discussed angle set.

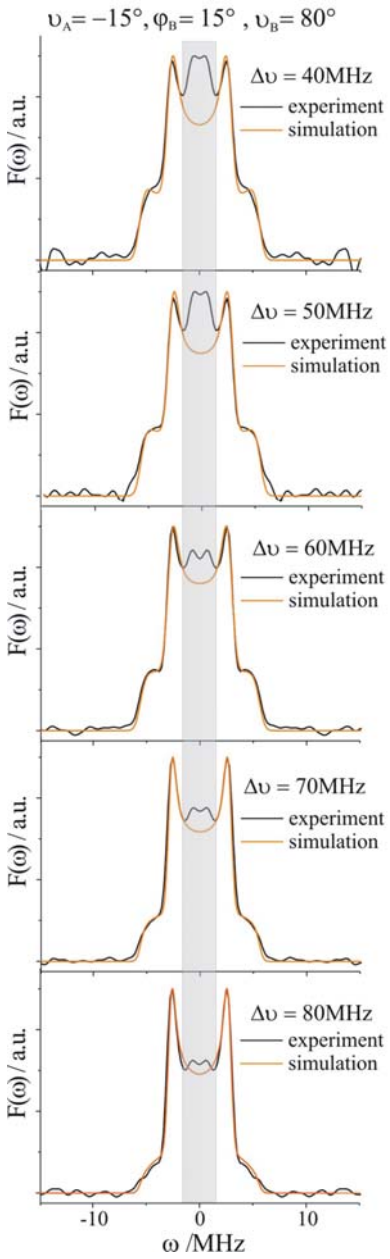

Figure 5.46: Simulated DPPs for the best fitting overall orientation ϑ_A=-15°, φ_B=15° and ϑ_B=80° are overlaid with the experimental data (black) for $\Delta\nu$=40, 50, 60, 70 and 80 MHz. The frequency range excluded from RMSD calculations is highlighted (gray bar).

in very good agreement. The increase of the intensity ratios of the perpendicular and parallel components of the spectra with increasing frequency offset $\Delta\nu$ is well reflected by the simulations. However, deviations are present in the low frequency range (gray bar in figure 5.46), which has been excluded from the analysis. Even under consideration of the whole frequency range in RMSD

calculations, the same overall orientation is obtained (data not shown). This supports the assumption that the peaks at low frequencies in the dipolar spectra mentioned before do not arise from the strong orientational correlation between the two spin labels, but from inter molecular inter spin distances.
For each frequency offset $\Delta\nu$ individual best fitting orientations were determined. These orientations agree within 10° for ϑ_A and φ_B and 20° for ϑ_B, wherein changes of spectral shapes and overall RMSDs are just minor. Hence, the uncertainty of the orientation determination is assumed to be in this range. Additionally, a small distribution of spin label z-axis orientations with respect to the dipolar axis within the given uncertainty can not be excluded and is most likely present in the experiment. Taking the mentioned uncertainty into account, for the average orientation of Z_A and Z_B with respect to the dipolar axis ϑ_A=-15° ± 10°, φ_B=15° ± 10° and ϑ_B=80° ± 20° is calculated.
The best agreement between experimental and simulated DPPs was obtained after convolution of the simulated spectra with a Gaussian distribution with a width of 0.4 MHz. Applying the approximations described in 4.1.3.3, the thereby caused broadening of the perpendicular spectral features (at 2.75 MHz) corresponds to a distance distribution of ca. 0.1 nm, and the broadening at small frequencies is related to a distribution of Θ_{dd} of approximately 10°.

5.5.3 Comparison between OS-DEER results and RLA

Sets of highly populated rotamers for spin label side chains attached to residues 901 and 957 of the Vt crystal structure were obtained by the rotamer library approach (see also chapter 5.1.3 and 5.1.4.2). For position 901 (H1), two of the three populated rotamers reveal a similar z-axis orientation. The third rotamer is much less populated (ca. 4%) and has a different z-axis orientation. In case of 957 (H3), two significantly populated rotamers with rather the same z-axis orientations were obtained. The occupied rotamers are shown in figure 5.47.
Furthermore, the orientations of each particular rotamer combination with respect to their dipolar axis were calculated for the two cases, in which 957R1 or 901R1 were treated as molecule A defining ϑ_A in terms of the discussed model. The given intensities were calculated by multiplication of the populations of the corresponding rotamer pairs. These intensities can be understood as the probability to find a certain rotamer combination in the experiment, which would contribute with the respective intensity to the overall DEER signal. The two combinations, in which the least populated rotamer of position 901 is involved, lead to very low intensity values (≈ 0.02), whereas the other four combinations lead to higher values of 0.24 in average. The average values of ϑ_A, φ_B and ϑ_B for the high and low intensity cases, corresponding to the considered octant (φ_B= -90° - +90°), are listed up in table 5.10.

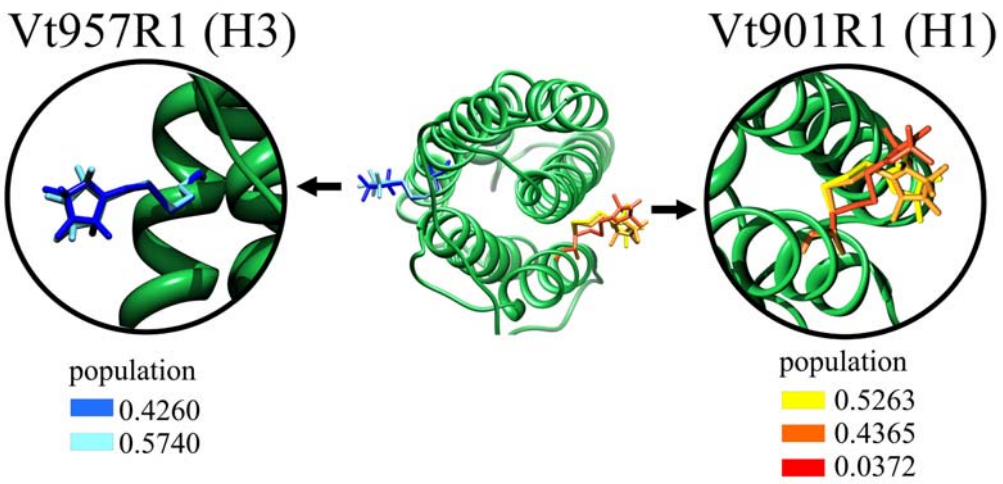

Figure 5.47: Results of the rotamer library approach on Vt. Top: Position 901 reveals three populated rotamers. The two high populated R1 reveal similar z-axis, whereas the z-axis orientation of the low populated rotamer differs in orientation. For position 957 two significantly populated rotamers exhibiting similar z-axis orientations were obtained. Bottom: The corresponding populations are given next to the bars colored with the same color code used for the particular rotamers.

	intensity	ϑ_A	φ_B	ϑ_B
957 as molecule A	high (0.96)	-19.2°	17.3°	38.3°
	low (0.04)	-12.8°	-46.4°	36.5°
901 as molecule A	high (0.96)	-10.2°	34.2°	39.6°
	low (0.04)	-27.2°	-24.7°	31.8°
experimental values		-15° ±10°	15° (-15°) ±10°	80° ±20°

Table 5.10: Table containing the average orientations ϑ_A, φ_B, ϑ_B from high and low populated rotamer combinations extracted from RLA results, treating position 901 and 957 as molecule A, respectively. Two low intensity cases, arising from rotamer combinations, in which the least populated rotamer of position 901 is involved, and four combinations of high populated rotamers, exhibiting similar z-axis orientations, respectively, are averaged. Experimentally obtained values are given for comparison.

In all cases, values obtained for ϑ_A are in agreement with the overall orientation determined by orientation selective DEER. The same applies for φ_B in both high intensity cases. In the low intensity cases, the largest deviations are obtained. The orientations extracted from RLA are plotted into the RMSD pattern for ϑ_A=-15° for comparison with the experimental results (figure 5.48). All cases reveal significant deviations in ϑ_B of ca. 40° from the experimentally obtained values. Since the here obtained values do not fully resemble the values

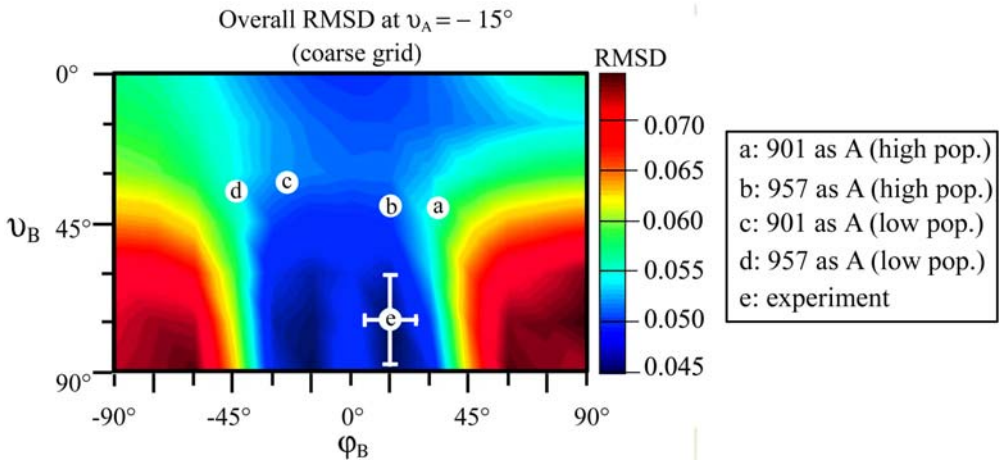

Figure 5.48: Average R1 z-axis orientations extracted form RLA (also given in table 5.10) are plotted into the RMSD pattern for ϑ_A=-15° together with the experimentally obtained best fitting orientation.

obtained by orientation selective DEER measurements, this leads to the conclusion that a structural rearrangement of the spin label side chains regarding their orientations compared to the RLA results takes place within Vt in aqueous solution, which might be due to small reorientations of protein side chains surrounding the particular R1 side chains.

In case 957R1 defines molecule A, the rotamer combinations with the highest probability values show the best agreement with the experimental values. Furthermore, the rotamer analysis indicates that Vt901R1 has a slightly larger spatial freedom than Vt957R1, leading to a larger orientation distribution. This fact is also reflected in the room temperature cw-EPR spectra of Vt901R1 and Vt957R1. In addition, compared to the Vt crystal structure, structural rearrangements involving 901R1 could be observed by EPR distance measurements for Vt in solution (see chapters 5.1.1 and 5.1.4). Due to these reasons it is assumed that 901R1 is mainly involved in the rearrangement of z-axis orientations observed here. Under the assumption that the z-axis orientation of Vt957R1 in the experiment is similar to that obtained by RLA, the z-axis of Vt901R1 has to undergo an reorientation as displayed in figure 5.49, to fulfill the experimentally obtained conditions. In order to illustrate the observed reorientation, a representative (and exemplary) R1 side chain orientation, being in agreement with the experimental results, was modeled and overlaid with the rotamers exhibiting the highest population values. These rotamers were introduced into the Vt crystal structure and the R1 molecule at position 901 was reoriented according to the experimental results, treating 957R1 as spin label A.

It has to be mentioned that the pyrroline ring alignment shown here is only one possibility which agrees with the experimental results, since reorientations

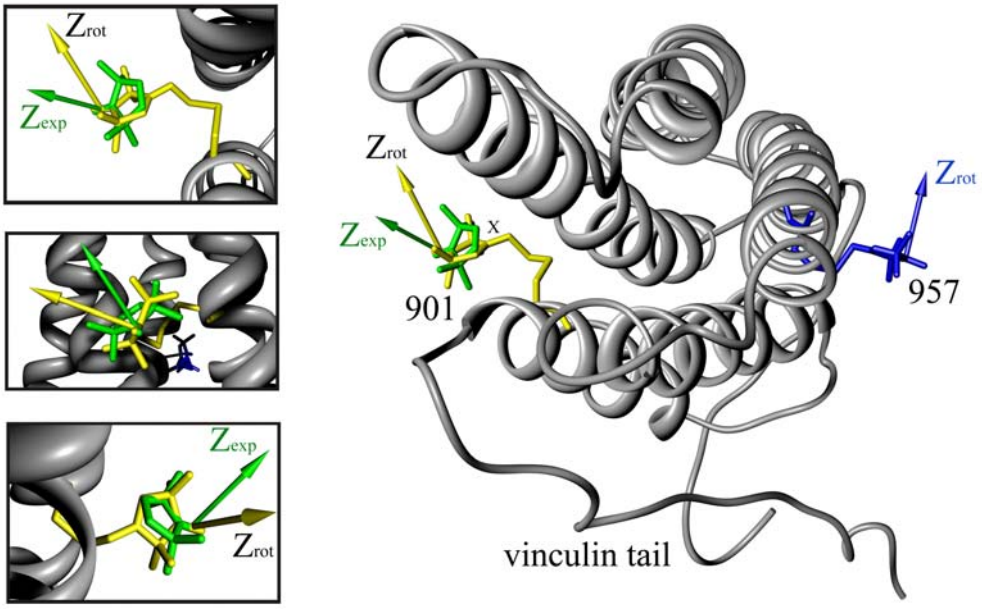

Figure 5.49: One possible alignment of R1 z-axis orientations as found by orientation selective DEER experiments. One rotamer pair bound to the Vt crystal structure obtained by RLA is shown. Since highly populated rotamers found for both positions, 901 (yellow) and 957 (blue), show very similar z-axis orientations (colored arrows), respectively, only the rotamers exhibiting the highest population values are shown for clarity. The z-axis of the modeled R1 pyrroline ring at position 901 (green) and the z-axis of R1 at position 957 (blue arrow) fulfill the orientational conditions found by orientation selective DEER experiments. The angle between the z-axis of R1 obtained by RLA (901, yellow arrow) and by experiment (green arrow) amounts ca. 40°. On the left panel different views on the R1 side chain at position 901 are shown. In the displayed example, it is assumed that the highly populated rotamers of 957 are also populated in the experiment, and R1 at position 901 is mainly involved in the relative reorientation. Furthermore, with respect to the here shown modeled ring orientation, all rotamers exhibiting a 180°-rotation (z-axis inversion) of the pyrroline ring around its C_1 - C_E bond (highlighted by X), slight shifts along the dipolar axis (within the experimental distance width) and rotations around the R1 z-axis, are allowed conformations as well, since due to the axially symmetry of the magnetic tensors, it can not experimentally be distinguished between these confomers.

of 957R1 can not be excluded. Furthermore, four different, but regarding the DEER response equivalent, triplets for ϑ_A, φ_B and ϑ_B were found in the experiments due to the symmetry of the system, resulting from the axial symmetry of the magnetic tensors. Thus, a 180°-rotation of the pyrroline ring around its C_1 - C_E bond, slight shifts along the dipolar axis and ring rotations around the R1 z-axis are still allowed transformations, which will not change the experimental results.

However, it could be shown that the determination of the mutual z-axis orientation of protein bound spin labels is possible using orientation selective DEER spectroscopy at X-band frequencies, if the orientation correlation of the spin label pair is as strong as in case of Vt901R1/Vt957R1.

6 Summary and Outlook

Vt in solution, bound to F-actin and acidic lipids The cytoskeletal protein vinculin plays a key role in cell adhesion and migration [82]. Vinculin is a 116 kDa, actin-binding protein, which consists of 1066 amino acids. It is built up of a globular head (domains D1-D4) and a tail domain (Vt). The latter is formed by a bundle of five antiparallel α-helices exhibiting N- and C-terminal extensions [7]. Although the crystal structure of vinculin is available, its role in the regulation of adhesion site turn over and its biological functions in cell migration are still not sufficiently understood.

The crystal structure of vinculin reveals that the actin binding domain (Vt) is masked by domains D1-D4, in the auto-inhibitory, inactive conformation. Thus, an activation mechanism accompanied by structural changes within vinculin is required to unmask ligand binding sites and to promote vinculin function.
Acidic phospholipids, such as PS and PIP_2, as part of cell membranes, play an essential role in the regulation of cell migration [45, 16, 6, 82]. Association of PIP_2 with Vt was suggested to dissociate the head to tail interaction, exposing binding sites for actin, and promoting assembly of focal adhesions [7, 24]. Therein, the *hydrophobic hairpin* of Vt is supposed to mediate the first contact to acidic lipids or the lipid membrane, respectively, resulting in a conformational rearrangement of the five-helix bundle [7, 6].
Moreover, binding of Vt to F-actin enables the connection of the cytoskeleton to the transmembrane receptors (*via* vinculin head binding to talin), and the stabilization of focal adhesion sites. The work of Bakolitsa et al. [7] supports a conformational change in Vt upon actin binding. Additionally, the existence of a dimerization site in Vt was demonstrated, which is activated upon binding to F-actin [38, 31], and Janssen et al. [33] recently introduced a three-dimensional model of the Vt-dimer bound to actin filaments, where no large scale conformational changes of Vt could be observed.
Furthermore, it is known that F-actin and acidic phospholipids together control Vt interaction in adhesion sites and allow regulation of assembly and disassembly of focal contacts, enabling cell migration. A competition between actin and acidic phospholipid binding exists, which induces a release of vinculin from focal contacts and consequently disassembly of these contacts at high lipid concentrations [25, 16]. How this process is controlled in cells is not well understood

at present. Moreover, structural details about Vt under physiological conditions in the absence and presence of the mentioned binding partners are still not available.

In this work, various *cw*- and pulse EPR methods in combination with SDSL were performed to investigate the Vt structure in aqueous solution and its structural changes upon interaction with acidic lipids and F-actin. The results obtained herein indicate that the five-helix bundle configuration, as defined in the Vt crystal structure, is largely preserved for Vt in solution. Additionally, it could be shown that Vt is to a small extent (ca. 10-30% of the molecules in case of the here applied concentrations) dimeric in aqueous solutions. Using the distance information, obtained by DEER measurements on singly labeled Vt, a model of dimeric Vt could be proposed. The results reveal a cross-like, antiparallel alignment of two Vt molecules, with partially asymmetric dimerization interfaces. For one Vt primarily helix five constitute the main part of the interaction domain, together with parts of helix H1 and smaller parts of helix H4. For the second Vt molecule, the main contact region can be allocated to parts of the N-terminal strap, followed by a large part of helix H1. The reasonable agreement of the computational rotamer library approach with EPR results supports these findings and shows that the time-saving rotamer library approach is a well applicable technique to predict spin label side chain movement, flexibility and orientation. The alignment between two Vt molecules in aqueous solutions determined in this work differs from the alignment found by Vt crystallization [7] and that suggested by NMR-experiments [55]. Possible reasons for this discrepancy might be unphysiological experimental conditions during cystallization, and especially in case of NMR experiments, missing information about protein parts, which are here shown to be involved in the dimerization interface.
The dimerization of Vt in the absence of ligands may constitute an initial step within the dimerization pathway induced by F-actin. Actin induced dimerization of monomeric Vt as well as already dimerized Vt molecules are assumed to lead to F-actin cross linking. Here it is assumed that the resulting structures of dimeric Vt bound to F-actin are very similar or even identical in both cases, and that the dimerization interface found for Vt in aqueous solution may be largely preserved in the presence of F-actin. However, the results for Vt bound to F-actin clearly show that the structure of the Vt dimer differs from the structure obtained for Vt in solution. For Vt bound to F-actin, it is proposed that the bundle domains H1/H2/H3 and H4/H5 separate from each other by a relative outward movement of H1/H2/H3 with respect to H4/H5 within one molecule, and a rotation of domain H4/H5 around helix H4 in case of the other. Non-equivalent dimerization sites of two Vt molecules might be

one reason for the assumed asymmetric conformational change within dimeric Vt upon F-actin binding. Furthermore, a reason for the observed Vt opening might be that a larger contact surface for actin filament binding is provided, that can better stabilize the filament bundling. In this way, the actin contact regions of Vt might be enlarged from H3 to areas including parts of H2 and H4 [33]. However, the structural model of Vt bound to actin filaments, presented in this work, is not in agreement with the model based on cryo-EM and molecular docking of X-ray structures, previously reported by Janssen et al., where no large scale conformational changes of Vt were predicted. In their approach, the unaltered Vt crystal structure was fitted into the electron density map, which exhibits a resolution of about 2 nm. This resolution might be insufficient to detect the here observed conformational changes within Vt. The model presented here can most likely also be fitted satisfactorily into the electron density map determined by Janssen and coworkers.
Analysis of Vt in the presence of PS-lipid vesicles by EPR spectroscopy suggests an opening of the Vt helix bundle, and an association to the lipid membrane surface. Thereby, the bundle parts H1/H2, H3/H4 and H5 are supposed to separate from each other and to exhibit specific orientational distributions with respect to each other. Here, the release of Vt from the lipid bound state may be regulated by the head domain D1, since D1 binding sites of Vt are located at the center of the opened Vt molecule, allowing for binding of D1 to Vt. This may lead to a vinculin-head induced pulling force, acting on the middle of the membrane bound Vt molecule. In turn, this interaction could lead to a release of Vt from the membrane, subsequently folding back into an antiparallel helical bundle. This process may be supported by Y1065 phosphorylation, which enhances vinculin exchange in focal adhesions, as propsed by Mohl et al. [49]. Furthermore, analyzing the models of Vt bound to PS and F-actin presented here, the PS-membrane binding region of Vt does not overlap with the proposed F-actin binding sites, still enabling the competitive nature of PS and F-actin binding to Vt. This competition was investigated by EPR spectroscopy and confocal laser scanning microscopy in this work as well. A concentration dependent lipid induced release of Vt from the actin bound state was monitored, corresponding to a turn over rate in the range of several minutes (in case of the here applied concentrations) at room temperature. Thus, the assumption that the release of Vt from focal adhesion contacts might be regulated by acidic lipids [73, 16], could be substantiated. The results were consolidated by confocal laser scanning microscopy.

In summary, EPR spectroscopy in combination with RLA, MD simulation and other computational methods allowed the construction of molecular models of Vt in solution, bound to F-actin and to PS-lipid membranes. In cell migration

Vt is supposed to exist in all of these proposed conformations, continuously undergoing transitions between these structural states, which in addition is regulated by vinculin head, F-actin, acidic lipids, Y1065 phosphorylation and other ligand interactions, such as paxillin.

Distance determination using DEER spectroscopy immensely contributes to the construction of the models presented here. Since the detectable distance range strongly depends on the relaxation times of the investigated system, EPR samples allowing longer DEER time traces, are of great importance. Especially, in the case of investigations on Vt in the presence of lipids, the applicable dipolar evolution times do not allow the determination of distances larger than ca. 3.5 nm. In general, the use of deuterated water, lipids and/or proteins can increase the relaxation times. Thus, the development of preparation methods, which utilize deuterated sample compounds, could improve the accuracy of the here presented models. Furthermore, MD-simulations, using the structural models as starting structure and experimentally obtained results as constraints, might increase the accuracy as well.
Numerous questions regarding the regulation of cell migration processes are still unanswered. The mechanisms, which can induce the mentioned transitions of Vt between the suggested states, require further characterization. Further experiments in presence of various vinculin tail binding partners, such as paxillin, PKC_{α} or even full length vinculin, would certainly contribute to a clarification of this issue.

OS-DEER spectroscopy on Vt DEER spectroscopy has become a routinely used method to determine inter spin distances between spin labels attached to protein molecules. It has been shown experimentally and also theoretically that DEER spectra depend on the mutual orientations of the spin label molecules. In case of spin labeled proteins the spin label motion and its spacial freedom is restricted by interactions with the protein backbone and neighboring side chain atoms, leading for doubly labeled proteins to a correlation of the orientations of the two spin label side chains. Using nitroxide spin labels exhibiting g-factor and hyperfine coupling anisotropies the DEER spectra shape depends on this orientation. Thus, distance distributions calculated from the DEER spectra under the assumption of an isotropic distribution of orientations may lead to misinterpretations. The determination of spin label orientations therefore would improve the analysis and interpretation of experimentally obtained distance distributions. In addition, conformational changes of proteins accompanied by reorientations of the spin label side chains could be revealed by the investigation of the spin label orientations.

Here, X-band orientation selective DEER measurements were applied on the Vt double mutant Vt901R1/Vt957R1 in order to determine mutual spin label orientations. The DEER spectra recorded at different pump and observer frequency offsets show clear differences, indicative for orientation correlation of the two spin label side chains. Orientation and frequency offset dependent distorted Pake patterns were simulated. Simulated Pake patterns were convoluted with a Gaussian distribution taking distance and orientational distributions into account, and then compared to the experimental spectra by calculation of the overall RMSD for each orientation. The analysis of the particular orientations obtained for each investigated frequency offset leads to an estimate of the angular distribution around the average orientation. In conclusion, it could be shown that the determination of the mutual orientation of protein bound spin labels is possible at X-band frequencies, if the orientation correlation of the spin label pair is strong (as in Vt901R1/Vt957R1). The method established here can be used to determine valuable information about proteins and nucleic acids, expanding the virtue of DEER spectroscopy as a tool for structure determination.

The simulations in this work were done considering a defined inter spin distance and a single mutual spin label orientation. Small distance and dipolar axis distributions were considered by convolution with a narrow Gaussian exhibiting a constant width in the frequency domain. In case of Vt901R1/957R1, this leads to reasonable results, but this is not necessarily the case for other systems. Taking distance distributions into account, such as those obtained by EPR spectroscopy and/or other methods (e.g. RLA) by calculating superpositions of the Pake pattern weighted by the corresponding intensities of the distributions, is likely to improve the method presented here. Moreover, in case of multiple different rotameric states of R1 side chains, a superposition of different orientations has to be considered in the simulation procedure. Hence, a more general approach would be a search and fitting algorithm for the simulation of spectra, governed by multiple distances and orientational distributions. Therefore, spectra, calculated using the orientations extracted from RLA and the corresponding populations for the particular contributions to the overall DEER spectrum (Pake pattern), could be used as initial input for example.

7 Appendix

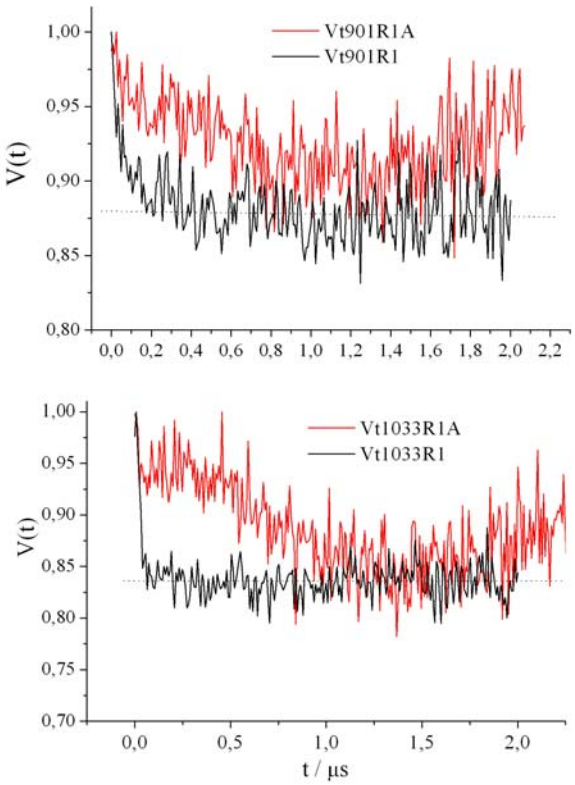

Figure 7.1: Dipolar evolution functions using larger dipolar evolution times obtained for Vt901R1 and Vt1033R1 in the absence (black) and in the presence of F-actin (red). No indications for modulations, exhibiting small dipolar frequencies (large distances) are present in the DEER traces in the absence of actin, whereas the traces obtained for Vt in the presence of actin reveal modulations, governed by smaller frequencies, which indicate the presence of larger inter spin distances.

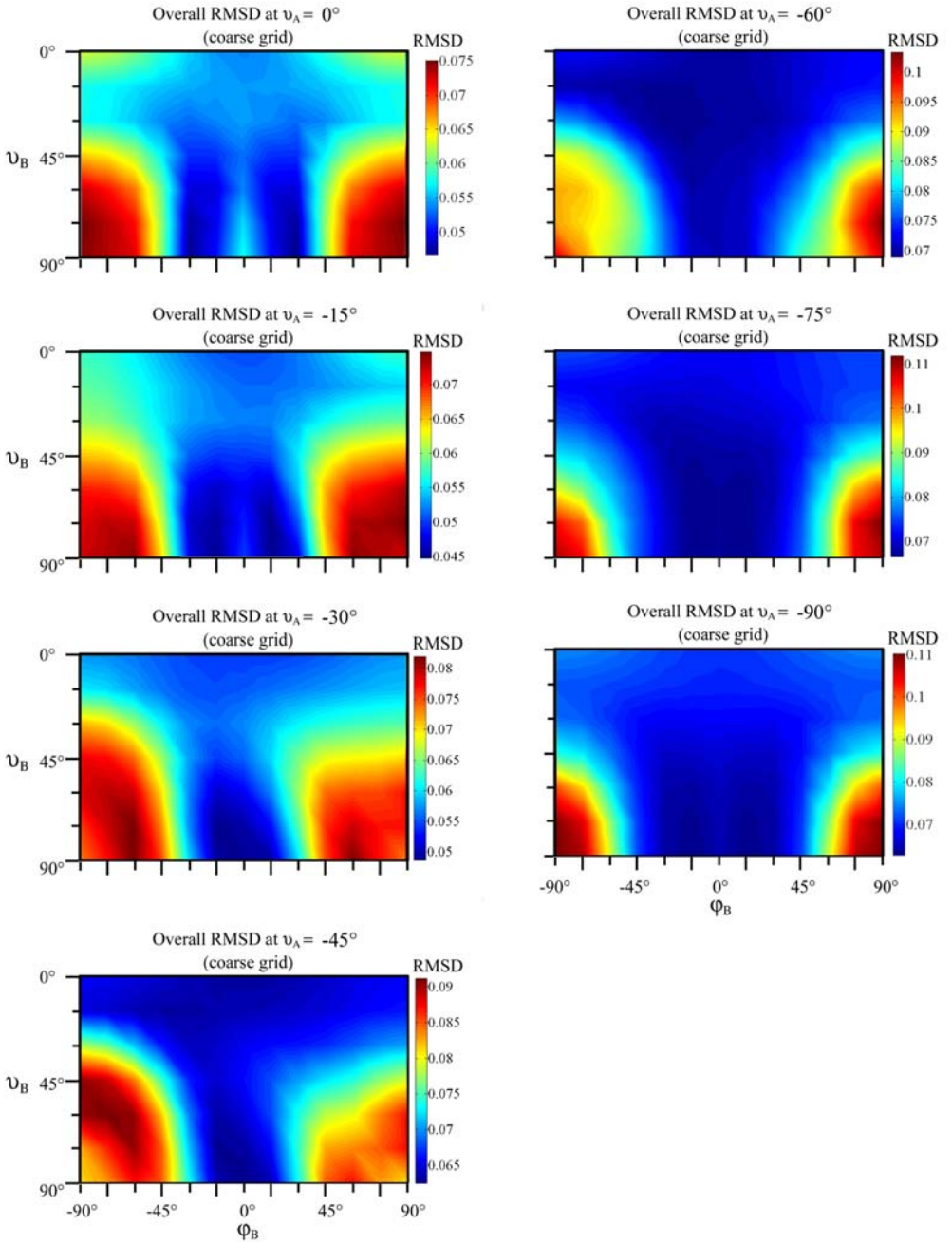

Figure 7.2: RMSD values in dependence of φ_B and ϑ_B at different ϑ_A (coarse grid: 15° steps). The RMSD values are displayed in a color code using dark red as highest and dark blue for the lowest RMSD value. The lowest RMSD was obtained for ϑ_A=-15°, ϑ_B=75° and φ_B=15° (-15°).

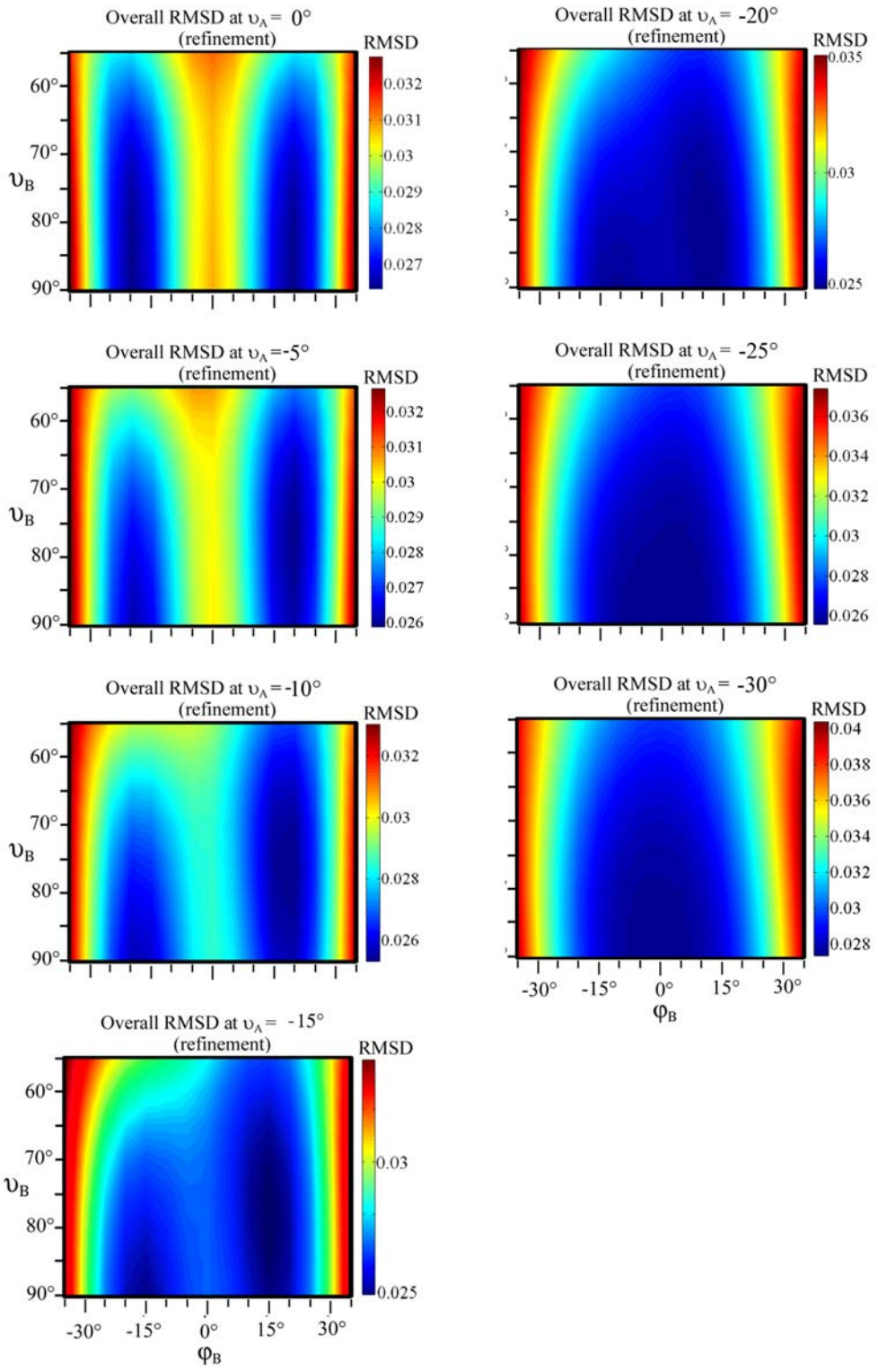

Figure 7.3: RMSD values in dependence of φ_B and ϑ_B at different ϑ_A (refinement range: 5° steps). The RMSD values are displayed in a color code using dark red as highest and dark blue for the lowest RMSD value. The lowest RMSD was obtained at ϑ_A=-15°, ϑ_B=80° and φ_B=15°.

Bibliography

[1] C. Altenbach, W. Froncisz, R. Hemker, H. Mchaourab, and W. L. Hubbell. Accessibility of nitroxide side chains: Absolute heisenberg exchange rates from power saturation epr. *Biophysical Journal*, 89:2103–2112, 2005.

[2] C. Altenbach and W. L. Hubbell. A collision gradient method to determine the immersion depth of nitroxides in lipid bilayers: Application to spin-labeled mutants of bacteriorhodopsin. *Proc. Natl. Acad. Sci.*, 91:1667–1671, 1994.

[3] C. Altenbach, T. Marti, H. Khorana, and W. L. Hubbell. A method to determine transmembrane protein structure: spin-labeling of bacteriorhodopsin mutants. *Science*, 248:1088–1093, 1990.

[4] C. Altenbach, K. Oh, R.J. Trabanino, K. Hideg, and W.L. Hubbell. Estimation of inter-residue distances in spin labeled proteins at physiological temperatures: Experimental strategies and practical limitations. *Biochemistry*, 40:15471–15482, 2001.

[5] P. W. Atkins and R. S. Friedman. *Molecular Quantum Mechanics*.

[6] C. Bakolitsa, D. M. Cohen, L. A. Bankston, A. A. Bobkov, G. W. Cadwell, L. Jennings, D. R. Critchley, S. W. Craig, and R. C. Liddington. Structural basis for vinculin activation at sites of cell adhesion. *Nature*, 430:583–586, 2004.

[7] C. Bakolitsa, J. M. de Pereda, C. R. Bagshaw, D. R. Critchley, and R. C. Liddington. Crystal structure of the vinculin tail suggests a pathway for activation. *Cell*, 99:603–613, 1999.

[8] J.E. Banham, C.M. Baker, S. Ceola, I.J. Day, G.H. Grant, E.J.J. Groenen, C.T. Rodgers, G. Jeschke, and C.R. Timmel. Distance measurements in the borderline region of applicability of cw epr and deer: A model study on a homologous series of spin-labelled peptides. *Journal of Magnetic Resonance*, 191:202–218, 2008.

[9] **C. Beier and H.-J. Steinhoff. A structure-based simulation approach for electron paramagnetic resonance spectra using molecular and stochastic dynamics simulations. *Biophysical Journal*, 91:2647–2664, 2006.**

[10] **L. J. Berliner. *Spin Labeling, Theory and Applications.***

[11] **B. E. Bode, J. Plackmeyer, T. F. Prisner, and O. Schiemann. Peldor measurements on a nitroxide-labeled cu(ii) porphyrin: Orientation selection, spin-density distribution and conformational flexibility. *J. Phys. Chem.*, 112:5064–5073, 2008.**

[12] **P. R. Bois, B. P. O'Hara, D. Nietlispach, J. Kirkpatrick, and T. Izard. The vinculin binding sites of talin and alpha-actinin are sufficient to activate vinculin. *Journal of Biological Chemistry*, 281:7228–7236, 2006.**

[13] **E. Bordignon and H.-J. Steinhoff. In hemminga, m. a. and l. j. berliner, esr spectroscopy in membrane biophysics. *Springer Science and Business Media*, pages 129–164, 2007.**

[14] **C. Brakebusch and R. Fässler. The integrin-actin connection, an eternal love affair. *The EMBO Journal*, 22:2324–2333, 2003.**

[15] **H. Brutlach. *ESR-Hochfeldspektroskopie und Spinsondentechnik zur Untersuchung von Anisotropien in biologischen Makromolekülen.* PhD thesis, Universität Osnabrueck.**

[16] **I. Chandrasekar, T. E. B. Stradal, M. R. Holt, F. Entschladen, B. M. Jockusch, and W. H. Ziegler. Vinculin acts as a sensor in lipid regulation of adhesion-site turnover. *Journal of Cell Science*, 118:1461–1472, 2005.**

[17] **C. Le Clainche and M. Carlier. Regulation of actin assembly associated with protrusion and adhesion in cell migration. *Physiol Rev*, 88:489–513, 2008.**

[18] **D. M. Cohen, H. Chen, R. P. Johnson, B. Choudhury, and S.W. Craig. Two distinct head-tail interfaces cooperate to suppress activation of vinculin by talin. *Journal of Biological Chemistry*, 280:17109–17117, 2005.**

[19] **M. Doebber. *EPR Analysis of a Two-State Conformational Equilibrium in an N. pharaonis HAMP Domain.* PhD thesis, Universität Osnabrueck.**

[20] **J. L. Rodriguez Fernandez, B. Geiger, D. Salomon, I. Sabanay, M. Zö11er, and A. Ben-Ze'ev. Suppression of tumorigenicity in transformed cells after transfection with vinculin cdna. *The Journal of Cell Biology*, 119:427–438, 1992.**

[21] **J.H. Freed, G.V. Bruno, and C.F. Polnasze. Electron spin resonance line shapes and saturation in slow motional region. *Journal of Physical Chemistry*, 75:3385–3399, 1971.**

[22] **P. Gajula. *Computer simulation meets experiment: Molecular dynamics simulations of spin labeled proteins.* Dissertation, Universität Osnabrueck, 2008.**

[23] **P. Gajula, I.V. Borovykh, C. Beier, T. Shkuropatova, P. Gast, and H.-J. Steinhoff. Spin-labeled photosynthetic reaction centres from rhodobacter sphaeroides studied by electron paramagnetic resonance spectroscopy and molecular dynamcis simulations. *Appl. Magn. Reson.*, 31:167–178, 2007.**

[24] **A. Gilmore and K. Burridge. Regulation of vinculin binding to talin and actin by phosphatidyl-inositol-4-5-bisphosphate. *Letters to Nature*, 381:531–535, 1996.**

[25] **J. A. Greenwood, A. B. Theibert, G. D. Prestwich, and J. E. Murphy-Ullrich. Restructuring of focal adhesion plaques by pi 3-kinase. regulation by ptdins (3,4,5)-p(3) binding to alpha-actinin. *Journal of Cell Biology*, 150:627–642, 2000.**

[26] **A. Holt. Q-band esr-spektroskopie spinmarkierter bakteriorhodopsine. Master's thesis, Universität Osnabrück, 2003.**

[27] **J. Holterhues. *Analyse der Signalweiterleitung im spinmarkierten sensorischen Rhodopsin/Transducer-Komplex mittels zeitaufgelöster ESR-Spektroskopie.* Dissertation, Universität Osnabrueck, 2009.**

[28] **S. Hüttelmaier, O. Mayboroda, B. Harbeck, T. Jarchau, B.M. Jokusch, and M. Rüdiger. The interaction of the cell-contact proteins vasp and vinculin is regulated by phosphatidylinositol-4,5-bisphosphate. *Current Biology*, 8:479–488, 1998.**

[29] **W. L. Hubbel and C. Altenbach. Investigation of structure and dynamics in membrane proteins using site directed spin labeling. *Curr. Opin. Struct. Biol.*, 4:566–573, 1994.**

[30] **W. L. Hubbell and C. Altenbach. Investigation of structure and dynamics in membrane proteins using site-directed spin labeling. *Structural Biology*, 4:566–573, 1994.**

[31] **S. Huttelmaier, P. Bubeck, M. Rudiger, and B. M. Jockusch. Characterization of two f-actin-binding and oligornerization sites in the cell-contact protein vinculin. *Eur. J. Biochem*, 247:1136–1142, 1997.**

[32] **K. Jacobsen, W. L. Hubbell, O. P. Ernst, and T. Risse. Details of the partial unfolding of t4 lysozyme on quartz using site-directed spin labeling. *Angew. Chem.*, 45:3874–3877, 2006.**

[33] **M. Janssen, E. Kim, H. Liu, L. M. Fujimoto, A. Bobkov, N. Volkmann, and D. Hanein. A three-dimensional structure of vinculin bound to actin filaments. *Molecular Cell*, 21:271–281, 2006.**

[34] **G. Jeschke. Distance measurements in the nanometer range by pulse epr. *Chem. Phys. Chem.*, 3:927–932, 2002.**

[35] **G. Jeschke. Deer analysis 2006 - a comprehensive software package for analyzing pulsed eldor data. *Appl. Magn. Reson.*, 30:473, 2006.**

[36] **G. Jeschke, M. Sajid, M. Schulte, and A. Godt. Three-spin correlations in double electron-electron resonance. *Physical chemistry chemical physics*, 11:6580–6591, 2009.**

[37] **R. P. Johnson and S. W. Craig. F-actin binding site masked by the intramolecular association of vinculin head and tail domains. *Nature*, 373:261–264, 1995.**

[38] **R.P. Johnson and S. W. Craig. Actin activates a cryptic dimerization potential of the vinculin tail domain. *The Journal of Biological Biochemistry*, 275:95–105, 2000.**

[39] **M. Kühn. *Orientierung von Helix 9 in membrangebundenem Colicin A untersucht mit ESR Spektroskopie und SDSL.* Dissertation, Ruhr-Universität Bochum, 2003.**

[40] **J. P. Klare and H.-J. Steinhoff. Site-directed spin labeling and pulsed dipolar epr (unpublished). 2009.**

[41] **D. Klose. *DEER spectroscopy on the archaeal RNA polymerase subunits F and E.* PhD thesis, Universität Osnabrueck.**

[42] **J. Carlos Lopez, R. M. Fleissner, Z. Guo, A. K. Kusnetzow, and W. L. Hubbell. Osmolyte perturbation reveals conformational equilibria in spin-labeled proteins. *Protein Science*, 18:1637–1652, 2009.**

[43] **A. Martin M. Damian, D. Mesnier, J.-P. Pin, and J.-L. Baneres. Asymmetric conformational changes in a gpcr dimer controlled by g-proteins. *The EMBO Journal*, 25:5693–5702, 2006.**

[44] **D. Margraf, B. E. Bode, A. Marko, O. Schiemann, and T. F. Prisner. Conformational flexibility of nitroxide biradicals determined by x-band peldor experiments. *Molecular Physics*, 105:2153–2160, 2007.**

[45] **V. Martel, C. Racaud-Sultan, S. Dupe, C. Marie, F. Paulhe, A. Galmichei, M. R. Block, and C. Albiges-Rizo. Conformation, localization, and integrin binding of talin depend on its interaction with phosphoinositides. *Journal of Biological Chemistry*, 276:21217–21227, 2001.**

[46] **H. S. Mchaourab, T. Kálai, K. Hideg, and W. L. Hubbell. Determination of the nanostructure of polymer materials by electron paramagnetic resonance spectroscopy. *Biochemistry*, 38:2947–2955, 1999.**

[47] **H. S. Mchaourab, M. A. Lietzow, K. Hideg, and W. L. Hubbell. Motion of spin-labeled side chains in t4 lysozyme. correlation with protein structure and dynamics. *Biochemistry*, 35:7692–7704, 1996.**

[48] **F. M. Megli and K. Sabatini. Epr studies of phospholipid bilayers after lipoperoxidation, inner molecular order and fluidity gradient. *Chemistry and Physics of Lipids*, 125:161–172, 2003.**

[49] **C. Möhl, N. Kirchgeßner, C. Schäfer, K. Küpper, S. Born, G. Diez, W. H. Goldmann, R. Merkel, and Bernd Hoffmann. Becoming stable and strong: The interplay between vinculin exchange dynamics and adhesion strength during adhesion site maturation. *Cell Motility and the Cytoskeleton*, 66:350–364, 2009.**

[50] **C. Mierke, P. Kollmannsberger, D. Zitterbart, G. Diez, T. M. Koch, S. Marg, W. H. Ziegler, W. H. Goldmann, and B. Fabry. Vinculin facilitates cell invasion into 3d collagen matrices. *JBC*, 285:13121–13130, 2010.**

[51] C. T. Mierke, P. Kollmannsberger, D. P. Zitterbart, J. Smith, B. Fabry, and W. H. Goldmann. Mechano-coupling and regulation of contractility by the vinculin tail domain. *Biophysical Journal*, 94:661–670, 2008.

[52] A. D. Milov and Y. D. Tsvetkov. Double electron-electron resonance in electron spin echo: Conformations of spin-labeled poly-4-vinilpyridine in glassy solutions. *Appl. Magn. Reson.*, 12:495–504, 1997.

[53] G.T.V. Nhieu and T. Izard. Vinculin binding in its closed conformation by a helix addition mechanism. *The EMBO Journal*, 26:4588–4596, 2007.

[54] K. J. Oh, C. Altenbach, R. J. Collier, and W. L. Hubbell. Site-directed spin labeling of proteins, applications to diphtheria toxin. *Methods in Molecular Biology*, 145:147–169, 2000.

[55] S. M. Palmer, M. D. Schaller, and S. L. Campbell. Vinculin tail conformation and self-association is independent of ph and h906 protonation. *Biochemistry*, 47:12467–12475, 2008.

[56] M. Pannier, S. Veit, A. Godt, G. Jeschke, and H. W. Spiess. Dead-time free measurement of dipole-dipole interactions between electron spins. *Journal of Magnetic Resonance*, 142:331–340, 2000.

[57] M. Pfeiffer, T. Rink, K. Gerwert, D. Oesterhelt, and H.-J. Steinhoff. Site-directed spin-labeling reveals the orientation of the amino acid side-chains in the e-f loop of bacteriorhodopsin. *J. Mol. Biol.*, 287:163–171, 1999.

[58] M. Plato, H.-J. Steinhoff, C. Wegener, J. Torring, A. Savitsky, and K. Moebius. Molecular orbital study of polarity and hydrogen bonding effects on the g and hyperfine tensors of site directed no spin labelled bacteriorhodopsin. *Frontiers in Bioscience*, 100:3711–3721, 2002.

[59] Ye. Polyhach, A. Godt, C. Bauer, and G. Jeschke. Spin pair geometry revealed by high-field deer in the presence of conformational distributions. *Appl. Magn. Reson.*, 185:118–129, 2007.

[60] Ye. Polyhach and G. Jeschke. Distance measurements on spin-labelled biomacromolecules by pulsed electron paramagnetic res-

onance. *Physical Chemistry Chemical Physics*, 9:1895–1910, 2007.

[61] C. P. Poole. *Electron Spin Resonance.* 1983.

[62] L. Pulagam. *PHD-THESIS Universität Osnabrück.* PhD thesis, 2006.

[63] M. D. Rabenstein and Y.-K. Shin. Determination of the distance between two spin labels attached to a macromolecule. *Proc. Natl. Acad. Sci. USA*, 92:8239–8344, 1995.

[64] N. Radzwill, W. Thevis, V. Lenz, D. Brandenburg, A. Antson, G. Dodson, A. Wollmer, and H.-J. Steinhoff. Determination of interspin distances between spin labels attached to insulin: Comparison of electron paramagnetic resonance data with the x-ray structure. *Biophys. J.*, 73:3287–3298, 1997.

[65] M. Retzlaff, F. Hagn, L. Mitschke, M. Hessling, F. Gugel, H. Kessler, K. Richter, and J. Buchner. Asymmetric activation of the hsp90 dimer by its cochaperone aha1. *Molecular Cell*, 37:344–354, 2010.

[66] T. Risse and W. L. Hubbell. Structure and dynamics of annexin 12 bound to a planar lipid bilayer. *Physical Review Letters*, 91:188101/1–188101/4, 2003.

[67] A. Savitsky, A. Dubinskii, M. Flores, W. Lubitz, and K. Möbius. Orientation-resolving pulsed electron dipolar high-field epr spectroscopy on disordered solids: I. structure of spin-correlated radical pairs in bacterial photosynthetic reaction centers. *Journal of Physical Chemistry*, 111:6245–6262, 2007.

[68] A. Savitsky, M. Kühn, D. Duche, K. Möbius, and H.-J. Steinhoff. Spontaneous refolding of the pore-forming colicin a toxin upon membrane association as studied by x-band and w-band high-field electron paramagnetic resonance spectroscopy. *J. Phys. Chem.*, 108:9541–9548, 2004.

[69] O. Schiemann, P. Cekan, D. Margraf, T. F.Prisner, and S. T. Sigurdsson. Relative orientation of rigid nitroxides by peldor: beyond distance measurements in nucleic acids. *Angew. Chem.*, 48:3292–3295, 2009.

[70] T. Schlick. *Molecular modeling and simulation : an interdisciplinary guide.* 2006.

[71] A. Schweiger and G. Jeschke. *Princliples of Pulse EPR*. 2001.

[72] C. P. Slichter. *Principles of magnetic resonance*. 1996.

[73] P. A. Steimle, J. D. Hoffert, N. B. Adey, and S. W. Craig. Polyphosphoinositides inhibit the interaction of vinculin with actin filaments. *The Journal of Biological Biochemistry*, 274:18414–18420, 2006.

[74] H.-J. Steinhoff. Methods for study of protein dynamics an protein-protein interaction in proteinubiquitination by electron paramagnetic resonance spectroscopy. *Frontiers in Bioscience*, 7:97–110, 2002.

[75] S. Stoll and A. Schweiger. *In Hemminga and M. A. and L. J. Berliner, ESR Spectroscopy in Membrane Biophysics*. 2007.

[76] M.C. Subauste, O. Pertz, E.D. Adamson, C.E. Turner, S. Junger, and Hahn KM. Vinculin modulation of paxillin-fak interactions regulates erk to control survival and motility. *J. Cell Biology*, 165:371–381, 2004.

[77] A. P. Todd, J. Cong, F. Levinthal, C. Levinthal, and W. L. Hubbell. Site-directed mutagenesis of colicin e1 provides specific attachment sites for spin labels whose spectra are sensitive to local conformation. *Proteins*, 6:294–305, 1989.

[78] M. van Gastel. Pulsed epr spectroscopy. *Photosynth Res*, 102:367–373, 2009.

[79] C. Wegener. *Multifrequenz-(9 GHz und 95 GHz) ESR-Spektroskopie zur Analyse der Dynamik und Polarität von ortsspezifisch spinmarkiertem Bakteriorhodopsin*. PhD thesis, Ruhr-Universität Bochum.

[80] J. A. Weil, J. R. Bolton, and J. E. Wertz. *Electon Paramagnetic Resonance*.

[81] W. Xu, H. Baribault, and E. D. Adamson. Vinculin knockout results in heart and brain defects during emryonic emryonic development. *Development 1998a*, 125:327–337, 1998.

[82] W. H. Ziegler, R. C. Liddington, and D. R. Critchley. The structure and regulation of vinculin. *TRENDS in Cell Biology*, 16:453–460, 2006.

[83] W. H. Ziegler, U. Tigges, A. Zieseniss, and B. M. Jockusch. A lipid-regulated docking site on vinculin for protein kinase c. *J. Biol. Chem.*, 277:7396–7404, 2002.

Acknowledgement

First of all, I would like to express my deepest sense of gratitude to my supervisor Prof. Dr. Heinz-Jürgen Steinhoff for his guidance, excellent advice throughout this study, encouragement and support in many respects, the opportunity to work in this fascinating field, and beeing part of a likewise fascinating working group.

My sincere thanks to Prof. Dr. Manfred Neumann for his willingness to provide the second opinion, for the excellent work as speaker of the *Ph.D. Program* and for every kind of support during my studies in Osnabrueck.

I would like to express my gratitude to my scholarship sponsors *Ph.D. program of the State of Lower Saxony in Osnabrueck* for financing my study.

I gratefully acknowledge the tremendous support of Dr. Wolfgang H. Ziegler, Franziska Dietrich from IZKF Leipzig, and Ulrike Fock for providing a vast quantity of samples and for a lot of discussion not only about biological issues. I am thankful to Dr. Yevhen Polyhach (ETH Zürich) for many fruitful discussions concerning orientation selective DEER and for the great help in data analysis. I hope the three evil angles are not appearing in your dreams anymore.

I am indeed thankful to all colleagues of "my" working group. Especially, i have to mention Dr. Johann Klare for many, not only subject-specific, discussions. Your wide knowledge in chemistry, biology and physics was an immense help for me. All the best for your future and I hope, you will always take it from (and thereby reach) the top. I also thank Daniel for a lot of discussions, for starting measurements on weekend morning hours and for showing the absinth-vertigo effect. Many thanks to Sabine among others for a very amusing time in Berlin and creating earworms like: "Blau, blau, blau wie der Len...". I thank Ioan, the pyromanian, not only for letting me kick his ass in "MTG" every time, but also for the opportunity to work together with a genuine and sincere character. Micha, thank you for the amazing Pendulum-Tarantöse-Alaska-Seelachs-Sauce-des-Todes weekend in London. I hope there will be some more in the future. I am grateful to Julia for the nice time. Maybe i would not have come so far, if you wouldn't have let me copy numerous of homeworks during school times. Special thanks go to Meike (Maleikä). Here, it is really too much to mention and hard for me to pick out a representative example. Just one advise for your future: bananas are really more durable in a fridge.

I would like to extend my thanks to my office colleges: Vitali for relaxing and amusing smoking sessions, Dorith for her endurance to listen to stupid "man"-discussions, for saving me many times from dying of thirst and for introducing the gothic scene (Yes, Daniel did also his contribution).
Leszek deserves a loud mention: Thank you for the long friendship and for sharing the special kind of humour, *flash(12:30): "H"*. I stopped writing down all hilarious phrases and moments, because it would have been more effort than writing this thesis. It was really the best atmosphere in an office, that i could imagine. Thank you a lot.

I also thank people from other working groups, who have helped me in scientific and non-scientific ways, especially Mehmet Kadiroglu and Henning Wenke.

My deep and sincere thanks to my friends Christian and Kai. Friendship needs no words, however: "Danke für die Freundschaft! Danke, dass ihr treu wart! Ich liebe euch wie das Leben und das Licht! Ich habe euch und das haben die Meisten nicht!". And many thanks to all other people, who contribute to my life in a positive manner.

Finally, I take this opportunity to express my profound gratitude to my beloved family. Thank you for being there (for me), thank you for everything!

"There will come a time, when you believe everything is finished. That will be the beginning.". (Louis L'Amour)

Declaration

I declare that the submitted work has been completed by me the undersigned and that I have not used any other than permitted reference sources or materials. All references and other sources used by me have been appropriately acknowledged in the work. I further declare that this work has not been submitted for the purpose of academic examination, either in its original or similar form, anywhere else.

Osnabrueck, Germany
Mai, 2010

Christoph Abé